

UC Berkeley

UC Berkeley Electronic Theses and Dissertations

Title

Nitrous Oxide and Molecular Nitrogen Isotopic Compositions and Aerosol Optical Properties: Experiments and Observations Relevant to Planetary Atmospheres

Permalink

<https://escholarship.org/uc/item/5vs5n9x5>

Author

Croteau, Philip Louis

Publication Date

2010

Peer reviewed|Thesis/dissertation

Nitrous Oxide and Molecular Nitrogen Isotopic Compositions and Aerosol Optical Properties:
Experiments and Observations Relevant to Planetary Atmospheres

by

Philip Louis Croteau

A dissertation submitted in partial satisfaction of the

requirements for the degree of

Doctor of Philosophy

in

Chemistry

in the

Graduate Division

of the

University of California, Berkeley

Committee in charge:

Professor Kristie A. Boering, Chair

Professor Ronald C. Cohen

Professor Imke de Pater

Spring 2010

Nitrous Oxide and Molecular Nitrogen Isotopic Compositions and Aerosol Optical Properties:
Experiments and Observations Relevant to Planetary Atmospheres

© 2010

by

Philip Louis Croteau

Abstract

Nitrous Oxide and Molecular Nitrogen Isotopic Compositions and Aerosol Optical Properties: Experiments and Observations Relevant to Planetary Atmospheres

by

Philip Louis Croteau

Doctor of Philosophy in Chemistry

University of California, Berkeley

Professor Kristie A. Boering, Chair

Nitrous oxide (N_2O) and molecular nitrogen (N_2) isotopic compositions and aerosol optical properties were investigated through experiments and observations to elucidate their roles in atmospheric radiative transfer and chemistry. In Earth's atmosphere, the isotopic composition of N_2O , a potent greenhouse gas, is a useful tool for investigating its sources and sinks. N_2 is the main component of the atmospheres of Earth and Titan, and isotope effects in its photoionization may lead to isotopic fractionation. The optical properties of aerosols, a component of most planetary atmospheres, determine how they affect radiative transfer. A polarimeter was developed to measure aerosol optical properties *in situ* in an existing apparatus.

Three sets of measurements of N_2O isotopic composition provide new insight into its budget. First, a time-series from 1940 to 2005 from firn and archived air samples is consistent with the observed N_2O increase being largely due to isotopically light N_2O emissions from agriculture and reveals seasonal cycles due to the seasonally-varying influences of multiple N_2O sources and stratosphere-troposphere exchange. Second, measurements from the tropical free troposphere show coherent vertical variations in N_2O isotopic compositions consistent with the persistent influence of a regional surface source, most likely the ocean. Third, samples from the marine boundary layer with anomalously high N_2O mixing ratios and perturbed isotopic compositions were used to deduce a source isotopic composition that is perhaps representative of N_2O emitted from the South Atlantic Ocean.

Isotope effects in the non-dissociative photoionization of N_2 — investigated by measuring the photoionization efficiency spectrum for its three isotopologues — clarify peak identities and show that these previously ignored isotope effects may be important in planetary atmospheres. The shifts in peak energy due to isotopic substitution show that the controversial peak at 15.68 eV for $^{14}\text{N}_2$ is most likely due to a Rydberg state converging to the $v'=2$ level of the $\text{A}^2\Pi_u \text{N}_2^+$ state. A model of Titan's atmosphere shows that isotopic self-shielding in $^{14}\text{N}_2$ photoionization may cause isotopic fractionation between N_2 and other N-bearing molecules distinct from that caused by N_2 photodissociation, providing a possible mechanism for determining the relative importance of ion versus neutral photochemistry.

For Sweetie and the Plucot

Table of contents

List of figures	iv
List of tables	x
1. Introduction and overview.....	1
References	5
2. Methods	7
2.1 Measuring the isotopic composition of atmospheric N ₂ O at natural abundance.....	7
2.1.1 Measurement procedures.....	8
2.1.2 Reference standard calibration	10
2.1.3 Converting measurements to the Toyota Yoshida [1999] scale.....	11
2.1.4 Baseline issue for δ^{31} measurements	13
2.2 Box model of the isotopic composition of atmospheric N ₂ O.....	13
2.2.1 Model formulation.....	13
2.2.2 Model optimization	16
2.3 Data analysis for photoionization of the isotopologues of N ₂	17
2.4 Design and testing of a rotating quarter-wave plate polarimeter	24
2.4.1 Introduction to light scattering and Stokes polarimetry	24
2.4.2 Polarimeter construction and experimental set-up	27
2.4.3 Performance tests.....	29
2.4.4 Steps to incorporate the polarimeter in experiments	33
References	34
3. Trends, seasonal cycles and interannual variability in the isotopic composition of atmospheric nitrous oxide between 1940 and 2005	37
3.1 Methods	43
3.1.1 Firm air details: Sampling and storage.....	43
3.1.2 Firm air details: Corrections and mean age	44
3.1.3 Archived air details: Sampling and storage.....	44
3.1.4 IRMS Measurements	44
3.1.5 Box model details	45
3.1.6 Time series analysis details	45
3.1.7 Ratios of normalized seasonal amplitudes	45
References	47
Supplementary figures.....	52
Supplementary tables.....	63
4. The effect of local and regional sources on the isotopic composition of nitrous oxide in the tropical free troposphere and tropopause layer	65
4.1 Introduction	65
4.2 Methods	67
4.3 Results and discussion.....	71

4.3.1 Averaged vertical profiles in the tropics	71
4.3.2 Correlations between N ₂ O isotopic compositions and surface tracer mixing ratios	76
4.3.3 Isotopic composition in a combustion plume	79
4.4 Conclusions	80
Appendix	81
References	82
Supplementary figures	87
Supplementary tables.....	90
5. The isotopic composition of nitrous oxide over the ocean on a cruise between South Africa and Chile.....	94
5.1 Introduction	94
5.2 Methods	95
5.3 Results and discussion.....	102
5.4 Conclusions	107
References	109
6. Experimental determination of isotope effects in the non-dissociative photoionization of molecular nitrogen	112
6.1 Introduction	112
6.2 Methods	113
6.3 Results and discussion.....	116
6.4 Conclusions	123
References	124

List of figures

- 2.1** A schematic diagram of nitrous oxide, including labels for the central (α) and terminal (β) nitrogen atoms. **7**
- 2.2** A diagram of the CF-PreCon-GC-IRMS setup used for the nitrous oxide isotopic composition measurements reported throughout this dissertation (adapted from Park [2005]). **9**
- 2.3** Schematic of a two-box model of the isotopic composition of atmospheric nitrous oxide. **14**
- 2.4** Contour plot of $\delta\chi^2$ ($=\chi^2-\chi^2_{\min}$) between model output and measurements for χ^2 minimization runs for $\delta^{15}\text{N}^{\text{bulk}}$ for the natural ($\delta^{15}\text{N}_{\text{NAT}}^{\text{bulk}}$) and anthropogenic ($\delta^{15}\text{N}_{\text{ANT}}^{\text{bulk}}$) N_2O sources. The vertical and horizontal lines intersect the axes at the 95.4% confidence intervals for $\delta^{15}\text{N}_{\text{ANT}}^{\text{bulk}}$ (x-axis) and $\delta^{15}\text{N}_{\text{NAT}}^{\text{bulk}}$ (y-axis). **16**
- 2.5** Comparison of the raw and calibrated energy scales for three runs on two different days between 15.5 and 16.5 eV. The $^{14}\text{N}_2$ data from two runs performed on August 30, 2009 (black squares and blue circles) and one run performed on August 31, 2009 (red triangles) are shown. The top panel shows all the data on the raw energy scale (from the monochromator reading), the middle panel shows the data obtained on August 30 on the raw energy scale and the data from August 31 data on the raw energy scale with a -40 meV offset applied, and the bottom panel shows the data on the calibrated energy scale. The vertical lines represent the peak energies from Lofthus and Krupenie [1977] and used for the calibration. **17**
- 2.6** All of the runs on their calibrated energy scales. The vertical lines represent the peak energies used in the calibration from Lofthus and Krupenie [1977]. There is agreement between the calibrated peak energies and the values used in the calibration to within the 6.5 meV bandwidth of the experiment. **21**
- 2.7** Steps in the merging procedure for the $^{14}\text{N}_2$ photoionization efficiency spectrum. All data are shown on the calibrated energy scale. The top panel shows raw intensity for each run, the middle panel shows the data after the normalization was carried out, and the bottom panel shows the merged data after overlapping points were removed. **23**

- 2.8** Diagram of the rotating quarter-wave plate (QWP) polarimeter. The QWP is rotated by an angle, ϕ , which is controlled with a computerized rotation stage, relative to a stationary linear polarizer (LP). The light passes first through the QWP, then the LP, and finally into a photodiode detector and, based on how the optical components alter the polarization state of the light which passes through them, the signal intensity as a function of ϕ , $I(\phi)$, is used to determine the polarization state. **25**
- 2.9** Experimental setup for scattering matrix phase function determination; the polarimeter components are shown in Figure 2.8. **28**
- 2.10** Initial results for the retrieval of a linear polarization state for (a) $\psi=0^\circ$ and (b) $\psi=90^\circ$. The Stokes vectors $\{S_0, S_1, S_2, S_3\}$ are normalized to S_0 . P is the degree of polarization and ψ is the azimuth angle. The line is a least-squares fit to Equation 2.14. **30**
- 2.11** Measured phase functions for the Stokes vector elements (a) S_0 , (b) S_1 , (c) S_2 , and (d) S_3 for an aqueous dispersion of polystyrene latex spheres (diameter = $1.998 \pm 0.022 \mu\text{m}$, concentration = $7.5 \times 10^6 \text{ mL}^{-1}$, Refractive index = 1.58 @ 588 nm), with incident light polarizations of $\psi=0^\circ$ (circles) and $\psi=90^\circ$ (squares). **31**
- 2.12** Measured scattering matrix elements (circles) for (a) F_{11} and (b) $-F_{12}/F_{11}$ for an aqueous dispersion of standard polystyrene latex spheres (diameter = $1.998 \pm 0.022 \mu\text{m}$, concentration = $7.5 \times 10^6 \text{ mL}^{-1}$, Refractive index = 1.58 @ 588 nm), along with the results of Mie theory calculations for scattering at 633 nm by particles with a refractive index of 1.58 and a normal size distribution of $1.998 \mu\text{m}$ with a standard deviation of 1% (solid line) and 5% (dashed line) in a medium with a refractive index of 1.33. **32**
- 3.1** Measurements of (a) N_2O , and (b) $\delta^{15}\text{N}$ (‰ vs. air- N_2), (c) $\delta^{18}\text{O}$ (‰ vs. VSMOW), (d) $\delta^{15}\text{N}^\alpha$ (‰ vs. air- N_2) of N_2O ($\delta^{15}\text{N}^\beta$ and Site Preference are not shown) versus estimated mean age (for Antarctic firn samples; blue circles) or collection date (for archived Cape Grim air; black squares). Archived air samples are denoted by solid back circles, firn air samples from DSSW19K and DSSW20K by filled blue squares. The Poinsett fir air measurements (green triangles) have not been corrected for gravitation and diffusion effect in the firn (see Methods). Lines are unweighted linear least squares fits for the two data sets. 1σ error bars reflect the measurement uncertainty and, for the firn air samples, the fractionation corrections. **39**

- 3.2** Mean seasonal cycles from the time series analysis of the Cape Grim archived air measurements using a one-harmonic fit for (a) N₂O (in ppbv), and (b) δ¹⁵N (‰ vs. air-N₂), (c) δ¹⁵N^α (‰ vs. air-N₂), and (d) δ¹⁸O (‰ vs. VSMOW) of N₂O; and using a two-harmonic fit for (e) N₂O (in ppbv), and (f) δ¹⁵N (‰ vs. air-N₂), (g) δ¹⁵N^α (‰ vs. air-N₂), and (h) δ¹⁸O (‰ vs. VSMOW) of N₂O. Error bars indicate one standard deviation in the fits. **41**
- 3.S1** Model estimates based on a two-box model (solid curves) and measurements. (a) N₂O mixing ratios from this study (open circles) and N₂O records from the Law Dome ice core and firn air of MacFarling Meure *et al.* [MacFarling-Meure *et al.*, 2006] (open squares); (b) same for δ¹⁵N; (c) same for δ¹⁸O; (d) same for δ¹⁵N^α. For the isotopic compositions, (b), (c), and (d) 68% (dotted lines) and 95% (dashed lines) confidence intervals from the χ² minimization are shown. **52**
- 3.S2** Results of the time series analysis to extract a long-term trend and mean seasonal cycle from the Cape Grim archived air sample measurements for the 1-harmonic case (a) N₂O mixing ratio, (b) δ¹⁵N, (c) δ¹⁵N^α, and (d) δ¹⁸O and the 2-harmonic case (e) N₂O mixing ratio, (f) δ¹⁵N, (g) δ¹⁵N^α, and (h) δ¹⁸O. Top left panel: the statistical smoothing for long-term trend; Middle left and bottom left panels: the resulting growth ratios in ppb yr⁻¹ (a) and (e) or ‰ yr⁻¹ (b), (c), (d), (f), (g), and (h) and ‰ yr⁻¹; Top right panel: residuals from the smooth curve; Middle right panel: resulting seasonal cycles; and bottom right panel: the mean seasonal cycle. **53**
- 3.S3** Scatter plot of δ¹⁵N^α versus δ¹⁵N of N₂O. Shown are measurements from the lower stratospheric (filled pink circles, [Park *et al.*, 2004]), from tropical soil emissions (empty green squares; [Park *et al.*, 2010]), from the eastern tropical North Pacific ocean (empty blue and black diamonds; [Yamagishi *et al.*, 2007]), and a tropical biomass burning plume (filled red squares; [Croteau *et al.*, 2010]). The solid lines corresponding to each data set are the slope derived from a Williamson-York linear regression of the data, which represents the ratio of enrichment factors ε(¹⁵N^α)/ε(¹⁵N). Inset: normalized seasonal amplitudes for δ¹⁵N^α and δ¹⁵N of N₂O; the slope is also equivalent to ε(¹⁵N^α)/ε(¹⁵N); see Methods. **61**
- 3.S4** Residuals from the 2-harmonic time series analysis of the Cape Grim archived air measurements for (a) N₂O, (b) δ¹⁵N, (c) δ¹⁵N^α, and (d) δ¹⁸O. The largest residuals from the fit occur in 1997, implying a linkage with the large 1997-1998 ENSO event. **62**
- 4.1** Whole air samples analyzed for the isotopic composition of N₂O for the CRAVE and TC⁴ missions. Symbols show sampling location given by altitude (y-axis) vs. latitude (x-axis) for the CRAVE WB-57 samples (squares), TC⁴ WB-57 samples (triangles), and TC⁴ DC-8 samples (circles), colorscaled by the isotopic composition of N₂O: (a) δ¹⁵N^{bulk}, (b) δ¹⁵N^α and (c) δ¹⁸O. Aircraft landings in Costa Rica occur at 10°N, while other descents occur as dives on various flights, as noted in the text. **70**

- 4.2** Vertical profiles of the isotopic composition of N₂O for samples collected at latitudes <11°N: (a) $\delta^{15}\text{N}^{\text{bulk}}$, (b) $\delta^{15}\text{N}^{\alpha}$, and (c) $\delta^{18}\text{O}$ for the CRAVE WB-57 samples (circles), the TC⁴ WB-57 samples (triangles), and the TC⁴ DC-8 samples (squares). Measured values were binned and averaged in 1-km intervals. Error bars in each panel show the standard deviation of the mean for each bin, while the numbers in (a) give the number of samples in each bin; bins for which there is only one sample are indicated by dashed error bars. For reference, the tropopause was located on average at ~16.5 km during TC⁴ and ~17.5 km during CRAVE, as noted in the text. For comparison, the gray shading in each panel shows the $\pm 1\sigma$ (N=288 for $\delta^{15}\text{N}^{\text{bulk}}$ and $\delta^{18}\text{O}$ and N=239 for $\delta^{15}\text{N}^{\alpha}$) variability in measured tropospheric N₂O isotopic compositions in air sampled on the UCB campus (37.87°N, 122.26°W) between September 2001 and November 2006. **72**
- 4.3** Vertical profiles of the mixing ratio (open symbols) and $\delta^{15}\text{N}^{\text{bulk}}$ (closed symbols) of N₂O, averaged into 0.5 km bins for samples collected at latitudes <11°N and altitudes >15km for (a) CRAVE and (b) TC⁴. **73**
- 4.4** Individual measurements of $\delta^{15}\text{N}^{\text{bulk}}$ of N₂O for samples from the tropical lower stratosphere (<11°N and (a) > 17 km for CRAVE and (b) > 16 km for TC⁴) are shown here plotted in a Rayleigh isotope fractionation format, i.e., as $\ln(1 + \delta^{15}\text{N}^{\text{bulk}}/1000)$ vs. $\ln([\text{N}_2\text{O}]/[\text{N}_2\text{O}]_0)$, where $[\text{N}_2\text{O}]_0$ is the N₂O mixing ratio for air entering the stratosphere, taken to be the average of the N₂O mixing ratios measured below the cutoff altitude, 319.4 ± 0.9 and 320.7 ± 0.4 for CRAVE and TC⁴, respectively. **75**
- 4.5** Tracer-tracer plots of $\delta^{18}\text{O}$ of N₂O vs. mixing ratios of (a) CH₃ONO₂, (b) C₂H₅ONO₂, and (c) CH₃I from the 08 August 2007 DC-8 samples, parsed into sections of the flight corresponding to a dive over the Pacific (circles; latitude = 4.3 to 5.2°N, longitude = 79.1 to 83.1°W, altitude = 0.5 to 11.6 km), a dive over the Colombian jungle (triangles; latitude = 1.6 to 3.0°N, longitude = 70.5 to 79.1°W, altitude = 1.5 to 11.6 km), and the DC-8 cruise region in between (squares; latitude = 3.4 to 4.3°N, longitude = 71.9 to 79.1°W, altitude = 11.6 km). The values of the correlation coefficient, R, are given in the figure legends, while the regression line shown is for the Pacific Ocean dive measurements. **77**
- 4.6** (a) Vertical profiles of the mixing ratios of propane (squares; in pptv), ethane (circles; in pptv and offset by 500 pptv), benzene (triangles; in 100×pptv and offset by 2000 pptv), and tetrachloroethylene (C₂Cl₄, diamonds; in pptv, upper x-axis) from the WB-57 flight of 05 August 2007; solid symbols show the samples designated here as being in the combustion plume at ~14 km altitude. (b) Correlation between the N₂O isotopic composition and the ethane mixing ratio for the combustion plume samples in (a) ($\delta^{15}\text{N}^{\text{bulk}}$:squares; $\delta^{15}\text{N}^{\alpha}$:triangles; Site Preference (see text): circles; and $\delta^{18}\text{O}$: diamonds). **80**

4.S1	Correlations between $\delta^{15}\text{N}^{\text{bulk}}$ of N_2O versus various tracers for the DC-8 flight segments on 08 August 2007 over the Pacific Ocean (circles, solid regression line) and the Colombian jungle (triangles, dashed regression line). Points for the cruise between the dives are shown without regression lines (squares) Values for the correlation coefficients, R, and the probability, P, that N measurements (i.e., the number of points in the fit) of two uncorrelated variables would give a correlation coefficient as large as R are given in the figure. See the Figure 4.5 caption for additional information; the data are given in Supplementary Tables 4.S3 and 4.S4.	87
4.S2	The same as for Figure 4.S1 but for $\delta^{15}\text{N}^{\alpha}$ of N_2O .	88
4.S3	The same as for Figure 4.S1 but for $\delta^{18}\text{O}$ of N_2O .	89
5.1	Ship track for the Marion Dufresne. The first leg of the cruise, from South Africa to Chile (solid line) was from January 20 to February 5, 2007. The second leg, from Chile to South Africa (dashed line) was from March 1 to March 20, 2007. Sampling locations for N_2O mixing ratio outliers are shown (exes). Also indicated is the approximate location where the ship encountered phytoplankton blooms between January 31 and February 3, 2007.	96
5.2	Nitrous oxide isotopic composition as a function of mixing ratio for (a) $\delta^{15}\text{N}^{\text{bulk}}$, (b) $\delta^{18}\text{O}$, (c) $\delta^{15}\text{N}^{\alpha}$, (d) $\delta^{15}\text{N}^{\beta}$, and (e) Site Preference. Solid lines represent the mean of all samples excluding the 4 with outlying N_2O mixing ratios outliers and the dashed lines are the corresponding standard deviations.	99
5.3	Keeling plots for (a) $\delta^{15}\text{N}^{\text{bulk}}$, (b) $\delta^{18}\text{O}$, (c) $\delta^{15}\text{N}^{\alpha}$, (d) $\delta^{15}\text{N}^{\beta}$, and (e) Site Preference for samples with outlier N_2O mixing ratios. $[\text{N}_2\text{O}]^{-1}$ error bars shown are based on an uncertainty of 1.2% in $[\text{N}_2\text{O}]$ and isotopic composition error bars are standard deviations of the means. Since the actual mixing ratio uncertainty is unknown, several types of regression lines are shown for comparison: unweighted (dotted), weighted only by uncertainty in y-data (dashed), weighted by uncertainty in both x- and y-data [Cantrell, 2008] assuming 1.2% uncertainty (solid), and weighted by uncertainty in both x- and y- data [Cantrell, 2008] assuming 5% uncertainty. The y-intercept values, which represent the source isotopic composition under the assumptions of the Keeling plot analysis, are given in Table 5.3.	103

- 5.4** Comparison between (a) $\delta^{15}\text{N}^{\text{bulk}}$, (b) $\delta^{18}\text{O}$, and (c) Site Preference of N_2O for the source in the oligotrophic subtropical North Pacific gyre as a function of its fractional contribution to N_2O at the isotopic minimum (see text) from measurement-based isotopic mass balance calculations by *Popp et al.* [2002] (given by the squares and their connecting lines) and the source isotopic compositions determined by Keeling plot analyses for the N_2O -outlier samples from the doubly-weighted regression assuming 1.2% uncertainty in $[\text{N}_2\text{O}]$ (solid horizontal line) and the 1σ uncertainty in those values (dashed lines); see also Table 5.3. **105**
- 6.1** Normalized photoionization efficiency spectra for $^{14}\text{N}_2$, $^{15}\text{N}^{14}\text{N}$, and $^{15}\text{N}_2$ for (a) 15.5 – 17.0 eV and (b) 17.0 – 18.9 eV. The raw data have been scaled by the inverses of their respective calculated mole fractions (see text) to represent a 1:1:1 mixture. **116**
- 6.2** PIE spectra for $^{14}\text{N}_2$ (circles) and $^{15}\text{N}_2$ (triangles) from 15.6 to 15.7 eV. Dashed lines indicate peak-centers based on Voigt-profile fits. Based on the measured 16 meV isotope shift between $^{14}\text{N}_2$ and $^{15}\text{N}_2$, the peak at 15.68 eV for $^{14}\text{N}_2$ most likely corresponds to the autoionizing Rydberg state, $(A^2\Pi_u v'=2)4s\sigma_g^1\Pi_u$. **117**
- 6.3** Ratios of photoionization cross-sections for (a) $^{14}\text{N}_2/^{15}\text{N}^{14}\text{N}$ and its inverse $^{15}\text{N}^{14}\text{N}/^{14}\text{N}_2$ and (b) $^{14}\text{N}_2/^{15}\text{N}_2$ and its inverse $^{15}\text{N}_2/^{14}\text{N}_2$ over the range 15.5 – 17.5 eV (Note that because the isotope shifts are negligible between 17.5 and 18.9, this region is not included here). The solar spectrum at 625 km in Earth's atmosphere recorded by the TIMED/SEE instrument is shown in (c) over the same energy range. **120**
- 6.4** Left panel: Model-calculated rates for N_2 photoionization (solid line) and N_2 photodissociation (dotted line) for $^{14}\text{N}^{14}\text{N}$ in Titan's atmosphere, using the same N_2 profile as in Liang *et al.* [2007]. Right panel: Fractionation constants $(J(^{15}\text{N}^{14}\text{N})/J(^{14}\text{N}_2) - 1)$ for the model-calculated isotope-specific rate coefficients, J , for photoionization (solid line) and photodissociation (dotted line) showing the effects of isotopic self-shielding by $^{14}\text{N}^{14}\text{N}$. The values for photoionization have been multiplied by factor of 100 to give the fractionation constant in percent. **121**

List of tables

2.1	Overview of primary isotopic reference materials and their absolute isotope ratios used in this dissertation.	8
2.2	Comparison of the average isotopic composition of N ₂ O in UC Berkeley campus air samples before and after changing working reference standard ("WS").	11
2.3	Peak location differences in eV for the ¹⁴ N ₂ data on the uncalibrated energy scale. The peak locations were determined by fitting peaks with Voigt profiles.	19
2.4	Differences between peak energies in eV used for calibration and peak energies after the calibration for runs in the 15.5 – 16.5 eV range.	19
2.5	Peak energies in eV from Lofthus and Krupenie [1977] that were used in the energy scale calibration. Peak assignments are shown in Figure 6.1.	20
3.1	Linear trends in N ₂ O isotopic composition from unweighted linear least-squares fits to the firn air and archived air datasets and box-model results for the average isotopic composition of the anthropogenic (δ_{ANT}) and natural (δ_{NAT}) N ₂ O sources and of the pre-industrial troposphere ($\delta_{T,i}$). 1 σ uncertainties are also given.	40
3.S1	Mean age, N ₂ O mixing ratio, and N ₂ O isotopic compositions from firn air samples	63
3.S2	Collection date, N ₂ O mixing ratio, and N ₂ O isotopic compositions from archive air samples	63
4.S1	N ₂ O mixing ratio and isotopic composition for the CRAVE WB-57 samples	90
4.S2	N ₂ O mixing ratio and isotopic composition for the TC ⁴ WB-57 samples	91
4.S3	N ₂ O isotopic composition for the TC ⁴ DC-8 samples	92
4.S4	TC ⁴ DC-8 mixing ratio data	93
5.1	N ₂ O mixing ratios and isotopic compositions for samples collected during the OOMPH campaign. N ₂ O mixing ratios were measured on wet samples and corrected by 1.2% to determine the dry mixing ratio shown here. The samples in bold are the N ₂ O mixing ratio outliers discussed in section 5.3.	100
5.2	Summary of averages. Tropospheric averages are based on measurements of Boundary Layer air on the UC Berkeley campus between 2001 and 2006.	102

- 5.3** Summary of the Keeling plot results for the inferred source isotopic compositions (the y-intercepts in Figure 5.3 and their 1σ uncertainties) using different linear regression techniques. **104**
- 6.1** Summary of proposed state assignments for the feature at 15.68 eV and the associated isotope shifts between $^{14}\text{N}_2$ and $^{15}\text{N}_2$. The measured isotope shift matches most closely that predicted for the $(A^2\Pi_u v'=2)4s\sigma_g^1\Pi_u$ state. **118**
- 6.2** Energies and isotope shifts for the P(1) progression. The results here suggest that the peaks in this series correspond to autoionizing Rydberg states converging to the $v = 0 - 3$ levels of the $A^2\Pi_u$ electronic state. **118**

Acknowledgements

I owe many thanks to many people who have helped to make the research in this dissertation possible. I thank my adviser, Kristie Boering, for guiding me through this process and for her constant optimism. I also thank my committee members, Ron Cohen and Imke de Pater, for graciously reading this work and for support throughout my graduate career. I am also grateful to many collaborators for making this work possible, especially Elliot Atlas, Don Blake, Sue Schauffler, Glenn Diskin, Musa Ahmed, Oleg Kostko, Yuk Yung, Danie Liang, K.-R. Kim, Paul Steele, Ray Langenfelds, and everyone at CSIRO.

All of the Boering group members past and present have made this process much easier, Kate, Annalise, Amanda, and Katie who welcomed me into the group and taught me the ropes, Lauren and Aaron J. who made getting through classes better, Amadu who is a really cool dude, Aaron W. who didn't complain when I talked to my computer, Claire who did a lot of tedious work on N_2O , John who helped make the N_2 work happen, Bill who kept haze responsive while I was away, and Emily who let me crash on her futon. I also greatly appreciate all of the advice and assistance I received along the way from Boering group alums Sunyoung and Máté.

Thank you to my parents for raising me to believe that if I set my mind to do something, I could do it. Finally, I thank my wife, Beth, most of all. Without her love and support, I would never have done this.

Introduction and overview

In this dissertation, I report on experiments and observations related to the isotopic compositions of nitrous oxide (N_2O) and molecular nitrogen (N_2) and to the optical properties of aerosols. The goal of this work is to gain insight into chemistry and radiative transfer in planetary atmospheres, particularly those of Earth and Titan. In Earth's atmosphere, N_2O is a potent greenhouse gas; it absorbs infrared radiation emitted by the Earth's surface and re-emits it isotropically, causing a warming of the lower atmosphere [Forster *et al.*, 2007]. As discussed below, its isotopic composition in the atmosphere is a useful tool for examining the N_2O budget – that is, an accounting of the magnitudes of its sources and sinks [e.g. Kim and Craig, 1993; Toyoda *et al.*, 2002; Park *et al.*, 2004]. In the atmospheres of both Earth and Titan, N_2 is the main component and is a major absorber of solar extreme ultraviolet (EUV) radiation in the ionospheres of both bodies [Torr and Torr, 1979; Yung *et al.*, 1984]. Some of this EUV radiation causes ionization of N_2 to N_2^+ . Isotope effects in this ionization may play a role in changes in the isotopic composition of N_2 over billions of years due to isotope differences in the gravitational escape rates of nitrogen atoms (in the case of Titan's atmosphere [Lunine *et al.*, 1999]) and/or in affecting the isotopic composition of minor atmospheric species on much shorter photochemical timescales, such as NO on Earth [Aikin, 2001] or HCN on Titan (as hypothesized for N_2 photodissociation by Liang *et al.* [2007]). The extent to which photoionization may play a role, however, is unknown since the isotope effects have not been measured. Finally, on virtually every planetary body with an atmosphere, aerosols are present. Aerosols can greatly affect atmospheric radiative transfer and can be important in determining the surface temperature, either warming or cooling the surface, for example, depending on their optical properties (the "direct effect") or the nature and extent of their effect on cloud formation (the "indirect effect"). In Earth's atmosphere, the effect of aerosols on radiative transfer is one of the major uncertainties in future climate predictions [e.g., Forster *et al.*, 2007]. In Titan's atmosphere, aerosols are responsible for its stratosphere and are thought to cause a net cooling at the surface [Danielson *et al.*, 1973; McKay *et al.*, 1991], but the uncertainties in the chemistry and microphysics of aerosol formation and how these affect the resulting optical properties and hence radiative forcing in the atmosphere remain large [e.g. Lebonnois *et al.*, 2009 and references therein].

To address important unknowns in the processes that determine the concentrations and isotopic compositions of these species, and, in the case of aerosols, their optical properties, I pursued the research presented in the five chapters following this introduction. In Chapter 2, I describe in detail the methods used to obtain the measurements and model results presented and discussed in subsequent chapters, as well as the design and development of an experimental method for determining aerosol optical properties "in situ" in a reaction chamber (as opposed to collecting a film for "offline" analysis) using a rotating quarter-wave plate polarimeter, a technique which will be used in future experiments on aerosol formation from gaseous precursors. In the next three chapters, I present measurements and analysis of the isotopic composition of nitrous oxide in Earth's atmosphere (i) from archived air samples taken at the surface at Cape Grim, Tasmania dating back to 1978 and from air trapped in firn (densely packed snow) from Law Dome, Antarctica (Chapter 3), (ii) from samples collected

by aircraft from the boundary layer to the lower stratosphere in the tropics (Chapter 4), and (iii) from atmospheric samples collected by a ship cruise across the Southern Ocean (Chapter 5). Finally, in Chapter 6, I present the first measurements and analysis of isotope effects in the photoionization of N_2 to N_2^+ , an experiment performed using the VUV light at the Advanced Light Source at the Lawrence Berkeley National Laboratory. A brief overview of the results and advances presented in Chapters 3 through 6 is given below.

Chapter 3: Trends, seasonal cycles, and interannual variability in the isotopic composition of nitrous oxide between 1940 and 2005

Because N_2O is a potent greenhouse gas [e.g., *Forster et al.*, 2007] and has been targeted for regulation under international treaties, such as the Kyoto Protocol, an understanding of its budget is important. However, inverse models based on N_2O mixing ratio measurements alone have left the budget underconstrained [e.g. *Hirsch et al.*, 2006; *Huang et al.*, 2008]. Since the isotopic composition of N_2O in surface air is determined by the isotopic compositions of its sources and isotope effects in its sink reactions and the relative magnitudes of the associated N_2O fluxes, measurements of variations in its isotopic composition provide additional constraints on the N_2O budget [e.g., *Kim and Craig*, 1993; *Toyoda et al.*, 2002; *Park et al.*, 2004; *Bernard et al.*, 2006]. In Chapter 3, I present measurements and analysis of a time series of the nitrogen and oxygen isotopic compositions of N_2O in surface air. The data include measurements on 50 archived air samples collected at the surface at Cape Grim, Tasmania between 1978 and 2005, as well as 11 samples of firn air from Law Dome, Antarctica, with mean ages dating from 1940 to 1995.

The results show variations in N_2O isotopic compositions on multiple timescales: long-term trends, as has been observed and predicted previously [*Rahn and Wahlen*, 2000; *Sowers et al.*, 2002; *Röckmann and Levin*, 2005; *Bernard et al.*, 2006; *Ishijima et al.*, 2007] and — shown for the first time here — seasonal cycles and interannual variations, which is quite remarkable for a trace gas with a 120-year lifetime that has often been considered so well-mixed as to be uninteresting. I use the measurements to constrain the average natural and anthropogenic N_2O source isotopic compositions, which provide further evidence that the observed increase in N_2O mixing ratio in the troposphere is largely due to agriculture. The seasonal cycles in isotopic composition are attributed to seasonal variations in the relative strengths of the exchange of air between the stratosphere and troposphere (which transports isotopically-enriched, N_2O -depleted air from the stratosphere to the troposphere) versus the strengths of the N_2O surface sources such as ocean ventilation and biomass burning. The interannual variability suggests a role for El Niño in controlling the N_2O mixing ratio and isotopic composition. Overall, these results demonstrate that variations in the isotopic composition of tropospheric N_2O on multiple timescales provide unique information about the variations in surface sources of N_2O which cannot be derived from mixing ratio measurements alone. Thus, measurements of variations in N_2O isotopic compositions such as these could soon be used to constrain inverse models and, thereby, lead to improved estimates of the spatial distribution and identities of N_2O sources on regional and/or global scales.

Chapter 4: The effect of local and regional sources on the isotopic composition of nitrous oxide in the tropical free troposphere and tropopause layer

In Chapter 4 I present the first vertical profiles of the isotopic composition of N₂O that span altitudes of ~1 to 19 km — that is, from just above the boundary layer into the lower stratosphere in the tropics from ~1°S to 10°N. Somewhat surprisingly, given the 120-year lifetime of N₂O [Volk *et al.*, 1996] and emissions that, based on direct measurements of the isotopic compositions of the surface sources, are expected to be highly variable in space and time [e.g. Perez *et al.*, 2000, 2001; Popp *et al.*, 2002; Toyoda *et al.*, 2002], the profiles show predictable, repeatable behavior across several years, seasons, and aircraft platforms. The particular patterns observed in the troposphere, along with correlations between N₂O isotopic composition and tracers of marine influence, are consistent with an oceanic source of N₂O dominating on a regional scale. The results also include the first measurements of the isotopic composition of N₂O in a remote combustion plume, revealing a dramatic perturbation in the site-specific isotopic composition relative to the tropospheric background. Overall, these results demonstrate for the first time that the vertical variations in N₂O isotopic composition throughout the tropical troposphere, though small and near the measurement precision, are detectable and coherent and that they can provide unique constraints on the identities of its sources on a regional scale — important information for verification of international greenhouse gas emission treaties such as the Kyoto Protocol.

Chapter 5: The isotopic composition of nitrous oxide over the ocean on a cruise from South Africa to Chile

The results of the measurements and analyses in Chapters 3 and 4 continue to highlight that the ocean plays an important role in determining N₂O isotopic compositions in the troposphere. Yet very few measurements of N₂O isotopic composition just at and below the ocean surface have been made. In particular, there are large and significant uncertainties in the magnitude of the Southern Ocean source of N₂O [Nevison *et al.*, 2005; Hirsch *et al.*, 2006; Huang *et al.*, 2008], and its isotopic composition is largely unknown, complicating analyses such as that presented in Chapter 3. Measurements of the isotopic composition of N₂O over the Southern Ocean may thus help to constrain the isotopic composition and magnitude of this source. I measured the $\delta^{15}\text{N}^{\text{bulk}}$ and $\delta^{18}\text{O}$ isotopic compositions of N₂O in a set of 50 whole-air samples collected on a ship cruise in the Southern Ocean between Cape Town, South Africa and Tierra del Fuego, Chile, as part of the "Organics over the Ocean Modifying Particles in both Hemispheres" (OOMPH) campaign in January-March 2007. While most of the samples measured showed only small variations in the mixing ratios and isotopic compositions of N₂O, four samples showed both enhanced N₂O mixing ratios (by 4 to 25 ppb relative to a 320 ppb background) and depleted ¹⁵N and ¹⁸O isotope compositions (by as much as 1‰ in $\delta^{15}\text{N}^{\text{bulk}}$ and $\delta^{18}\text{O}$). For these four samples and four others which did not show N₂O enhancements, $\delta^{15}\text{N}^{\alpha}$ and $\delta^{15}\text{N}^{\beta}$ were also measured, and the samples with enhanced N₂O mixing ratio showed low values of $\delta^{15}\text{N}^{\alpha}$ by up to 2‰. Since the samples were collected over the open ocean, the most likely explanation for the N₂O enhancement (barring a shipboard artifact) is N₂O emitted by the ocean, and the various analyses given in Chapter 5, including calculation of the isotopic composition of the source and its uncertainty and comparisons with other known sources or measurements, are consistent with this

interpretation. Although additional measurements are clearly needed to confirm the robustness of this estimate of the isotopic composition of N₂O emitted from the Southern Ocean across both space and time, the measurements in Chapter 5 do provide a new constraint on this isotopic composition which can now be included in the global N₂O isotope budget. Continued improvement of constraints on the isotopic compositions of N₂O sources will also eventually allow inverse modeling of the small but significant spatial and temporal variations in the mixing ratio and isotopic composition of N₂O — such as those presented and discussed in Chapters 3 and 4 — to determine the magnitudes and geographic distributions of N₂O sources so that more effective mitigation strategies and treaty verifications can ultimately be achieved.

Chapter 6: Experimental determination of isotope effects in the non-dissociative photoionization of molecular nitrogen

In Chapter 6, I present results of measurements of isotope effects in the non-dissociative photoionization of molecular nitrogen (R1.1)



using synchrotron radiation from 15.5 eV to 18.9 eV (80.0 nm to 65.6 nm) to photoionize a molecular beam consisting of a 1:1:1 mixture of ¹⁴N¹⁴N, ¹⁵N¹⁴N, and ¹⁵N¹⁵N. While isotope effects in reaction R1.1 may be important in determining the isotopic composition of N₂ and other nitrogen-bearing species in a variety of environments including the atmospheres of Earth and Titan [e.g. *Aikin*, 2001; *McEwan and Anicich*, 2007], they had not been measured experimentally prior to the work reported here. The results show significant shifts in peak energies and intensities upon isotopic substitution. The measured isotopic shifts largely resolve recent controversy over several peak assignments in the ¹⁴N¹⁴N spectra from previous work [*Sommavilla and Merkt*, 2006; *Lefebvre-Brion*, 2005; *Jungen et al.*, 2003]. They also show that the isotope effects are large enough to cause isotopic fractionation of species in planetary atmospheres under some conditions. Under optically thin conditions, the isotope effects integrated over all wavelengths (i.e., "white light") cancel out, leading to a ratio of photoionization cross-sections of ¹⁴N¹⁵N to ¹⁴N¹⁴N of unity (1.01±0.02), which suggests that, under these conditions, reaction R1.1 would not lead to isotopic fractionation. Under optically thick conditions, however, self-shielding of the predominant species ¹⁴N¹⁴N occurs that can lead to an enhancement in the photoionization rate constant of ¹⁴N¹⁵N relative to that of ¹⁴N₂. In Titan's atmosphere, this self-shielding will lead to the formation of HCN (e.g., by the reaction of N₂⁺ with C₂H₂ [*McEwan and Anicich*, 2007]) that is isotopically heavier compared to the N₂ reservoir. Thus isotope effects in reaction R1.1 may contribute to a quantitative explanation of the fact that in Titan's atmosphere the ¹⁵N/¹⁴N ratio of HCN — as determined from both ground-based millimeter observations [*Marten et al.*, 2002; *Gurwell*, 2004] and the Cassini Composite Infrared Spectrometer (CIRS) [*Vinatier et al.*, 2007] — is higher than that of N₂ (from which all of the N in HCN should originate), as observed *in situ* by the Huygens Gas Chromatograph Mass Spectrometer (GCMS) [*Niemann et al.*, 2005] and the Cassini Ion and Neutral Mass Spectrometer (INMS) [*Waite et al.*, 2005].

References

- Aikin, A. C. (2001), Isotope identification in NO as chemical tracer in the middle atmosphere, *Phys. Chem. Earth (C)*, 26(7), 527-532.
- Bernard, S., T. Röckmann, J. Kaiser, J.-M. Barnola, H. Fischer, T. Blunier, and J. Chappellaz (2006), Constraints on N₂O budget changes since pre-industrial time from new firn air and ice core isotope measurements, *Atmos. Chem. Phys.*, 6, 493-503.
- Danielson, R. E., J. J. Caldwell, and D. R. Larach (1973), An inversion in the atmosphere of Titan, *Icarus*, 20, 437-443.
- Forster, P., et al. (2007), In Climate Change 2007: The Physical Science Basis; Solomon, S., Qin, D., Manning, M., Chen, Z., Marquis, M., Averyt, K. B., Tignor, M., and Miller, H. L., Eds.; Cambridge University Press: Cambridge U.K.
- Gurwell, M. A. (2004), Submillimeter observations of Titan: Global measures of stratospheric temperature, CO, HCN, HC₃N, and the isotopic ratios ¹²C/¹³C and ¹⁴N/¹⁵N, *Astrophys. J.*, 616, L7-L10.
- Hirsch, A. I., A. M. Michalak, L. M. Bruhwiler, W. Peters, E. J. Dlugokencky, and P. P. Tans (2006), Inverse modeling estimates of the global nitrous oxide surface flux from 1998–2001, *Global Biogeochem. Cycles*, 20, GB1008.
- Huang, J., et al. (2008), Estimation of regional emissions of nitrous oxide from 1997 to 2005 using multinetwork measurements, a chemical transport model, and an inverse method, *J. Geophys. Res.*, 113, D17313.
- Ishijima, K., S. Sugawara, K. Kawamura, G. Hashida, S. Morimoto, S. Murayama, S. Aoki, T. Nakazawa (2007), Temporal variations of the atmospheric nitrous oxide concentration and its δ¹⁵N and δ¹⁸O for the latter half of the 20th century reconstructed from firn air analyses, *J. Geophys. Res.*, 112, D03305, doi:10.1029/2006JD007208.
- Jungen, Ch., K. P. Huber, M. Jungen, and G. Stark (2003), The near-threshold absorption spectrum of N₂, *J. Chem. Phys.*, 118(10), 4517-4538.
- Kim, K.-R. and H. Craig (1993), Nitrogen-15 and oxygen-18 characteristics of nitrous oxide: A global perspective, *Science*, 262, 1855-1857.
- Lebonnois, S., P. Rannou, and F. Hourdin (2009), The coupling of winds, aerosols and chemistry in Titan's atmosphere, *Phil. Trans. R. Soc. A*, 367, 665–682
- Lefebvre-Brion, H. (2005), Assignment in the near-threshold absorption spectrum of N₂, *J. Chem. Phys.*, 122, 144315.
- Lunine, J. I., Y. L. Yung, and R. D. Lorenz (1999), On the volatile inventory of Titan from isotopic abundances in nitrogen and methane, *Planet. Space Sci.*, 47, 1291-1303.
- Marten, A., T. Hidayat, Y. Biraud and R. Moreno (2002), New millimeter heterodyne observations of Titan: Vertical distributions of nitriles HCN, HC₃N, CH₃CN, and the isotopic ratio ¹⁵N/¹⁴N in its atmosphere, *Icarus*, 158, 532–544.
- McEwan, M. J. and V. G. Anicich (2007), Titan's ion chemistry: A laboratory perspective, *Mass Spectrom. Rev.*, 26, 281-319.
- McKay, C. P., J. B. Pollack, and R. Courtin (1991), The Greenhouse and Antighreenhouse effects on Titan, *Science*, 253(5024), 1118-1121.
- Nevison, C. D., R. F. Keeling, R. F. Weiss, B. N. Popp, X. Jin, P. J. Fraser, L. W. Porter, and P. G. Hess (2005), Southern ocean ventilation inferred from seasonal cycles of atmospheric N₂O and O₂/N₂ at Cape Grim, Tasmania, *Tellus*, 57B, 218-229.

- Niemann, H. B., et al. (2005), The abundances of constituents of Titan's atmosphere from the GCMS instrument on the Huygens probe, *Nature*, 438, 779–784.
- Park, S., E. L. Atlas, and K. A. Boering (2004), Measurements of N₂O isotopologues in the stratosphere: Influence of transport on the apparent enrichment factors and the isotopologue fluxes to the troposphere, *J. Geophys. Res.*, 109, D01305.
- Pérez, T., S. E. Trumbore, S. C. Tyler, E. A. Davidson, M. Keller, and P. B. de Camargo (2000), Isotopic Variability of N₂O Emissions From Tropical Forest Soils, *Global Biogeochem. Cycles*, 14(2), 525–535.
- Pérez, T., S. E. Trumbore, S. C. Tyler, P. A. Matson, I. Ortiz-Monasterio, T. Rahn, and D. W. T. Griffith (2001), Identifying the agricultural imprint on the global N₂O budget using stable isotopes, *J. Geophys. Res.*, 106(D9), 9869–9878.
- Popp, B. N., et al. (2002), Nitrogen and oxygen isotopomeric constraints on the origins and sea-to-air flux of N₂O in the oligotrophic subtropical North Pacific gyre, *Global Biogeochem. Cycles*, 16 (4), 1064-1073.
- Rahn, T., and M. Wahlen (2000), A reassessment of the global budget of atmospheric nitrous oxide, *Global Biogeochem. Cycles*, 14(2), 537-543.
- Röckmann, T., and I. Levin (2005), High-precision determination of the changing isotopic composition of atmospheric N₂O from 1990 to 2002, *J. Geophys. Res.*, 110, D21304.
- Sommavilla, M. and F. Merkt (2006), On the rotational structure of a prominent band in the vacuum-ultraviolet spectrum of molecular nitrogen, *J Electron Spectrosc. Rel. Phenom.*, 151, 31-33.
- Sowers, T., A. Rodebaugh, N. Yoshida, and S. Toyoda (2002), Extending the records of the isotopic composition of atmospheric N₂O back to 1800 A.D. from firn air trapped in snow at the South Pole and the Greenland Ice Sheet Project II ice core, *Global Biogeochem. Cycles*, 16 (4), 1129-1138.
- Torr, D. G. and M. R. Torr (1979), Chemistry of the thermosphere and ionosphere, *J. Atmos. Terr. Phys.*, 41, 789-839.
- Toyoda, S., N. Yoshida, T. Miwa, Y. Matsui, H. Yamagishi, U. Tsunogai, Y. Niojiri, and N. Tsurushima (2002), Production mechanism and global budget of N₂O inferred from its isotopomers in the western North Pacific, *Geophys. Res. Lett.*, 29(3), doi: 10.1029/2001GL014311.
- Vinatier, S. B. Bézard, and C. A. Nixon (2007), The Titan ¹⁴N/¹⁵N and ¹²C/¹³C isotopic ratios in HCN from Cassini/CIRS, *Icarus*, 191, 712-721.
- Volk, C. M., et al. (1996), Quantifying transport between the tropical and mid-latitude lower stratosphere, *Science*, 272, 1763-1768.
- Waite, J. H., et al. (2005), Ion neutral mass spectrometer results from the first flyby of Titan, *Science*, 308, 982–986.
- Yung, Y. L., M. Allen, and J. P. Pinto (1984), Photochemistry of the atmosphere of Titan: Comparison between model and observations, *Astrophys. J. Suppl. Ser.*, 55(3), 465-506.

Chapter 2

Methods

In this chapter, some of the key experimental and analytical aspects of the work comprising this dissertation are given in detail. Sections 2.1 and 2.2 pertain to measurements and modeling of the isotopic composition of nitrous oxide (N_2O) and are relevant to research presented in Chapters 3 through 5. In Section 2.3, techniques for the measurement and analysis of isotope effects in the nondissociative photoionization of molecular nitrogen are described and are relevant to research presented in Chapter 6. In Section 2.4, development and initial testing of a custom polarimeter for laboratory experiments on photochemically generated aerosols are discussed.

2.1. Measuring the isotopic composition of atmospheric N_2O at natural abundance

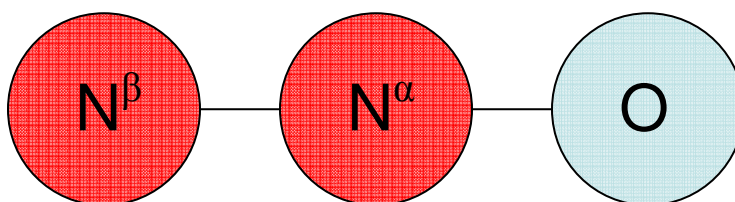


Figure 2.1. A schematic diagram of nitrous oxide, including labels for the central (α) and terminal (β) nitrogen atoms.

Nitrous oxide N_2O is a linear molecule consisting of two adjacent nitrogen atoms and one oxygen atom as shown in Figure 2.1. The two nitrogen atoms are not equivalent, and in order to distinguish between the atoms at the central and terminal positions they are referred to as N^α and N^β , respectively. Nitrogen has two stable isotopes, ^{14}N and ^{15}N and oxygen has three, ^{16}O , ^{17}O , and ^{18}O . ^{14}N and ^{16}O are the most abundant isotopes and account for greater than 99% of each. Because of the low abundances of the rare isotopologues (i.e., the "isotopically-substituted" molecules), their abundances are not typically measured absolutely. Rather, isotopic compositions are measured as the ratio of the rare isotopologue to the common isotopologue in an isotope ratio mass spectrometer (IRMS) since the ratio can be measured much more precisely than the absolute abundances. For example, to determine the ^{18}O isotopic composition of a sample, the ratio of $(m/z\ 46)/(m/z\ 44)$ is measured, which is essentially $[^{14}\text{N}^{14}\text{N}^{18}\text{O}]/[^{14}\text{N}^{14}\text{N}^{16}\text{O}]$. Furthermore, in order to compare isotopic composition measurements between different laboratories and to account for isotope fractionation in the isotope ratio mass spectrometer, it is necessary to measure the ratios relative to a working reference that has been calibrated against a standard isotopic reference material. Isotopic composition measurements are therefore reported as part-per-thousand, or per mil (‰), deviations from these references and are referred to as δ -values, for example,

$$\delta^{18}\text{O} = (^{18}R_{sam} / ^{18}R_{std} - 1) \times 1000 \text{‰}, \quad (2.1)$$

where $^{18}R=(^{18}O/^{16}O)$ is the elemental isotopic ratio derived from the measurements and "sam" and "std" refer to the sample and standard, respectively. The standards for nitrogen and oxygen are air-N₂ and Vienna Standard Mean Ocean Water (VSMOW), respectively. The elemental isotopic ratios for these standards are given in Table 2.1.

Table 2.1. Overview of primary isotopic reference materials and their absolute isotope ratios used in this dissertation.

Species	Scale	R/10 ⁻⁶	Reference
¹⁵ N/ ¹⁴ N	air-N ₂	3676.5±4.1	[Junk and Svec, 1958]
¹⁷ O/ ¹⁶ O	VSMOW	379.9±0.8	[Li et al., 1988]
¹⁸ O/ ¹⁶ O	VSMOW	2005.2±0.45	[Baertschi, 1978]

Both the oxygen-18 isotopic composition, $\delta^{18}O$, and the average nitrogen-15 isotopic composition over the two nitrogen atom positions, $\delta^{15}N^{bulk}$, are obtained from IRMS measurements of the ratios of N₂O⁺ signals at m/z 44, 45, and 46. [Note that for the work in this dissertation, it is assumed that $\delta^{17}O$ and $\delta^{18}O$ of N₂O follow a mass-dependent relationship such that $^{17}R = A(^{18}R)^\beta$, where $A = 0.00937035$ and $\beta = 0.516$ (see Kaiser et al., 2003 for a detailed discussion) so that the portion of the signal at m/z 45 due to ¹⁴N¹⁴N¹⁷O is accounted for; this is a good approximation for atmospheric N₂O at our measurement precision [Cliff and Thiemens, 1994; Kaiser, 2002]. However, since $\delta^{17}O$ is not measured *per se*, its value is not reported.] In addition, the nitrogen isotopic compositions at the central (α) and terminal (β) position in N₂O can also be determined by measuring the ratio of NO⁺ fragment ion signals in the IRMS at m/z 31 and m/z 30, as described further in the following section. These are referred to "site-specific" isotopic compositions and are denoted $\delta^{15}N^\alpha$ and $\delta^{15}N^\beta$. The "Site Preference," which is the enrichment at the α -position relative to that at the β -position can also be defined and is given by 2.2.

$$SP = (^{15}R^\alpha / ^{15}R^\beta - 1) \times 1000\text{‰} \quad (2.2)$$

Measurements of $\delta^{18}O$, $\delta^{15}N^{bulk}$, $\delta^{15}N^\alpha$, $\delta^{15}N^\beta$, and SP of N₂O are reported in Chapters 3 through 5.

2.1.1. Measurement procedures

The measurements of isotopic compositions reported in Chapters 3-5 were all made using Continuous Flow Isotope Ratio Mass Spectrometry with online PreConcentration and Gas Chromatography ("CF-PreCon-GC-IRMS"). CF-PreCon-GC-IRMS was developed in the 1990s and allows for precise determination of N₂O isotopic compositions at natural abundances using samples of ~100 mL STP, which corresponds to ~1.4 nmol N₂O [Brand et al., 1995]. A diagram of the system is shown in Figure 2.2. A continuous flow of helium (99.999% purity) pushes an air sample through a chemical trap consisting of MgClO₄ and Ascarite (NaOH-coated silica) which removes H₂O and the bulk of the CO₂. After the chemical trap, the sample is cryofocused by freezing out the condensable species, including >99.999% of the N₂O in a cold-trap at the boiling point of liquid nitrogen, -196°C, while venting the bulk of the air (i.e., N₂ and O₂). The sample is then injected into a gas

chromatograph, where the N₂O is separated from the remaining traces of CO₂ and other condensable trace gases using a 25 m Poraplot Q column. The pulse of N₂O in helium is then introduced into the ionization region of a Finnigan MAT-252 IRMS via an open split interface, where it is bombarded with electrons at 100 eV to form ions which are accelerated by a 10 kV potential, separated with a magnetic sector, and detected with Faraday cups. In this work, the timing of the PreCon-GC processing steps and the helium flow rates in the different sections of the apparatus are identical to those of Park [2005] except when otherwise specified.

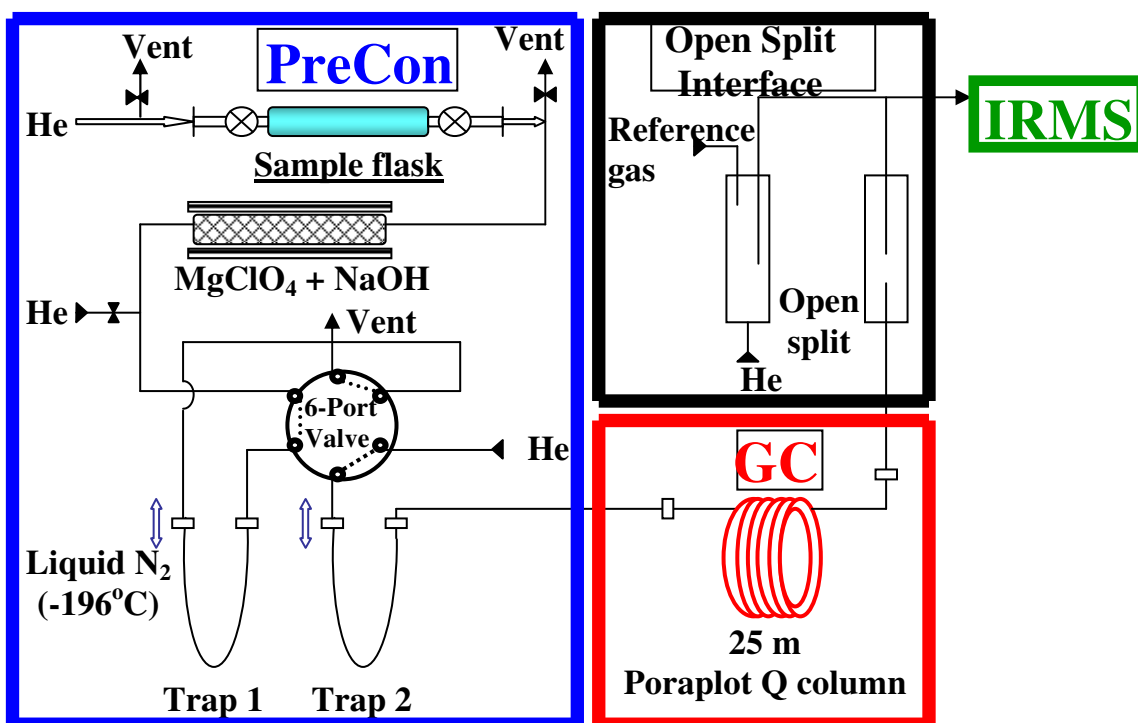


Figure 2.2. A diagram of the CF-PreCon-GC-IRMS setup used for the nitrous oxide isotopic composition measurements reported throughout this dissertation (adapted from Park [2005]).

Traditional N₂O IRMS measurements consisted only of $\delta^{15}\text{N}^{\text{bulk}}$ and $\delta^{18}\text{O}$. This is because measurements of the parent ion alone, NNO^+ , yield no information about the position dependence of the ^{15}N in the N₂O molecules of the sample. However, the position dependence of the ^{15}N is an important piece of information for understanding the biological production mechanisms as well as the isotope effects in the sink reactions of N₂O. In order to measure the site-specific nitrogen isotopic composition, as opposed to simply $\delta^{15}\text{N}^{\text{bulk}}$ and $\delta^{18}\text{O}$, it is necessary to measure two aliquots of the sample because the physical configuration of the Faraday cups in the MAT-252 does not allow for the simultaneous determination of all the required mass-to-charge ratios (m/z). For the first aliquot, the ratios m/z 45/44 (^{45}R) and 46/44 (^{46}R) are measured, which correspond to the parent ion ratios of the rare isotopologues ($^{15}\text{NNO}^+$, N^{15}NO^+ , and NN^{17}O^+ for m/z 45 and NN^{18}O^+ , $^{15}\text{N}^{15}\text{NO}^+$, $^{15}\text{NN}^{17}\text{O}^+$, and $\text{N}^{15}\text{N}^{17}\text{O}^+$ for m/z 46) to the common isotopologue. This allows for determination of $\delta^{15}\text{N}^{\text{bulk}}$ and $\delta^{18}\text{O}$, but provides no information about the position dependence of the ^{15}N isotopic composition.

In order to determine $\delta^{15}\text{N}^\alpha$, $\delta^{15}\text{N}^\beta$, and SP, the NO^+ fragment ion and its ^{15}N - and ^{17}O -substituted analogues are measured as the ratio m/z 31/30 (or ^{31}R). Most of the nitrogen atoms in the NO^+ fragment ions come from the α position since most of the fragment ions form simply by cleavage of the N-N bond. However, a small number of the NO^+ fragment ions formed come from a cyclic intermediate NNO^+ ion so that when this cyclic intermediate fragments it is possible that the nitrogen atom in the β position may be the one retained in the NO^+ fragment ion [Friedman and Bigeleisen, 1950]. The fraction of NO^+ which includes N^β is known as the scrambling factor, s , and has been determined for the instrument used for all of the N_2O isotopic measurements presented in this dissertation to be 8.46% [Kaiser et al., 2004], based on measurements of increasingly diluted standards of pure N^{15}NO and ^{15}NNO in natural abundance N_2O gas samples. Knowing this scrambling factor, the ^{31}R measurement can be combined with the bulk nitrogen isotope measurements to determine $\delta^{15}\text{N}^\alpha$; $\delta^{15}\text{N}^\beta$ can then be calculated since $\delta^{15}\text{N}^{\text{bulk}}$ is the average of $\delta^{15}\text{N}^\alpha$ and $\delta^{15}\text{N}^\beta$. Each of the two aliquots of sample required (one for N_2O^+ , one for NO^+) are run against a laboratory working standard (99.998% purity N_2O) which has been calibrated relative to the international standards; the reference standard is run into the IRMS via the open split, twice just before the sample N_2O elutes from the GC column and twice just after.

2.1.2. Reference standard calibration

Accurate measurements of the isotopic composition of N_2O by CF-PreCon-GC-IRMS rely upon the accurate calibration of the reference cylinder of N_2O . During the work reported in this dissertation, it was necessary to switch to a new reference cylinder N_2O because the gas in the cylinder used by Park [2005] had been used up to such an extent that the pressure began to decrease to less than the vapor pressure of N_2O , beyond which point the N_2O from the tank begins to fractionate. Several means were used to maintain our calibration relative to the international standards. Intercomparison runs of a new cylinder relative to the old cylinder were performed, and the isotopic composition of tropospheric N_2O contained in whole air samples collected on campus were compared before and after switching to the new working reference tank.

More specifically, three small samples of N_2O were obtained from the original standard cylinder (prior to its pressure decrease) and three small samples were obtained from the new cylinder before it was installed on the PreCon apparatus. After “zero-run” tests between samples from the same cylinder showed that the samples were not fractionated relative to samples from the same cylinder, within the high precision of the dual inlet measurements, samples from the new reference cylinder were measured relative to samples from the old reference cylinder to determine δ^{45} , δ^{46} , and δ^{31} . The results were $\delta^{45} = -0.77302 \pm 0.01222\text{‰}$, $\delta^{46} = -2.73692 \pm 0.027654\text{‰}$, and $\delta^{31} = 1.23196 \pm 0.15234\text{‰}$ for the new reference gas relative to the old reference gas, where the uncertainty is the standard deviation and $N = 24$ for δ^{45} and δ^{46} and $N = 13$ for δ^{31} . These results were used to calculate the isotope ratios of the new standard which are used in calculations of sample δ -values. As shown in Table 2.2, measurements of air collected on the UC Berkeley campus using the new reference standard yield results in good agreement with measurements made using the old reference standard, showing that the new reference cylinder can be used to measure samples relative to the international standards. These conclusions, however, should be followed up with a full

calibration against international standards, as is standard practice approximately every three years.

Table 2.2. Comparison of the average isotopic composition of N₂O in UC Berkeley campus air samples before and after changing working reference standard ("WS").

	Tropospheric Average at UC Berkeley	
	Old WS	New WS
$\delta^{18}\text{O}$	44.3±0.4 ^a	44.1±0.3 ^c
$\delta^{15}\text{N}^{\text{bulk}}$	6.2±0.3 ^a	6.1±0.3 ^c
$\delta^{15}\text{N}^{\alpha}$	15.8±1.2 ^b	16.0±0.8 ^d
$\delta^{15}\text{N}^{\beta}$	3.3±1.2 ^b	-3.6±0.8 ^d
SP	19.2±2.4 ^b	19.6±1.6 ^d

^a N = 288, September 2001 – November 2006

^b N = 239, September 2001 – November 2006

^c N = 23, March 2008

^d N = 7, March 2008

2.1.3. Converting measurements to the Toyoda and Yoshida [1999] scale

When work began on the measurements reported in this dissertation, there was a large discrepancy in the site-specific isotopic composition of tropospheric nitrous oxide relative to the international air-N₂ [Yoshida and Toyoda, 2000; Kaiser *et al.*, 2004]. This discrepancy of 23.7‰ for SP was not due to actual differences in the isotopic composition of N₂O at different locations, but rather the different methods employed to bring the site-specific measurements onto the international standard scale of air-N₂. The method originally used to calibrate the site-specific N₂O isotopic composition in our UC Berkeley lab and the Brenninkmeijer lab at the Max-Planck-Institut-fuer-Chemie in Mainz was based upon serial additions of nearly pure ¹⁵N¹⁵NO to the N₂O reference gas used [Kaiser *et al.*, 2004; Park, 2005]. In contrast, the method used by Toyoda and Yoshida [1999] was based upon synthesizing N₂O from NH₄NO₃ for which the individual isotopic compositions relative to air-N₂ of the NH₄⁺ and the NO₃⁻ were known; hence, the isotopic composition at the N^α and N^β sites in the resulting N₂O relative to air-N₂ were known; they also measured pure NO of known isotopic composition. Recent work [Westley *et al.*, 2007] attempting to reproduce the calibrations of Kaiser *et al.* [2004] and Toyoda and Yoshida [1999] has shown that previously unconsidered isotope effects that depend on conditions in the ion source region affect the purely mass-spectrometric technique of Kaiser *et al.* [2004]. The artifacts were difficult to detect using Finnigan's 252 instruments since ion extraction from the source region at 10 keV is very efficient but was more obvious in the lower source voltage in Finnigan Delta-Plus instruments of 3 keV used by Westley *et al.* Even more recently, a Fourier Transform Infrared Absorption technique [Parkes, 2008; Griffith *et al.*, 2009] was used to determine the Site Preference of tropospheric N₂O, and the results for the site-specific isotopic composition of tropospheric N₂O were in good agreement with those of Toyoda and Yoshida. These results demonstrate that the purely mass-spectrometric techniques to calibrate site-specific N₂O isotope compositions on the air-

N₂ scale, although much simpler to perform than the N₂O synthesis of Toyoda and Yoshida, are inaccurate and that the Toyoda and Yoshida [1999] air-N₂ scale should be used.

Since new calibration runs and/or intercomparison runs with a standard which has been calibrated using the method described in Toyoda and Yoshida [1999] have yet to be performed, in order to report our measurements of $\delta^{15}\text{N}^{\alpha}$ and $\delta^{15}\text{N}^{\beta}$ relative to air-N₂, the isotopic composition of tropospheric N₂O is used as a transfer standard, as has been done provisionally by many authors in recent peer-reviewed literature due to these difficulties encountered in establishing an accepted international air-N₂ standard. Since N₂O is generally well-mixed throughout the troposphere, variations in its isotopic composition are relatively small, at least compared to the continuous flow IRMS measurement precision. Furthermore, its isotopic composition is changing only slowly relative to its measurement precision (see Chapter 3 for a determination of this rate of change). Thus, comparing measurements of tropospheric N₂O relative to our working standard with measurements of tropospheric N₂O calibrated relative to air-N₂ allows us to convert our measurements to the air-N₂ scale of Toyoda and Yoshida [1999]. The first step is to convert our measurements on the Kaiser *et al.* [2004] air-N₂ scale to a tropospheric N₂O scale. This is done using measurements of the isotopic composition of tropospheric N₂O on samples collected on the UC Berkeley campus. The basic equation for a δ -value (without the 1000x scaling factor for per mil) is $\delta = R_{\text{sam}}/R_{\text{std}} - 1$, so in order to convert a sample measured relative to the Kaiser air-N₂ scale to a tropospheric N₂O scale, the following relationships are used:

$$(\delta_{\text{sam-vs-air-N}_2} + 1) = R_{\text{sam}}/R_{\text{air-N}_2} \quad (2.3)$$

and

$$(\delta_{\text{trop-N}_2\text{O-vs-air-N}_2} + 1)^{-1} = R_{\text{air-N}_2}/R_{\text{trop-N}_2\text{O}}. \quad (2.4)$$

Combining these two equations yields

$$\delta_{\text{sam-vs-trop-N}_2\text{O}} = [(\delta_{\text{sam-vs-air-N}_2} + 1) / (\delta_{\text{trop-N}_2\text{O-vs-air-N}_2} + 1)] - 1. \quad (2.5)$$

Given that the sample measurements in 2.5 are relative to tropospheric N₂O, it is trivial to write similar transfer equations to bring these values onto the air-N₂ scale given the Site Preference of tropospheric N₂O of 18.7‰ [Yoshida and Toyoda, 2000] and the value of $\delta^{15}\text{N}^{\text{bulk}}$ of tropospheric N₂O. For the work reported in this dissertation, a value for $\delta^{15}\text{N}^{\text{bulk}}$ of 6.2‰ is used, based on the average of 288 samples of tropospheric N₂O measured at Berkeley between September 2001 and November 2006. Accounting for the uncertainties in the measured quantities used in the calculations, this method yields an overall 1 σ uncertainty of ~1.6‰, 1.7‰, and 2.4‰ for $\delta^{15}\text{N}^{\alpha}$, $\delta^{15}\text{N}^{\beta}$, and SP, respectively. However, the absolute accuracy of the results is somewhat more uncertain than this since different values for SP of tropospheric N₂O have been measured by different groups [Griffith *et al.*, 2009] which range from 18.7‰ [Yoshida and Toyoda, 2000] to 21.5‰ [Sutka *et al.*, 2003]. An international intercomparison of standards and tropospheric samples between the relatively few laboratories making site-specific nitrogen isotopic composition measurements will be required to reduce the uncertainty in the relative accuracy between laboratories below these values.

2.1.4. Baseline issue for δ^{31} measurements

Prior to this work, there had been some anomalous site-specific measurements, such as occasionally very large differences in the standard peak measurements of up to $\sim 5\%$. Close examination of the recorded data for samples with anomalous results showed that in each anomalous run there was a low intensity, broad peak superimposed on one or more of the recorded standard or sample peaks in the ^{31}R data. By continuing the runs of typical samples of tropospheric air for ~ 1 hr after the last standard peak was measured, it was determined that these peaks occurred with repeatable timing and width and are, therefore, most likely due to compounds which are present in air samples that elute slowly from the GC column and which form m/z 31 ions in the IRMS. Thus, the anomalies in the baseline for a given run are caused by two species which elute from the GC long after the N_2O does from the previous sample and which can interfere with the standard or sample measurement in the subsequent run of the next sample. With sample pressures of about 1 atm in 100-mL flasks under normal operating conditions, interference from these slowly-eluting species can be avoided by starting subsequent runs within $< \sim 5$ minutes from the end of the previous run. If this is not feasible, the operator must then wait $> \sim 20$ minutes before running the subsequent sample. Note, however, that the precise timing and width of the interfering peaks varies also with the exact flow rate of He in the GC and should therefore be determined prior to measuring a set of samples.

2.2. Box model of the isotopic composition of atmospheric N_2O

In Chapter 3, the results of the optimized parameterization of a simple box model of the time evolution of mixing ratio and isotopic composition of N_2O since 1700 are discussed. In this section, additional details of that model formulation and optimization are described.

2.2.1. Model formulation

To determine the source implications of a time-series of measurements of the isotopic composition of N_2O , a two-box-model consisting of the troposphere and stratosphere was constructed. Because the wide range in measured isotopic compositions for the different natural and anthropogenic sources from a variety of studies precludes accurate assignment of representative values for individual sources, here only the flux-weighted average natural and anthropogenic sources are considered. A schematic diagram of the box model is shown in Figure 2.3.

The time dependence of the mixing ratio of nitrous oxide in the troposphere is given by the following equation:

$$\frac{d[\text{N}_2\text{O}]_T}{dt} = \frac{F_{STE} ([\text{N}_2\text{O}]_S - [\text{N}_2\text{O}]_T) + F_{NAT} + F_{ANT}}{\text{Mol}T}, \quad (2.6)$$

where F_{STE} is the amount of air in molar units exchanged between the stratosphere and troposphere per unit time, F_{NAT} is the amount of N_2O emitted from natural sources per unit time, and F_{ANT} is the amount of N_2O emitted from anthropogenic sources per unit time. $\text{Mol}T$ is the total number of moles of air in the troposphere and the subscripts S and T refer to the stratosphere and troposphere, respectively. The stratospheric mixing ratio is given by:

$$\frac{d[N_2O]_S}{dt} = \frac{F_{STE}([N_2O]_T - [N_2O]_S) - \frac{(MolT \cdot [N_2O]_T + MolS \cdot [N_2O]_S)}{\tau}}{MolS}, \quad (2.7)$$

where $MolS$ is the total number of moles of air in the stratosphere and τ is the global atmospheric lifetime of N_2O .

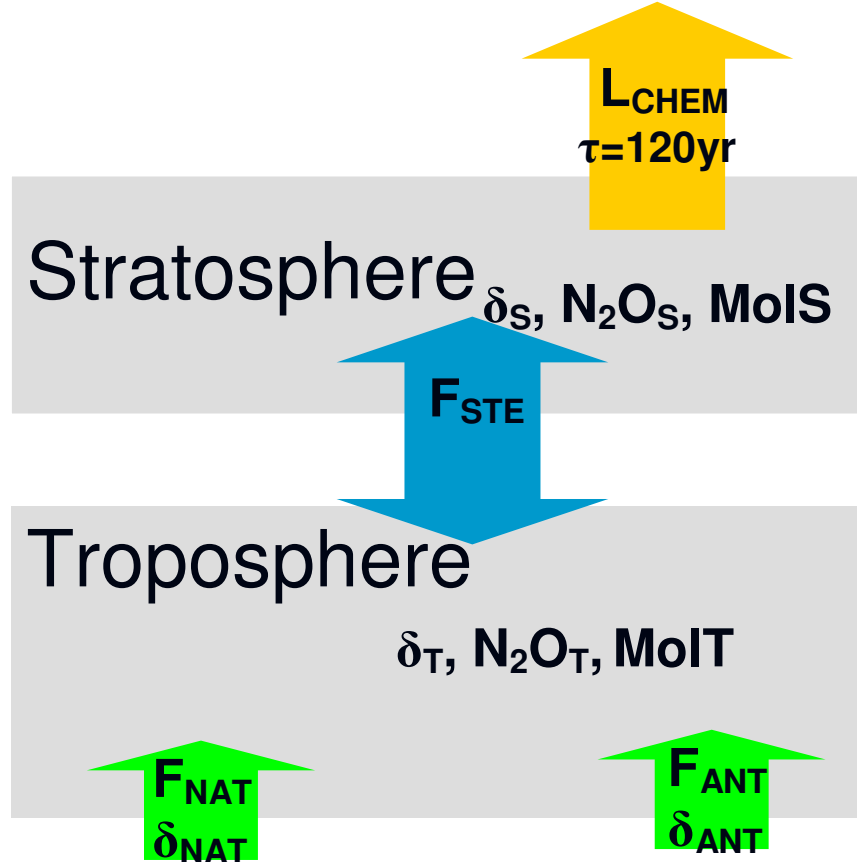


Figure 2.3. Schematic of a two-box model of the isotopic composition of atmospheric nitrous oxide.

The time dependence of the δ -values for the N_2O isotopic compositions in the troposphere is adapted from Sowers et al. [2006] and is given by:

$$\frac{d\delta_T}{dt} = \frac{F_{STE}[N_2O]_S(\delta_S - \delta_T) + F_{NAT}(\delta_{NAT} - \delta_T) + F_{ANT}(\delta_{ANT} - \delta_T)}{MolT \cdot [N_2O]_T}, \quad (2.8)$$

where δ_S is the characteristic δ -value of the isotopic composition of N_2O in the stratospheric return flux to the troposphere (see equation (2.9) below), and δ_{ANT} and δ_{NAT} are the average source isotopic signatures for the respective sources. Finally, a value for δ_S can be calculated based on the measured apparent enrichment factors, ϵ_{APP} , for the lower stratosphere of Park *et al.* [2004], by:

$$\delta_S = 1000 \cdot \left\{ \exp \left[\varepsilon_{APP} \ln \left(\frac{[N_2O]_S}{[N_2O]_T} \right) + \ln \left(\frac{\delta_T}{1000} + 1 \right) \right] - 1 \right\}. \quad (2.9)$$

Using these equations requires values for some of the parameters that are not being solved for. A pre-industrial mixing ratio of 272 ppb is assumed based on the average of ice-core data from MacFarling Meure *et al.* [2006] between 1700 and 1800, and the global lifetime, τ , is assumed to be constant and equal to 120 years [Forster *et al.*, 2007]. A value for F_{STE} is based on radiative calculations of the total annual downward mass flux across the 380K isentropic surface [Appenzeller *et al.*, 1996]. Fortunately, however, as demonstrated previously for CO₂ [Luz *et al.*, 1999] and N₂O [Park *et al.*, 2004], results for δ_T are not highly sensitive to using other values of F_{STE} , such as those calculated from dynamical considerations [Holton, 1990]: although the F_{STE} estimates can differ by a factor of 3, a higher F_{STE} will yield a higher $[N_2O]_S$ and, as can be seen from equation 2.9, δ_S is lower for a higher $[N_2O]_S$ and vice versa, so a large variation in F_{STE} causes only a small variation in the product $F_{STE} \cdot [N_2O]_S \cdot \delta_S$ in equation 2.8.

Next, the tropospheric mixing ratio ($[N_2O]_S$) and isotopic composition (δ_T) is assumed to be at steady-state prior to significant fluxes of anthropogenic N₂O to the atmosphere in order to initialize the model, and the δ -value of the natural N₂O source in the absence of an anthropogenic flux can then be calculated according to equation (2.10):

$$\delta_{NAT} = \delta_T - \frac{F_{STE} \cdot [N_2O]_S (\delta_S - \delta_T)}{F_{NAT}}. \quad (2.10)$$

We will then assume that δ_{NAT} does not change does not change over time.

Finally, F_{ANT} is modeled as an exponential increase, as is typical in box models of time-dependent changes in atmospheric N₂O since the change in N₂O mixing ratio since 1700 is well approximated by an exponential increase [e.g. Rahn and Wahlen, 2000; Bernard *et al.*, 2006]:

$$F_{ANT} = a \cdot \exp[b \cdot (t - t_0)]. \quad (2.11)$$

It is important to note, however, that it is possible that the isotopic composition of anthropogenic N₂O has been changing over time. For example, beginning around the 1960s there was a large increase in the amount of fertilizer used in agriculture [Davidson, 2009]. Since fertilized soil tends to emit lighter nitrous oxide, the average anthropogenic signature may have become lighter since the 1960s [Perez *et al.*, 2001]. As a starting point, however, we have assumed it to be constant in this study, and an analysis taking into account possible temporal variations in the anthropogenic isotopic signature is beyond the scope of the work presented here.

2.2.2. Model Optimization

The parameters a and b in equation (2.11) were adjusted to minimize the χ^2 value of the model output for N_2O mixing ratios compared to the archived and firm air measurements of N_2O presented in Chapter 3, combined with the firm and ice-core data from MacFarling Meure *et al.* [2006] for measurements prior to ~ 1940 . Note that while the minimization procedure applied here, which is run over only a small range (chosen by a χ -by-eye procedure), does not rule out that the best fit parameterization is a local minimum, this approach yields good agreement with the most recent IPCC estimates of natural and anthropogenic total flux [Forster *et al.*, 2007]; a natural source flux of 11.1 TgN yr^{-1} and an anthropogenic source flux of 6.6 TgN yr^{-1} at the end of 2009 are calculated using this model and this approach, and the corresponding IPCC results are 11.0 and 6.7 TgN yr^{-1} , respectively [Forster *et al.*, 2007].

After optimizing the N_2O fluxes in the model against the mixing ratio observations, δ_{ANT} and δ_{NAT} were then adjusted to minimize χ^2 between the measured and modeled values of δ_T . Using the χ^2 data from the minimization runs, the 68.3 and 95.4% confidence intervals for the parameters δ_{ANT} and δ_{NAT} were calculated by using the contours for $\chi^2 - \chi^2_{\min} = \delta\chi^2 = 2.3$ and 6.17 on a plot of δ_{ANT} versus δ_{NAT} [Press *et al.*, 1986]. The minimization results for $\delta^{15}N^{\text{bulk}}$ are shown in Figure 2.4. Such model results, optimized to fit the N_2O isotope measurements from a time series of data from archived air from Cape Grim, Tasmania and from firm air from Law Dome, Antarctica, are used in Chapter 3 to place new constraints on the isotopic compositions of the natural and anthropogenic sources of N_2O .

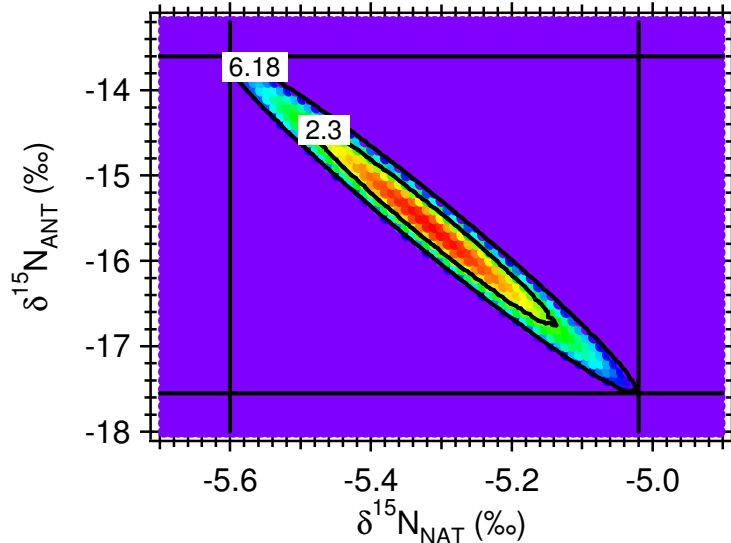


Figure 2.4. Contour plot of $\delta\chi^2$ ($= \chi^2 - \chi^2_{\min}$) between model output and measurements for χ^2 minimization runs for $\delta^{15}N^{\text{bulk}}$ for the natural ($\delta^{15}N_{NAT}^{\text{bulk}}$) and anthropogenic ($\delta^{15}N_{ANT}^{\text{bulk}}$) N_2O sources. The vertical and horizontal lines intersect the axes at the 95.4% confidence intervals for $\delta^{15}N_{ANT}^{\text{bulk}}$ (x-axis) and $\delta^{15}N_{NAT}^{\text{bulk}}$ (y-axis).

2.3. Data analysis for photoionization of the isotopologues of N₂

Photoionization efficiency spectra of the isotopologues of N₂ measured at the Chemical Dynamics Beamline of the Advanced Light Source at LBNL are presented in Chapter 6. Here, three important aspects of the data analysis are discussed: (1) the calibration of the energy scale, (2) the merging of different runs, and (3) the calculation of the ratios of the photoionization rate constants.

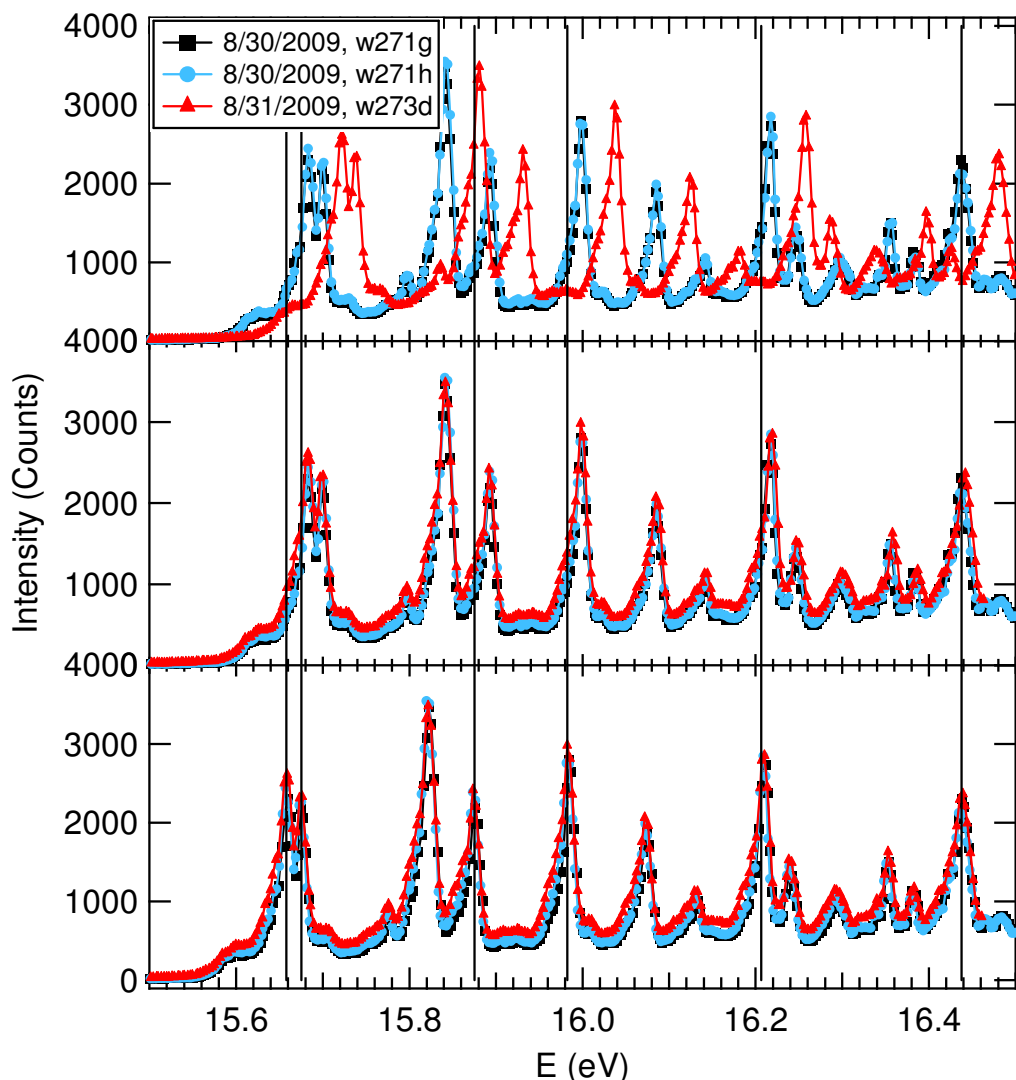


Figure 2.5. Comparison of the raw and calibrated energy scales for three runs on two different days between 15.5 and 16.5 eV. The ¹⁴N₂ data from two runs performed on August 30, 2009 (black squares and blue circles) and one run performed on August 31, 2009 (red triangles) are shown. The top panel shows all the data on the raw energy scale (from the monochromator reading), the middle panel shows the data obtained on August 30 on the raw energy scale and the data from August 31 data on the raw energy scale with a -40 meV offset applied, and the bottom panel shows the data on the calibrated energy scale. The vertical lines represent the peak energies from Lofthus and Krupenie [1977] and used for the calibration.

There is significant uncertainty in the energy scale recorded during the course of the two-day ALS experiment due to mechanical precision of the monochromator, as discussed in Chapter 6, which requires the energy scale to be calibrated. The data from three different runs from 15.5 to 16.5 eV are shown in Figure 2.5 to demonstrate the nature and extent of the run-to-run differences. The top panel shows the data on their raw energy scales. Clearly there is a significant change in the apparent peak energies between the measurements performed on August 30 and August 31. However, as shown in the middle panel, where the energy scale for the data obtained on August 31 have simply been shifted by -40 meV, the differences are largely linear. This is further demonstrated by Table 2.3, which summarizes the energy differences between different runs. The differences in peak energies between all of the peaks in the two given runs are similar; the range of these differences is less than the 6.5 meV bandwidth used in the experiment. Despite the fact that the run-to-run differences are largely linear, a calibration of the raw energy scale from the monochromator using known peak energies is required in order to obtain an accurate energy scale. For example, the need for such a calibration can be seen by comparing the known peak energies from *Lofthus and Krupenie* [1977] – shown by vertical lines in Figure 2.5 – with the peak energies recorded during the ALS experiment. While the peak at 16.44 eV is in good agreement, the energies of the other peaks based on the raw monochromator data do not agree well, suggesting that the recorded energy scale is contracted. The energy scale calibration is achieved using a linear regression between the recorded peak energies and the well-known peak energies in the $^{14}\text{N}_2$ spectrum from Lofthus and Krupenie [1977]. The vertical lines shown in all panels of Figure 2.5 and in Figure 2.6 represent the peak energies used to calibrate the energy scale. The differences between the peak energies from Lofthus and Krupenie [1977] used in the calibration and the calibrated peak energies in the PIE spectra are shown in Table 2.4 for the peaks shown in Figure 2.5 showing that the peak energies are now in agreement with the values used for the calibration to within the 6.5 meV bandwidth of the experiment. The average of the differences is 0.5 meV and the average of the absolute values of the differences is 1.4 meV. Similar agreement is seen throughout the spectrum on the calibrated energy scale as shown in Figure 2.6. For reference, the peak energies used for the calibration for the entire energy range are listed with the corresponding peak assignments (which are shown in Figure 6.1) in Table 2.5 for the entire 15.5 – 18.9 eV range.

After the energy scale calibration, data from individual runs – which cover a range of ≤ 1 eV because of file-size limitations of the PC used for data acquisition – were normalized for differences in detection efficiency and merged into a single dataset. The merging and normalization was performed first for the $^{14}\text{N}_2$ data, and the resulting normalization factors were then used to normalize the $^{15}\text{N}^{14}\text{N}$ and $^{15}\text{N}_2$ data so that the relative peak intensities between different isotopologues remained the same. The merging procedure is summarized in Figure 2.7. The recorded $^{14}\text{N}_2$ intensity data for the runs used to create the merged dataset (w273d, w273a, w273b, w272d, and w273c) are shown in the top panel. To facilitate merging the data from different runs into a single spectrum encompassing the entire 15.5 – 18.9 eV range, each run was designed to include overlap with a peak measured in a different run. For the runs shown here, differences in detection efficiency between runs led to the maximum intensities of the overlapping peaks differing by between 0.6 and 10%. In order to account for these differences, each run was normalized by dividing each data-point in that run by the maximum intensity of the overlapping peak in that run. The result of the normalization is

Table 2.3. Peak location differences in eV for the $^{14}\text{N}_2$ data on the uncalibrated energy scale. The peak locations were determined by fitting peaks with Voigt profiles.

Peak Assignment	Peak Energy Difference (eV)			Run Identifier			
	Run #2 – Run #1	Run #3 – Run #1	Run #4 – Run #1	Run #1	Run #2	Run #3	Run #4
$(\text{B}^2\Sigma_g^-, v'=0) 3s\sigma_g^+ \Sigma_u$	0.0007	0.0384	-	w271g	w271h	w273d	-
$(\text{A}^2\Pi_u, v'=2) 4s\sigma_g^+ \Pi_u$	0.0010	0.0392	-	w271g	w271h	w273d	-
$(\text{A}^2\Pi_u, v'=2) 3d\sigma_g^+ \Pi_u$	0.0007	0.0396	-	w271g	w271h	w273d	-
$(\text{A}^2\Pi_u, v'=0) 4d\sigma_g^+ \Pi_u$	0.0010	0.0400	-	w271g	w271h	w273d	-
$(\text{A}^2\Pi_u, v'=1) 4d\sigma_g^+ \Pi_u$	0.0004	0.0410	-	w271g	w271h	w273d	-
$(\text{A}^2\Pi_u, v'=2) 4d\sigma_g^+ \Pi_u$	0.0010	0.0423	-	w271g	w271h	w273d	-
$(\text{A}^2\Pi_u, v'=3) 4d\sigma_g^+ \Pi_u$	0.0175	-	-	w272b	w273a	-	-
$(\text{A}^2\Pi_u, v'=1) 6d\sigma_g^+ \Pi_u$	0.0211	-	-	w272b	w273a	-	-
$(\text{A}^2\Pi_u, v'=2) 6d\sigma_g^+ \Pi_u$	0.0169	-	-	w272b	w273a	-	-
$(\text{B}^2\Sigma_g^-, v'=0) 4d\sigma_g^+ \Sigma_u$	0.0182	0.0066	0.0203	w272b	w273a	w272c	w272d
$(\text{B}^2\Sigma_g^-, v'=0) 5d\sigma_g^+ \Sigma_u$	0.0084	-0.0307	0.0045	w272b	w272c	w272d	w273b
$(\text{B}^2\Sigma_g^-, v'=0) 6d\sigma_g^+ \Sigma_u$	0.0291	-	-	w272a	w272d	-	-
$(\text{B}^2\Sigma_g^-, v'=0) 7d\sigma_g^+ \Sigma_u$	0.0289	-	-	w272a	w272d	-	-
$(\text{B}^2\Sigma_g^-, v'=0) 8d\sigma_g^+ \Sigma_u$	0.0285	-	-	w272a	w272d	-	-
$(\text{B}^2\Sigma_g^-, v'=0) 9d\sigma_g^+ \Sigma_u$	0.0267	-	-	w272a	w272d	-	-
$(\text{B}^2\Sigma_g^-, v'=0) 10d\sigma_g^+ \Sigma_u$	0.0281	-0.0089	-0.0153	w272a	w272d	w273e	w273c
$(\text{B}^2\Sigma_g^-, v'=0) 11d\sigma_g^+ \Sigma_u$	-0.0020	-	-	w272e	w273c	-	-
$(\text{B}^2\Sigma_g^-, v'=0) 12d\sigma_g^+ \Sigma_u$	-0.0031	-	-	w272e	w273c	-	-
$(\text{B}^2\Sigma_g^-, v'=0) 13d\sigma_g^+ \Sigma_u$	0.0001	-	-	w272e	w273c	-	-

Table 2.4. Differences between peak energies in eV used for calibration and peak energies after the calibration for runs in the 15.5 – 16.5 eV range.

Peak Assignment	Energy Difference (eV)		
	w271g	w271h	w273d
$(\text{B}^2\Sigma_g^-, v'=0) 3s\sigma_g^+ \Sigma_u$	-0.0014	0.0006	-0.0004
$(\text{A}^2\Pi_u, v'=2) 4s\sigma_g^+ \Pi_u$	-0.0007	-0.0018	0.0001
$(\text{A}^2\Pi_u, v'=2) 3d\sigma_g^+ \Pi_u$	0.0012	-0.0028	0.0025
$(\text{A}^2\Pi_u, v'=0) 4d\sigma_g^+ \Pi_u$	-0.0037	0.0028	-0.0034
$(\text{A}^2\Pi_u, v'=1) 4d\sigma_g^+ \Pi_u$	-0.0005	-0.0012	0.0000
$(\text{A}^2\Pi_u, v'=2) 4d\sigma_g^+ \Pi_u$	-0.0007	-0.0004	0.0011

Table 2.5. Peak energies in eV from Lofthus and Krupenie [1977] that were used in the energy scale calibration. Peak assignments are shown in Figure 6.1.

Peak Assignment	Peak Energy (eV)
$(B^2\Sigma_g v'=0) 3s\sigma_g^1\Sigma_u$	15.657
$(A^2\Pi_u v'=2) 4s\sigma_g^1\Pi_u$	15.677
$(A^2\Pi_u v'=2) 3d\sigma_g^1\Pi_u$	15.877
$(A^2\Pi_u v'=0) 4d\sigma_g^1\Pi_u$	15.981
$(A^2\Pi_u v'=1) 4d\sigma_g^1\Pi_u$	16.210
$(A^2\Pi_u v'=2) 4d\sigma_g^1\Pi_u$	16.438
$(A^2\Pi_u v'=1) 6d\sigma_g^1\Pi_u$	16.585
$(A^2\Pi_u v'=3) 4d\sigma_g^1\Pi_u$	16.663
$(A^2\Pi_u v'=2) 6d\sigma_g^1\Pi_u$	16.812
$(B^2\Sigma_g v'=0) 4d\sigma_g^1\Sigma_u$	17.151
$(B^2\Sigma_g v'=0) 5d\sigma_g^1\Sigma_u$	17.865
$(B^2\Sigma_g v'=0) 6d\sigma_g^1\Sigma_u$	18.187
$(B^2\Sigma_g v'=0) 7d\sigma_g^1\Sigma_u$	18.363
$(B^2\Sigma_g v'=0) 8d\sigma_g^1\Sigma_u$	18.467
$(B^2\Sigma_g v'=0) 9d\sigma_g^1\Sigma_u$	18.534
$(B^2\Sigma_g v'=0) 10d\sigma_g^1\Sigma_u$	18.580
$(B^2\Sigma_g v'=0) 11d\sigma_g^1\Sigma_u$	18.612
$(B^2\Sigma_g v'=0) 12d\sigma_g^1\Sigma_u$	18.637
$(B^2\Sigma_g v'=0) 13d\sigma_g^1\Sigma_u$	18.653

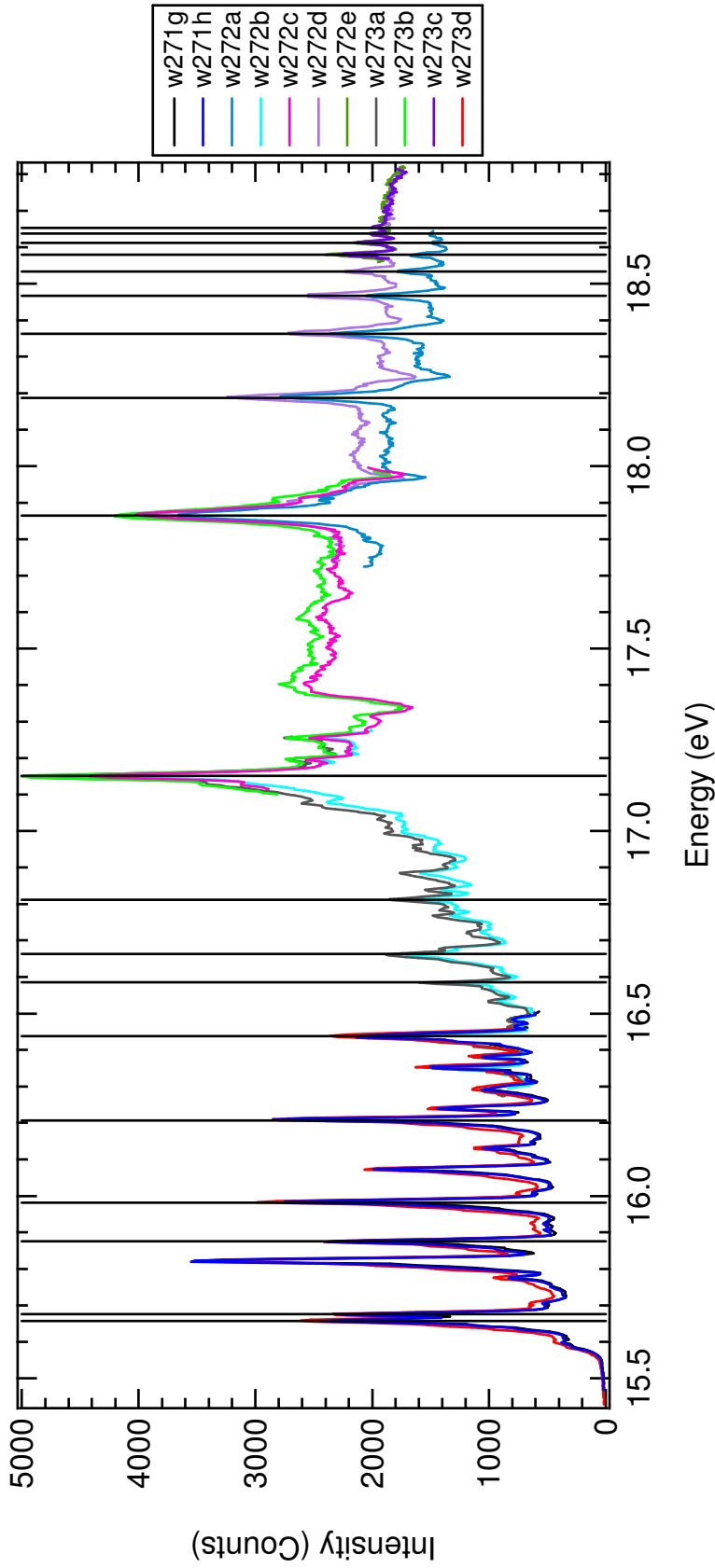


Figure 2.6. All of the runs on their calibrated energy scales. The vertical lines represent the peak energies used in the calibration from Lofthus and Krupenie [1977]. There is agreement between the calibrated peak energies and the values used in the calibration to within the 6.5 meV bandwidth of the experiment.

shown in the middle panel of Figure 2.7. The normalization procedure was performed from left to right; the first two runs were normalized using the peaks labeled “1” in the top panel, then all of the data in both of these runs was then divided by the maximum intensity of the peak in the second run, which overlapped the third run (*i.e.* the peak labeled “2”), and so on. Finally, the overlapping data from the higher energy run was removed as shown in the bottom panel of Figure 2.7 in order to create a dataset with a monotonically increasing energy scale. After merging, the resulting PIE spectrum for each isotopologue was then scaled by the inverse of its mole fraction in the gas mixture, as described in Chapter 6.

Using this merged dataset, the ratios of the photoionization rate constants, or J-values, and their uncertainties were calculated for two scenarios: first, assuming a radiation source with constant intensity and, second, assuming solar irradiation at the top of Earth’s atmosphere. The J-value is defined by equation (2.12).

$$J = \int_{E_i}^{E_f} \sigma(E)I(E)dE \quad (2.12)$$

where $\sigma(E)$ is the energy dependent photoionization cross-section, $I(E)$ is the intensity of the radiation and the integral is over the entire range, E_i to E_f . The integrals were calculated using the rectangle rule and the uncertainties were calculated by propagating the uncertainty for each parameter. In the first case, $I(E)$ is taken as exactly unity and only $\sigma(E)$ and dE (which becomes ΔE in the numeric integration) require uncertainty estimates. The uncertainty in $\sigma(E)$ was calculated by comparing the recorded signals between the three runs between 15.5 and 16.5 eV shown in Figure 2.5. The data were normalized and interpolated onto the same energy scale and the standard deviation was calculated to be 14%. The uncertainty in ΔE was set to 0.001 eV, based on the standard deviation of the difference between sequential points in the calibrated energy scale. For the calculation of the second scenario, the uncertainty in $I(E)$, the solar flux in this case, was taken to be the accuracy of the TIMED/SEE instrumental, which is 10% [Woods *et al.*, 2005].

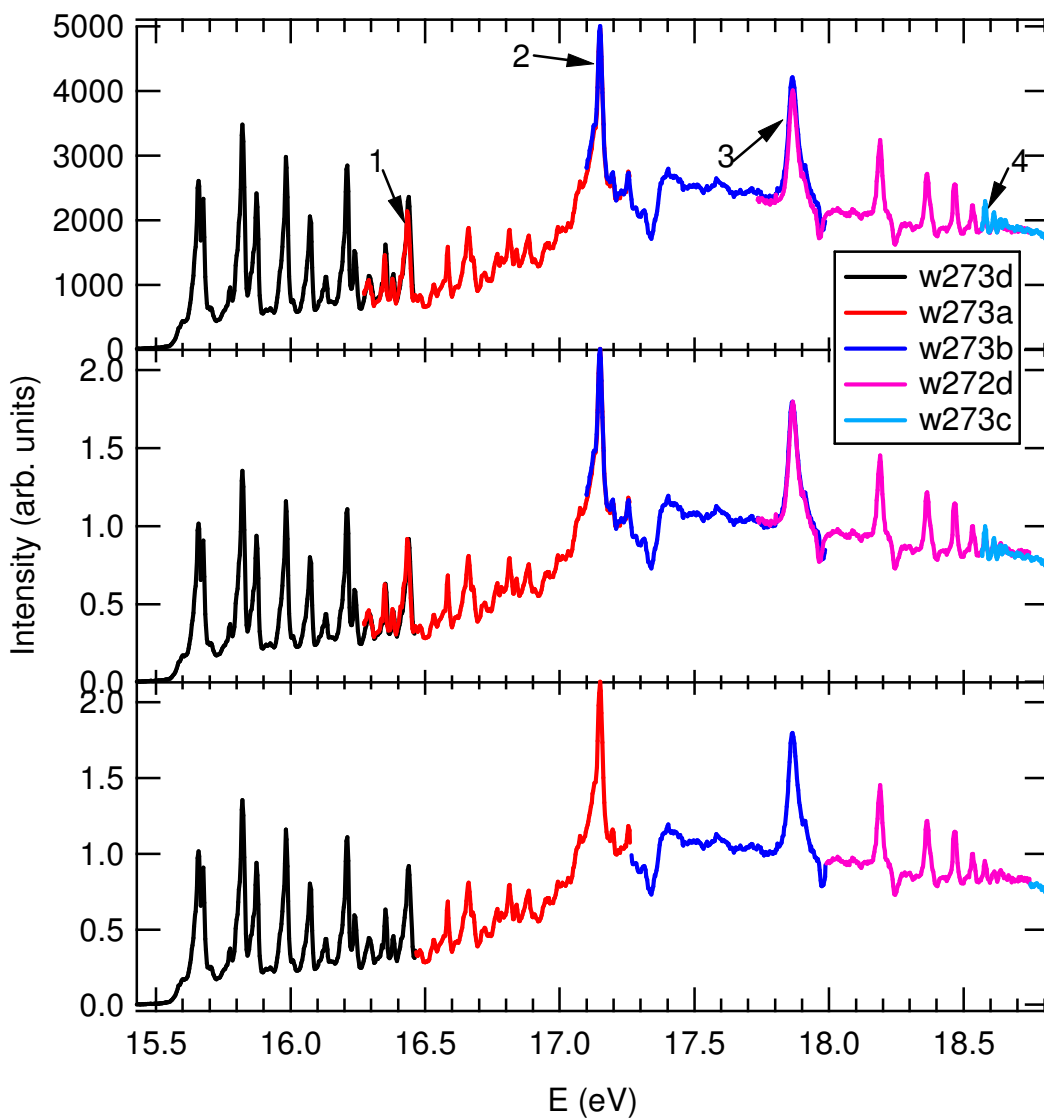


Figure 2.7. Steps in the merging procedure for the $^{14}\text{N}_2$ photoionization efficiency spectrum. All data are shown on the calibrated energy scale. The top panel shows raw intensity for each run, the middle panel shows the data after the normalization was carried out, and the bottom panel shows the merged data after overlapping points were removed.

2.4. Design and testing of a rotating quarter-wave plate polarimeter

Aerosols play an important role in radiative transfer and chemistry in planetary atmospheres, including those of the Earth and of Saturn's moon, Titan. Here, the development of a laboratory apparatus for measuring the Stokes vector of light scattered from aerosols in laboratory experiments, the results of initial tests, and the necessary steps for coupling the apparatus to an existing experimental set-up which has been used to monitor the kinetics of the formation of higher molecular weight species and aerosol during the UV irradiation of methane (as in *Ádámkovics and Boering [2003]*) are discussed.

In the experimental set-up, hydrocarbons, such as methane, or a mixture of hydrocarbon and other gases such as carbon dioxide, are introduced into an evacuated 6-L stainless steel chamber where they are photolyzed by VUV radiation from a deuterium lamp. The radiation from this lamp drives a series of photochemical reactions of which aerosols are a product, and which may be similar to those which occur in the atmosphere of interest (e.g., Titan or Early Earth). The gas phase mixture is sampled through a precision leak valve to a quadrupole mass spectrometer to study the gas phase photochemistry. A HeNe laser is directed through a viewport or fiber-optically coupled into the chamber and directed into a beam dump on the opposite end of chamber; as aerosols are formed, they scatter this light. In previous studies with this apparatus [*Ádámkovics and Boering, 2003; Ádámkovics, 2004*], the time-resolved intensity of scattered laser light was detected at a fixed angle relative to the incident laser beam using a photomultiplier tube (“PMT”) that was fiber-optically coupled to the reaction chamber. Recently, the fiber-optically coupled PMT detection scheme has been replaced with a photodiode inside of the chamber mounted on a rotation stage to allow determination of the time-varying angular dependence, or phase function, of light scattering intensity. The work described in this section involves the development and testing of a polarimeter which will be incorporated into the experiments and allow for measurements of the time-dependent phase function of the polarization state of light scattered by the aerosols. The overall goal of such measurements is to retrieve the time-resolved optical properties of the particles — such as the size distribution and complex index of refraction — from the *in situ* measurements using inverse models of light scattering, such as those currently being developed at the NASA Ames Lunar Dust Laboratory [*Richard and Davis, 2008*]. In Section 2.4.1, brief overviews of the theory behind light scattering, Stokes polarimetry in general, and rotating quarter-wave plate polarimetry in particular are given. In Section 2.4.2, the details of the construction of the polarimeter are discussed. In Section 2.4.3, results of initial tests of the polarimeter and comparison with Mie theory calculations are given. In Section 2.4.4, some important practical aspects of the eventual incorporation of the polarimeter into the existing laboratory apparatus are discussed.

2.4.1 Introduction to light scattering and Stokes polarimetry

How the polarization state of light changes when it is scattered by a medium consisting of small particles depends on the size distribution of the particles, their refractive indices, and the wavelength of the scattered light [*van de Hulst, 1957*]. Thus, measuring the polarization state of light scattered by small particles at a fixed angle provides some information about their size distribution and index of refraction. More complete information about the size distribution and index of refraction can be obtained by measuring the angular

dependence, or phase function, of the polarization state of light scattered by the particles and comparing the results to model predictions.

The polarization state of light can be described by the four-component Stokes vector, $\mathbf{S} = \{S_0, S_1, S_2, S_3\}$. S_0 is proportional to the total flux of the beam, S_1 and S_2 are the differences between the two orthogonally-oriented oscillating electric field components of the wave, and S_3 is the difference between two oppositely circularly polarized components. For light scattered by randomly oriented small particles, the incident and scattered Stokes vectors are related by a 16-member scattering matrix, \mathbf{M} [van de Hulst, 1957]:

$$\begin{pmatrix} S_{0s} \\ S_{1s} \\ S_{2s} \\ S_{3s} \end{pmatrix} = \frac{\lambda^2}{4\pi^2 r^2} \begin{pmatrix} F_{11} & F_{12} & F_{13} & F_{14} \\ F_{21} & F_{22} & F_{23} & F_{24} \\ F_{31} & F_{32} & F_{33} & F_{34} \\ F_{41} & F_{42} & F_{43} & F_{44} \end{pmatrix} \begin{pmatrix} S_{0i} \\ S_{1i} \\ S_{2i} \\ S_{3i} \end{pmatrix}, \quad (2.13)$$

where λ is the wavelength, r is the distance from the scattering region to the detector, and the subscripts i and s refer to the incident and scattered beam, respectively, and the matrix with elements F_{ij} is \mathbf{M} .

The work described here involves construction and testing of a rotating quarter wave-plate (QWP) polarimeter [Goldstein and Collett, 2003], which consists of a QWP mounted in a rotation stage, followed by a stationary linear polarizer (LP), and then a detector, as shown in Figure 2.8.

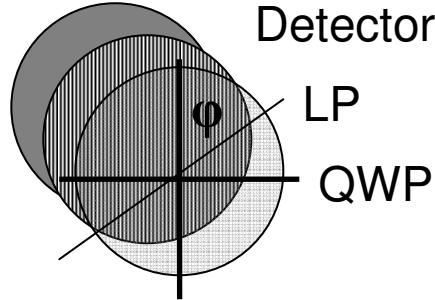


Figure 2.8: Diagram of the rotating quarter-wave plate (QWP) polarimeter. The QWP is rotated by an angle, φ , which is controlled with a computerized rotation stage, relative to a stationary linear polarizer (LP). The light passes first through the QWP, then the LP, and finally into a photodiode detector and, based on how the optical components alter the polarization state of the light which passes through them, the signal intensity as a function of φ , $I(\varphi)$, is used to determine the polarization state.

The intensity of the light passing through the QWP and LP to reach the detector, I , can be calculated by multiplying the Mueller matrices of the QWP and LP (which describe how these components transform the polarization state of the light that reaches the detector) to show that, with the QWP at an angle, φ , relative to the LP, I is given by

$$I(\varphi) = \frac{1}{2}(S_0 + S_1 \cos^2 2\varphi + S_2 \sin 2\varphi \cos 2\varphi - S_3 \sin 2\varphi). \quad (2.14)$$

The components of the Stokes vector of the light entering the polarimeter can be determined by measuring $I(\varphi)$. By rewriting equation (2.14) as a Fourier series, and after some trigonometric transformations, it can be shown that the elements of the Stokes vector can be determined by the following equations:

$$S_0 = A - C, \quad (2.15)$$

$$S_1 = 2C, \quad (2.16)$$

$$S_2 = 2D, \quad (2.17)$$

and

$$S_3 = B, \quad (2.18)$$

where

$$A = \frac{1}{\pi} \int_0^{2\pi} I(\varphi) d\varphi, \quad (2.19)$$

$$B = \frac{2}{\pi} \int_0^{2\pi} I(\varphi) \sin(2\varphi) d\varphi, \quad (2.20)$$

$$C = \frac{2}{\pi} \int_0^{2\pi} I(\varphi) \cos(4\varphi) d\varphi, \quad (2.21)$$

and

$$D = \frac{2}{\pi} \int_0^{2\pi} I(\varphi) \sin(4\varphi) d\varphi \quad (2.22)$$

[Goldstein and Collett, 2003]. In practice, the QWP is not continuously rotated but rather achieves a full rotation (i.e., 360°) in a certain number of steps, N , of angular size $\Delta\varphi$, the intensity is recorded for each of those steps, and the integrals are replaced with sums over N as follows:

$$A = \frac{2}{N} \sum_{n=1}^N I(n\Delta\varphi), \quad (2.23)$$

$$B = \frac{4}{N} \sum_{n=1}^N I(n\Delta\varphi) \sin(2n\Delta\varphi), \quad (2.24)$$

$$C = \frac{4}{N} \sum_{n=1}^N I(n\Delta\varphi) \cos(4n\Delta\varphi), \quad (2.25)$$

and

$$D = \frac{4}{N} \sum_{n=1}^N I(n\Delta\varphi) \sin(4n\Delta\varphi) \quad (2.26)$$

[Goldstein and Collett, 2003] and the results of these sums are used in equations 2.15 – 2.18 to calculate the elements of the Stokes vector, S_0 , S_1 , S_2 , and S_3 .

For experiments in which the polarimeter is used to determine the polarization state of scattered light, the measured Stokes vector of the scattered light can be combined with the Stokes vector of the incident light to determine components of the scattering matrix, \mathbf{M} . With a sufficient combination of incident polarization states, all 16 elements can be determined from equation 2.13 above.

However, in many studies the complete scattering matrix is not determined due to its complexity; instead only certain parameters of the scattering are determined which may be easier to measure. One common scattering parameter is the “degree of polarization,” P , which is given by equation 2.27,

$$P = (S_1^2 + S_2^2 + S_3^2)^{1/2} / S_0 \quad (2.27)$$

which describes the extent to which the light is polarized (i.e., $P=1$ for completely polarized light and $P=0$ for completely unpolarized light).

In the tests discussed in Section 2.4.3 below, the Stokes vector of linearly polarized light is determined in the presence and absence of scattering. With the orientation used in these tests, the angle of linear polarization should be the same as the azimuth angle, ψ , which can be calculated using equation (2.28) [Giudicotti and Brombin, 2007].

$$\psi = \begin{cases} \frac{1}{2} \arctan(S_2 / S_1) & \text{for } S_1 > 0 \text{ and } S_2 \geq 0 \\ \frac{1}{2} \arctan(S_2 / S_1) + \pi & \text{for } S_1 > 0 \text{ and } S_2 < 0 \\ \frac{1}{2} \arctan(S_2 / S_1) + \frac{\pi}{2} & \text{for } S_1 < 0 \end{cases} \quad (2.28)$$

For tests in the absence of scattering, the Stokes vector is used to calculate P and ψ which are then compared to their known values. For scattering tests, the phase functions of some of the elements of \mathbf{M} are determined and are compared to the results of calculations based on Mie theory.

2.4.2. Polarimeter construction and experimental set-up

A rotating QWP polarimeter, as shown in Figure 2.6, was constructed by mounting a QWP (WPMQ05M-633, ThorLabs, Newton, NJ) in a rotating stage (PR50CC, Newport, Irvine, CA), behind which was mounted a LP (5511, New Focus, Santa Clara, CA), and

behind that a Si photodiode detector with a responsivity at 633 nm of ~ 0.4 A/W (ThorLabs, PDA55) with a 633 nm laser line filter (Newport). The rotation stage was controlled and the data acquisition was performed using software built using LabWindows/CVI (National Instruments, Austin, TX). The software is capable of controlling the length and frequency of averaging of the photodiode signal (either a raw signal, which is used for tests in the absence of scattering, or an amplified signal, which is used in the scattering tests) and the angular step size and number of steps for the QWP rotation stage. The light source for all of the tests was a 15 mW, 632.8 nm HeNe laser (Melles Griot, Albuquerque, NM). For tests in the absence of a scattering medium, the laser beam was directed through the polarimeter and the signal from the photodiode as a function of QWP angle (i.e., $I(\varphi)$) was simply recorded as a voltage.

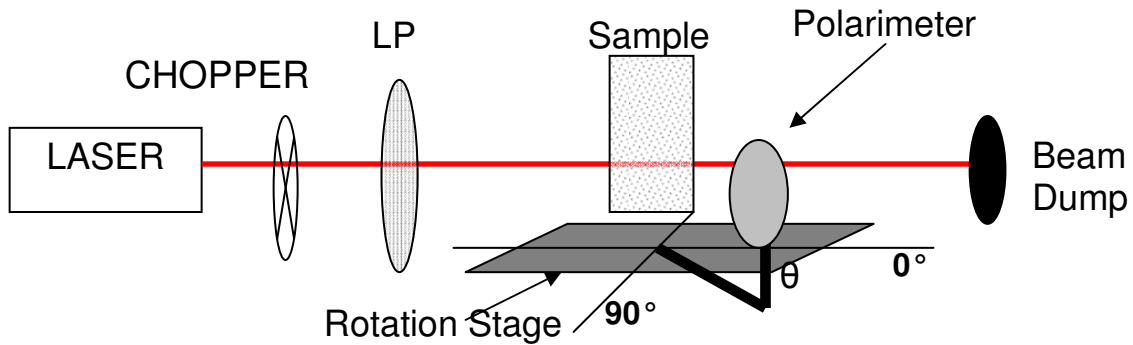


Figure 2.9. Experimental setup for scattering matrix phase function determination; the polarimeter components are shown in Figure 2.8.

For tests with a scattering medium, the experimental set-up used is shown in Figure 2.9. The entire polarimeter was mounted on a second rotation stage (New Focus, 8401), which was oriented at an angle, θ , relative to the incident laser beam. This rotation stage can be computer controlled, although it was positioned manually for these initial tests. As will be the case when the polarimeter is incorporated into the experimental apparatus for which it was designed, the laser light was chopped with a mechanical chopper, and a lock-in amplifier (SR830, Stanford Research Systems, Sunnyvale, CA) was used to process the photodiode signal. The scattering medium for these tests was an aqueous dispersion of polystyrene latex spheres (Duke Scientific, Palo Alto, CA, 4K-02, diameter= $1.998 \pm 0.022 \mu\text{m}$, $7.5 \times 10^6 \text{ mL}^{-1}$, refractive index= 1.58 at 588 nm) in a 20 mL Pyrex vial. A diameter of $\sim 2 \mu\text{m}$ was chosen because the results of Ádámkóvics and Boering [2003] showed that 1 to 3 μm was the typical range of particle sizes produced in experiments in the apparatus for which this polarimeter was designed. The vial rested on a platform, centered above the rotation stage. After passing through the chopper and a LP (New Focus, 551), the laser beam, which was vertically aligned with the photodiode, passed through the vial. For each value of θ , the spheres in the vial scattered some of the laser light towards the polarimeter, and the intensity from the lock-in amplifier signal, recorded as a function of QWP angle (i.e., $I(\varphi)$), was used to calculate the Stokes vector of this light. In order to obtain data with sufficient signal-to-noise for all values of θ , the lock-in amplifier signal was averaged at 500 Hz for 0.2s for each value of φ and the QWP was rotated a total of 720° with a step-size of $\Delta\varphi=5^\circ$. The total measurement time for each value of θ , which included the time it took to rotate the stage and take the measurements was ~ 3 minutes.

For the tests described below using this set-up, two corrections are applied to the $I(\varphi)$ data prior to calculating the Stokes vector. First, a small background signal was present for some values of θ ; this background was found to be constant for all values of φ and ψ and a correction was applied to the recorded intensities by subtracting the background signal. It was later determined that by placing baffles in front of the LP, the background could be eliminated. The second correction was scaling all of the recorded intensities by a factor of $\sin(\theta)$ to compensate for the different scattering volumes ‘seen’ by the detector at different angles [Volten *et al.*, 1998].

2.4.3. Performance Tests

After the polarimeter was designed and built, two initial sets of tests of its performance were conducted, for which an overview is given in this paragraph and more details follow in later paragraphs. The first set was designed to test the performance of the polarimeter in the absence of scattering. In these tests, linearly polarized light was directed through the polarimeter, data were recorded and used to calculate the polarization state, and the results were compared to the known polarization state and were found to give reasonable agreement, as discussed below. The second set was designed to test the performance of the polarimeter for scattered light in order to determine how the polarimeter will function in the experimental apparatus. In these tests, linearly polarized light was scattered by an aqueous dispersion of 2 μm spheres (described in the previous section), and the polarization state of this scattered light was measured using the polarimeter. This was done for θ from 20° to 150° in 5° steps and for two values of ψ , 0° and 90°. These measurements were then used to calculate the phase functions for the four elements in the top left corner of the scattering matrix, \mathbf{M} . Two of the elements of \mathbf{M} , F_{11} and $-F_{12}/F_{11}$, are compared with results of Mie theory calculations and show some general agreement, but there are also some issues that need to be resolved.

The first set of tests in the absence of scattering was performed to determine whether a linear polarization state could be set and then retrieved with the polarimeter, which would show that the polarimetry data analysis is accurately calculating a Stokes vector. These tests consisted of simply setting the linear polarization of the incident laser beam at an angle, ψ , relative to the LP of the polarimeter and using that data to calculate the Stokes vector, $\mathbf{S} = \{S_0, S_1, S_2, S_3\}$, the degree of polarization, P , and the azimuth angle, ψ , which should be the same as the angle of linear polarization for these tests. The data from these tests, which were performed for $\psi = 0^\circ$ and $\psi = 90^\circ$, are shown in Figure 2.10 (a) and (b), respectively, along with the numerical results of the analysis for \mathbf{S} , P , and ψ , which appear in the figure's text boxes.

These tests were performed with completely polarized light in the absence of a scattering medium; therefore, P should be unity and ψ should be identical to the angle of the LP of the incident light relative to the LP in the polarimeter. For $\psi = 0^\circ$, $P = 0.944 \pm 0.014$ and $\psi = 2.67 \pm 0.24^\circ$. For $\psi = 90^\circ$, $P = 1.003 \pm 0.006$ and $\psi = 92.84 \pm 0.06^\circ$. In both cases, as expected, P is close to unity, although for the $\psi = 0^\circ$ test, the value is not statistically identical to 1. This may be related to the fact that, with the two LPs in parallel alignment, a greater total flux is incident on the detector than when they are aligned perpendicularly, making incomplete polarization easier to detect. The measured value of ψ is greater than the set polarization angle in both cases by a similar amount. This discrepancy is most likely due to a

slight misalignment of the incident laser polarizer relative to that of the polarimeter. The alignment for these initial tests was performed simply by adjusting the relative angle of the polarizers to minimize the raw voltage signal from the photodiode using a voltmeter. This imprecise method of alignment can be improved for further testing. Thus, with improved alignment, the polarimeter can be expected to retrieve a precisely set angle of linear polarization in the absence of scattering and that the data analysis routine will yield reasonably accurate Stokes vectors.

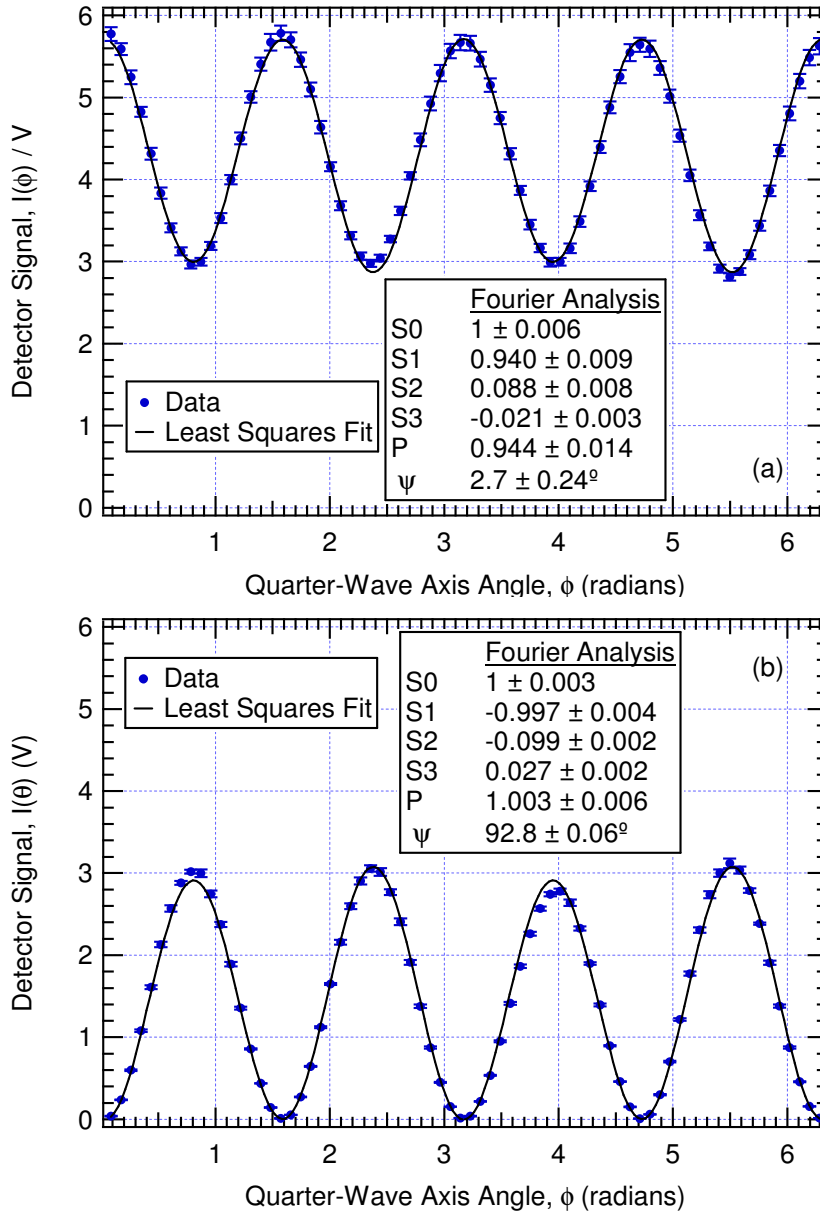


Figure 2.10. Initial results for the retrieval of a linear polarization state for (a) $\psi=0^\circ$ and (b) $\psi=90^\circ$. The Stokes vectors $\{S_0, S_1, S_2, S_3\}$ are normalized to S_0 . P is the degree of polarization and ψ is the azimuth angle. The line is a least-squares fit to Equation 2.14.

After the initial polarimeter tests described above were performed, the next step towards including the polarimeter in the aerosol apparatus was to determine the phase function of the Stokes vector for a well-characterized sample and to use such data to calculate phase function elements of the scattering matrix, \mathbf{M} . The phase function of the Stokes vector of light scattered by the aqueous dispersion of polystyrene latex spheres was determined for $\theta = 20 - 150^\circ$ with a resolution of 5° and with linearly polarized incident light at $\psi = 0^\circ$ and $\psi = 90^\circ$. The results of these measurements are shown in Figure 2.11.

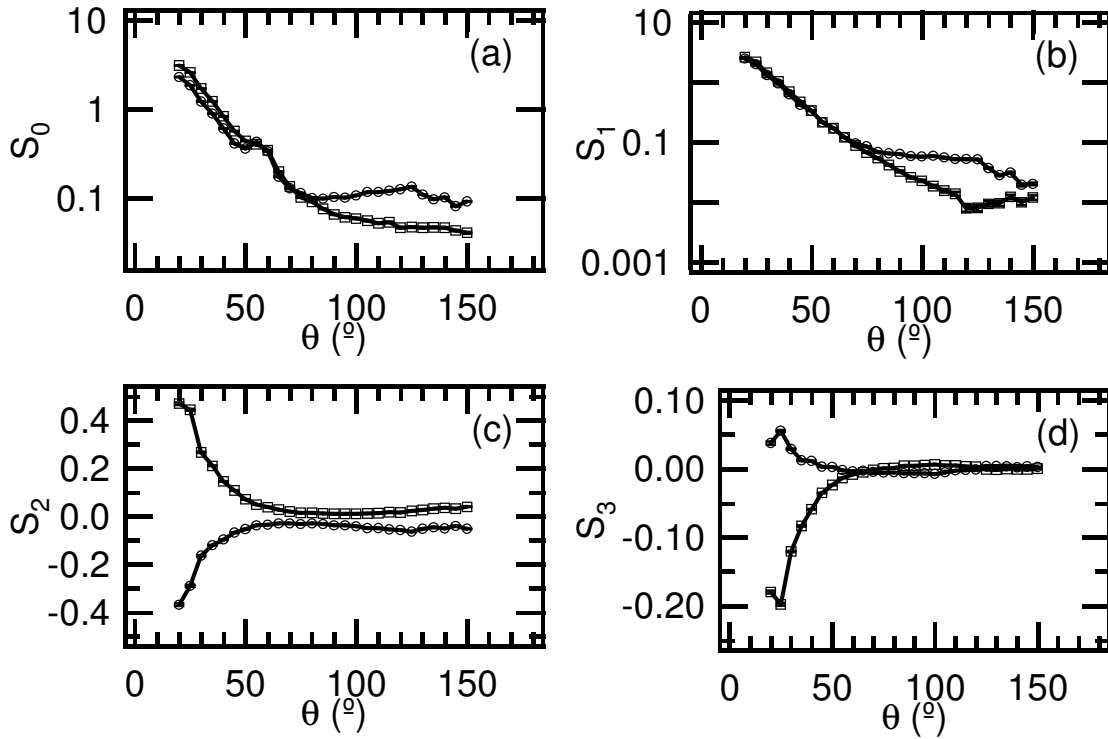


Figure 2.11. Measured phase functions for the Stokes vector elements (a) S_0 , (b) S_1 , (c) S_2 , and (d) S_3 for an aqueous dispersion of polystyrene latex spheres (diameter = $1.998 \pm 0.022 \mu\text{m}$, concentration = $7.5 \times 10^6 \text{ mL}^{-1}$, Refractive index = 1.58 @ 588 nm), with incident light polarizations of $\psi = 0^\circ$ (circles) and $\psi = 90^\circ$ (squares).

Using the Stokes vectors of the incident light — $\mathbf{S}_i(\psi = 0^\circ) = \{1, 1, 0, 0\}$ and $\mathbf{S}_i(\psi = 90^\circ) = \{1, -1, 0, 0\}$ — and the measured scattered Stokes vectors, \mathbf{S}_s , shown in Figure 2.11, equation 2.13 can then be solved for the elements in the left half of the scattering matrix, \mathbf{M} . For example, $F_{11} = (S_{0s}(\psi = 0^\circ) + S_{0s}(\psi = 90^\circ))/2$, where the factor of $\lambda^2/4\pi^2 r^2$, which is a constant for these experiments, has been included in F_{11} . The elements F_{11} and $-F_{12}/F_{11}$ of the scattering matrix, \mathbf{M} , (which are two of the most routinely discussed elements [e.g. *Volten et al.* 1998]) for the $2 \mu\text{m}$ polystyrene latex spheres are shown in Figure 2.12.

In order to determine whether the measured phase functions were in agreement with theory, Mie calculations were carried out using freely-available software, MiePlot version 4.2 [*Laven, 2003*] which solves the equations of Mie theory using the algorithm of *Bohren and Huffman* [2003]. These calculations were performed for spheres with a normal distribution of $1.998 \mu\text{m}$ with a 1% standard deviation (which is the nominal size distribution of the

polystyrene spheres used) and with a 5% standard deviation (for comparison) and with a refractive index of 1.58 in a medium with the refractive index of water (1.33). The results are shown in Figure 2.12 along with the measured values for (a) F_{11} and (b) $-F_{12}/F_{11}$. Note that the calculated values of F_{11} have been empirically scaled to provide reasonable agreement with the data, which is necessary since the calculated intensity is in arbitrary units. No scaling has been applied to $-F_{12}/F_{11}$.

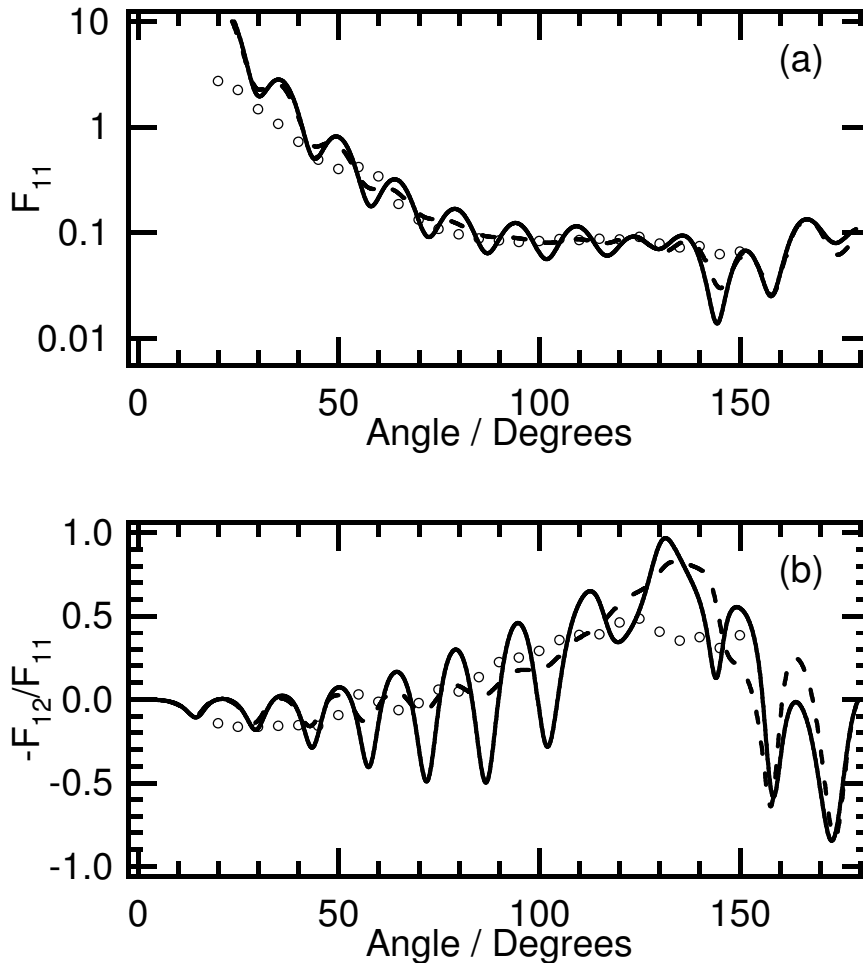


Figure 2.12. Measured scattering matrix elements (circles) for (a) F_{11} and (b) $-F_{12}/F_{11}$ for an aqueous dispersion of standard polystyrene latex spheres (diameter = $1.998 \pm 0.022 \mu\text{m}$, concentration = $7.5 \times 10^6 \text{ mL}^{-1}$, Refractive index = 1.58 @ 588 nm), along with the results of Mie theory calculations for scattering at 633 nm by particles with a refractive index of 1.58 and a normal size distribution of $1.998 \mu\text{m}$ with a standard deviation of 1% (solid line) and 5% (dashed line) in a medium with a refractive index of 1.33.

The comparison of the values derived from the measurements with Mie Theory calculations shows that, while the measurements do not resolve much of the oscillating structure in the calculated phase functions for F_{11} , the general pattern is the same: the phase function decreases between 20° and $\sim 80^\circ$ at which point it flattens out. Furthermore, in the

measurements, an increase in F_{11} between 50 and 55° is observed, which is some evidence of the oscillating structure that appears in the Mie Theory results. The results for $-F_{12}/F_{11}$ also show a general pattern which is similar between the theoretical and measured data, and there is also an apparent oscillation between 50 and 70° in the measurements. In both cases, when the Mie theory calculations are carried out for a wider size distribution, the magnitudes of the oscillations decrease. Unlike the mean diameter, the nominal size distribution is not a NIST traceable quantity, and other investigators have reported observations of wider than nominal size distributions with polystyrene particle sizing standards from the same vendor [e.g., *Maltsev et al.*, 1996], which is one possible explanation for the absence of significant oscillations in the measurements. While the theoretical and experimental results are not in perfect agreement, the results are promising and suggest that, with further testing and improvements, the polarimeter will be able to satisfactorily retrieve elements of the scattering matrix which can be combined with inverse models to determine optical properties of the scattering medium.

2.4.4. Steps to incorporate the polarimeter in experiments

In order to incorporate the polarimeter into the experimental apparatus for which it was designed, the rotation stage upon which the polarimeter is mounted will be mounted in the center of the chamber such that the laser beam is directly above the center of the rotation stage and parallel to the plane of the rotation stage, as it was for the tests presented here outside of the chamber. The first tests in the experimental chamber should simply be time-resolved determination of the degree of polarization at a fixed angle. However, towards the goal of determining the time-resolved phase functions of elements of the scattering matrix, \mathbf{M} , additional improvements will likely be required in order to obtain measurements rapidly enough that the assumption that the aerosol optical properties are constant over the measurement time is likely to be valid and perhaps in order to detect the potentially smaller number of particles.

The total time to obtain phase functions with the conditions presented above is ~ 80 minutes which is a significant fraction of the total time during which aerosols were observed in the experiments of *Ádámkovic* and *Boering* [2003] (~ 40 hrs), suggesting that the optical properties of the aerosols are likely to change on a shorter timescale than the time currently required to obtain a phase function. This time could be decreased by using a more sensitive photodetector, which would reduce the required averaging time, or by decreasing the angular resolution of the QWP (i.e., using a larger step size for φ) and/or using a single rotation cycle, or by decreasing the phase function angular resolution (i.e., using a larger step size for θ). Finally, a series of self-consistent estimates of the number density, n , of the particles generated in the experiments of *Ádámkovic* and *Boering* [2003] yielded a wide range depending on the assumptions ($n = \sim 10 - 10^8 \text{ cm}^{-3}$); thus, whether the signal-to-noise ratio achieved in these initial tests with $n = 7.5 \times 10^6 \text{ cm}^{-3}$ is representative of what is likely to be observed in experiments is uncertain and further improvements to the detector sensitivity may be required. The best strategies for the required improvements will need to be determined based on tests of the polarimeter in the experimental chamber. However, these initial results suggest that the eventual incorporation of the polarimeter into the experimental chamber is feasible.

References

- Ádámkóvics, M. (2004), Hydrocarbon photochemistry in planetary atmospheres: Laboratory and observational investigations of organic aerosols, Ph.D. dissertation, Dept. of Chem., Univ. of California, Berkeley, California.
- Ádámkóvics, M. and K. A. Boering (2003), Photochemical formation rates of organic aerosols through time-resolved in situ laboratory experiments, *J. Geophys. Res.*, *108*(E8), 5092.
- Appenzeller, C., J. R. Holton, and K. H. Rosenlof (1996), Seasonal variation of mass transport across the tropopause, *J. Geophys. Res.*, *101*(D10), 15,071–15,078.
- Baertschi, P. (1976) Absolute O-18 content of standard mean ocean water, *Earth Planet. Sci. Lett.*, *31*(3), 341-344.
- Bohren, C. F. and D. R. Huffman (1983), *Absorption and Scattering of Light by Small Particles*, Wiley, New York.
- Brand, W. A. (1995), Precon: A fully automated interface for the Pre-GC concentration of trace gases in air for isotopic analysis, *Isotopes Environments and Health Study*, *31*, 277-284.
- Cliff, S. S. and M. H. Thiemens (1994), High-precision isotopic determination of the $^{18}\text{O}/^{16}\text{O}$ and $^{17}\text{O}/^{16}\text{O}$ ratios in nitrous oxide, *Analytical Chemistry*, *66*, 2791-2793.
- Forster, P., *et al.* (2007), In *Climate Change 2007: The Physical Science Basis*; Solomon, S., Qin, D., Manning, M., Chen, Z., Marquis, M., Averyt, K. B., Tignor, M., and Miller, H. L., Eds.; Cambridge University Press: Cambridge U.K.
- Friedman, L. and Bigeleisen (1950), J. Oxygen and Nitrogen isotope effects in the decomposition of ammonium nitrate, *J. Chem. Phys.* *18* (10), 1325-1331.
- Giudicotti, L. and M. Brombin (2007), Data analysis for a rotating quarter-wave, far-infrared Stokes polarimeter, *Appl. Opt.*, *46*(14), 2638-2648.
- Griffith, D. W. T., S. D. Parkes, V. Haverd, C. Paton-Walsh, and S. R. Wilson (2009), Absolute calibration of the intramolecular site preference of ^{15}N fractionation in tropospheric N_2O by FT-IR spectroscopy, *Anal. Chem.*, *81*(6), 2227–2234.
- Goldstein, D. H. and E. Collett (2003), *Polarized Light*, Marcel Dekker, Inc., New York.
- Holton, J. R. (1990), On the global exchange of mass between the stratosphere and troposphere, *J. Atmos. Sci.*, *47*(3), 392-395.
- Junk, G. and H. J. Svec (1958), The absolute abundance of the nitrogen isotopes in the atmosphere and compressed gas from various sources, *Geochim. Cosmochim. Acta.*, *14* (3), 234-243.
- Kaiser, J. (2002), Stable isotope investigations of atmospheric nitrous oxide, PhD dissertation, Johannes Gutenberg Universität.
- Kaiser, J., T. Röckmann, and C. A. M. Brenninkmeijer (2003), Complete and accurate mass spectrometric isotope analysis of tropospheric nitrous oxide, *J. Geophys. Res.*, *108* (D15), 4476-4492.
- Kaiser, J., S. Park, K. A. Boering, C. A. M. Brenninkmeijer, A. Hilker, and T. Röckmann (2004), Mass spectrometric method for the absolute calibration of the intramolecular nitrogen isotope distribution in nitrous oxide, *Anal. Bioanal. Chem.*, *378*, 256-269.
- Laven, P. (2003), Simulations of rainbows, coronas, and glories by use of Mie theory, *Appl. Opt.*, *42*(3), 436-444.

- Li, W.-J., B. Ni, D. Jin, and T.-L. Chang (1988), Measurement of the absolute abundance of O-17 in VSMOW, *Chin. Sci. Bull.*, 33, 1610-1613.
- Lofthus, A. and P. H. Krupenie (1977), The spectrum of molecular nitrogen, *J. Chem. Phys. Ref. Data*, 6(R5.1), 113-307.
- Luz, B., E. Barkan, M. L. Bender, M. H. Thieme, and K. A. Boering (1999), Triple-isotope composition of atmospheric oxygen as a tracer of biosphere productivity, *Nature*, 400, 547-550.
- MacFarling-Meure, C., D. M. Etheridge, C. M. Trudinger, L. P. Steele, R. L. Langenfelds, T. van Ommen, A. Smith, and J. W. Elkins (2006), Law Dome CO₂, CH₄, and N₂O ice core records extended to 2000 years BP, *Geophys. Res. Lett.*, 33, L14810.
- Maltsev, V. P., A. V. Chernyshev, K. A. Sem'yanov, and E. Soini (1996), Absolute real-time measurement of particle size distribution with the flying light-scattering indicatrix method, *Appl. Opt.*, 35(18), 3275-3280.
- Park, S. (2005), Measurements of N₂O isotopologues (¹⁵N¹⁴NO, ¹⁴N¹⁵NO, and N₂¹⁸O): Insights into Global Biogeochemical Cycling and Atmospheric Chemistry and Transport, Ph.D. dissertation, Dept. of Earth and Planet. Sci., Univ. of California, Berkeley, California.
- Park, S., E. L. Atlas, and K. A. Boering (2004), Measurements of N₂O isotopologues in the stratosphere: Influence of transport on the apparent enrichment factors and the isotopologue fluxes to the troposphere, *J. Geophys. Res.*, 109, D01305.
- Parkes, S. (2008), The isotopic signature of nitrous oxide emitted from agricultural soils measured by FTIR spectroscopy, Ph.D. thesis, School of Chem., Univ. of Wollongong, Wollongong, New South Wales, Australia.
- Press, W. H., S. A. Teukolsky, W. T. Vetterling, and B. P. Flannery (2007), *Numerical Recipes: The Art of Scientific Computing*, Cambridge University Press, New York.
- Richard, D. T. and S. S. Davis (2008), Lunar dust characterization by polarimetric signature I. Negative polarization branch of sphere aggregates of various porosities, *Astron. Astrophys.*, 483(2), 643-649.
- Sowers, T., A. Rodebaugh, N. Yoshida, and S. Toyoda (2002), Extending the records of the isotopic composition of atmospheric N₂O back to 1800 A.D. from firn air trapped in snow at the South Pole and the Greenland Ice Sheet Project II ice core, *Global Biogeochem. Cycles*, 16 (4), 1129-1138.
- Sutka, R. L., N. E. Ostrom, P. H. Ostrom, H. Gandhi, and J. A. Breznak (2003), Nitrogen isotopomer site-preference of N₂O produced by *Nitrosomonas europaea* and *Methylococcus capsulatus* bath, *Rapid. Commun. Mass. Spectrom.*, 17, 738-745.
- Toyoda, S., and N. Yoshida (1999), Determination of nitrogen isotopomers of nitrous oxide on a modified isotope ratio mass spectrometer, *Anal. Chem.*, 71, 4711-4718.
- van de Hulst, H. C. (1957), *Light Scattering by Small Particles*, John Wiley, New York.
- Volten, H., J. F. de Haan, J. W. Hovenier, R. Schreurs, W. Vassen, A. G. Dekker, H. J. Hoogenboom, F. Charlton, and R. Wouts (1998), Laboratory measurements of angular distributions of light scattered by phytoplankton and silt, *Limnol. Oceanogr.*, 43(6), 1180-1197.
- Westley, M. B., B. N. Popp, and T. M. Rust (2007), The calibration of the intramolecular nitrogen isotope distribution in nitrous oxide measured by isotope ratio mass spectrometry, *Rapid Commun. Mass Spectrom.*, 21, 391-405.

- Woods, T. N., F. G. Eparvier, S. M. Bailey, P. C. Chamberlin, J. Lean, G. J. Rottman, S. C. Solomon, W. K. Tobiska, and D. L. Woodraska (2005), Solar EUV Experiment (SEE): Mission overview and first results, *J. Geophys. Res.*, *110*, A01312, doi:10.1029/2004JA010765.
- Yoshida, N. and S. Toyoda (2000), Constraining the atmospheric N₂O budget from intramolecular site preference in N₂O isotopomers, *Nature*, *405*, 330-334.

Trends, seasonal cycles, and interannual variability in the isotopic composition of atmospheric nitrous oxide between 1940 and 2005

Atmospheric N₂O is a potent greenhouse gas produced by microbial activity in soils and the oceans as well as by industry and destroyed mainly by photolysis and photooxidation in the stratosphere, where its break-down products participate in catalytic cycles of ozone destruction that determine the balance of ozone. Current atmospheric concentrations are larger than the preindustrial values by nearly 20% [MacFarling-Meure *et al.*, 2006] and are growing at a rate of ~ 0.25% per year [Hall *et al.*, 2007], reflecting changes in its biogeochemical cycling thought to be driven primarily by agriculture due to exponential increases in fertilizer use and manure production [Davidson, 2009]. Anthropogenic emissions of N₂O are targeted for regulation under the Kyoto Protocol climate treaty [e.g., Schulze *et al.*, 2009], and have recently been suggested for control under the Montreal Protocol as the single most important ozone-depleting emission now that CFC emissions have declined [Ravishankara *et al.*, 2009]. However, large uncertainties in the magnitudes of the natural and anthropogenic sources of N₂O, how these have changed in the past, and how they may change in the future due directly to land use changes and agricultural activities and indirectly to potential feedbacks induced by climate change, make establishing effective strategies for regulation and verification difficult [Bouwman *et al.*, 1995; Hirsch *et al.*, 2006; Crutzen *et al.*, 2008; Galloway *et al.*, 2008; Huang *et al.*, 2008; Schulze *et al.*, 2009]. Here, we present new measurements of the isotopic composition of atmospheric N₂O spanning the years 1940 to 2005 in firn air from Antarctica and archived air samples collected at Cape Grim, Tasmania, that reveal not only a decreasing trend in the heavy isotopologues of N₂O as N₂O concentrations have increased, as has been previously observed [Sowers *et al.*, 2002; Röckmann *et al.*, 2003; Röckmann and Levin, 2005; Bernard *et al.*, 2006; Ishijima *et al.*, 2007], but also seasonal and interannual variations. Together, these variations yield strong new constraints on the magnitudes of the various natural and anthropogenic N₂O sources and how they have changed on annual, interannual, and decadal time scales, thus providing additional insight into what environmental variables control the biogeochemical cycling of atmospheric N₂O. They also demonstrate that, even at current measurement precision, inverse modeling of the atmospheric N₂O isotopic measurements may provide a newly feasible means of inferring quantitatively not only the source magnitudes but also their geographic distributions, which will ultimately be needed to formulate sound regulation and verification policies.

Due to its long atmospheric lifetime of ~120 years [Volk *et al.*, 1996] and predominantly stratospheric sink, N₂O is relatively well-mixed in the troposphere, showing only small variations in mixing ratios apart from the long-term trend. Recently, however, time series analyses of high-precision N₂O mixing ratio measurements at several surface sites [Liao *et al.*, 2004; Nevison *et al.*, 2004a; Nevison *et al.*, 2007; Nevison *et al.*, 2005] have revealed detectable seasonal cycles and interannual variations likely due to variations in surface fluxes, tropospheric transport, and/or in stratosphere-troposphere exchange (STE), which delivers N₂O-poor stratospheric air to the troposphere. Recent attempts to use inverse modeling to quantify the relative contributions of these different processes in order to extract detailed information about the surface fluxes including their geographic distributions [Hirsch

et al., 2006; *Huang et al.*, 2008] have shown that the resulting flux estimates, particularly on a sub-hemispheric scale, are highly uncertain, mainly due to significant sensitivity to the assumed STE rates that strongly influence interhemispheric gradients.

For a number of years, measurements of the isotopic composition of N₂O have yielded additional constraints on the magnitudes of the sources and sinks of N₂O [*Yoshida and Matsuo*, 1983; *Kim and Craig*, 1993; *Pérez et al.*, 2000; *Yoshida and Toyoda*, 2000; *Pérez et al.*, 2001]. Isotopic mass balance calculations have provided further information than mixing ratios alone since the various sources as well as N₂O-depleted air from the stratosphere have distinct isotopic compositions: the microbial sources generally emit N₂O with isotopic compositions that are depleted in ¹⁵N and ¹⁸O relative to N₂O in the free troposphere [*Yoshida*, 1985; *Pérez et al.*, 2001; *Park et al.*, 2004; *Park et al.*, 2010], while N₂O returning from the stratosphere is enriched in ¹⁵N and ¹⁸O due to isotope effects in the sink reactions [*Yung and Miller*, 1997; *Kaiser et al.*, 2002; *Kaiser et al.*, 2003b; *Park et al.*, 2004; *Toyoda et al.*, 2004; *von Hessberg et al.*, 2004]. However, such isotopic analyses have been almost entirely limited to mean annual estimates on a global scale [*Kim and Craig*, 1993; *Yoshida and Toyoda*, 2000; *McLinden et al.*, 2003; *Park et al.*, 2004] and to investigations of the long-term isotopic trends from measurements on air trapped in firn or ice [*Röckmann et al.*, 2003; *Sowers et al.*, 2003; *Bernard et al.*, 2006; *Ishijima et al.*, 2007] for which any seasonal and interannual variations in N₂O isotopic composition have been smoothed out due to thermal diffusion and gravitational separation in the firn. The long-term trends in the isotopic composition of atmospheric N₂O from these firn and ice studies have shown that the increase in N₂O has been accompanied by decreases in δ¹⁵N and δ¹⁸O, which is expected since most of the sources of N₂O, whether natural or anthropogenic, are typically isotopically light relative to the tropospheric background. Röckmann and Levin [2005] measured similar trends in N₂O isotopic compositions of several hundredths of ‰ yr⁻¹ from 23 samples of archived air collected in Antarctica from 1990 to 2002, but no seasonal or interannual variations were apparent given the temporal resolution of the sampling and the length of the record.

We have measured δ¹⁵N, site-specific δ¹⁵N^α and δ¹⁵N^β (i.e., the isotopic composition at the central "α" nitrogen atom position and terminal "β" position in NNO, respectively), δ¹⁸O, and the mixing ratio of N₂O on 11 samples from firn air pumped from Law Dome, Antarctica (67°S, 113°E) in 1993, with mean ages ranging from 15 to 68 years, and on 50 archived air samples collected from 1978 to 2005 at Cape Grim, Tasmania (40.7°S, 144.8°E); see Methods. The isotope measurements show long-term decreases as N₂O has increased (Figure 3.1). Unweighted linear least squares fits to the firn and archived air measurements yield the linear trends in Table 3.1, which are similar to previous studies [*Röckmann et al.*, 2003; *Röckmann and Levin*, 2005; *Bernard et al.*, 2006; *Ishijima et al.*, 2007] (Note that the δ¹⁵N^α and δ¹⁵N^β trends from Röckmann and Levin [2005] are not consistent with this and the other studies, most likely due to a measurement artifact [*Bernard et al.*, 2006]). A box model analysis optimized to match the N₂O mixing ratio and isotopic data in Figure 3.1 (see Methods and Figure 3.S1) demonstrates that the anthropogenic source that has caused the increase in N₂O must be substantially isotopically lighter in ¹⁵N than the natural (or preindustrial) source (see Table 3.1); while this is similar to the conclusion of Röckmann *et al.* [2003], our analysis is self-contained within a fit to the observations alone (see Methods) rather than a calculation based on the IPCC N₂O flux budget estimates that have large uncertainties [*Houghton et al.*, 2001]. This result supports the conclusion that the increase in

the atmospheric N_2O burden is a result of agricultural activities such as nitrogen-based fertilizer use: when the nitrogen substrate in the form of fertilizer is plentiful, the enzyme kinetics of the microbial N_2O production processes favor the lighter ^{14}N [Stein and Yung, 2003], making the N_2O emitted isotopically lighter than in natural or unfertilized agricultural soils [Pérez *et al.*, 2001; Park *et al.*, 2010]. No difference in $\delta^{18}\text{O}$ is observed between the natural and anthropogenic sources, as was hypothesized by Rahn and Wahlen [Rahn and Wahlen, 2000], since in both cases the oxygen originates from a combination of molecular O_2 and oxygen in water.

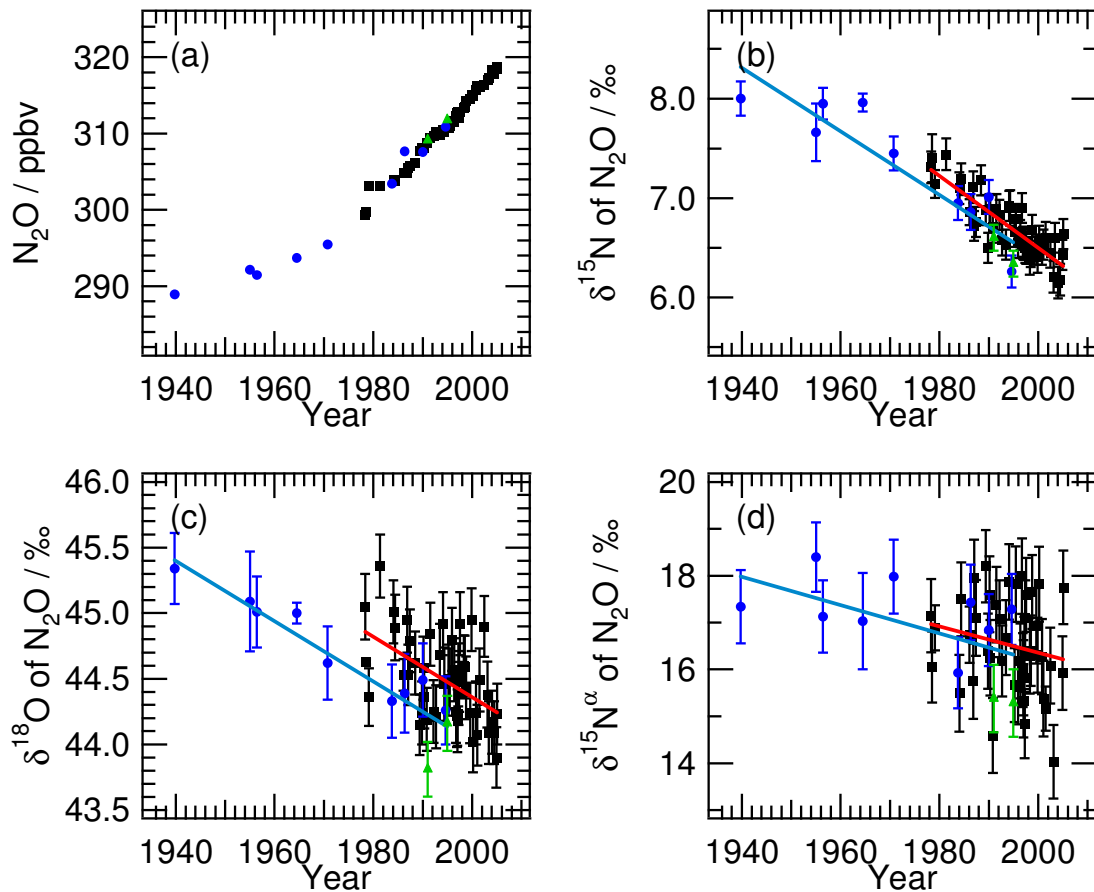


Figure 3.1 Measurements of (a) N_2O , and (b) $\delta^{15}\text{N}$ (‰ vs. air- N_2), (c) $\delta^{18}\text{O}$ (‰ vs. VSMOW), (d) $\delta^{15}\text{N}^\alpha$ (‰ vs. air- N_2) of N_2O ($\delta^{15}\text{N}^\beta$ and Site Preference are not shown) versus estimated mean age (for Antarctic firn samples; blue circles) or collection date (for archived Cape Grim air; black squares). Archived air samples are denoted by solid back circles, firn air samples from DSSW19K and DSSW20K by filled blue squares. The Poinsett fir air measurements (green triangles) have not been corrected for gravitation and diffusion effect in the firn (see Methods). Lines are unweighted linear least squares fits for the two data sets. 1σ error bars reflect the measurement uncertainty and, for the firn air samples, the fractionation corrections.

Table 3.1 Linear trends in N₂O isotopic composition from unweighted linear least-squares fits to the firn air and archived air datasets and box-model results for the average isotopic composition of the anthropogenic (δ_{ANT}) and natural (δ_{NAT}) N₂O sources and of the pre-industrial troposphere ($\delta_{\text{T,i}}$). 1 σ uncertainties are also given.

	Linear Trends		Model Results		
	Firn Air (‰/yr)	Archived Air (‰/yr)	δ_{ANT} (‰)	δ_{NAT} (‰)	$\delta_{\text{T,i}}$ (‰)
$\delta^{15}\text{N}$	-0.033(0.004)	-0.036(0.003)	-15.6(1.2)	-5.3(0.2)	9.3(0.2)
$\delta^{18}\text{O}$	-0.023(0.003)	-0.023(0.006)	32.0(1.3)	32.0(0.2)	45.5(0.2)
$\delta^{15}\text{N}^{\alpha}$	-0.031(0.014)	-0.028(0.022)	-7.6(6.2)	-3.3(1.0)	18.8(1.0)
$\delta^{15}\text{N}^{\beta}$	-0.034(0.017)	-0.038(0.022)	-20.5(7.1)	-7.5(1.1)	-0.6(1.1)
SP*	0.003(0.030)	0.010(0.043)	13.1(9.4)	4.2(1.5)	19.4(1.5)

*SP, Site Preference, is the enrichment at the α -N position relative to that at the β -N [Yoshida and Toyoda, 2000]

In addition to the observed secular decrease in isotopic ratios, a time series analysis of the Cape Grim archived air measurements shown in Figure 3.1 (see Methods and Figure 3.S2) reveals for the first time detectable seasonal and interannual variations. The detrended, one-harmonic fits to the 50 measurements show statistically significant mean seasonalities in the mixing ratio, $\delta^{15}\text{N}$, $\delta^{18}\text{O}$, and $\delta^{15}\text{N}^{\alpha}$ of N₂O, as shown in Figures 3.2(a)-(d). For the N₂O mixing ratio, the seasonal cycle derived from these 50 discrete samples is similar in amplitude and phasing to that derived from the continuous AGAGE N₂O data at Cape Grim [Jiang *et al.*, 2007; Nevison *et al.*, 2004a; Nevison *et al.*, 2005], with an annual peak-to-peak amplitude of 0.5 ppbv and an N₂O minimum in May in the one-harmonic fit. The timing of the minimum, as well as the correlation of N₂O variations with those of CFC-11 and CFC-12 (which are also long-lived tracers that are destroyed in the stratosphere), has been used to suggest [Liao *et al.*, 2004; Nevison *et al.*, 2004a; Nevison *et al.*, 2005] that this minimum in N₂O mixing ratio at Cape Grim is related to the maximum in the seasonality of stratosphere-troposphere exchange [Appenzeller *et al.*, 1996] bringing N₂O-depleted air into the troposphere. The one-harmonic seasonal cycles of $\delta^{15}\text{N}$, $\delta^{18}\text{O}$, and $\delta^{15}\text{N}^{\alpha}$ of N₂O are qualitatively consistent with this interpretation: N₂O is enriched in ¹⁵N and ¹⁸O within a month or two of when N₂O is at a minimum in April–May and is relatively depleted in ¹⁵N and ¹⁸O when the mixing ratio is near its maximum; the slight phase-delay beyond 180° of the isotopic ratios could result from isotopic disequilibrium effects, as shown to occur for $\delta^{13}\text{C}$ of CH₄ by Tans *et al.* [1993]. Importantly, however, the normalized amplitude of the seasonal cycle for $\delta^{15}\text{N}^{\alpha}$ is substantially larger relative to $\delta^{15}\text{N}$ and $\delta^{18}\text{O}$ than expected based on a purely stratospheric sink-driven seasonality and stratospheric observations; for example, the ratio of normalized seasonal changes in $\delta^{15}\text{N}^{\alpha}$ versus $\delta^{15}\text{N}$ in the one-harmonic fit is 7.9±0.6 while that from stratospheric measurements [Park *et al.*, 2004] is 1.6±0.1 (see Methods and Figure 3.S3). Furthermore, $\delta^{15}\text{N}$ and $\delta^{18}\text{O}$ are also slightly out of phase with each other, implying that there may in fact be more than one sink and/or source component involved in the seasonal variations.

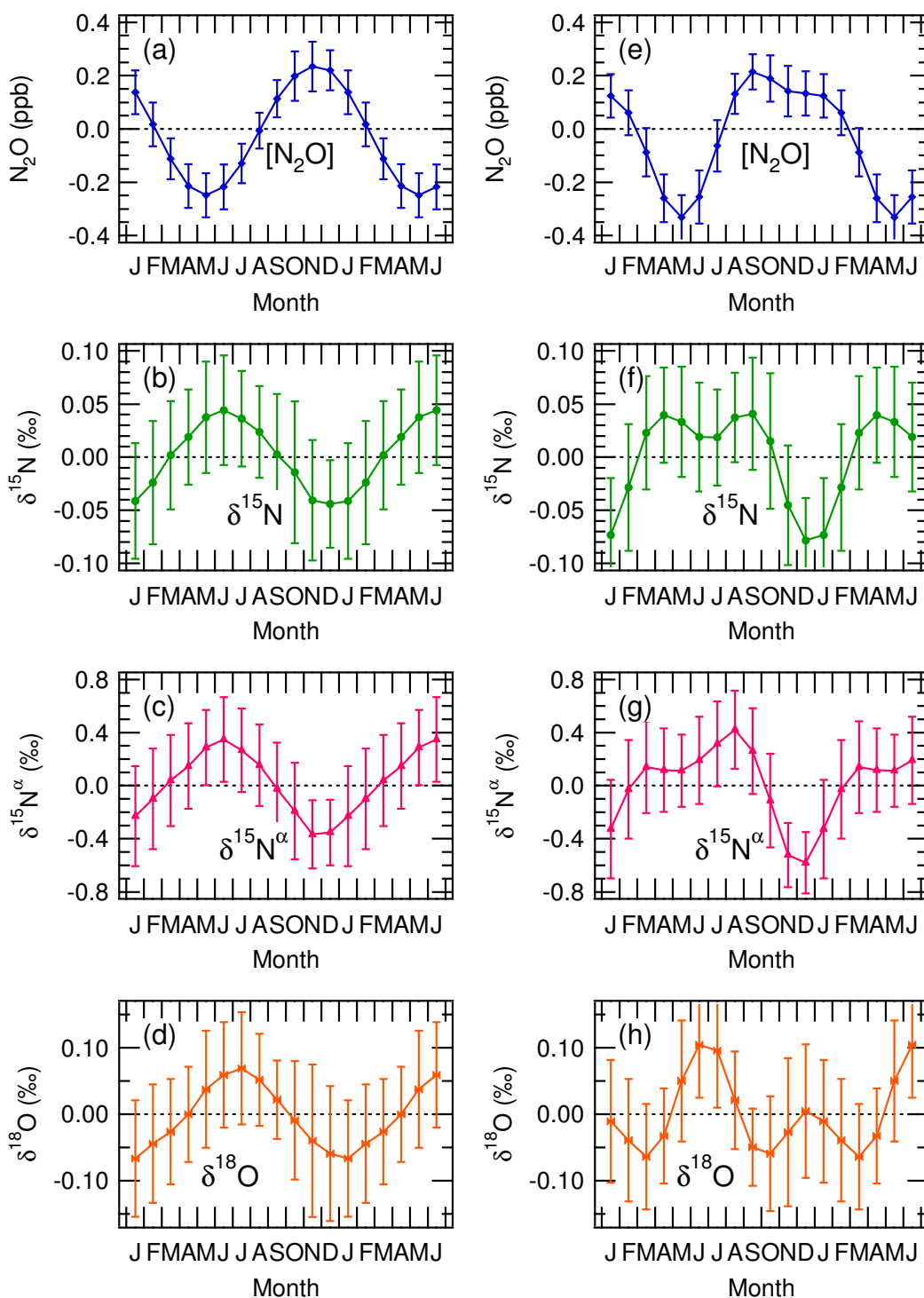


Figure 3.2 Mean seasonal cycles from the time series analysis of the Cape Grim archived air measurements using a one-harmonic fit for (a) N_2O (in ppbv), and (b) $\delta^{15}\text{N}$ (‰ vs. air- N_2), (c) $\delta^{15}\text{N}^\alpha$ (‰ vs. air- N_2), and (d) $\delta^{18}\text{O}$ (‰ vs. VSMOW) of N_2O ; and using a two-harmonic fit for (e) N_2O (in ppbv), and (f) $\delta^{15}\text{N}$ (‰ vs. air- N_2), (g) $\delta^{15}\text{N}^\alpha$ (‰ vs. air- N_2), and (h) $\delta^{18}\text{O}$ (‰ vs. VSMOW) of N_2O . Error bars indicate one standard deviation in the fits.

Motivated by these discrepancies, a two-harmonic fit algorithm was applied to the measurements, and the results are shown in Figures 3.2(e)-(h). A minimum in N₂O occurs in April and May as in the one-harmonic fit, with a maximum in September and a broad secondary maximum following in November–December. For both $\delta^{15}\text{N}$ and $\delta^{15}\text{N}^\alpha$, the June maxima in the one-harmonic fit become parsed into two peaks, one in March–April and the other in September, corresponding to the N₂O mixing ratio minimum and maximum, respectively. The $\delta^{15}\text{N}$ and $\delta^{15}\text{N}^\alpha$ minima occur in November–December, and are correlated with the secondary maximum of the mixing ratio. As for the one-harmonic fit, the April–May minimum of N₂O can be ascribed to the return flux of N₂O-depleted air from the stratosphere, and the ratio of seasonal amplitudes between $\delta^{15}\text{N}^\alpha$ versus $\delta^{15}\text{N}^{\text{bulk}}$ for March–May for the two-harmonic fit of 2.7 ± 0.7 is now consistent with a stratospheric signal of 1.6 ± 0.1 . The N₂O maximum in September, which corresponds to the largest $\delta^{15}\text{N}^\alpha$ maximum, is most likely explained by a significant regional source such as biomass burning: A recent study of biomass burning in Indonesia using a continuous monthly satellite record from 1960 to 2006 showed that the main fire season typically peaks in September–October [Field *et al.*, 2009], and the seasonal amplitude ratio of $\delta^{15}\text{N}^\alpha$ to $\delta^{15}\text{N}$ around September of 7.9 ± 0.6 is so large that, to our knowledge, only biomass burning, based on recent measurements of a combustion plume over the Tropical Pacific yielding a ratio $\delta^{15}\text{N}^\alpha/\delta^{15}\text{N}$ of 16.8 ± 8.5 [Croteau *et al.*, 2010], can account for it (see Figure 3.S3). We note that CO at Cape Grim is also at a maximum in September and October, further supporting a biomass burning source [Langenfelds *et al.*, 2002]. Finally, the second-harmonic fit preserves at least a secondary N₂O mixing ratio maximum in November–December, which Nevison *et al.* [2005] attributed to ventilation of microbially-produced N₂O from the deep Southern Ocean. The minima in $\delta^{15}\text{N}$ and $\delta^{15}\text{N}^\alpha$ are consistent with such an ocean source. Based on measured depth profiles of the concentration, $\delta^{15}\text{N}$ and $\delta^{18}\text{O}$ of N₂O in the subtropical North Pacific, Popp *et al.* [2002] estimated $\delta^{15}\text{N}$, $\delta^{15}\text{N}^\alpha$ and $\delta^{18}\text{O}$ of microbially-produced N₂O, with values of $\delta^{15}\text{N}^\alpha$ and $\delta^{15}\text{N}$ of oceanic N₂O lower than atmospheric N₂O by $\sim 12\%$ and 4% , respectively, yielding a ratio of ~ 3 , which is similar to the observed ratio of the amplitudes of their seasonal cycles around November and December of 6.1 ± 3.3 . The $\delta^{15}\text{N}^\alpha/\delta^{15}\text{N}$ ratio also falls in the range of 1.9 ± 0.1 to 4.2 ± 0.8 derived from recent measurements in the eastern tropical North Pacific [Yamagishi *et al.*, 2007], which is the closest sampling location to Cape Grim among published data. Thus, the two-harmonic fits to both the N₂O mixing ratio and nitrogen isotopic data are not only qualitatively consistent but appear to be largely quantitatively consistent (at least based on available data on the isotopic composition of ocean and biomass burning sources): the seasonality in isotopic compositions is driven by both long-range transport from the stratosphere and regional and/or hemispheric sources of N₂O from biomass burning and the ocean. Indeed, the unexpectedly large biomass burning signal inferred here may be hemispheric in scale, given recent N₂O vertical profiles over Amazonia from which N₂O fluxes from biomass burning were derived that are an order of magnitude larger than the global IPCC estimates [D’Amelio *et al.*, 2009].

The same analysis is less straightforward for $\delta^{18}\text{O}$ but arguably still qualitatively consistent with the two-harmonic seasonality results. The maximum in $\delta^{18}\text{O}$ of N₂O is phase-delayed by only one month with respect to the minimum in N₂O mixing ratio, and the ratios of the isotopic amplitudes for all the isotopic maxima in April–May are consistent with those

expected from the stratosphere. The oxygen atoms in N₂O produced by biomass burning likely originate mainly from air O₂, which is light in ¹⁸O relative to tropospheric N₂O, whereas N₂O produced in the deep ocean is often enriched in ¹⁸O [e.g., Yamagishi *et al.*, 2007]. Variations in the relative contributions of these sources of oxygen atoms and possibly in their isotopic compositions may lead to a more complex seasonal behavior for oxygen isotope ratios in N₂O than for the nitrogen isotope ratios.

In addition to the discovery of significant mean seasonal cycles in the isotopic compositions of N₂O for the Cape Grim archived air dataset, interannual variability is also apparent in the time series analysis. During the large El Niño Southern Oscillation (ENSO) of 1997-1998, several large and distinctive positive and negative residuals are evident not only in the N₂O mixing ratio data, as has been observed in previous analyses of N₂O time series [Nevison *et al.*, 2007; Nevison *et al.*, 2005], but also in $\delta^{15}\text{N}^\alpha$ and, to a lesser extent, in $\delta^{15}\text{N}$ and $\delta^{18}\text{O}$ of N₂O (see Figure 3.S4). N₂O may be perturbed by ENSO through drought-induced enhancement of biomass burning [Simmonds *et al.*, 2005], reduction in upwelling of deep water which ventilates N₂O-enriched waters to the atmosphere [Nevison *et al.*, 2007], and/or an El Niño-induced decrease in the rate of interhemispheric transport [Nevison *et al.*, 2007]. The relative magnitudes of the isotopic residuals appear to favor biomass burning, but the largest residuals occur before July 1997 and thus predate the largest fires, and the uncertainties in the magnitudes of the residuals themselves are likely too large to interpret their relative magnitudes accurately. In principle, however, these results show that additional N₂O isotope measurements for air from the 1997-1998 period and a comparison with one or more non-ENSO years could serve to pinpoint the underlying cause(s) of the interannual variations in N₂O discovered in this dataset.

In addition to demonstrating that seasonal and interannual variations in N₂O isotopic compositions are detectable, using the seasonality to infer an unexpectedly large contribution of biomass burning to the Cape Grim N₂O variations, and confirming that the anthropogenic source responsible for the increase in N₂O must be isotopically lighter in ¹⁵N than the natural preindustrial sources, these results serve as "proof-of-concept" that variations in N₂O isotopic compositions can be used to study regional, seasonal, and interannual variations in N₂O fluxes and transport and that simply having more isotope measurements — even at the current measurement precision — will allow detailed information on the identity, magnitude, and geographic distribution of N₂O sources to the atmosphere to be derived from inverse modeling of atmospheric N₂O and its isotopic composition. In particular, we have shown that the ¹⁵N, ¹⁵N^α, and ¹⁸O isotopic compositions of N₂O can be used to separate the influence of stratospheric (and long-range tropospheric) transport on N₂O mixing ratios from source signals due to biomass burning and ocean ventilation; thus, by including N₂O isotopic compositions in inverse models, the largest single uncertainty hindering their success — that is, their current inability to distinguish the contribution of N₂O-depleted air from the stratosphere to the N₂O concentration in air at a given location — can be addressed.

3.1 Methods

3.1.1 Firm air details: Sampling & Storage

Firm air samples were collected at three sites on Law Dome, East Antarctica (DSSW20K and DSSW19K, which are 20km and 19km west of the deep DSS drill site,

respectively, and the coastal site Poinsett) using a firm air sampling device (FASD) to pump air from depths ranging from 15.6 to 50.1 m into 35-L stainless steel cylinders by the technique described by Sturrock *et al.* 2002]. For the isotopic analyses, a fraction of the air in each of the 35-L cylinders was transferred to either 500-ml glass flasks or 3-liter stainless steel flasks to pressures of between ~18 and 44 psig.

3.1.2 Firm air details: Corrections and mean age

A correction for the different rates of gravitational and diffusional separation for the different isotopologues [Trudinger *et al.*, 1997] has been applied to the firm data, except for the two points from the Poinsett drilling site, where the physical characteristics of the firm are not well enough quantified to allow for accurate determination of the correction factors. The diffusion coefficients used were $D(\text{CO}_2)/D(\text{N}_2\text{O}) = 1.004$, $D(^{15}\text{N}_2\text{O})/D(\text{N}_2\text{O}) = 0.9958$, $D(^{18}\text{N}_2\text{O})/D(\text{N}_2\text{O}) = 0.9918$ [Perry and Chilton, 1973; Trudinger *et al.*, 1997]. For DSSW20K and DSSW19K, the diffusion corrections are relatively small (up to ~0.08 per mil for $\delta^{15}\text{N}$, $\delta^{15}\text{N}^\alpha$, and $\delta^{15}\text{N}^\beta$ and 0.16 per mil for $\delta^{18}\text{N}_2\text{O}$), with an uncertainty of about 20% of the correction. The accuracy of the correction factors is supported by a comparison of $\delta^{13}\text{CO}_2$ in the firm air with archived air [Francey *et al.*, 1998; Francey *et al.*, 1999]. The gravity correction is based on the firm $\delta^{15}\text{N}_2$ measurements for DSSW20K. There are no $\delta^{15}\text{N}_2$ measurements for DSSW19K, so the average of the DSSW20K measurements for a similar depth range was used for DSSW19K, resulting in an uncertainty of ~5-10% of the correction. Effective, or mean, ages of the firm air were also estimated, with typical age spectra widths of ~10-15 years; the firm data are plotted against these mean ages for all but the Poinsett site.

3.1.3 Archived air details: Sampling & Storage

Fifty whole air samples collected at Cape Grim, Tasmania (40.7°S, 144.8°E) and archived at the CSIRO Global Atmospheric Sampling Laboratory (GASLAB) in either 34- or 35-L, stainless steel (SS) cylinders or 48-L, spectra-seal treated aluminum (Al) cylinders between 1978 and 2003 were sampled by transferring a fraction of the air into 500-ml glass flasks or into 3-liter stainless steel flasks to pressures ranging from 15 to 23 psig. N_2O mixing ratios in these samples were measured using a Shimadzu Model GC-8A with an electron capture detector. Both the SS and Al cylinders have been tested for N_2O mixing ratio stability to within a few tenths of a ppb over several years. However, two early samples from 35-L SS cylinders, collected on 19790206 and 19810520 showed evidence of drift in N_2O mixing ratio by 2.5 and 1.0 ppb, respectively, as evident in Figure 3.1(a). These samples did not, however, show any evidence of isotopic fractionation.

3.1.4 IRMS Measurements

Measurements of the isotopic composition of N_2O from the firm and archived air samples appear in Tables 3.S1 and 3.S2, respectively. The N_2O isotope measurements were performed using a Finnigan MAT 252 isotope ratio mass spectrometer operated in continuous flow mode with online preconcentration and gas chromatography [Park *et al.*, 2004]. Isotope measurements are reported as δ -values, which are the per mil (‰) deviations of the isotopic ratios from international standards (air- N_2 for N and Vienna Standard Mean Ocean Water (VSMOW) for O). That is, $\delta = (R_{\text{sample}}/R_{\text{standard}} - 1) \cdot 1000\text{‰}$, where, for example, $R = ^{18}\text{O}/^{16}\text{O}$. Two separate 100 mL aliquots of air (equivalent to ~2 nmol of N_2O) were measured, one for

the $\delta^{15}\text{N}^{\text{bulk}}$ and $\delta^{18}\text{O}$ measurements and one for the site-specific $\delta^{15}\text{N}^{\alpha}$ measurement [Park *et al.*, 2004]. Short-term precision is based on the standard deviations of multiple runs of a given sample: $\delta^{15}\text{N}^{\text{bulk}} = \pm 0.2 \text{ ‰}$, $\delta^{18}\text{O} = \pm 0.2 \text{ ‰}$, and $\delta^{15}\text{N}^{\alpha} = \pm 0.8 \text{ ‰}$. Long-term measurement precisions are $\pm 0.3 \text{ ‰}$ for $\delta^{15}\text{N}^{\text{bulk}}$ and $\delta^{18}\text{O}$ and $\pm 0.8 \text{ ‰}$ for $\delta^{15}\text{N}^{\alpha}$ based on measurements of N_2O isotopes in air samples taken at the ground level on the UC Berkeley campus over. The accuracy of the measurements are estimated to be 1 ‰ for $\delta^{15}\text{N}^{\text{bulk}}$ and $\delta^{18}\text{O}$ and 4 ‰ for $\delta^{15}\text{N}^{\alpha}$ and $\delta^{15}\text{N}^{\beta}$ based on a comparison of the average isotopic composition of tropospheric N_2O reported by different groups, including ours [Griffith *et al.*, 2009; Kaiser *et al.*, 2003a; Yoshida and Toyoda, 2000].

3.1.5 Box model details

In a two-box model of the troposphere and stratosphere, similar to ones used by Rahn and Wahlen [2000], Kaiser [2002] and Sowers *et al.* [2002], the anthropogenic flux of N_2O was constrained by the mixing ratio of N_2O in our measurements combined with firn and ice-core data from MacFarling Meure *et al.* [2006] to expand the time range of the model. The natural flux was assumed to remain constant over time and was determined by calculating a steady state, assuming a 120 year lifetime for N_2O [Volk *et al.*, 1996] and an anthropogenic source of zero at the year 1700 CE. The anthropogenic flux term was modeled as an exponential function of time and was determined by performing a χ^2 minimization for the parameters of the exponential, fixing all of the other model parameters. The predicted natural and anthropogenic source fluxes corresponding to the present time were 11.1 TgN yr^{-1} and 6.6 TgN yr^{-1} , respectively, showing excellent agreement with the IPCC estimates of 11.0 TgN yr^{-1} and 6.7 TgN yr^{-1} , respectively [Forster *et al.*, 2007]. Isotopic ratios were then incorporated into the model run in order to simulate the isotopic trends of atmospheric N_2O . The model was run over a wide range of average natural and anthropogenic isotopic ratios to determine the best fit and the uncertainty, based on a two-parameter χ^2 minimization [Press *et al.*, 2007] (i.e. assuming that all other model parameters are well constrained), for the average isotopic ratios of the N_2O sources.

3.1.6 Time Series Analysis details

The time-series analysis of the archived air measurements for N_2O mixing ratio, $\delta^{15}\text{N}$, $\delta^{15}\text{N}^{\alpha}$, and $\delta^{18}\text{O}$ is based on the method described by Thoning *et al.* [1989]. The data are fit to a function $f(t)$, which is the sum of a quadratic function and one or two harmonics. The residuals from the fit are smoothed by a low pass filter with cutoff times of 80 days and 650 days. A smooth curve is generated by adding the 80-day smoothed residuals to $f(t)$. A trend curve is generated by adding the 650-day smoothed residuals to the quadratic component of $f(t)$, thus showing the long term trend with the mean seasonal cycle removed. The mean seasonal cycle is given by the harmonic component of $f(t)$. The growth rate is the first derivative of the trend curve. The residuals from the smoothed curve (shown in the top right panel of Figures 3.S2(a)-(h)) are an indicator of interannual variability.

3.1.7 Ratios of normalized seasonal amplitudes

Small changes in δ -values, $\Delta\delta$, relative to their tropospheric averages, δ_{trop} , are related to the mixing ratio by (1)

$$\Delta\delta \approx \varepsilon(1 + \delta_{trop})\Delta[N_2O]/[N_2O]_0, \quad (1)$$

where ε is the enrichment factor for the process causing the change [Allan *et al.*, 2001]. Taking the ratio of (1) for $\delta^{15}N^\alpha/\delta^{15}N^{bulk}$ yields (2).

$$\frac{\Delta\delta^{15}N^\alpha/(1 + \Delta\delta^{15}N_{trop}^\alpha/1000)}{\Delta\delta^{15}N/(1 + \Delta\delta^{15}N_{trop}/1000)} \approx \frac{\varepsilon(^{15}N^\alpha)}{\varepsilon(^{15}N)} \quad (2)$$

Thus, the slope of a plot of $\Delta\delta^{15}N^\alpha/(1 + \delta^{15}N_{trop}^\alpha/1000)$ vs. $\Delta\delta^{15}N^{bulk}/(1 + \delta^{15}N_{trop}/1000)$, as shown in Figure 3.S3, will equal $\varepsilon(^{15}N^\alpha)/\varepsilon(^{15}N)$. For the analyses given in this chapter, the slopes and their uncertainties were calculated using the Williamson-York regression method which accounts for errors in both the x- and y-data [Cantrell, 2008].

References

- Allan, W., M. R. Manning, K. R. Lassey, D. C. Lowe, and A. J. Gomez (2001), Modeling the variation of $\delta^{13}\text{C}$ in atmospheric methane: Phase ellipses and the kinetic isotope effect, *J. Geophys. Res.*, *106*, 467-481.
- Appenzeller, C., J. R. Holton, and K. H. Rosenlof (1996), Seasonal variation of mass transport across the tropopause, *J. Geophys. Res.*, *101*(D10), 15071.
- Bernard, S., T. Röckmann, J. Kaiser, J.-M. Barnola, H. Fischer, T. Blunier, and J. Chappellaz (2006), Constraints on N₂O budget changes since pre-industrial time from new firn air and ice core isotope measurements, *Atmos. Chem. Phys.*, *6*, 493-503.
- Bouwman, A. F., K. W. V. d. Hoek, and J. G. J. Oliver (1995), Uncertainties in the global source distribution of nitrous oxide *J. Geophys. Res.*, *100*, 2785.
- Cantrell, C. A. (2008), Technical Note: Review of methods for linear least-squares fitting of data and application to atmospheric chemistry problems, *Atmos. Chem. Phys.*, *8*, 5477-5487.
- Croteau, P., E. L. Atlas, S. M. Schauffler, D. R. Blake, G. S. Diskin, and K. A. Boering (2010), The effect of local and regional sources on the isotopic composition of nitrous oxide in the tropical free troposphere and tropopause layer, *J. Geophys. Res.*, in press.
- Crutzen, P. J., A. R. Mosier, K. A. Smith, and W. Winiwarter (2008), N₂O release from agro-biofuel production negates global warming reduction by replacing fossil fuels, *Atmos. Chem. Phys.*, *8*, 389-395.
- D'Amelio, M. T. S., L. V. Gatti, J. B. Miller, and P. Tans (2009), Regional N₂O fluxes in Amazonia derived from aircraft vertical profiles, *Atmos. Chem. Phys.*, *9*, 8785-8797.
- Davidson, E. A. (2009), The contribution of manure and fertilizer nitrogen to atmospheric nitrous oxide since 1860, *Nature Geosci.*, *2*, 659-662, doi:610.1038/ngeo1608.
- Field, R. D., G. R. v. d. Werf, and S. S. P. Shen (2009), Human amplification of drought-induced biomass burning in Indonesia since 1960, *Nature Geosci.*, *2*, 185 - 188.
- Forster, P., et al. (2007), in *Climate Change 2007: The Physical Science Basis*, edited by S. Solomon, D. Qin, M. Manning, Z. Chen, M. Marquis, K. B. Averyt, M. Tignor and H. L. Miller, Cambridge University Press, Cambridge, U.K.
- Francey, R. J., M. R. Manning, C. E. Allison, S. A. Coram, D. M. Etheridge, R. L. Langenfelds, D. C. Lowe, and L. P. Steele (1999), A history of $\delta^{13}\text{C}$ in atmospheric CH₄ from the Cape Grim Air Archive and Antarctic firn air, *J. Geophys. Res.*, *104*(D19), 23, 631-623, 643.
- Francey, R. J., et al. (1998), Atmospheric carbon dioxide and its stable isotope ratios, methane, carbon monoxide, nitrous oxide and hydrogen from Shetland Isles, *Atmospheric Environment*, *32*(19), 3331-3338.
- Galloway, J. N., A. R. Townsend, J. W. Erisman, M. Bekunda, Z. Cai, J. R. Freney, L. A. Martinelli, S. P. Seitzinger, and M. A. Sutton (2008), Transformation of the nitrogen cycle: Recent trends, questions, and potential solutions, *Science*, *320*, 889-892, doi:810.1126/science.1136674.
- Griffith, D. W. T., S. D. Parkes, V. Haverd, C. Paton-Walsh, and S. R. Wilson (2009), Absolute calibration of the intramolecular site preference of ¹⁵N fractionation in tropospheric N₂O by FT-IR spectroscopy, *Anal. Chem.*, *81*(6), 2227-2234.

- Hall, B. D., G. S. Dutton, and J. W. Elkins (2007), The NOAA nitrous oxide standard scale for atmospheric observations, *J. Geophys. Res.*, *112*, D09305, doi:10.1029/2006JD007954.
- Hirsch, A. I., A. M. Michalak, L. M. Bruhwiler, W. Peters, E. J. Dlugokencky, and P. P. Tans (2006), Inverse modeling estimates of the global nitrous oxide surface flux from 1998–2001, *Global Biogeochem. Cycles*, *20*, GB1008.
- Houghton, J. T., Y. Ding, D. J. Griggs, M. Nogueur, van der Linden, P. J., X. Dai, L. Maskell, and C. A. Johnson (2001), *Climate Change 2007: The Scientific Basis*, Cambridge University Press, Cambridge, UK.
- Huang, J., et al. (2008), Estimation of regional emissions of nitrous oxide from 1997 to 2005 using multinetwork measurements, a chemical transport model, and an inverse method, *J. Geophys. Res.*, *113*(D17313), doi:10.1029/2007JD009381.
- Ishijima, K., S. Sugwara, K. Kawamura, G. Hashida, S. Morimoto, S. Murayama, S. Aoki, and T. Nakazawa (2007), Temporal variations of the atmospheric nitrous oxide concentration and its $\delta^{15}\text{N}$ and $\delta^{18}\text{O}$ for the latter half of the 20th century reconstructed from firn air analyses, *J. Geophys. Res.*, *112*, D03305, doi:10.1029/2006JD007208.
- Jiang, X., W. L. Ku, R. L. Shia, Q. Li, J. W. Elkins, R. G. Prinn, and Y. L. Yung (2007), Seasonal cycle of N_2O : Analysis of data, *Global Biogeochem. Cycles*, *21*(GB1006), doi:10.1029/2006GB002691.
- Kaiser, J. (2002), Stable isotope investigations of atmospheric nitrous oxide, PhD dissertation thesis, Johannes Gutenberg Universitat.
- Kaiser, J., T. Röckmann, and C. A. M. Brenninkmeijer (2002), Intramolecular ^{15}N and ^{18}O fractionation in the reaction of N_2O with $\text{O}(^1\text{D})$ and its implications for the stratospheric N_2O isotope signature, *J. Geophys. Res.*, *107*(D14), 4214, doi:10.1029/2001JD001506.
- Kaiser, J., T. Röckmann, and C. A. M. Brenninkmeijer (2003a), Complete and accurate mass spectrometric isotope analysis of tropospheric nitrous oxide, *J. Geophys. Res.*, *108*(D15), 4476, doi:10.1029/2003JD003613.
- Kaiser, J., T. Röckmann, C. A. M. Brenninkmeijer, and P. J. Crutzen (2003b), Wavelength dependence of isotope fractionation in N_2O photolysis, *Atmos. Chem. Phys.*, *3*, 303–315.
- Kim, K.-R., and H. Craig (1993), Nitrogen-15 and oxygen-18 characteristics of nitrous oxide: a global perspective, *Science*, *262*, 1855–1857.
- Kroeze, C., E. Dumont, and S. P. Seitzinger (2005), New estimates of global emissions of N_2O from rivers and estuaries, *J. Integr. Environ. Sci.*, *2*, 159–165.
- Langenfelds, R. L., R. J. Francey, B. C. Pak, L. P. Steele, J. Lloyd, C. M. Trudinger, and C. E. Allison (2002), Interannual growth rate variations of atmospheric CO_2 and its $\delta^{13}\text{C}$, H_2 , CH_4 , and CO between 1992 and 1999 linked to biomass burning, *Global Biogeochem. Cycles*, *16*(3), 1048, doi:10.1029/2001GB001466
- Liao, T., C. D. Camp, and Y. L. Yung (2004), The seasonal cycle of N_2O , *Geophys. Res. Lett.*, *31*(L17108), doi:10.1029/2004GL020345.
- MacFarling-Meure, C., D. M. Etheridge, C. M. Trudinger, L. P. Steele, R. L. Langenfelds, T. v. Ommen, A. Smith, and J. W. Elkins (2006), Law Dome CO_2 , CH_4 , and N_2O ice core records extended to 2000 years BP, *Geophys. Res. Lett.*, *33*(14), doi:10.1029/2006GL026152.

- McLinden, C. A., M. J. Prather, and M. S. Johnson (2003), Global modeling of N₂O isotopomers: Stratospheric enrichment, isotope-budgets and the 17O-18O mass-independent anomaly, *J. Geophys. Res.*, *108*(D8), 4233, doi:10.1029/2002JD002560.
- Nevison, C. D., D. E. Kinnison, and R. F. Weiss (2004a), Stratospheric influences on the tropospheric seasonal cycles of nitrous oxide and chlorofluorocarbons, *Geophys. Res. Lett.*, *31*(L20103), doi:10.1029/2004GL020398.
- Nevison, C. D., T. J. Lueker, and R. F. Weiss (2004b), Quantifying the nitrous oxide source from coastal upwelling, *Global Biogeochem. Cycles*, *18*, GB1018, doi:10.1029/2003GB002110.
- Nevison, C. D., N. M. Mahowald, R. F. Weiss, and R. G. Prinn (2007), Interannual and seasonal variability in atmospheric N₂O, *Global Biogeochem. Cycles*, *21*(GB3017), doi:10.1029/2006GB002755.
- Nevison, C. D., R. F. Keeling, R. F. Weiss, B. N. Popp, X. Jin, P. J. Fraser, L. W. Porter, and P. G. Hess (2005), Southern ocean ventilation inferred from seasonal cycles of atmospheric N₂O and O₂/N₂ at Cape Grim, Tasmania, *Tellus*, *57*(3), 218-229.
- Park, S., E. L. Atlas, and K. A. Boering (2004), Measurements of N₂O isotopologues in the stratosphere: Influence of transport on the apparent enrichment factors and the isotopologue fluxes to the troposphere, *J. Geophys. Res.*, *109*, D01305, doi:10.1029/2003JD003731.
- Park, S., T. Pérez, K. A. Boering, S. E. Trumbore, J. Gil, S. Marquina, and S. C. Tyler (2010), Can N₂O stable isotopes and isotopomers be useful tools to characterize sources and microbial pathways of N₂O production and consumption in tropical soils?, *Global Biogeochem. Cycles*, submitted.
- Pérez, T., S. E. Trumbore, S. C. Tyler, P. A. Matson, I. Ortiz-Monasterio, T. Rahn, and D. W. T. Griffith (2000), Isotopic variability of N₂O emissions from tropical forest soils, *Global Biogeochem. Cycles*, *14*(2), 525-535.
- Pérez, T., S. E. Trumbore, S. C. Tyler, P. A. Matson, I. Ortiz-Monasterio, T. Rahn, and D. W. T. Griffith (2001), Identifying the agricultural imprint on the global N₂O budget using stable isotopes, *J. Geophys. Res.*, *106*(D9), 9869-9878.
- Perry, R. H., and C. H. Chilton (1973), *Chemical Engineers' Handbook*, McGraw-Hill, New York.
- Popp, B. N., et al. (2002), Nitrogen and oxygen isotopomeric constraints on the origins and sea-to-air flux of N₂O in the oligotrophic subtropical North Pacific gyre, *Global Biogeochem. Cycles*, *16*(4), 1064, doi:10.1029/2001GB001806.
- Press, W. H., S. A. Teukolsky, W. T. Vetterling, and B. P. Flannery (2007), *Numerical Recipes: The Art of Scientific Computing*, Cambridge University Press, New York.
- Rahn, T., and M. Wahlen (2000), A reassessment of the global isotopic budget of atmospheric nitrous oxide, *Global Biogeochem. Cycles*, *14*(2), 537-543.
- Ravishankara, A. R., J. S. Daniel, and R. W. Portman (2009), Nitrous oxide (N₂O): The dominant ozone-depleting substance emitted in the 21st century, *Science*, *326*, 123-125, doi:10.1126/science.1176985.
- Röckmann, T., and I. Levin (2005), High-precision determination of the changing isotopic composition of atmospheric N₂O from 1990 to 2002, *J. Geophys. Res.*, *110*(D21304), doi:10.1029/2005JD006066.

- Röckmann, T., J. Kaiser, and C. A. M. Brenninkmeijer (2003), The isotopic fingerprint of the pre-industrial and the anthropogenic N₂O source, *Atmos. Chem. Phys.*, *3*, 315-323.
- Schulze, E. D., et al. (2009), Importance of methane and nitrous oxide for Europe's terrestrial greenhouse-gas balance, *Nature Geosci.*, *2*, 842-850, doi:810.1038/ngeo1686.
- Simmonds, P. G., A. J. Manning, R. G. Derwenf, P. Ciais, M. Rammonet, V. Kazan, and D. Ryall (2005), A burning question. Can recent growth rate anomalies in the greenhouse gases be attributed to large-scale biomass burning events?, *Atmos. Environ.*, *39*(14), 2513-2517.
- Sowers, T., R. B. Alley, and J. Jubenville (2003), Ice core records of atmospheric N₂O covering the last 106,000 years, *Science*, *301*(5635), 945-948.
- Sowers, T., A. Rodebaugh, N. Yoshida, and S. Toyoda (2002), Extending the records of the isotopic composition of atmospheric N₂O back to 1800 A.D. from firn air trapped in snow at the South Pole and the Greenland Ice Sheet Project II ice core, *Global Biogeochem. Cycles*, *16*(4), 1129-1138.
- Stein, L. Y., and Y. L. Yung (2003), Production, isotopic composition, and atmospheric fate of biologically produced nitrous oxide, *Annul. Rev. Earth Planet. Sci.*, *31*, 329-356.
- Sturrock, G. A., D. M. Etheridge, C. M. Trudinger, P. J. Fraser, and A. M. Smith (2002), Atmospheric histories of halocarbons from analysis of Antarctic firn air: Major Montreal Protocol species, *J. Geophys. Res.*, *107*(D24), 4765, doi:10.1029/2002JD002548.
- Tans, P. P., J. A. Berry, and R. F. Keeling (1993), Oceanic C-13/C-12 observations - A new window on ocean CO₂ uptake, *Global Biogeochem. Cycles*, *7*(2), 353-368.
- Thoning, K. W., P. P. Tans, and W. D. Komhyr (1989), Atmospheric carbon dioxide at Mauna Loa Observatory 2. Analysis of the NOAA GMCC Data, 1974-1985., *J. Geophys. Res.*, *94*(D6), 8549-8565.
- Toyoda, S., et al. (2004), Temporal and latitudinal distributions of stratospheric N₂O isotopomers, *J. Geophys. Res.*, *109*, D08308, doi: 10.01029/02003JD004316.
- Trudinger, C., L. Enting, D. Etheridge, R. Francey, V. Levchenko, L. Steele, D. Raynaud, and L. Arnaud (1997), Modeling air movement and bubble trapping in firn *J. Geophys. Res.*, *102*(D6), doi:10.1029/1096JD03382.
- Volk, C. M., et al. (1996), Quantifying transport between the tropical and mid-latitude lower stratosphere, *Science*, *272*(5269), 1763-1768.
- von Hessberg, P., J. Kaiser, M. B. Enghoff, C. A. McLinden, S. S. Sorensen, T. Röckmann, and M. S. Johnson (2004), Ultra-violet absorption cross-sections of isotopically substituted nitrous oxide species: ¹⁴N¹⁴NO, ¹⁵N¹⁴NO, ¹⁴N¹⁵NO and ¹⁵N¹⁵NO, *Atmos. Chem. Phys.*, *4*, 1237-1253.
- Yamagishi, H., M. B. Westley, B. N. Popp, S. Toyoda, N. Yoshida, S. Watanabe, K. Koba, and Y. Yamanaka (2007), Role of nitrification and denitrification on the nitrous oxide cycle in the eastern tropical North Pacific and Gulf of California, *J. Geophys. Res.*, *112*, G02015, doi:10.1029/2006JG000227.
- Yoshida, N. (1985), ¹⁵N-depleted N₂O as a product of nitrification, *Nature*, *335*, 528-529.
- Yoshida, N., and S. Matsuo (1983), Nitrous isotope ratio of atmospheric N₂O as a key to the global cycle of N₂O, *Geochem. J.*, *17*, 231-239.
- Yoshida, N., and S. Toyoda (2000), Constraining the atmospheric N₂O budget from intramolecular site preference in N₂O isotopomers, *Nature*, *405*, 330-334.

Yung, Y. L., and C. E. Miller (1997), Isotopic fractionation of stratospheric nitrous oxide, *Science*, 278(5344), 1778-1780.

Supplementary Figures

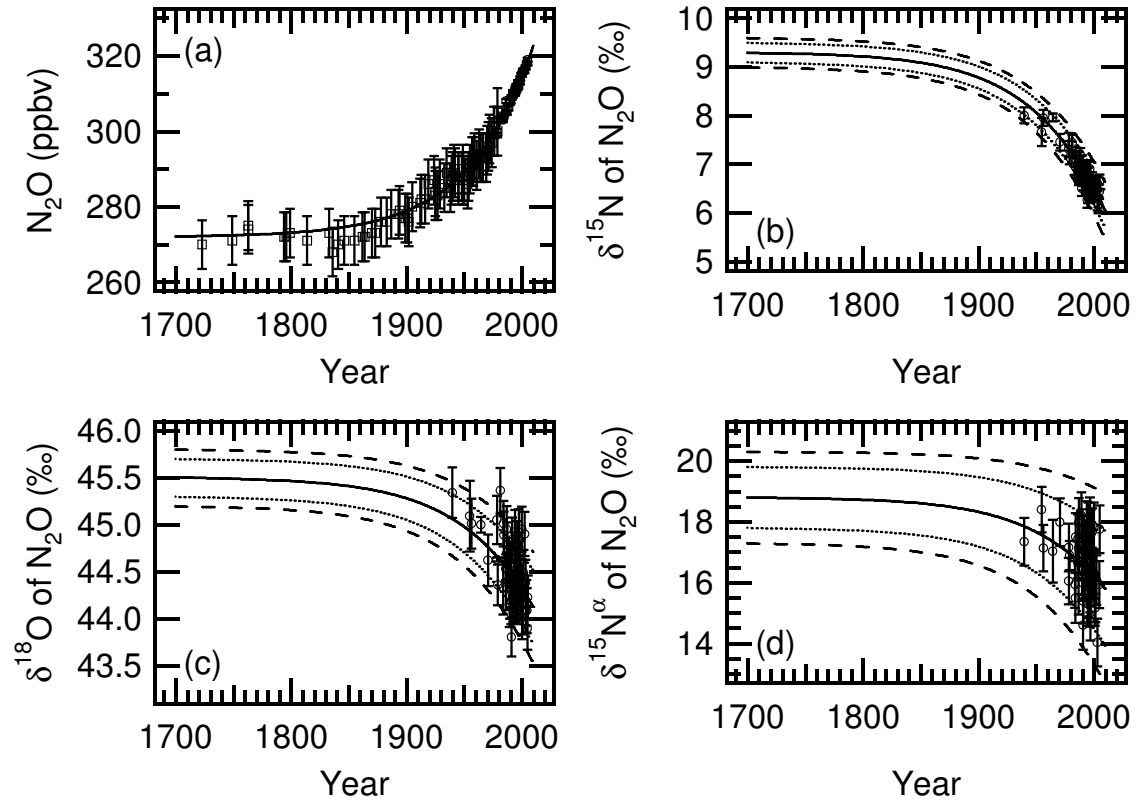


Figure 3.S1: Model estimates based on a two-box model (solid curves) and measurements. (a) N₂O mixing ratios from this study (open circles) and N₂O records from the Law Dome ice core and firn air of MacFarling Meure *et al.* [MacFarling-Meure *et al.*, 2006] (open squares); (b) same for δ¹⁵N; (c) same for δ¹⁸O; (d) same for δ¹⁵N^α. For the isotopic compositions, (b), (c), and (d) 68% (dotted lines) and 95% (dashed lines) confidence intervals from the χ^2 minimization are shown.

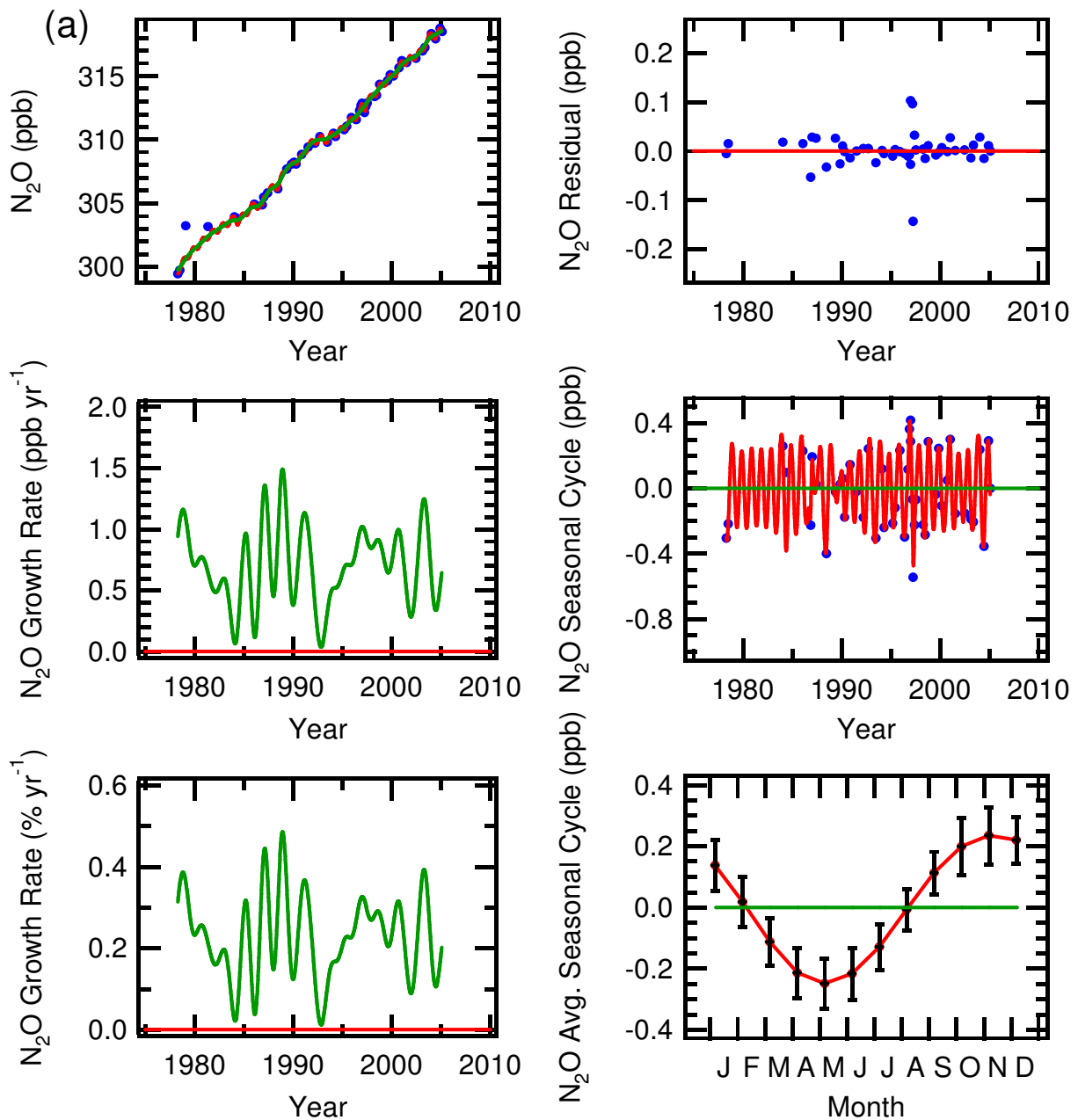


Figure 3.S2 Results of the time series analysis to extract a long-term trend and mean seasonal cycle from the Cape Grim archived air sample measurements for the 1-harmonic case (a) N_2O mixing ratio, (b) $\delta^{15}\text{N}$, (c) $\delta^{15}\text{N}^a$, and (d) $\delta^{18}\text{O}$ and the 2-harmonic case (e) N_2O mixing ratio, (f) $\delta^{15}\text{N}$, (g) $\delta^{15}\text{N}^a$, and (h) $\delta^{18}\text{O}$. Top left panel: the statistical smoothing for long-term trend; Middle left and bottom left panels: the resulting growth ratios in ppb yr⁻¹ (a) and (e) or % yr⁻¹ (b), (c), (d), (f), (g), and (h) and % yr⁻¹; Top right panel: residuals from the smooth curve; Middle right panel: resulting seasonal cycles; and bottom right panel: the mean seasonal cycle.

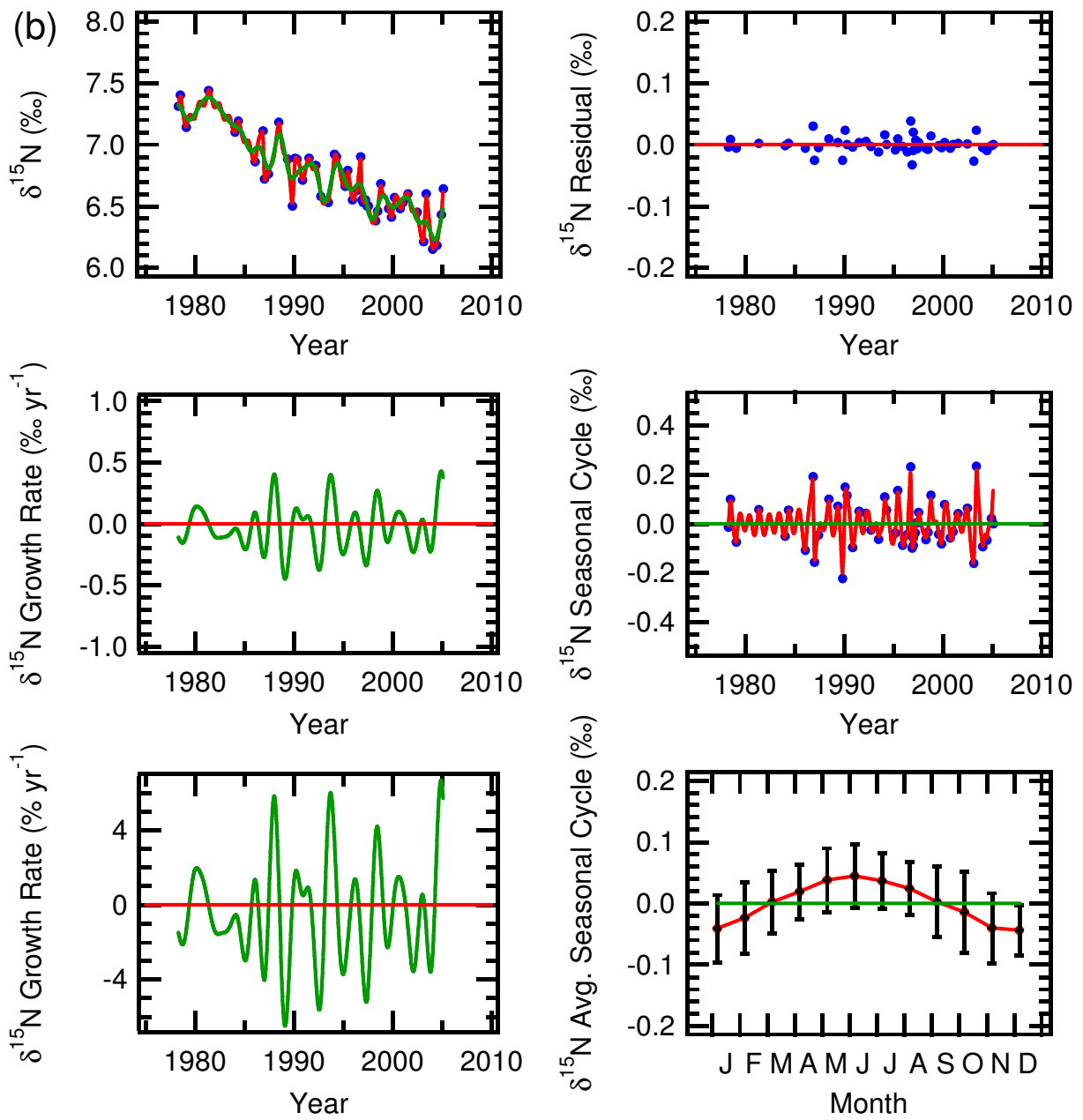


Figure 3.S2b

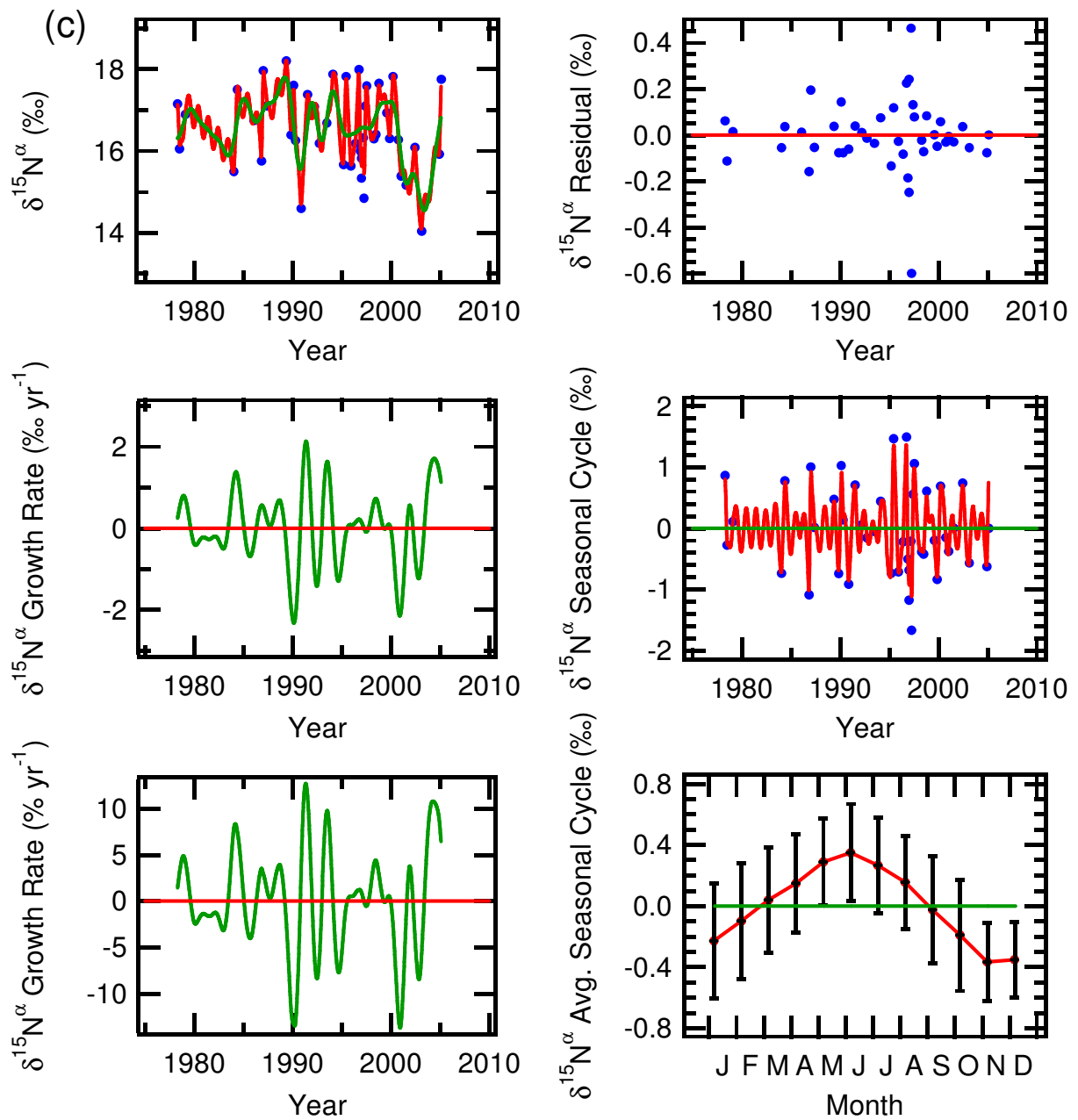


Figure 3.S2c

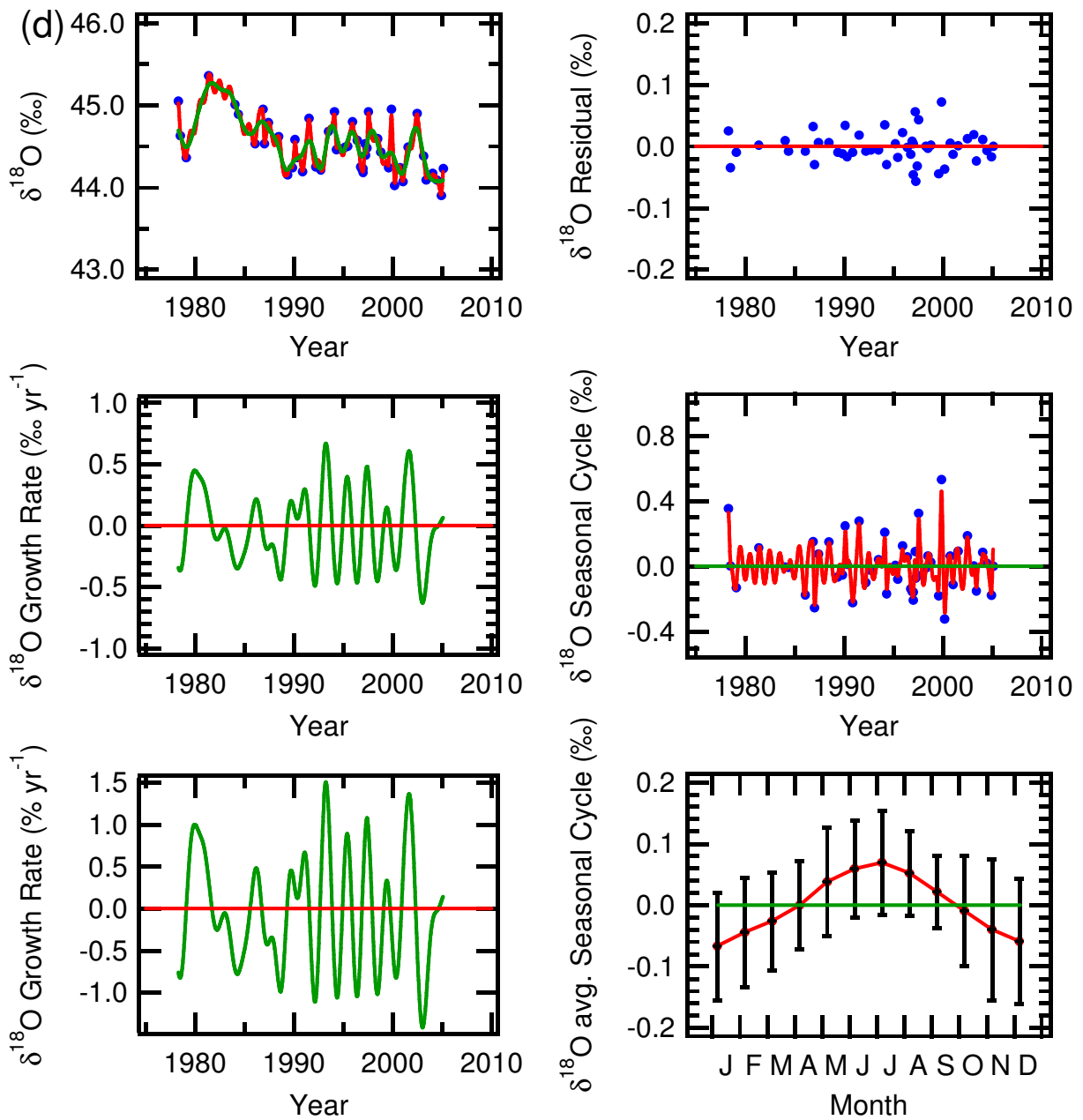


Figure 3.S2d

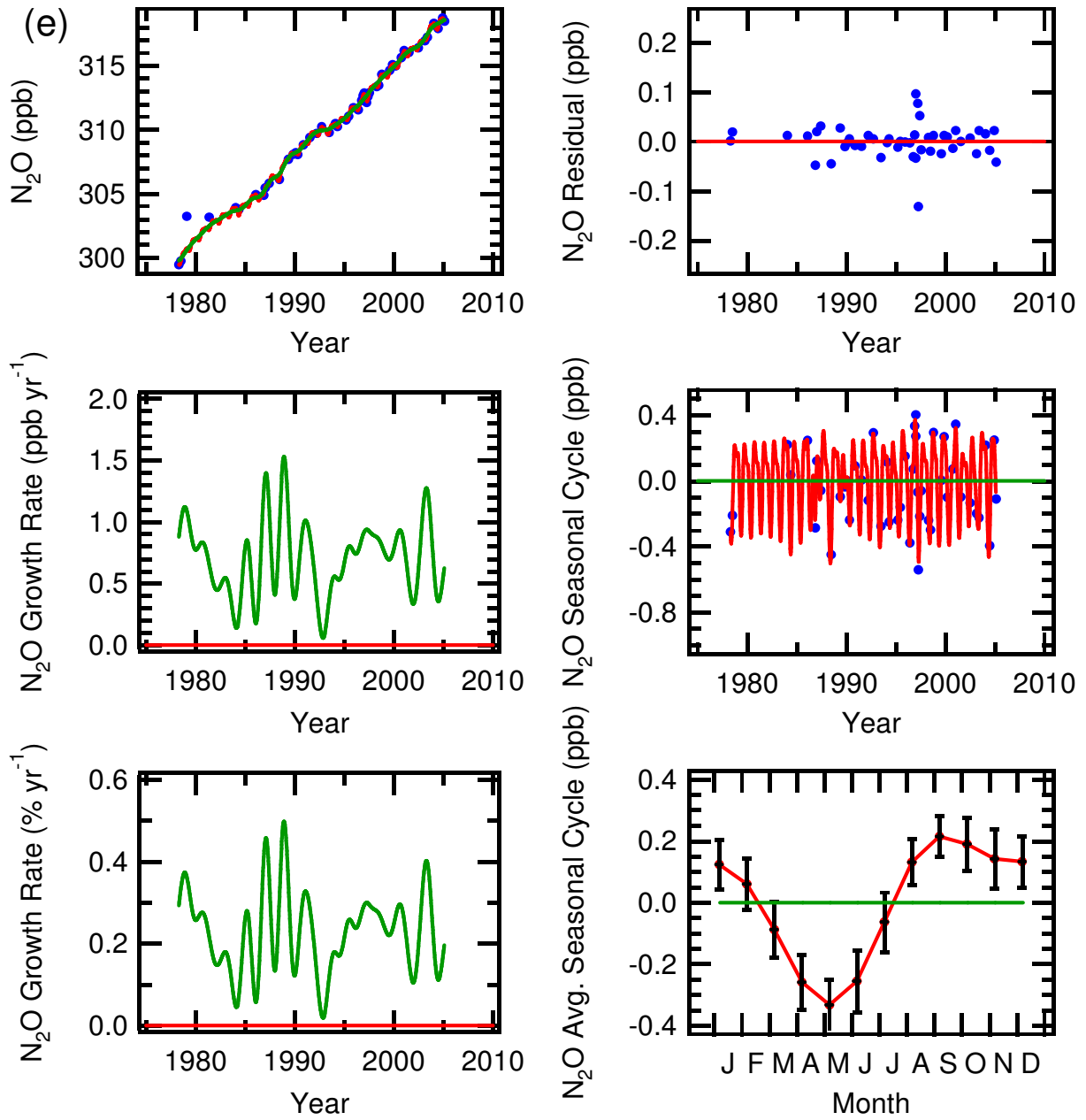


Figure 3.S2e

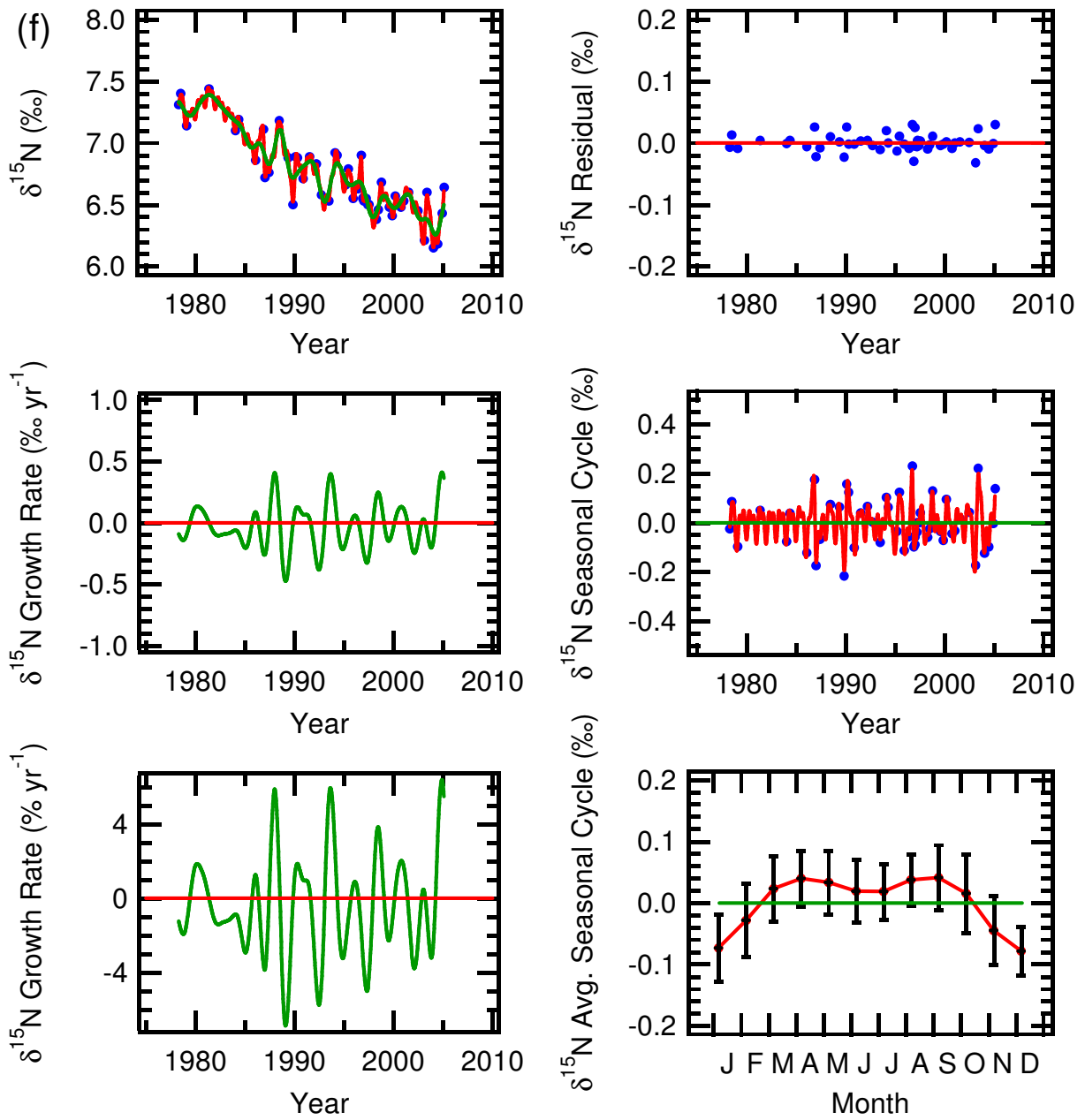


Figure 3.S2f

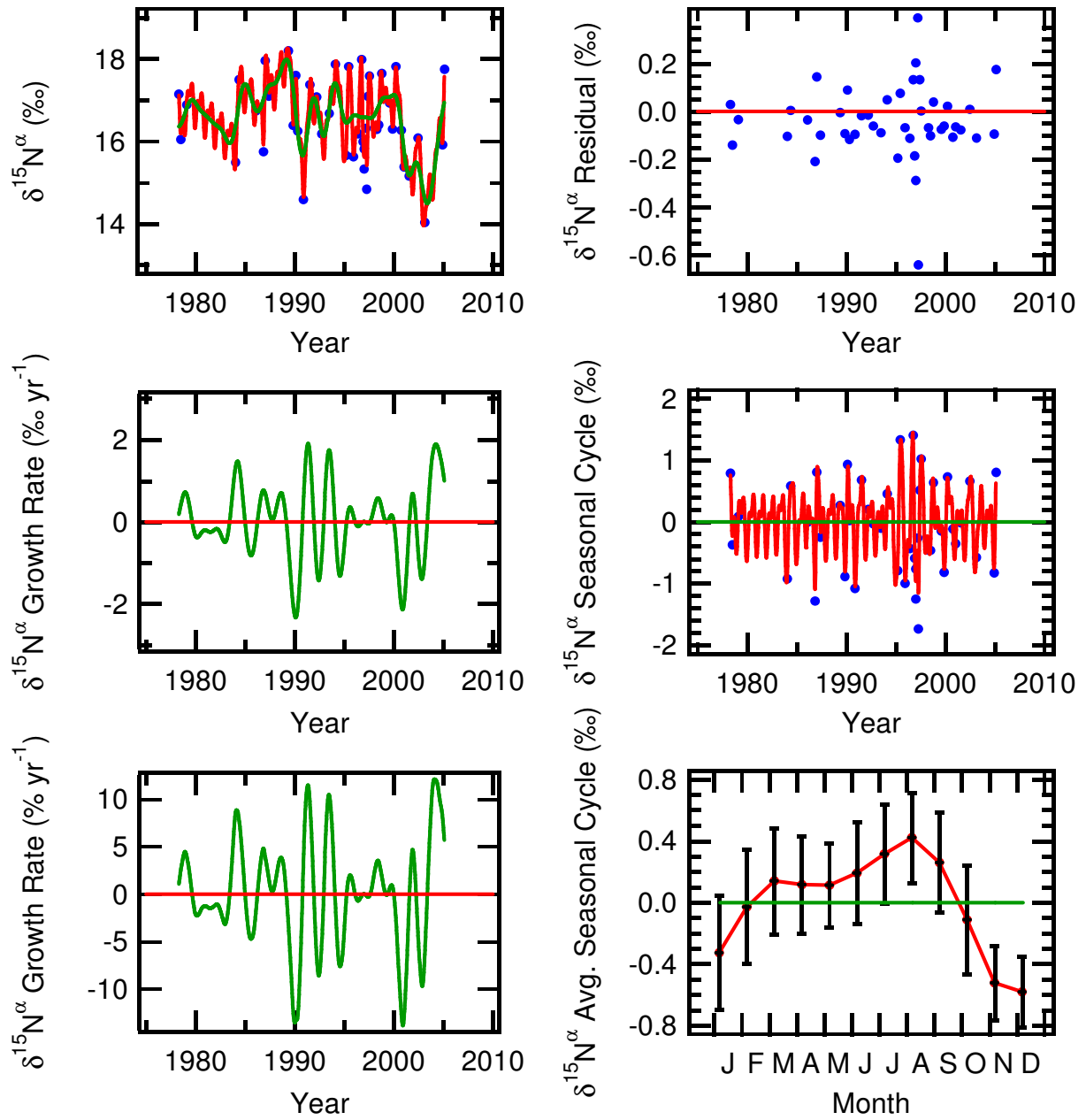


Figure 3.S2g

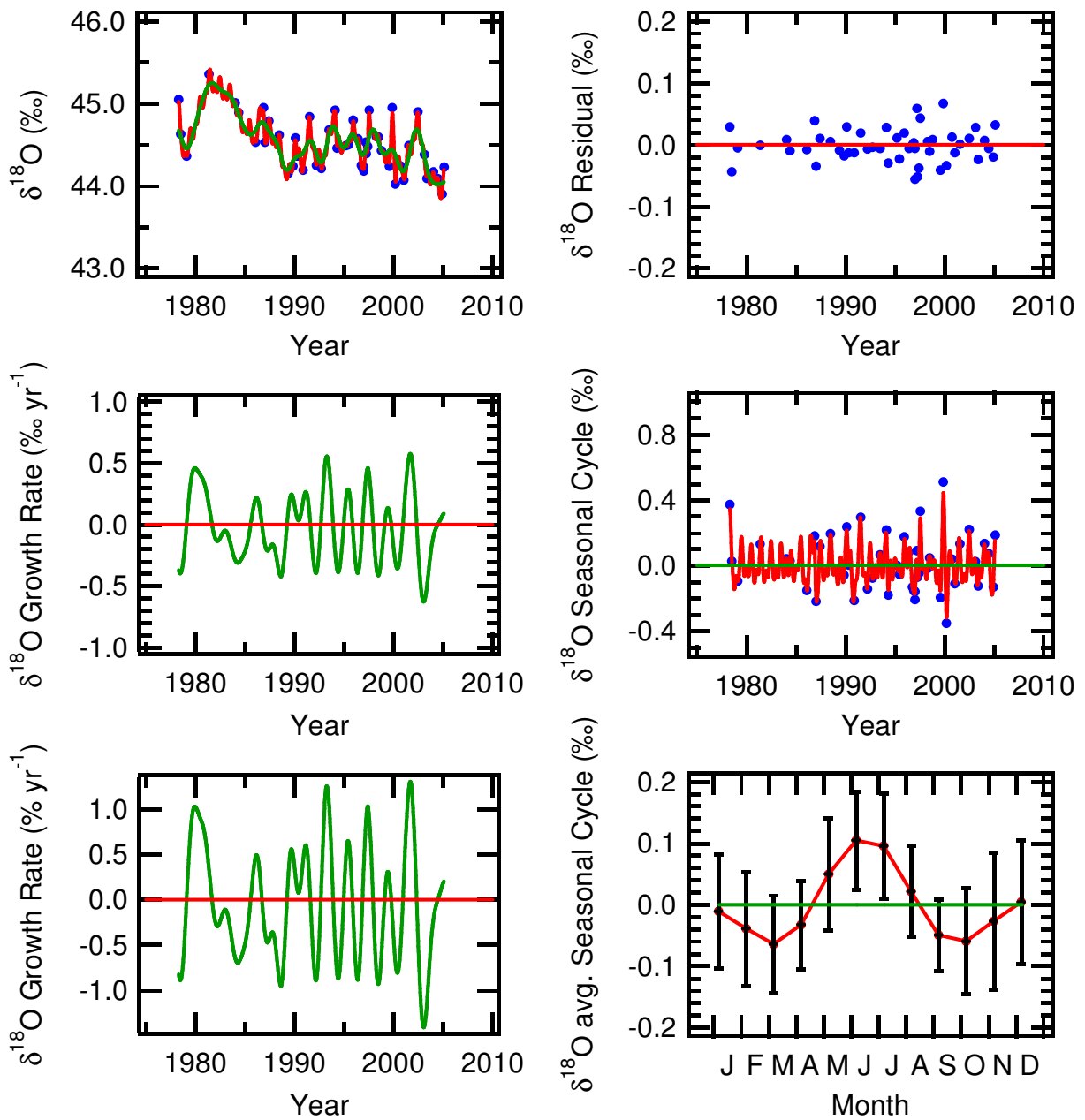


Figure 3.S2h

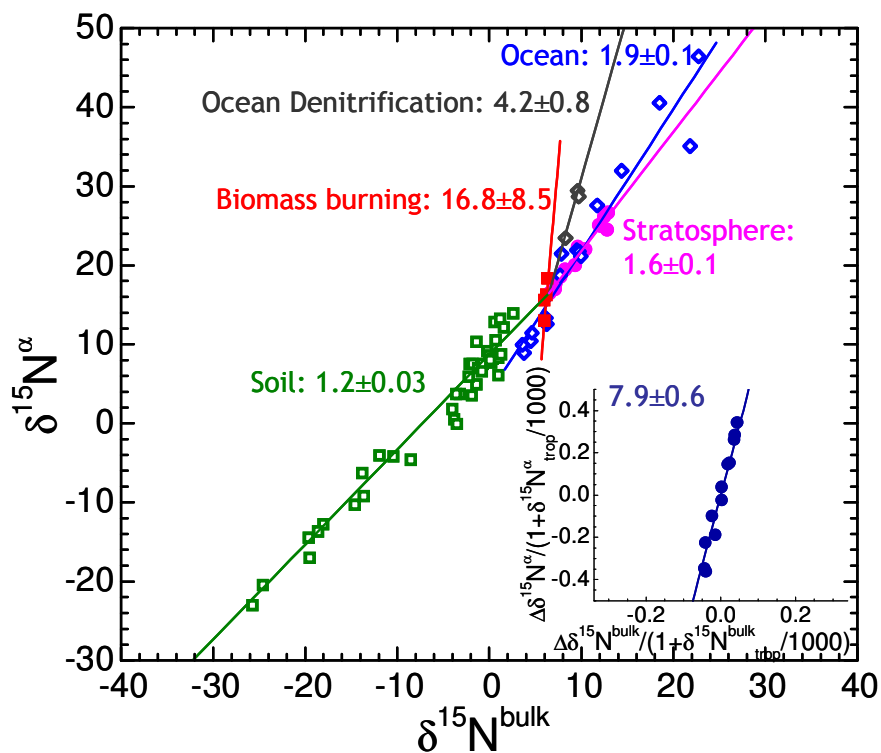


Figure 3.S3: Scatter plot of $\delta^{15}\text{N}^{\alpha}$ versus $\delta^{15}\text{N}$ of N_2O . Shown are measurements from the lower stratospheric (filled pink circles, [Park *et al.*, 2004]), from tropical soil emissions (empty green squares; [Park *et al.*, 2010]), from the eastern tropical North Pacific ocean (empty blue and black diamonds; [Yamagishi *et al.*, 2007]), and a tropical biomass burning plume (filled red squares; [Croteau *et al.*, 2010]). The solid lines corresponding to each data set are the slope derived from a Williamson-York linear regression of the data, which represents the ratio of enrichment factors $\epsilon(^{15}\text{N}^{\alpha})/\epsilon(^{15}\text{N})$. Inset: normalized seasonal amplitudes for $\delta^{15}\text{N}^{\alpha}$ and $\delta^{15}\text{N}$ of N_2O ; the slope is also equivalent to $\epsilon(^{15}\text{N}^{\alpha})/\epsilon(^{15}\text{N})$; see Methods.

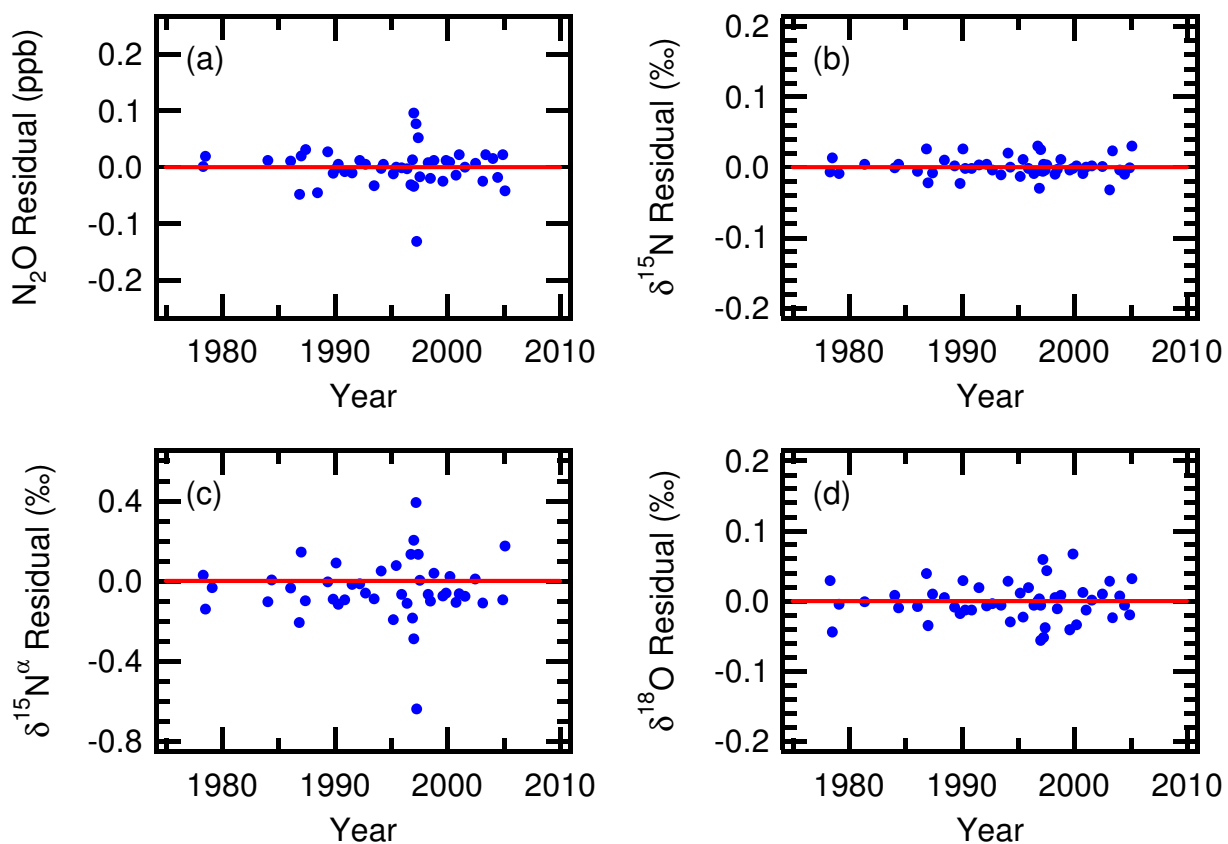


Figure 3.S4 Residuals from the 2-harmonic time series analysis of the Cape Grim archived air measurements for (a) N₂O, (b) δ¹⁵N, (c) δ¹⁵N^α, and (d) δ¹⁸O. The largest residuals from the fit occur in 1997, implying a linkage with the large 1997-1998 ENSO event.

Supplementary Tables

Table 3.S1 Mean age, N₂O mixing ratio, and N₂O isotopic compositions from firn air samples

Mean Age	[N ₂ O] (ppb)	$\delta^{15}\text{N}^{\text{bulk}}$ (‰)	$\delta^{18}\text{O}$ (‰)	$\delta^{15}\text{N}^{\alpha}$ (‰)	$\delta^{15}\text{N}^{\beta}$ (‰)	Site Preference (‰)
1939.78	288.9	8.00	45.34	17.34	-1.15	18.51
1955.04	292.2	7.66	45.09	18.40	-2.90	21.36
1956.46	291.5	7.95	45.01	17.13	-1.02	18.17
1964.48	293.7	7.96	45.00	17.03	-0.90	17.95
1970.78	295.5	7.45	44.62	17.98	-2.90	20.94
1983.79	303.4	6.95	44.33	15.93	-1.84	17.80
1986.34	307.7	6.86	44.39	17.43	-3.54	21.04
1990.01	307.6	7.01	44.49	16.84	-2.63	19.53
1991.00*	309.1*	6.60*	43.81*	15.38*	-1.98*	17.40*
1994.62	310.9	6.26	44.26	17.28	-4.59	21.98
1995.00*	311.7*	6.34*	44.16*	15.28*	-2.38*	17.70*

* Samples are from Poinsett drilling site and have not been corrected for gravitational and diffusional separation

Table 3.S2 Collection date, N₂O mixing ratio, and N₂O isotopic compositions from archive air samples

Collection Date (yyyymmdd)	[N ₂ O] (ppb)	$\delta^{15}\text{N}^{\text{bulk}}$ (‰)	$\delta^{18}\text{O}$ (‰)	$\delta^{15}\text{N}^{\alpha}$ (‰)	$\delta^{15}\text{N}^{\beta}$ (‰)	Site Preference (‰)
19780426	299.4	7.31	45.05	17.15	-2.33	19.53
19780707	299.7	7.40	44.63	16.05	-1.04	17.11
19790206	303.2	7.14	44.36	16.89	-2.42	19.35
19810520	303.2	7.44	45.36	–	–	–
19840120	303.9	7.10	45.01	15.49	-1.07	16.57
19840523	303.8	7.19	44.89	17.50	-2.94	20.49
19860206	304.9	6.86	44.53	16.74	-2.84	19.63
19861112	304.9	7.11	44.95	15.75	-1.31	17.09
19870108	305.5	6.72	44.53	17.96	-4.37	22.43
19870528	305.8	6.76	44.79	17.10	-3.40	20.57
19880621	306.1	7.18	44.62	–	–	–
19890519	307.7	6.88	44.15	18.20	-4.29	22.59
19891108	308.1	6.50	44.24	16.39	-3.21	19.66
19900216	308.2	6.89	44.58	17.60	-3.66	21.35
19900426	308.1	6.88	44.36	16.25	-2.30	18.59
19901115	308.8	6.71	44.19	14.59	-0.95	15.55
19910715	309.4	6.89	44.84	17.38	-3.43	20.88
19920318	309.7	6.83	44.25	17.08	-3.25	20.39
19920923	310.2	6.58	44.21	16.18	-2.82	19.06
19930629	309.8	6.53	44.68	16.68	-3.44	20.19
19940211	310.5	6.92	44.92	17.87	-3.86	21.81
19940427	310.2	6.90	44.46	–	–	–
19950313	310.8	6.66	44.49	15.66	-2.13	17.83
19950613	311.0	6.79	44.50	17.82	-4.09	22.00
19951204	311.7	6.55	44.80	15.63	-2.33	18.01

Table 3.S2 continued

Collection Date (yyyymmdd)	[N ₂ O] (ppb)	$\delta^{15}\text{N}^{\text{bulk}}$ (‰)	$\delta^{18}\text{O}$ (‰)	$\delta^{15}\text{N}^{\alpha}$ (‰)	$\delta^{15}\text{N}^{\beta}$ (‰)	Site Preference (‰)
19960528	311.6	6.63	44.57	16.18	-2.73	18.96
19961003	312.3	6.90	44.25	17.99	-4.04	22.11
19961120	312.7	6.55	44.22	15.99	-2.68	18.72
19970107	312.9	6.56	44.18	15.82	-2.51	18.37
19970107	312.7	6.53	44.23	15.33	-2.06	17.43
19970313	312.6	6.53	44.53	16.32	-3.07	19.46
19970404	312.1	6.55	44.39	14.84	-1.52	16.39
19970530	312.6	6.50	44.48	17.09	-3.92	21.09
19970715	312.9	6.50	44.92	17.59	-4.42	22.11
19980415	313.4	6.38	44.60	16.29	-3.34	19.70
19980625	313.5	6.46	44.59	16.40	-3.30	19.76
19981015	314.3	6.68	44.43	17.65	-4.13	21.86
19990804	314.6	6.48	44.24	16.93	-3.79	20.80
19991116	315.1	6.41	44.95	16.30	-3.30	19.67
20000314	315.0	6.57	44.02	17.82	-4.52	22.44
20000929	315.7	6.48	44.24	16.27	-3.12	19.45
20010115	316.2	6.53	44.07	15.38	-2.11	17.53
20010719	316.1	6.60	44.49	15.16	-1.75	16.94
20020620	316.4	6.45	44.90	16.08	-2.98	19.12
20030217	317.0	6.21	44.38	14.03	-1.39	15.44
20030521	317.3	6.60	44.09	–	–	–
20040120	318.3	6.15	44.17	–	–	–
20040617	317.9	6.18	44.09	–	–	–
20041201	318.8	6.43	43.90	15.92	-2.87	18.84
20050210	318.5	6.64	44.23	17.75	-4.32	22.16

The effect of local and regional sources on the isotopic composition of nitrous oxide in the tropical free troposphere and tropopause layer[§]

[§]Adapted from a manuscript of the same title which was accepted for publication by *J. Geophys Res.* on 7 April 2010 authored by Croteau, P.L., E. L. Atlas, S. M. Schauffler, D. R. Blake, G. S. Diskin, and K. A. Boering.

Abstract

Measurements and models of the spatiotemporal variability of surface N₂O mixing ratios and isotopic compositions are increasingly used to constrain the global N₂O budget. However, large variability observed on the small spatial scales of soil chambers and shipboard sampling, which appears to be very sensitive to local environmental conditions, has made extrapolation to the global scale difficult. In this study, we present measurements of the isotopic composition of N₂O ($\delta^{15}\text{N}^{\text{bulk}}$, $\delta^{15}\text{N}^{\alpha}$, $\delta^{15}\text{N}^{\beta}$, and $\delta^{18}\text{O}$) from whole-air samples collected at altitudes of 0.5 to 19km by the NASA DC-8 and WB-57 aircraft during the Costa Rica Aura Validation Experiment (CRAVE) and the Tropical Composition Cloud and Climate Coupling (TC⁴) campaigns in January-February 2006 and July-August 2007, respectively. The vertical profiles of isotopic composition showed predictable, repeating patterns consistent with the influence of a surface source at lower altitudes and the influence of stratospheric photochemistry in the lower stratosphere. Their correlations with marine tracers at lower altitudes are consistent with a predominantly oceanic source, although a soil source cannot be ruled out. Measurements in a combustion plume revealed a strong depletion in ¹⁵N at the central nitrogen atom (i.e., low $\delta^{15}\text{N}^{\alpha}$ values), providing new information on N₂O isotopic compositions from combustion. This new dataset demonstrates that a coherent picture of the isotopic composition of tropospheric N₂O is possible at currently attainable precisions and that its variations from 0.5 km to the lower stratosphere is a useful tool in investigating the sources and distributions of this important greenhouse gas.

4.1. Introduction

Nitrous oxide, N₂O, is an important greenhouse gas with a tropospheric mixing ratio that has risen from a pre-industrial level of ~270 ppbv to current levels of ~320 ppbv [e.g., *MacFarling-Meure et al.*, 2006], revealing an imbalance between the N₂O sources and sinks of ~5 TgNyr⁻¹ [*Forster et al.*, 2007]. The magnitudes of the particular processes that contribute to this imbalance (and how these may change as climate changes and as a side-effect of CO₂ mitigation strategies) have large uncertainties [e.g., *Forster et al.*, 2007]. Atmospheric N₂O originates predominantly at Earth's surface as a product or by-product of microbial nitrification and denitrification in water and in both natural and agricultural soils, and is emitted to the atmosphere by air-sea and air-soil exchange. These processes yield N₂O with oxygen and nitrogen isotopic compositions that depend on the isotopic composition of the N and O reservoirs from which it is produced as well as isotope effects associated with the microbiogeochemistry of N₂O production and consumption. The only major N₂O sink is destruction by photolysis and reaction with O(¹D) in the stratosphere, which enriches the remaining N₂O in the heavy isotopes ¹⁵N and ¹⁸O [e.g., *Kim and Craig*, 1993]. Since the

sources and sinks of atmospheric N₂O determine its isotopic composition, isotope measurements can provide additional constraints on the N₂O budget beyond those based on measurements of N₂O mixing ratios alone [e.g., Kim and Craig, 1993; Toyoda et al., 2002; Park et al., 2004].

So far, however, the large variability in N₂O isotopic compositions measured in and above soils [e.g., Pérez et al., 2000, 2001] and the oceans [e.g., Popp et al., 2002; Toyoda et al., 2002] has precluded a “bottom up” approach to simultaneously balancing the global N₂O concentration and isotope budgets. Isotopic compositions of emitted N₂O appear to depend sensitively on small-scale variations in many environmental parameters such as soil texture, soil water content, and substrate isotopic composition (e.g., nitrates), as well as the relative amounts of N₂O production (during nitrification and denitrification) and consumption (e.g., during denitrification under anaerobic conditions). Indeed, apportioning the relative amounts of N₂O production and consumption in the soils before emission to the atmosphere is one of the goals of using isotope measurements at the field scale [e.g., Bol et al., 2003; Pérez et al., 2006]; knowledge of how the magnitudes of these processes change with environmental variables could be used to adjust agricultural parameters, such as soil water content during fertilization, in order to mitigate the release of N₂O to the atmosphere and to better predict effective mitigation strategies as mean surface temperatures rise [e.g., Fujinuma and Balster, 2009; Baggs, 2008]. However, this large variability has also meant that a “bottom up” approach to balancing the regional, hemispheric, and global budgets is unlikely to be sufficiently constrained.

A “top-down” approach via inverse modeling of N₂O measurements [Hirsch et al., 2006] has also been underconstrained, at least apart from box model studies of the long-term increase in N₂O concentrations and the concurrent depletion in its heavy isotopes that have been measured in air from firn and ice cores [Rahn and Wahlen, 2000; Sowers et al., 2002; Röckmann and Levin, 2005; Bernard et al., 2006; Ishijima et al., 2007]. Due to its long atmospheric lifetime of 120 years, N₂O (and hence its isotopic composition) has commonly been assumed to be well-mixed and thus was expected to show little variation in the troposphere, leaving inverse models underconstrained. Recently, however, time series analyses [Nevison et al., 2005, 2007; Jiang et al., 2007] of nearly continuous high-precision N₂O mixing ratio measurements at the surface have revealed detectable seasonal cycles and interannual variations in N₂O concentrations, and new N₂O isotope measurements on archived air samples from the surface at Cape Grim, Tasmania reveal the same [Park et al. 2005, 2008], demonstrating that a top-down approach using these datasets might ultimately help constrain the magnitudes of different sources. Further information on the isotopic compositions of N₂O emitted from the oceans and soils and the degree to which they may affect regional and hemispheric N₂O isotopic compositions are greatly needed to proceed, however, as there is a dearth of observations.

Here, we report measurements of the ¹⁸O and ¹⁵N isotopic compositions (including site-specific ¹⁵N) of N₂O in whole air samples collected from 0.5 km to the lower stratosphere in the tropics. The N₂O isotope altitude profiles obtained in both January and July in different years show a persistent pattern that, based on our initial analysis, appears to reflect the influence at lower altitudes of N₂O most likely from the ocean, transitioning at high altitudes in the lower stratosphere to the influence of stratospheric photochemistry. Although the variations are small, they are detectable at current measurement precisions using Continuous-

Flow Isotope Ratio Mass Spectrometry (CF-IRMS) and serve as the basis for hypotheses regarding the sources that control the isotopic composition of tropospheric nitrous oxide that we put forth here to be tested by future measurements and analyses. As such, these measurements, combined with future vertical profiles in different regions and with increased measurement precision, may finally succeed in allowing isotopes to be used in a “top down” approach to constrain the magnitude and distribution of anthropogenic and natural N₂O sources.

4.2. Methods

Whole air samples were collected from the WB-57 aircraft in January and February 2006 during the Costa Rica Aura Validation Experiment (CRAVE) and from the WB-57 and DC-8 aircraft in July and August 2007 during Tropical Composition, Cloud and Climate Coupling (TC⁴), both NASA missions based in San Jose, Costa Rica (9.99°N, 84.21°W). The University of Miami (UM) whole air sampler (WAS) [Flocke *et al.* 1999], which flew on the WB-57, included 50 1.5-liter electropolished stainless steel canisters equipped with automated metal valves. The evacuated canisters were pressurized to 40 psi using a 4-stage bellows pump in flight. The University of California, Irvine (UCI) whole air sampler [Colman *et al.*, 2001], which flew on the DC-8, used a stainless-steel bellows pump to pressurize 2-L stainless steel canisters to 40 psi. The canisters were equipped with stainless steel bellows valves and were evacuated and then filled with ~20 Torr of water vapor prior to the flights. Samples were collected in the planetary boundary layer, the free troposphere, and into the Tropical Tropopause Layer (or "TTL", defined here as the region between ~12-20km [Toon *et al.*, 2010], which includes the tropical lower stratosphere). Most of the WB-57 samples selected for isotopic analysis (see below) were collected between ~10 and 20 km, and those selected from among the DC-8 samples were collected between ~0.5 and 11.5 km. For reference, the cold-point tropopause was located on average at ~16.5 km during TC⁴ and ~17.5 km during CRAVE. Most of the samples selected for isotopic analysis were collected between ~1°S and 10°N, but 25 of the samples were collected between ~20 and 30°N on two similar WB-57 transit flights (one for TC⁴ and one for CRAVE) between Costa Rica and Houston, Texas. Sample selection was based largely on obtaining representative latitude and altitude distributions from both missions and on what samples were still available for analysis (i.e., those which had not been "recycled" to collect additional samples for trace gas analyses), with the exception of the plume samples which were selected because they were of interest based on the tracer mixing ratios.

After sample collection, the WB-57 and the DC-8 whole air samples were first measured for numerous trace gas mixing ratios at UM and UCI, respectively, by gas chromatography (GC) and gas chromatography-mass spectrometry (GC-MS). For the WB-57 WAS samples, measurements that are relevant for this study are mixing ratios of N₂O, ethane (C₂H₆), propane (C₃H₈), benzene (C₆H₆), and tetrachloroethylene (C₂Cl₄). In particular, N₂O mixing ratio measurements were made using an HP5890 II+ series GC fitted with an electron capture detector (ECD) relative to a 314 ppbv N₂O secondary standard of whole air calibrated against a National Institute of Standards and Technology (NIST) reference gas, Standard Reference Material #2608 with an N₂O mixing ratio of 300 nmol/mol ± 1%. The average uncertainty (2σ) for the N₂O mixing ratio data is less than 0.7 ± 1% [Hurst *et al.*, 2002]. Hydrocarbon species were measured by GC with flame ionization detection (GC-FID) with

limits of detection (LOD) of about 2 ppt. C_2Cl_4 was measured with GC mass spectrometry (GC-MS) with LOD of better than 0.1 pptv. For the DC-8 samples, measurements that are relevant for this study include mixing ratios of methyl iodide (CH_3I), methyl nitrate (CH_3ONO_2), and ethyl nitrate ($C_2H_5ONO_2$), ethyne and benzene. CH_3I , CH_3ONO_2 , and $C_2H_5ONO_2$ were measured by GC-ECD with LODs of 0.01, 0.02, and 0.02 pptv, respectively. Ethyne and benzene were measured by GC-FID, both with LODs of 3 pptv. Our analyses of the DC-8 samples also included correlations of the N_2O isotope measurements with *in situ* measurements of carbon monoxide (CO) and methane (CH_4) mixing ratios from a tunable diode laser instrument, DACOM [Sachse *et al.*, 1987, 1991]; measurements were made at 1 Hz measurement with 0.1% precision and were averaged over the whole air canister sampling interval to compare with the whole air sample measurements. N_2O mixing ratio measurements sometimes made using the DACOM instrument are not available for these flights, nor were N_2O mixing ratios for the DC-8 samples measured at UCI. Since the ratio of the m/z 44 peak area of N_2O (measured on the IRMS at University of California at Berkeley (UCB)) to the sample pressure is proportional to the N_2O mixing ratio, we attempted to retrieve an N_2O mixing ratio from the IRMS data and the sample pressure at the time of the isotope analyses. However, because the pressure measurements during sample transfer from the canister to the IRMS flask (see below) were intended only as a housekeeping measure and not as an accurate absolute pressure measurement independent of the gaseous composition, a convection-enhanced pirani gauge that was not calibrated for samples of widely varying water content was used, and our attempt to retrieve a proxy for the N_2O mixing ratio of the sample was therefore not successful.

After these and other trace gas mixing ratio measurements at UM and UCI, a total of 125 samples were selected for isotopic analysis and shipped to UCB. The isotopic composition of N_2O in the whole air samples was measured at UCB by CF-IRMS on a Finnigan MAT-252 coupled with preconcentration (PreCon) and gas chromatography (GC) devices – i.e., “PreCon/GC/CF-IRMS.” Prior to the isotope measurements, the CRAVE whole-air samples were archived in 1.5-liter Pyrex flasks; aliquots for the isotope measurements were taken from these archival flasks by expansion into evacuated 100-200mL measurement flasks. The TC^4 samples were not archived; 100 ml aliquots for isotope analysis were taken directly from the sample canisters.

N_2O isotopic compositions are reported here as δ -values in “per mil” (‰), which is the part per thousand difference of the isotope ratio of the sample relative to a standard: $\delta = 1000 \cdot (R/R_{\text{standard}} - 1)$, where $R = {}^{15}N/{}^{14}N$ or ${}^{18}O/{}^{16}O$ and the subscript ‘standard’ refers to an international reference material, which is air- N_2 for $\delta^{15}N$ and Vienna Standard Mean Ocean Water (VSMOW) for $\delta^{18}O$. Two types of nitrogen isotopic compositions are reported: (1) $\delta^{15}N^{\text{bulk}}$, which is the ${}^{15}N$ isotope composition averaged over the two nitrogen atom sites in N_2O , and (2) $\delta^{15}N^\alpha$ and $\delta^{15}N^\beta$, which represent the “site-specific” isotopic compositions – i.e., the ${}^{15}N$ isotopic composition at the central nitrogen atom (the “ α ” site) and the ${}^{15}N$ isotopic composition at the terminal nitrogen atom (the “ β ” site), respectively. In addition, we report the ‘Site Preference’ (SP) of the α -position relative to the β -position ($SP = {}^{15}R^\alpha/{}^{15}R^\beta - 1$), a form of the site-specific isotopic composition that is now frequently used, particularly in ecological studies in which it may be useful in discriminating between different production mechanisms [e.g. Bol *et al.*, 2003, Sutka *et al.*, 2006, Pérez *et al.*, 2006]. While some studies have used an alternative definition of SP as simply the difference between $\delta^{15}N^\alpha$ and $\delta^{15}N^\beta$

values (i.e. $SP = \delta^{15}N^{\alpha} - \delta^{15}N^{\beta}$), a difference between truncated ratios is not a mathematically rigorous quantity [Gros *et al.*, 2003]. However, for the small values of SP usually encountered, the two expressions are equivalent.

Since the details of the isotopic measurements have been described elsewhere [Park *et al.*, 2004], only a brief overview is given here. Two aliquots are required to determine the site-specific isotopic composition of N₂O using the MAT-252 IRMS, one for $\delta^{15}N^{\text{bulk}}$ and $\delta^{18}O$, and a second for $\delta^{15}N^{\alpha}$ and $\delta^{15}N^{\beta}$. To determine $\delta^{15}N^{\text{bulk}}$ and $\delta^{18}O$ values, m/z 44, 45, and 46 (which correspond to isotopologues of N₂O⁺) are measured and compared with a standard for the first aliquot. To determine $\delta^{15}N^{\alpha}$, the NO⁺ fragment ion at m/z 30 and 31 is measured and compared with a standard for the second aliquot and the degree of ‘scrambling’ — i.e., the fraction of NO⁺ in the sample that included the β N-atom — is taken into account; the ‘scrambling factor’ measured for our Finnigan MAT-252 is 8.04% [see Kaiser *et al.*, 2004], which is similar to that measured for other 252 series instruments [e.g., Toyoda and Yoshida, 1999]. The measured values for $\delta^{15}N^{\text{bulk}}$ and $\delta^{15}N^{\alpha}$ are then used to calculate $\delta^{15}N^{\beta}$, which in turn is combined with $\delta^{15}N^{\alpha}$ to calculate SP.

Although for several years there had been controversy regarding how to convert $\delta^{15}N^{\alpha}$ and $\delta^{15}N^{\beta}$ IRMS measurements onto the international air-N₂ scale [e.g., Toyoda and Yoshida, 1999; Yoshida and Toyoda, 2000; Kaiser *et al.* 2004; Park *et al.*, 2004; Westley *et al.* 2007], Griffith *et al.* [2009] recently determined the SP of tropospheric N₂O using a Fourier Transform infrared spectroscopic technique which is independent of mass spectrometric measurements, yielding values that are in agreement with the Yoshida and Toyoda [2000] air-N₂ scale. Thus, we report $\delta^{15}N^{\alpha}$ and $\delta^{15}N^{\beta}$ values on the Yoshida and Toyoda [2000] scale using tropospheric N₂O as a ‘transfer standard’ given the SP value of tropospheric N₂O from Yoshida and Toyoda [2000] of 18.7‰, the value of $\delta^{15}N^{\text{bulk}}$ of tropospheric N₂O measured at UCB of 6.2‰, and the measured site-specific isotopic composition relative to tropospheric N₂O at UCB to effect the conversion.

The 1 σ measurement precisions are ~0.2‰ for $\delta^{15}N^{\text{bulk}}$, 0.3‰ for $\delta^{18}O$, 0.8‰ for $\delta^{15}N^{\alpha}$, and 0.9‰ for $\delta^{15}N^{\beta}$, determined by repeated measurements of different volumes of tropospheric air collected at UCB and by runs of a 1‰ N₂O-in-air laboratory standard (see, e.g., Park *et al.* [2004]; Kaiser *et al.* [2003]). The precision is limited by instrumental noise, sample size, and the number of measurements for a given sample. In addition, the site-specific precisions are limited by the fact that two different aliquots are required for our MAT-252 since it is not possible to fit ion collectors for simultaneous measurements of m/z 30, 31, 44, 45, and 46 into the detection region. Of the 125 samples in this dataset, 27 were measured in duplicate and showed repeatability that was similar to the precision. The accuracy of the measurements reported here are estimated to be 1‰ for $\delta^{15}N^{\text{bulk}}$ and $\delta^{18}O$ and 4‰ for $\delta^{15}N^{\alpha}$ and $\delta^{15}N^{\beta}$ based on a comparison of the average isotopic composition of tropospheric N₂O reported by different groups, including ours, which show a range of differences of these magnitudes [Yoshida and Toyoda, 2000; Kaiser *et al.*, 2003; Griffith *et al.*, 2009]. Laboratory intercomparisons should improve the relative accuracies, and the implications of any future laboratory intercomparisons for the measurements reported here will be published when available.

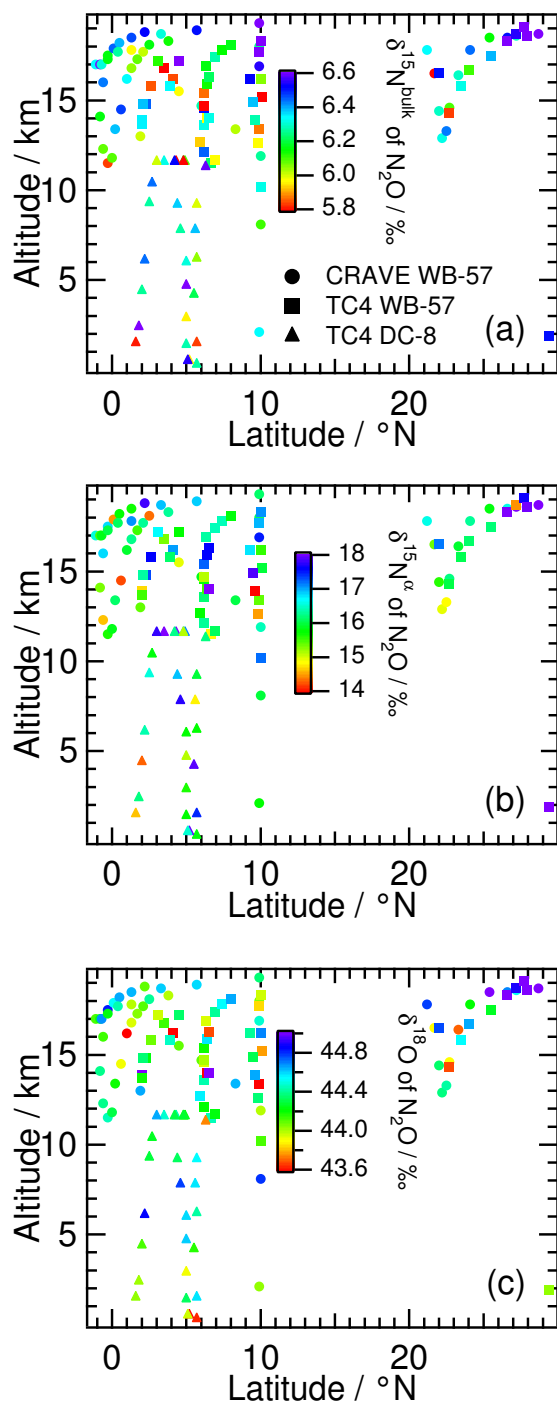


Figure 4.1. Whole air samples analyzed for the isotopic composition of N₂O for the CRAVE and TC⁴ missions. Symbols show sampling location given by altitude (y-axis) vs. latitude (x-axis) for the CRAVE WB-57 samples (squares), TC⁴ WB-57 samples (triangles), and TC⁴ DC-8 samples (circles), colorscaled by the isotopic composition of N₂O: (a) δ¹⁵N^{bulk}, (b) δ¹⁵N^α and (c) δ¹⁸O. Aircraft landings in Costa Rica occur at 10°N, while other descents occur as dives on various flights, as noted in the text.

4.3. Results and Discussion

Figure 4.1 shows the latitude and altitude distribution of the 125 samples from CRAVE and TC⁴ measured for N₂O isotopic compositions. Measured values for $\delta^{15}\text{N}^{\text{bulk}}$, $\delta^{15}\text{N}^{\alpha}$, and $\delta^{18}\text{O}$ are represented by the color scaling shown in the legends and are also given in Tables 4.S1, 4.S2, and 4.S3 in supplementary materials. As expected, the isotopic variability is small, with a range in δ -values for each equivalent to ~ 4 times the corresponding 1σ measurement precision, as is evident in the range of the legend. In the following sections, we examine both the averaged vertical profiles for the different aircraft and missions as well as unaveraged portions of particular flights that show interesting correlations with marine and combustion tracers. In this paper, we focus on the tropical measurements ($<11^{\circ}\text{N}$) but include the subtropical points between 20° and 29°N in Figure 4.1 and the supplementary data files for completeness.

4.3.1. Averaged Vertical Profiles in the Tropics

Figure 4.2 shows the results for averaging the tropical data (i.e., $<11^{\circ}\text{N}$) in 1-km altitude bins, parsed and color-coded by aircraft (WB-57 and DC-8) and campaign (CRAVE and TC⁴). The error-bars shown are the 1σ standard deviation of the average of the data for that altitude bin (solid bars) or, for the few bins for which there is only a single datum, the measurement precision (dotted bars); the number of samples per altitude bin is also indicated in Figure 4.2 (a) in the corresponding color. For comparison, the gray shading in each panel shows the $\pm 1\sigma$ ($N=288$ for $\delta^{15}\text{N}^{\text{bulk}}$ and $\delta^{18}\text{O}$ and $N=239$ for $\delta^{15}\text{N}^{\alpha}$) variability in measured tropospheric N₂O isotopic compositions in air sampled on the UCB campus (37.87°N , 122.26°W) between September 2001 and November 2006. (Note that the shaded ranges therefore include small trends and are thus larger than the day-to-day variability of tropospheric N₂O isotopic composition, which is similar to the measurement precision, suggesting no major influence from local sources. Furthermore, the meridional gradients between UCB and the tropics are expected to be well within these ranges [*Kaiser et al.*, 2003].) For $\delta^{15}\text{N}^{\text{bulk}}$, the average values and variability for the tropical profiles shown in 4.2 (a) fall within the range of those measured at the surface at midlatitudes at UCB. The largest deviation appears in the lower stratosphere, where average $\delta^{15}\text{N}^{\text{bulk}}$ values increase; this is shown more clearly in Figure 4.3 in which the measurements are binned into 0.5 km rather than 1 km ranges and then averaged. The increase in the $^{15}\text{N}/^{14}\text{N}$ ratio in N₂O with altitude is due primarily to the photolysis of N₂O in the stratosphere, which preferentially dissociates the $^{14}\text{N}^{14}\text{N}^{16}\text{O}$ isotopologue with a smaller contribution from photo-oxidation of N₂O by reaction with O(¹D) [e.g., *Blake et al.*, 2003; *Johnson et al.*, 2001; *Kaiser et al.*, 2002a; *Yung and Miller*, 1997]. As the N₂O mixing ratios decrease with altitude in the stratosphere, the $\delta^{15}\text{N}^{\text{bulk}}$ values increase, as expected based on previous stratospheric measurements [e.g., *Toyoda et al.*, 2001; *Röckmann et al.*, 2001; *Park et al.*, 2004, *Kaiser et al.*, 2006].

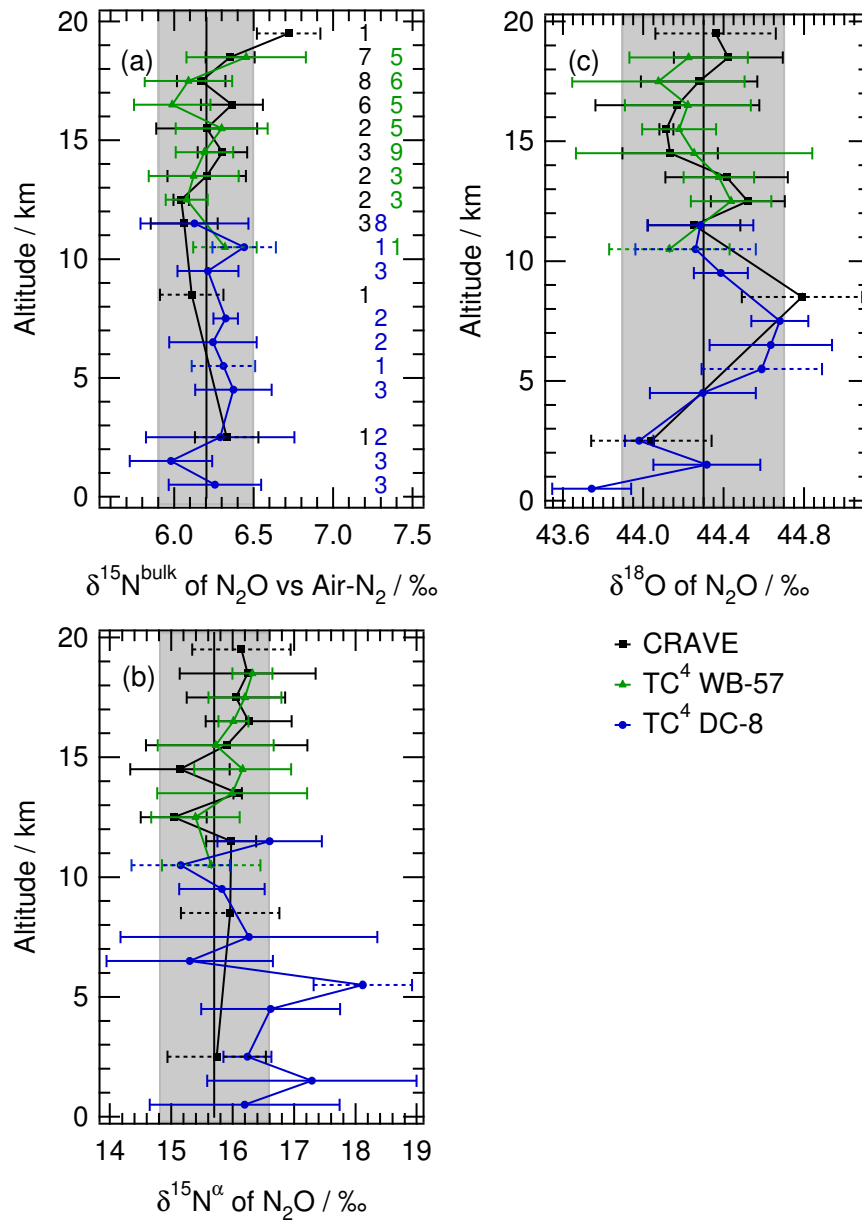


Figure 4.2. Vertical profiles of the isotopic composition of N₂O for samples collected at latitudes <11°N: (a) $\delta^{15}\text{N}^{\text{bulk}}$, (b) $\delta^{15}\text{N}^{\alpha}$, and (c) $\delta^{18}\text{O}$ for the CRAVE WB-57 samples (circles), the TC⁴ WB-57 samples (triangles), and the TC⁴ DC-8 samples (squares). Measured values were binned and averaged in 1-km intervals. Error bars in each panel show the standard deviation of the mean for each bin, while the numbers in (a) give the number of samples in each bin; bins for which there is only one sample are indicated by dashed error bars. For reference, the tropopause was located on average at ~16.5 km during TC⁴ and ~17.5 km during CRAVE, as noted in the text. For comparison, the gray shading in each panel shows the $\pm 1\sigma$ (N=288 for $\delta^{15}\text{N}^{\text{bulk}}$ and $\delta^{18}\text{O}$ and N=239 for $\delta^{15}\text{N}^{\alpha}$) variability in measured tropospheric N₂O isotopic compositions in air sampled on the UCB campus (37.87°N, 122.26°W) between September 2001 and November 2006.

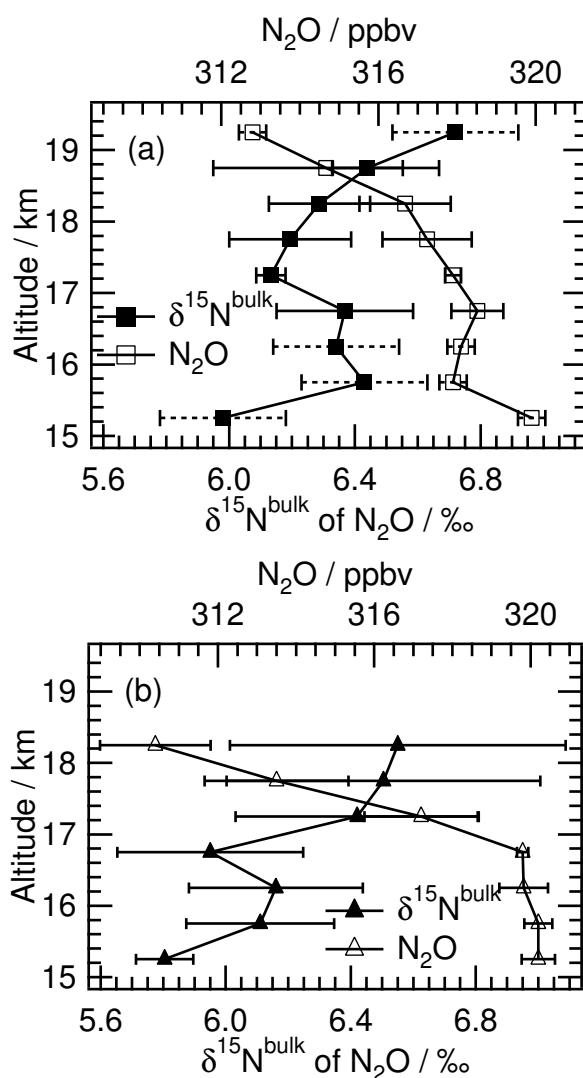


Figure 4.3. Vertical profiles of the mixing ratio (open symbols) and $\delta^{15}\text{N}^{\text{bulk}}$ (closed symbols) of N₂O, averaged into 0.5 km bins for samples collected at latitudes <11°N and altitudes >15km for (a) CRAVE and (b) TC⁴.

When the $\delta^{15}\text{N}^{\text{bulk}}$ and N₂O values for individual samples are plotted in a Rayleigh isotope fractionation format in Figure 4.4 (i.e., as $\ln(1 + \delta^{15}\text{N}^{\text{bulk}}/1000)$ vs. $\ln([\text{N}_2\text{O}]/[\text{N}_2\text{O}]_0)$ where $[\text{N}_2\text{O}]_0$ is the N₂O mixing ratio for air entering the stratosphere) apparent fractionation constants, ϵ_{app} , of $-21 \pm 7 \text{‰}$ and $-19 \pm 7 \text{‰}$ are obtained for CRAVE and TC⁴, respectively, from the slope of the fit line as determined by the Williamson-York method which considers uncertainty in both the x- and y-data [Cantrell, 2008 and references therein]. While the correlations are statistically significant ($R = -0.527$, $P < 0.03$ and $R = -0.610$, $P < 0.03$ for CRAVE and TC⁴, respectively), the uncertainties are large since the N₂O mixing ratios decrease by only ~4 to 8 ppbv and the $\delta^{15}\text{N}^{\text{bulk}}$ values increase by only ~0.5‰ in the lowest 2 kilometers of the stratosphere, which are intrinsically small and are close to the isotope measurement precision of $\pm 0.2 \text{‰}$. Nevertheless, these values for ϵ_{app} are within the range of

–14 to –19‰ obtained in the stratosphere for N₂O mixing ratios > 200 ppbv at 18°N [Kaiser *et al.*, 2006], midlatitudes [e.g., Toyoda *et al.*, 2001; Röckmann *et al.*, 2001], and high latitudes [e.g., Park *et al.*, 2004]. As discussed in the previous studies, these values for ϵ_{app} are at least a factor of two smaller than the fractionation constant expected in an isolated system – that is, one in which chemistry alone is acting to alter the isotopic composition and not transport or mixing of air of different isotopic compositions. For example, a value of –34.7‰ is expected based on broadband photolysis of N₂O at room temperature in the laboratory and a 10% contribution from N₂O oxidation by O(¹D) [Kaiser *et al.*, 2002a; Röckmann *et al.*, 2001]; transport and mixing decrease the slope of the Rayleigh fractionation line, yielding a value for ϵ_{app} that is necessarily smaller than that for an isolated system.

This isotope fractionation cannot be due to *in situ* photochemistry in the lowest 2 km of the tropical stratosphere, however. The lifetime of N₂O at altitudes below 20 km in the tropics is ~70 years [e.g., Minschwaner *et al.*, 1993]. Thus, on the time scales for tropical ascent, which require only about 4 months to ascend from 17 to 19 km [e.g., Eluszkiewicz *et al.*, 1996; Rosenlof, 1995; Boering *et al.*, 1996; Mote *et al.*, 1996], N₂O mixing ratios should not decrease and N₂O should not become enriched in ¹⁵N to the extent observed by *in situ* photochemistry occurring in the tropics, as shown by a simple Rayleigh model analysis given in the appendix. Rather, as shown previously using measurements of the mixing ratios of a number of trace gas species below ~23 km, photochemically-aged stratospheric air from midlatitudes must be transported and mixed isentropically into the tropical upwelling region [e.g., Avallone and Prather, 1996; Boering *et al.*, 1996; Volk *et al.*, 1996]; it is this mixing in of older midlatitude air rather than *in situ* N₂O destruction in the tropics that results in the decreasing N₂O mixing ratio and increasing ¹⁵N enrichment with altitude above the tropical tropopause in Figure 4.3. In subsequent work, we will attempt to quantify this in-mixing of midlatitude air as a function of altitude and compare it with previous estimates based on the tracer mixing ratio models noted above since such a number is of interest for stratospheric dynamics, mean ages, and residence times and how these may or may not be changing over time (e.g., Engel *et al.*, 2009; Austin and Li, 2006). Finally, we note that an increase in $\delta^{18}\text{O}$ above the tropopause (e.g., Figure 4.2 (c)) is not as clear as for $\delta^{15}\text{N}^{\text{bulk}}$ and not apparent at all in $\delta^{15}\text{N}^{\alpha}$ (e.g., Figure 4.2 (b)); this difference with respect to $\delta^{15}\text{N}^{\text{bulk}}$ is likely due to a fractionation constant for $\delta^{18}\text{O}$ that is smaller than that for $\delta^{15}\text{N}^{\text{bulk}}$ by 10% and to a measurement precision that is 4 times larger for $\delta^{15}\text{N}^{\alpha}$ than for $\delta^{15}\text{N}^{\text{bulk}}$ so that stratospheric enrichments may be masked by noise in this dataset.

For $\delta^{18}\text{O}$, the averaged tropical profiles in Figure 4.2 show a remarkably consistent pattern between the CRAVE and TC⁴ missions. At the lowest altitudes, N₂O is relatively depleted in ¹⁸O, and is outside the $\pm 1\sigma$ range observed on average at the surface at UCB (gray shaded area). Values for $\delta^{18}\text{O}$ then increase up to ~8 or 9 km and then generally decrease up to the tropopause. Such repeatability between the two missions suggests that the profiles are determined by an interplay of similar processes. One possibility is that the drivers underlying this profile pattern are analogous to those for other species that exhibit a common “inverse C”-shaped altitude profile that is determined by convection of surface air combined with chemistry and/or mixing [e.g., Prather and Jacob, 1997]. For $\delta^{18}\text{O}$, an inverse C pattern could

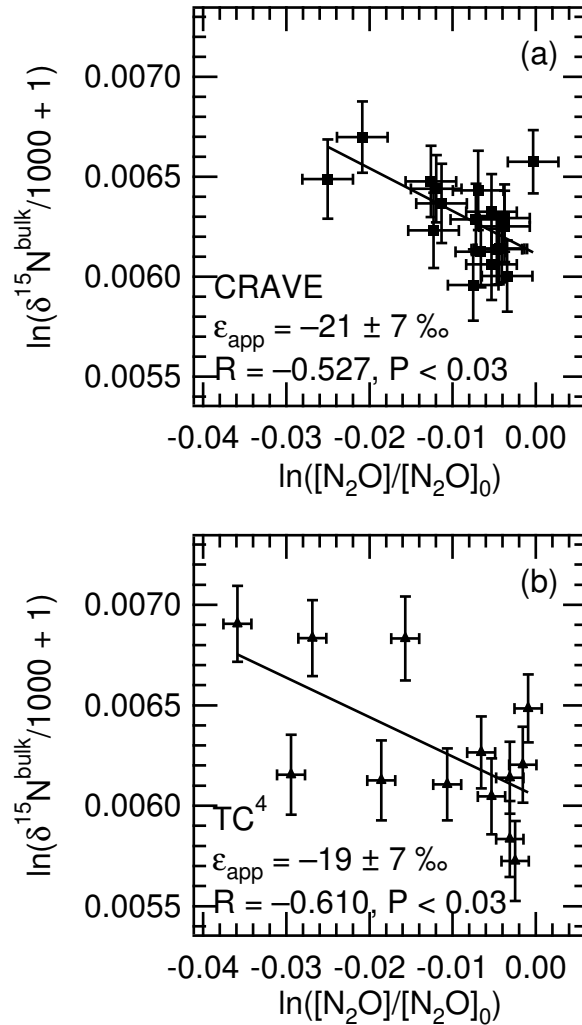


Figure 4.4. Individual measurements of $\delta^{15}\text{N}^{\text{bulk}}$ of N_2O for samples from the tropical lower stratosphere ($<11^\circ\text{N}$ and (a) > 17 km for CRAVE and (b) > 16 km for TC^4) are shown here plotted in a Rayleigh isotope fractionation format, i.e., as $\ln(1 + \delta^{15}\text{N}^{\text{bulk}}/1000)$ vs. $\ln([\text{N}_2\text{O}]/[\text{N}_2\text{O}]_0)$, where $[\text{N}_2\text{O}]_0$ is the N_2O mixing ratio for air entering the stratosphere, taken to be the average of the N_2O mixing ratios measured below the cutoff altitude, 319.4 ± 0.9 and 320.7 ± 0.4 for CRAVE and TC^4 , respectively.

result from a source of N_2O that is depleted in ^{18}O relative to the free troposphere at the surface, either from soils or the ocean. Tropical convection takes this near-surface N_2O and deposits it at altitudes up to 10 to 14 km, thus leading to a decrease in $\delta^{18}\text{O}$ values at these higher altitudes influenced by convective outflow. In between these altitudes, the air may be more characteristic of background tropical and/or midlatitude air, with higher values of $\delta^{18}\text{O}$; the further from the surface source, the more it resembles background air (i.e., $\delta^{18}\text{O}$ increases with altitude) until convective outflow of surface air deposited higher altitudes begins to turn the profile back around towards lower $\delta^{18}\text{O}$ values. The vertical profiles for $\delta^{15}\text{N}^{\text{bulk}}$ and $\delta^{15}\text{N}^{\alpha}$ (Figure 4.2 (a)) do not show such a pattern.

Comparing these characteristics of the vertical profiles for $\delta^{18}\text{O}$, $\delta^{15}\text{N}^{\text{bulk}}$, and $\delta^{15}\text{N}^{\alpha}$ with the range of isotopic compositions measured to date in soils and the ocean suggests that the source that may be influencing the lower altitudes may be more similar in isotopic composition to an ocean source than to a soil source, although a mixture of the two cannot be ruled out, particularly since both the Eastern Tropical North Pacific Ocean off the coast of Central America and tropical soils are thought to be significant sources of N_2O [e.g., *Cohen and Gordon, 1978; Nevison et al., 1995; Matson and Vitousek, 1990*]. For example, the isotopic composition of N_2O in the subtropical North Pacific gyre was measured by Popp *et al.* [2002] and indicates that N_2O transferred from ocean to the air should be slightly depleted in bulk N and slightly more so in ^{18}O relative to the background troposphere; they suggest a range for the ocean source of 3.5 to 5.5‰ for $\delta^{15}\text{N}^{\text{bulk}}$ and 35.5 to 41.5‰ for $\delta^{18}\text{O}$. Different ranges for the isotopic composition of emitted N_2O have been measured in other ocean regions [e.g., *Toyoda et al., 2002*]; in the absence of more comprehensive ocean measurements and an understanding of what controls them, the ranges relevant for this study will remain uncertain. In contrast, while there is great variability in measurements of the isotopic composition of N_2O emitted from soils, in general it is significantly more depleted in ^{15}N and ^{18}O relative to the tropospheric averages than an ocean source, and significantly more so in bulk ^{15}N than in ^{18}O . For example, the emission weighted isotope signature from unfertilized Costa Rican tropical rainforest soil $\delta^{15}\text{N}^{\text{bulk}} = -26 \pm 2.5\text{‰}$ and $\delta^{18}\text{O} = 26 \pm 6\text{‰}$ [*Pérez et al., 2000*]. If a soil source of N_2O were the dominant factor determining the lower $\delta^{18}\text{O}$ values in the lower altitudes of the vertical profile, then a signal in $\delta^{15}\text{N}^{\text{bulk}}$ would be expected to be even stronger and yet such behavior appears to be absent, as noted above. Furthermore, although measurements of the site-specific isotopic composition of oceanic N_2O are even more rare than $\delta^{15}\text{N}^{\text{bulk}}$ and $\delta^{18}\text{O}$, *Toyoda et al.* [2002] have shown ocean profiles in which $\delta^{15}\text{N}^{\alpha}$ values are high and $\delta^{15}\text{N}^{\beta}$ are low relative to background tropospheric air; as a result, $\delta^{15}\text{N}^{\text{bulk}}$ values would be more similar to tropospheric air than either $\delta^{15}\text{N}^{\alpha}$ or $\delta^{15}\text{N}^{\beta}$ since it is the average of the two. Such a source could also be consistent with the observations since $\delta^{15}\text{N}^{\alpha}$ appears to be higher below 5 km, although such a pattern is arguably in the noise of the measurements. Overall, these characteristics of ocean N_2O isotopic compositions seem more similar to the trends and differences in the averaged profiles shown here than to a soil source, assuming the averaged profiles are indeed representative of regional profiles in general.

4.3.2. Correlations between N_2O isotopic compositions and surface tracer mixing ratios

Examining unaveraged measurements from the flight of 08 August 2007 for the TC⁴ mission may provide further insight into the possible influence of a surface source on the isotopic composition of N_2O in the tropical profiles. The DC-8 flight on this date included 3 distinct segments: a dive over the Pacific Ocean into the boundary layer, followed by an 11.5 km cruise and then a dive over the Colombian jungle. Particularly striking are the significant negative correlations between measurements of $\delta^{18}\text{O}$ of N_2O and the measured mixing ratios of methyl iodide (CH_3I), methyl nitrate (CH_3ONO_2), and ethyl nitrate ($\text{C}_2\text{H}_5\text{ONO}_2$), which are all tracers of marine convection, shown in Figure 4.5. While the correlations between $\delta^{18}\text{O}$ and the marine tracers for all 3 flight segments included together were significant ($P < 0.04$ for each marine tracer), inspection of the individual flight segments shows that the negative

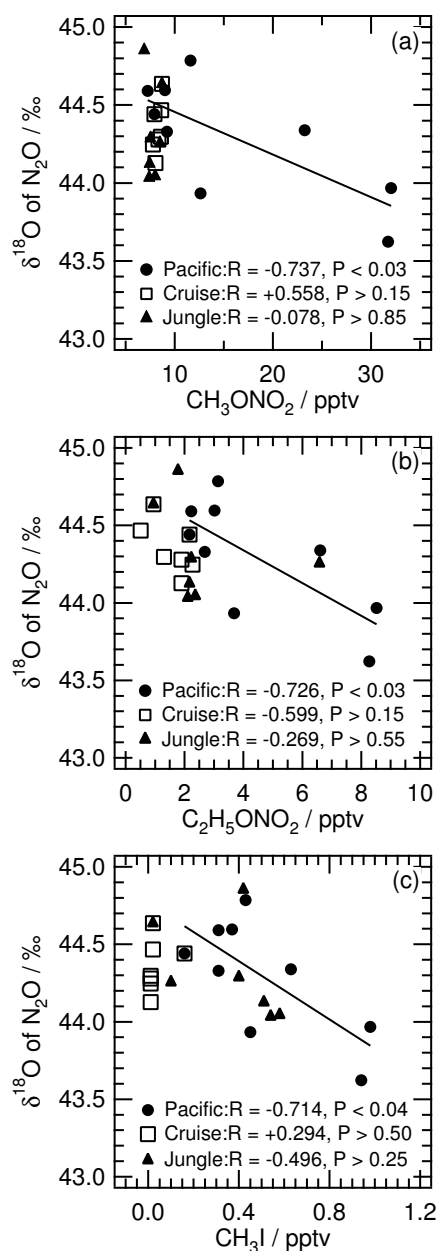


Figure 4.5. Tracer-tracer plots of $\delta^{18}\text{O}$ of N_2O vs. mixing ratios of (a) CH_3ONO_2 , (b) $\text{C}_2\text{H}_5\text{ONO}_2$, and (c) CH_3I from the 08 August 2007 DC-8 samples, parsed into sections of the flight corresponding to a dive over the Pacific (circles; latitude = 4.3 to 5.2°N, longitude = 79.1 to 83.1°W, altitude = 0.5 to 11.6 km), a dive over the Colombian jungle (triangles; latitude = 1.6 to 3.0°N, longitude = 70.5 to 79.1°W, altitude = 1.5 to 11.6 km), and the DC-8 cruise region in between (squares; latitude = 3.4 to 4.3°N, longitude = 71.9 to 79.1°W, altitude = 11.6 km). The values of the correlation coefficient, R, are given in the figure legends, while the regression line shown is for the Pacific Ocean dive measurements.

correlation is largely due to the Pacific dive. For the Pacific dive data, $R = -0.737$ and $P < 0.03$ for CH_3ONO_2 (Fig 5a), $R = -0.726$ and $P < 0.03$ $\text{C}_2\text{H}_5\text{ONO}_2$ (Fig 5b), and $R = -0.714$

and $P < 0.04$ for CH_3I (Fig 5c) whereas the 2 other flight segments do not show statistically significant correlations ($P > 0.15$ for all). That these tracers of marine convection show a strong anti-correlation with $\delta^{18}\text{O}$, especially during the dive over the ocean, suggests that N_2O from the ocean may be influencing $\delta^{18}\text{O}$ of N_2O in the tropical profiles from both CRAVE and TC⁴. Unfortunately, as noted above, the N_2O mixing ratios for these samples were not measured and, therefore, a Keeling plot analysis (in which the y-intercept of a plot of isotopic composition versus the reciprocal of the mixing ratio yields an estimate of the isotopic composition of the “undiluted” source [Keeling, 1958]) is impossible. Rather, the correlation with the marine tracers is only suggestive of an ocean link for the source, or at least one of the sources, influencing the decrease in $\delta^{18}\text{O}$ values towards the surface in the profiles shown here. For $\delta^{15}\text{N}^{\text{bulk}}$ and $\delta^{15}\text{N}^{\alpha}$, the individual datapoints show no significant correlation with the marine tracers (see Supplemental Figures 4.S1 and 4.S2).

For samples from the descent over the Colombian jungle, $\delta^{18}\text{O}$ is significantly anti-correlated with the surface tracers CO ($P < 0.02$) and ethyne ($P < 0.01$), which is consistent with either a soil or an ocean source since both are depleted in ^{18}O relative to background tropospheric N_2O ; see Supplementary Figure 4.S3. (We note that only 1 whole air sample from an altitude of 1.5 km for the jungle dive into the boundary layer was still available for isotopic analysis and it did not display the highly elevated isoprene mixing ratios of many of the other boundary layer samples taken at the bottom of the dive.) For $\delta^{15}\text{N}^{\text{bulk}}$, no significant correlation with surface tracers was observed ($P > 0.15$ for all), analogous to the lack of $\delta^{15}\text{N}^{\text{bulk}}$:marine tracer correlations for the ocean dive (Figure 4.S1). Interestingly, however, there were significant positive correlations between $\delta^{15}\text{N}^{\alpha}$ and the surface tracers CH_4 ($P < 0.01$), ethyne ($P < 0.03$), and benzene ($P < 0.01$) in the jungle dive (Figure 4.S2). Such a positive correlation is not expected for a soil source of N_2O . There are two interesting possibilities that might yield such positive correlations based on details of the flight. One is that the N_2O isotopic composition still reflects an ocean source (which is more likely to be enriched in ^{15}N at the α -position); back trajectory calculations by M. R. Schoeberl, P. A. Newman, and L. R. Lait (available through the NASA/ARC Earth Science Project Office Archive at <http://espoarchive.nasa.gov> [see also Schoeberl and Sparling, 1995]) suggest that the samples at 500 mbar pressure and lower altitudes had been over the Atlantic within 2 to 7 days of the flight. Another possibility is based on observations by the DC-8 whole air sampler scientist that at the bottom of the Colombian jungle dive there were a surprising number of swampy areas as well as cattle. Both are potential sources of N_2O enriched in ^{15}N at the α position relative to a soil source and, most likely, the background troposphere as well since in both systems N_2O may be reduced to N_2 during denitrification [Boontanon *et al.*, 2000; Mahimairaja *et al.*, 1995] which can cause ^{15}N accumulation in the remaining N_2O at the α position [e.g. Toyoda *et al.*, 2005]. Given these two apparently plausible scenarios, it is unclear whether the positive correlations between $\delta^{15}\text{N}^{\alpha}$ and the surface tracers are rather local (as might be expected from cows and swamps) or more regional in nature (an ocean source, or a mixture of ocean and soil sources).

In summary, the significant correlations observed between $\delta^{18}\text{O}$ and marine tracers from a dive over the Pacific Ocean suggest the influence of an ocean source on the N_2O isotopic composition in the lower tropical troposphere, while the correlations between $\delta^{18}\text{O}$ and $\delta^{15}\text{N}^{\alpha}$ and other surface tracers are consistent with the influence of either a continental and/or oceanic source. While more measurements are clearly needed to test the hypotheses

put forth in this section, this new dataset provides new constraints and points to specific needs for the further characterization of the isotopic composition of the various possible surface sources.

4.3.3. Isotopic composition in a combustion plume

Another flight yielding interesting correlations between the measured N₂O isotopic compositions and other atmospheric tracers was the WB-57 flight of 05 August 2007 from the TC⁴ mission. Samples from this flight yielded several measurements of site-specific N₂O isotopologues that showed a large deviation (4σ) from the average tropospheric values and a striking correlation with greatly enhanced mixing ratios of several tracers indicative of industrial combustion or biomass burning processes but only slightly enhanced N₂O mixing ratios of up to ~1 ppbv. The (unaveraged) altitude profiles for measurements of ethane, propane, benzene, and tetrachloroethylene are shown in Figure 4.6 (a). The plume, encountered at altitudes between 14 and 15 km is clearly visible. Trajectory-based convective influence calculations provided by L. Pfister [Pfister *et al.*, 2001; Pfister, L., H. B. Selkirk, D. O’C. Starr, P. A. Newman, and K. H. Rosenlof, A meteorological overview of the TC⁴ mission, submitted to *J. Geophys. Res.*] suggest that these samples were likely affected by convection within one day of the sampling, and that this convection was at least partially over Central America, near Panama City, Panama. Figure 4.6 (b) shows the anti-correlation between $\delta^{15}\text{N}^{\text{bulk}}$, $\delta^{15}\text{N}^{\alpha}$, Site Preference (the relative enrichment at the α versus β nitrogen atom sites; see Methods), and $\delta^{18}\text{O}$ of N₂O and the ethane mixing ratio for the 4 samples with the highest ethane mixing ratios. Values for $\delta^{15}\text{N}^{\alpha}$ and Site Preference are very strongly anti-correlated with ethane ($R = -0.9999$, $P < 0.0003$ and $R = -0.998$, $P < 0.003$, respectively), consistent with both expectations for and measurements of N₂O produced through biomass and fossil fuel combustion, which show that N₂O produced by combustion processes is depleted in ¹⁵N at the α nitrogen atom position relative to the β nitrogen atom position [Toyoda *et al.*, 2008; Ogawa and Yoshida, 2005a, 2005b]. Because the N₂O mixing ratio in the plume samples varies by only 1 ppb or less against a background of 320 ppb, however, the isotopic composition of the source cannot be accurately quantified using a Keeling plot analysis [see, e.g., Pataki *et al.*, 2003 in the context of CO₂]. Overall, based on other tracers measured on the aircraft or in the samples, including CO, CO₂, particles, methyl chloride, methane, ethyne, and other non-methane hydrocarbons (not shown), and the fact that samples were collected directly in the outflow of a convective cloud, it is most likely that the plume represents a mixture of both urban pollution and biomass burning. To our knowledge, this is the first time that N₂O isotope measurements in such a plume influenced by combustion have been made in the remote atmosphere.

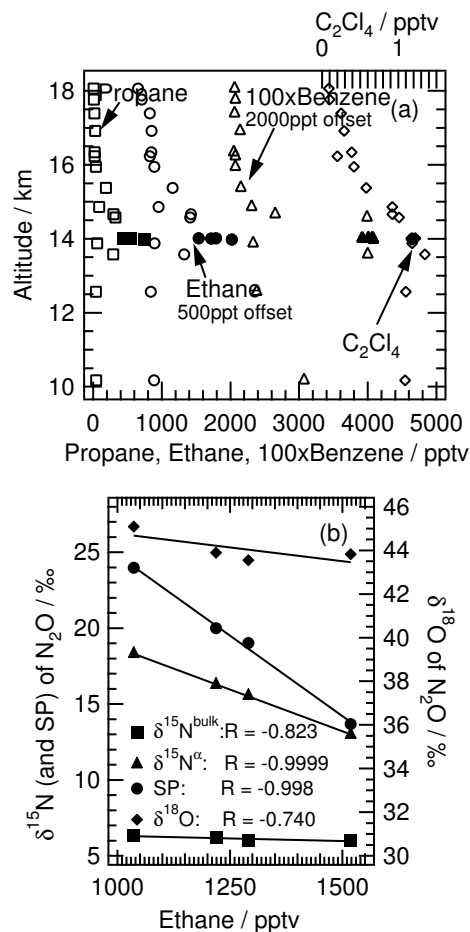


Figure 4.6. (a) Vertical profiles of the mixing ratios of propane (squares; in pptv), ethane (circles; in pptv and offset by 500 pptv), benzene (triangles; in 100×pptv and offset by 2000 pptv), and tetrachloroethylene (C₂Cl₄, diamonds; in pptv, upper x-axis) from the WB-57 flight of 05 August 2007; solid symbols show the samples designated here as being in the combustion plume at ~14 km altitude. (b) Correlation between the N₂O isotopic composition and the ethane mixing ratio for the combustion plume samples in (a) (δ¹⁵N^{bulk}: squares; δ¹⁵N^α: triangles; Site Preference (see text): circles; and δ¹⁸O: diamonds).

4.4. Conclusions

We have demonstrated that the isotopic composition of nitrous oxide varies throughout the tropical troposphere with an average vertical structure in δ¹⁸O, discernible at current measurement precision, but that is not observed in the δ¹⁵N measurements – characteristics that are at least consistent with the influence of an oceanic source of N₂O on a regional scale, or perhaps a mixture of ocean and soil sources. This hypothesis is supported by correlations observed between δ¹⁸O of N₂O and tracers of marine convection, which are particularly strong during a dive over the Pacific Ocean. In addition, we have further demonstrated the dramatic effect of an industrial or biomass burning plume on the site-specific isotopic composition of N₂O. The hypotheses put forth here regarding the sources of N₂O and the extent of their regional and hemispheric influence on tropospheric profiles will

require additional measurements to test them. On the other hand, we note that it is somewhat surprising that the variations in observed N₂O isotopic compositions and their coherent patterns with respect to altitude and the mixing ratios of a number of surface tracers is large enough to at least formulate the hypotheses put forth here. Nevertheless, the variations in the measurements of the isotopic composition of tropospheric N₂O reported here are small compared to the measurement precision – the range of measured isotopic compositions is only about 4 σ – suggesting that improvements in analytical techniques (and/or using the more time-consuming dual inlet IRMS technique of Kaiser *et al.* [2003] or much larger samples sizes for many replicate CF-IRMS measurements on the same sample) would be useful, allowing more information to be extracted from the data. Ultimately, these measurements are “proof-of-concept” that persistent and coherent variations in atmospheric N₂O isotopic compositions are measurable and could aid in using, e.g., inverse models to constrain the sources of N₂O on hemispheric to regional scales. Such modeling capabilities will be highly desirable not only for greenhouse gas concentration predictions and feedbacks but also for verification of future adherence to, e.g., Kyoto Protocol-like international agreements for N₂O emissions.

Appendix

Using the $\delta^{15}\text{N}^{\text{bulk}}$ measurements (shown in Figure 4.3), we can calculate a lower limit for the vertical ascent rate in the tropical lower stratosphere (TLS) during CRAVE assuming no in-mixing of midlatitude air based on Rayleigh fractionation in an isolated system – i.e., by calculating how long it would take to enrich N₂O from the average $\delta^{15}\text{N}^{\text{bulk}}$ value observed at 17.25 km to that observed at 19.25 km based on the *in situ* destruction rate of N₂O. Using the fractionation constant of -34.7‰ noted above and a 70-year lifetime for N₂O with respect to photolysis yields an ascent rate of 0.063 mm s^{-1} (or 0.17 km/month), which implies that, if there were no in-mixing of midlatitude air, the air at 19.25 km would require 12 months to ascend to that altitude from 17.25 km in order to obtain the observed enrichment. In contrast, annually averaged vertical ascent rates in the TLS derived from observations of the propagation of annual cycles in CO₂ [Boering *et al.*, 1996] and water vapor [e.g., Mote *et al.*, 1996] and from radiative calculations [e.g., Eluszkiewicz *et al.*, 1996; Rosenlof, 1995] are $\sim 0.2 \text{ mm s}^{-1}$ ($\sim 0.5 \text{ km/month}$) and are even larger ($\sim 0.35 \text{ mm s}^{-1} = 0.88 \text{ km/month}$) during northern winter when the CRAVE samples were collected, indicating that the transit time for air from ~ 17 to 19 km is on average 4 months, not 12 months, the value yielded by a Rayleigh model for an isolated lower stratosphere. Using temperature-dependent rather than room temperature photolysis fractionation constants, which gives an expected fractionation constant of -48 to -51‰ for the lower tropical stratosphere [Kaiser *et al.*, 2002a, 2002b], decreases that transit time to ~ 9 months, a time scale that is still more than a factor of two larger than the generally accepted ascent time scales noted above. Thus there is simply not enough time using a closed-system Rayleigh model to enrich tropical N₂O in ¹⁵N to the extent observed by *in situ* photochemistry occurring in the tropics. Therefore, photochemically-processed air that is isotopically enriched in ¹⁵N must have mixed into the tropics, a conclusion that is consistent with the current understanding of the chemical composition of the TLS and the time scales for transport of older, midlatitude air into the tropics.

References

- Austin, J. and F. Li (2006), On the relationship between the strength of the Brewer-Dobson circulation and the age of stratospheric air, *Geophys Res. Lett.*, *33*, L17807.
- Avallone, L. M. and M. J. Prather (1996), Photochemical evolution of ozone in the lower tropical stratosphere, *J. Geophys. Res.*, *101*(D1), 1457-1461.
- Baggs, E. M. (2008), A review of stable isotope techniques for N₂O source partitioning in soils: recent progress, remaining challenges and future considerations, *Rapid Commun. Mass Spectrom.*, *22*(11), 1664-1672.
- Bernard, S., T. Röckmann, J. Kaiser, J.-M. Barnola, H. Fischer, T. Blunier, and J. Chappellaz (2006), Constraints on N₂O budget changes since pre-industrial time from new firn air and ice core isotope measurements, *Atmos. Chem. Phys.*, *6*, 493-503.
- Blake, G. A., M.-C. Liang, C. G. Morgan, and Y. L. Yung (2003), A Born-Oppenheimer photolysis model of N₂O fractionation, *Geophys. Res. Lett.*, *30*(12), 1656, doi:10.1029/2003GL016932.
- Boering, K. A., S. C. Wofsy, B. C. Daube, H. R. Schneider, M. Lowenstein, J. R. Podolske and T. J. Conway (1996), Stratospheric mean ages and transport rates from observations of carbon dioxide and nitrous oxide, *Science*, *274*, 1340-1343.
- Bol, R., S. Toyoda, S. Yamulki, J. M. B. Hawkins, L. M. Cardenas, and N. Yoshida (2003), Dual isotope and isotopomer ratios of N₂O emitted from a temperate grassland soil after fertilizer application, *Rapid Commun. Mass Spectrom.*, *17*, 2550-2556.
- Boontanon, N., S. Ueda, P. Kanatharana, E. Wada (2000), Intramolecular stable isotope ratios of N₂O in the tropical swamp forest in Thailand, *Naturwissenschaften*, *87*, 188-192.
- Cantrell, C. A. (2008), Technical Note: Review of methods for linear least-squares fitting of data and application to atmospheric chemistry problems, *Atmos. Chem. Phys.*, *8*, 5477-5487.
- Cohen, Y. and L. I. Gordon (1978), Nitrous oxide in the oxygen minimum of the eastern tropical North Pacific: evidence for its consumption during denitrification and possible mechanisms for its production, *Deep-Sea Res.*, *25*, 509-524.
- Colman, J. J., A. L. Swanson, S. Meinardi, and D. R. Blake (2001), Description of the analysis of a wide range of volatile organic compounds in whole air samples collected during PEM-Tropics A and B, *Anal. Chem.*, *73*, 3273-3731.
- Eluszkiewicz, J. D. Crisp, R. Zurek, L. Elson, E. Fishbein, J. Waters, R. G. Grainger, A. Lambert, R. Harwood, and G. Peckham (1996), Residual circulation in the stratosphere and mesosphere as diagnosed from Microwave Limb Sounder data, *J. Atmos. Sci.*, *53*(2), 217-240.
- Engel, A., *et al.* (2009), Age of stratospheric air unchanged within uncertainties over the past 30 years, *Nature Geosci.*, *2*(1), 28-31.
- Flocke, F., *et al.* (1999), An examination of chemistry and transport processes in the tropical lower stratosphere using observations of long-lived and short-lived compounds obtained during STRAT and POLARIS, *J. Geophys. Res.*, *104*(D21), 26,625–26,642.
- Forster, P., *et al.* (2007), In *Climate Change 2007: The Physical Science Basis*; Solomon, S., Qin, D., Manning, M., Chen, Z., Marquis, M., Averyt, K. B., Tignor, M., and Miller, H. L., Eds.; Cambridge University Press: Cambridge U.K.
- Fujinuma, R., and N.J. Balster (2009), Using stable isotopes to reconcile the difference in nitrogen uptake efficiency relative to late season fertilization of northern red oak

- seedlings in Wisconsin bare-root nurseries, *Eos Trans. AGU*, 90(52), Fall Meet. Suppl., Abstract B53B-0387.
- Griffith, D. W. T., S. D. Parkes, V. Haverd, C. Paton-Walsh, and S. R. Wilson (2009), Absolute calibration of the intramolecular site preference of ^{15}N fractionation in tropospheric N_2O by FT-IR spectroscopy, *Anal. Chem.*, 81(6), 2227–2234.
- Gros, V., C. A. M. Brenninkmeijer, P. Jocke, J. Kaiser, D. Lowry, E. G. Nisbet, P. O'Brien, T. Röckmann, and N. Warwick (2004), Use of isotopes, in *Emissions of Atmospheric Trace Compounds*, *Adv. Global Change Res. Ser.*, vol. 18, edited by C. Granier, P. Artaxo, and C. E. Reeves, pp 375-440, Springer, New York.
- Hirsch, A. I., A. M. Michalak, L. M. Bruhwiler, W. Peters, E. J. Dlugokencky, and P. P. Tans (2006), Inverse modeling estimates of the global nitrous oxide surface flux from 1998–2001, *Global Biogeochem. Cycles*, 20, GB1008.
- Hurst, D. F., *et al.* (2002), Construction of a unified, high-resolution nitrous oxide data set for ER-2 flights during SOLVE, *J. Geophys. Res.*, 105(D15), 19,811-19,822.
- Ishijima, K., S. Sugawara, K. Kawamura, G. Hashida, S. Morimoto, S. Murayama, S. Aoki, T. Nakazawa (2007), Temporal variations of the atmospheric nitrous oxide concentration and its $\delta^{15}\text{N}$ and $\delta^{18}\text{O}$ for the latter half or the 20th century reconstructed from firn air analyses, *J. Geophys. Res.*, 112, D03305, doi:10.1029/2006JD007208.
- Jiang, X, W. L. Ku, R.-L. Shia, Q. Li, J. W. Elkins, R. G. Prinn, Y. L. Yung (2007), Seasonal cycle of N_2O : Analysis of data, *Global Biogeochem. Cycles*, 21, GB1006.
- Johnson, M. S., G. D. Billing, A. Groudis, M. H. M. Janssen (2001), Photolysis of nitrous oxide isotopomers studied by time-dependent Hermite propagation, *J. Phys. Chem. A*, 105, 8672-8680, doi:10.1021/jp011449x.
- Kaiser, J., C. A. M. Brenninkmeijer, and T. Röckmann (2002a) Intramolecular ^{15}N and ^{18}O fractionation in the reaction of N_2O with $\text{O}(^1D)$ and its implications for the stratospheric N_2O isotope signature, *J. Geophys. Res.*, 107(D14), 4214, doi:10.1029/2001JD001506.
- Kaiser, J., T. Röckmann, and C. A. M. Brenninkmeijer (2002b), Temperature dependence of isotope fractionation in N_2O photolysis, *Phys. Chem. Chem. Phys.*, 4, 4420-4430.
- Kaiser, J., T. Röckmann, and C. A. M. Brenninkmeijer (2003), Complete and accurate mass spectrometric isotope analysis of tropospheric nitrous oxide, *J. Geophys. Res.*, 108 (D15), 4476-4492.
- Kaiser, J., S. Park, K. A. Boering, C. A. M. Brenninkmeijer, A. Hilkert, and T. Röckmann (2004), Mass spectrometric method for the absolute calibration of the intramolecular nitrogen isotope distribution in nitrous oxide, *Anal. Bioanal. Chem.*, 378, 256-269.
- Kaiser, J., A. Engel, R. Borchers, and T. Röckmann (2006), Probing stratospheric transport and chemistry with new balloon and aircraft observations of the meridional and vertical N_2O distribution, *Atmos. Chem. Phys.*, 6, 3535-3556.
- Keeling, C. D. (1958), The concentration and isotopic abundances of atmospheric carbon dioxide in rural areas, *Geochim. Cosmochim. Acta*, 13, 322-334.
- Kim, K.-R. and H. Craig (1993), Nitrogen-15 and oxygen-18 characteristics of nitrous oxide: A global perspective, *Science*, 262, 1855-1857.
- MacFarling-Meure, C., D. M. Etheridge, C. M. Trudinger, L. P. Steele, R. L. Langenfelds, T. van Ommen, A. Smith, and J. W. Elkins (2006), Law Dome CO_2 , CH_4 , and N_2O ice core records extended to 2000 years BP, *Geophys. Res. Lett.*, 33, L14810.

- Mahimairaja, S., N. S. Bolan, and M. J. Hedley (1995), Denitrification losses of N from fresh and composted manures, *Soil Bio. Biochem.*, 27(9), 1223-1225.
- Matson, P. A. and P. M. Vitousek (1990), Ecosystem approach to a global nitrous oxide budget, *BioScience*, 40(9), 667-672.
- Minschwaner, K., R. J. Salawitch, and M. B. McElroy (1993), Absorption of solar radiation by O₂: Implications for O₃ and lifetimes of N₂O, CFC₁₃ and CF₂Cl₂, *J. Geophys. Res.*, 98(D6), 10,543-10,561.
- Mote, P. W., K. H. Rosenlof, M. E. McIntyre, E. S. Carr, J. C. Gille, J. R. Holton, J. S. Kinnersley, H. C. Pumphrey, J. M. Russel III, and J. W. Waters (1996), An atmospheric tape recorder: The imprint of tropical tropopause temperatures on stratospheric water vapor, *J. Geophys. Res.*, 101(D2), 3989-4006.
- Nevison, C. D., R. F. Weiss, D. J. Erickson III (1995), Global oceanic emissions of nitrous oxide, *J. Geophys. Res.*, 100(C8), 15,809-15,820.
- Nevison, C. D., R. F. Keeling, R. F. Weiss, B. N. Popp, X. Jin, P. J. Fraser, L. W. Porter, and P. G. Hess (2005), Southern ocean ventilation inferred from seasonal cycles of atmospheric N₂O and O₂/N₂ at Cape Grim, Tasmania, *Tellus*, 57B, 218-229.
- Nevison, C. D., N. M. Mahowald, R. F. Weiss, R. G. Prinn (2007), Interannual and seasonal variability in atmospheric N₂O, *Global Biogeochem. Cycles*, 21, GB3017.
- Ogawa, M., and N. Yoshida (2005a), Intramolecular distribution of stable nitrogen and oxygen isotopes of nitrous oxide emitted during coal combustion, *Chemosphere*, 61, 877-887.
- Ogawa, M., and N. Yoshida (2005b), Nitrous oxide emission from the burning of agricultural residue, *Atmos. Environ.*, 39, 3421-3429.
- Park, S., E. L. Atlas, and K. A. Boering (2004), Measurements of N₂O isotopologues in the stratosphere: Influence of transport on the apparent enrichment factors and the isotopologue fluxes to the troposphere, *J. Geophys. Res.*, 109, D01305.
- Park, S., K. A. Boering, D. M. Etheridge, D. Forretti, K.-R. Kim, R. L. Langenfelds, T. van Ommen, L. P. Steele, and C. M. Trudinger (2005), Trends in the Nitrogen and Oxygen Isotopic Compositions of Tropospheric Nitrous Oxide and Implications for the Global Budget, *Eos Trans.*, 86 (52), Abstract A44B-03.
- Park, S., et al. (2008), Trends, seasonal cycles, and interannual variability in the isotopic composition of nitrous oxide between 1940 and 2008, *Eos Trans.*, 89 (53), Abstract A21A-0125.
- Pataki, D. E., J. R. Ehleringer, L. B. Flannagan, D. Yakir, D. R. Bowling, C. J. Still, N. Buchmann, J. O. Kaplan, and J. A. Berry (2003), The application and interpretation of Keeling plots in terrestrial carbon cycle research, *Global. Biogeochem. Cycles*, 17(1), 1022, doi:10.1029/2001GB001850.
- Pérez, T., S. E. Trumbore, S. C. Tyler, E. A. Davidson, M. Keller, and P. B. de Camargo (2000), Isotopic Variability of N₂O Emissions From Tropical Forest Soils, *Global Biogeochem. Cycles*, 14(2), 525-535.
- Pérez, T., S. E. Trumbore, S. C. Tyler, P. A. Matson, I. Ortiz-Monasterio, T. Rahn, and D. W. T. Griffith (2001), Identifying the agricultural imprint on the global N₂O budget using stable isotopes, *J. Geophys. Res.*, 106(D9), 9869-9878.

- Pérez, T., D. Garcia-Montiel, S. Trumbore, S. Tyler, P. de Camargo, M. Moriera, M. Piccolo, and C. Cerri (2006), Nitrous oxide nitrification and denitrification ^{15}N enrichment factors from Amazon forest soils, *Ecol. Appl.*, *16*(6), 2153-2167.
- Pfister, L., et al. (2001), Aircraft observations of thin cirrus clouds near the tropical tropopause, *J. Geophys. Res.*, *106*(D9), 9765-9786.
- Popp, B. N., et al. (2002), Nitrogen and oxygen isotopomeric constraints on the origins and sea-to-air flux of N_2O in the oligotrophic subtropical North Pacific gyre, *Global Biogeochem. Cycles*, *16* (4), 1064-1073.
- Prather, M. J., and D. J. Jacob (1997), A persistent imbalance in HO_x and NO_x photochemistry of the upper troposphere driven by deep tropical convection, *Geophys. Res. Lett.*, *24*(24), 3189-3192.
- Rahn, T., and M. Wahlen (2000), A reassessment of the global budget of atmospheric nitrous oxide, *Global Biogeochem. Cycles*, *14*(2), 537-543.
- Röckmann, T., and I. Levin (2005), High-precision determination of the changing isotopic composition of atmospheric N_2O from 1990 to 2002, *J. Geophys. Res.*, *110*, D21304.
- Röckmann, T., J. Kaiser, C. A. M. Brenninkmeijer, J. N. Crowley, R. Borchers, W. A. Brand, and P. J. Crutzen (2001), Isotopic enrichment of nitrous oxide ($^{15}\text{N}^{14}\text{NO}$, $^{14}\text{N}^{15}\text{NO}$, $^{14}\text{N}^{14}\text{N}^{18}\text{O}$) in the stratosphere and in the laboratory, *J. Geophys. Res.*, *106*(D10), 10,403-10,410.
- Rosenlof, K. H. (1995), Seasonal cycle of the residual mean meridional circulation in the stratosphere, *J. Geophys. Res.*, *100*(D3), 5173-5191.
- Sachse, G. W., G. F. Hill, L. O. Wade, and M. G. Perry (1987), Fast-response, high precision carbon monoxide sensor using a tunable diode laser absorption technique, *J. Geophys. Res.*, *92*, 2071-2081.
- Sachse, G. W., J. E. Collins, G. F. Hill, L. O. Wade, L. G. Burney, and J. A. Ritter (1991), Airborne tunable diode laser sensor for high precision concentration and flux measurements of carbon monoxide and methane, *Proc. SPIE Int. Opt. Eng.*, *1433*, 145-156.
- Schoeberl, M. R. and Sparling, L. (1995), Trajectory Modeling, in: Diagnostic Tools in Atmospheric Physics, edited by: Fiocco, G. and Visconti, G., Proceedings of the International School of Physics "Enrico Fermi", *124*, 289-306.
- Sowers, T., A. Rodebaugh, N. Yoshida, and S. Toyoda (2002), Extending the records of the isotopic composition of atmospheric N_2O back to 1800 A.D. from firn air trapped in snow at the South Pole and the Greenland Ice Sheet Project II ice core, *Global Biogeochem. Cycles*, *16* (4), 1129-1138.
- Sutka, R. L., N. E. Ostrom, P. H. Ostrom, J. A. Breznak, H. Gandhi, A. J. Pitt, and F. Li (2006), Distinguishing nitrous oxide production from nitrification and denitrification on the basis of isotopomer abundances, *Appl. Environ. Microbio.*, *72*(1), 638-644.
- Toon, O. B., et al. (2010), Planning, implementation and first results of the Tropical Composition, Cloud and Climate Coupling Experiment (TC4), *J. Geophys. Res.*, this special issue.
- Toyoda, S., and N. Yoshida (1999), Determination of nitrogen isotopomers of nitrous oxide on a modified isotope ratio mass spectrometer, *Anal. Chem.*, *71*, 4711-4718.

- Toyoda, S., N. Yoshida, T. Urabe, S. Aoki, T. Nakazawa, S. Sugawara, and H. Honda (2001), Fractionation of N₂O isotopomers in the stratosphere, *J. Geophys. Res.*, *106*(D7), 7515-7522.
- Toyoda, S., N. Yoshida, T. Miwa, Y. Matsui, H. Yamagishi, U. Tsunogai, Y. Niojiri, and N. Tsurushima (2002), Production mechanism and global budget of N₂O inferred from its isotopomers in the western North Pacific, *Geophys. Res. Lett.*, *29*(3), doi: 10.1029/2001GL014311.
- Toyoda, S., H. Mutoke, H. Yamagishi, N. Yoshida, Y. Tanji (2005), Fractionation of N₂O isotopomers during production by denitrifier, *Soil Biol. Biochem.*, *37*, 1535-1545, doi:10.1016/j.soilbio.2005.01.009.
- Toyoda, S., S.-I. Yamamoto, S. Arai, H. Nara, N. Yoshida, K. Kashiwakura, and K.-I. Akiyama (2008), Isotopomeric characterization of N₂O produced, consumed, and emitted by automobiles, *Rapid Commun. Mass Spectrom.*, *22*, 603-312.
- Volk, C. M., et al. (1996), Quantifying transport between the tropical and mid-latitude lower stratosphere, *Science*, *272*, 1763-1768.
- Westley, M. B., B. N. Popp, and T. M. Rust (2007), The calibration of the intramolecular nitrogen isotope distribution in nitrous oxide measured by isotope ratio mass spectrometry, *Rapid Commun. Mass Spectrom.*, *21*, 391-405.
- Yoshida, N. and S. Toyoda (2000), Constraining the atmospheric N₂O budget from intramolecular site preference in N₂O isotopomers, *Nature*, *405*, 330-334.
- Yung, Y.L., and C.E. Miller (1997), Isotopic fractionation of stratospheric nitrous oxide, *Science*, *278*, 1778-1780.

Supplementary figures

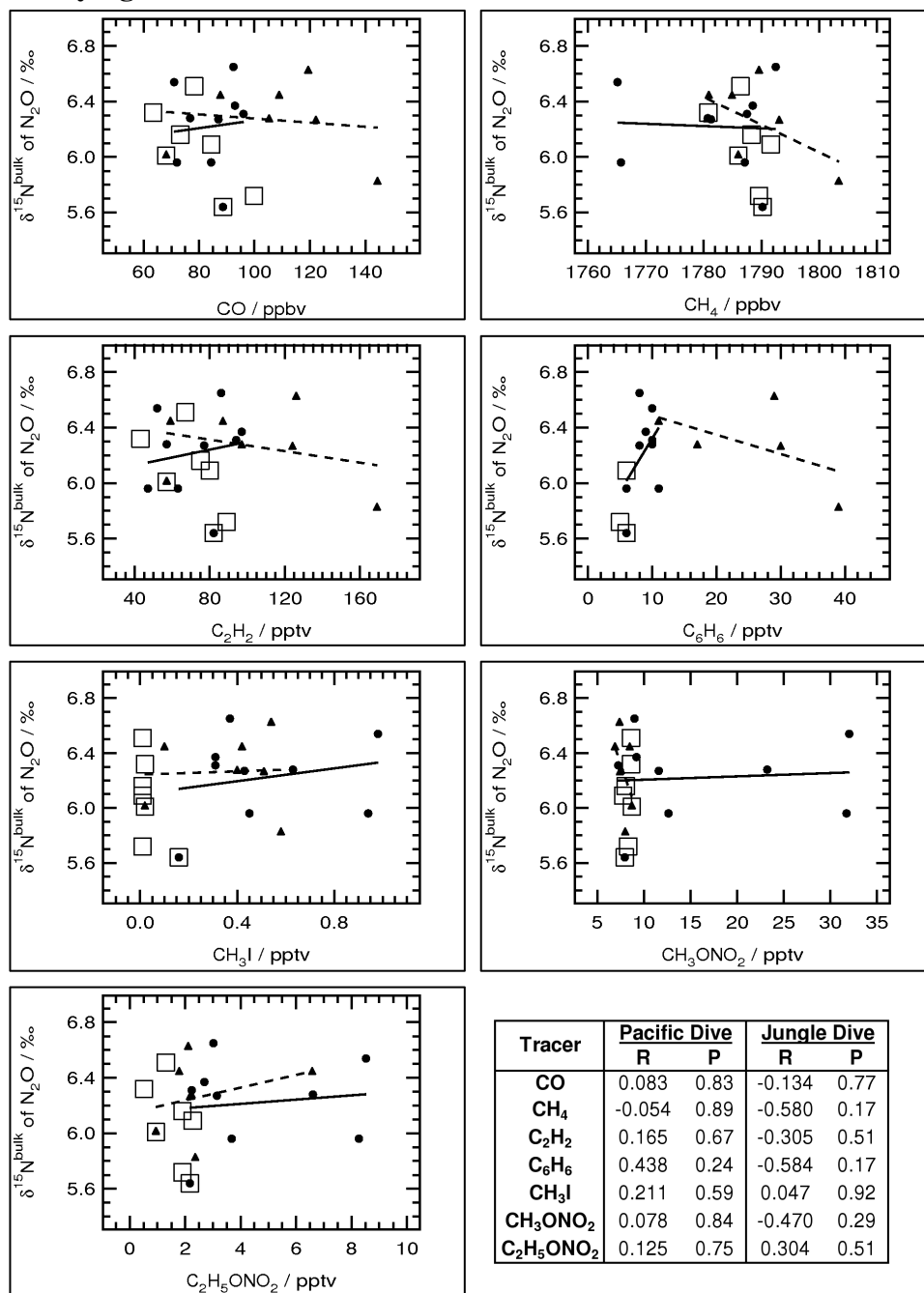


Figure 4.S1. Correlations between $\delta^{15}\text{N}^{\text{bulk}}$ of N_2O versus various tracers for the DC-8 flight segments on 08 August 2007 over the Pacific Ocean (circles, solid regression line) and the Colombian jungle (triangles, dashed regression line). Points for the cruise between the dives are shown without regression lines (squares). Values for the correlation coefficients, R, and the probability, P, that N measurements (i.e., the number of points in the fit) of two uncorrelated variables would give a correlation coefficient as large as R are given in the figure. See the Figure 4.5 caption for additional information; the data are given in Supplementary Tables 4.S3 and 4.S4.

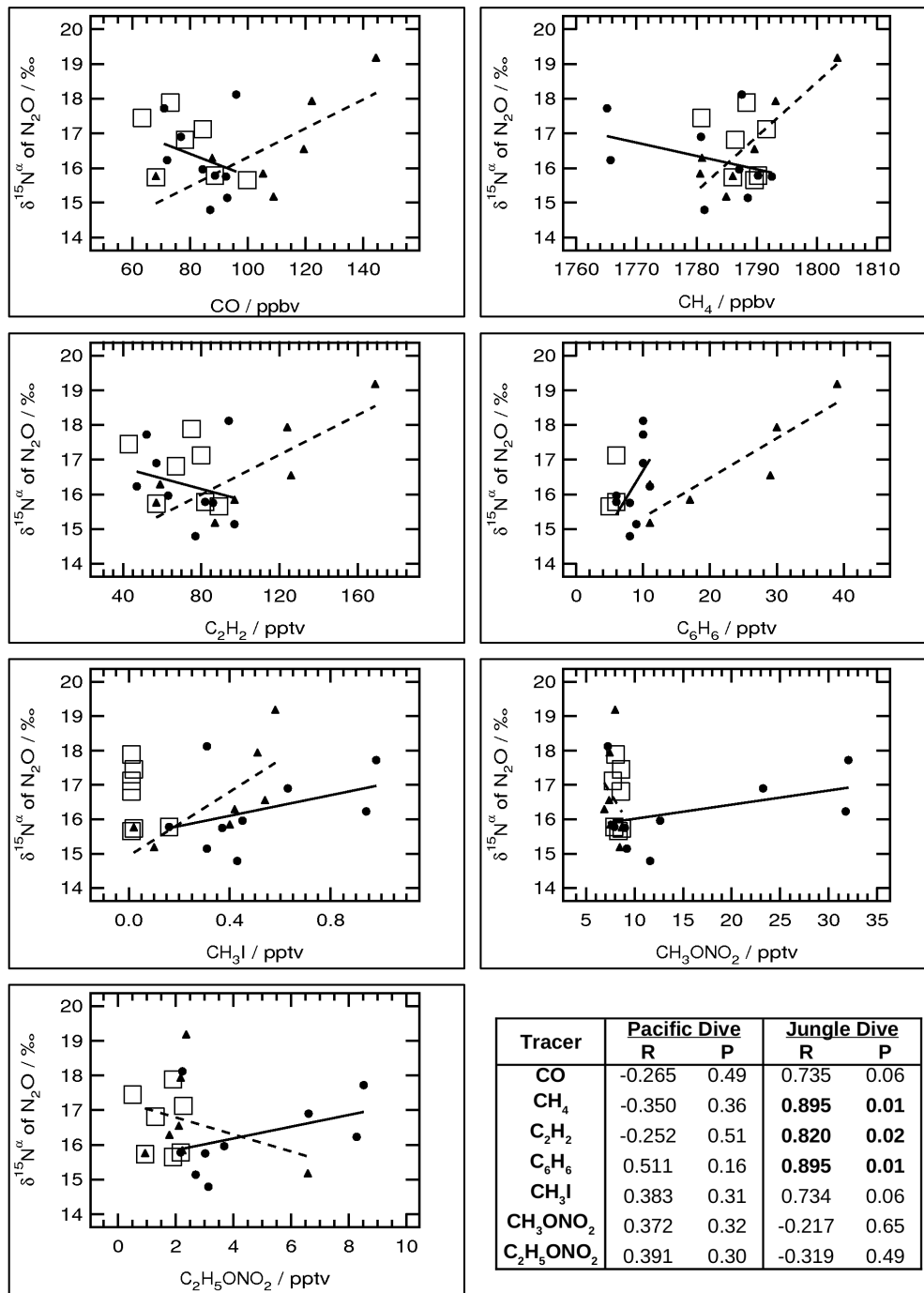


Figure 4.S2. The same as for Figure 4.S1 but for $\delta^{15}\text{N}^\alpha$ of N_2O .

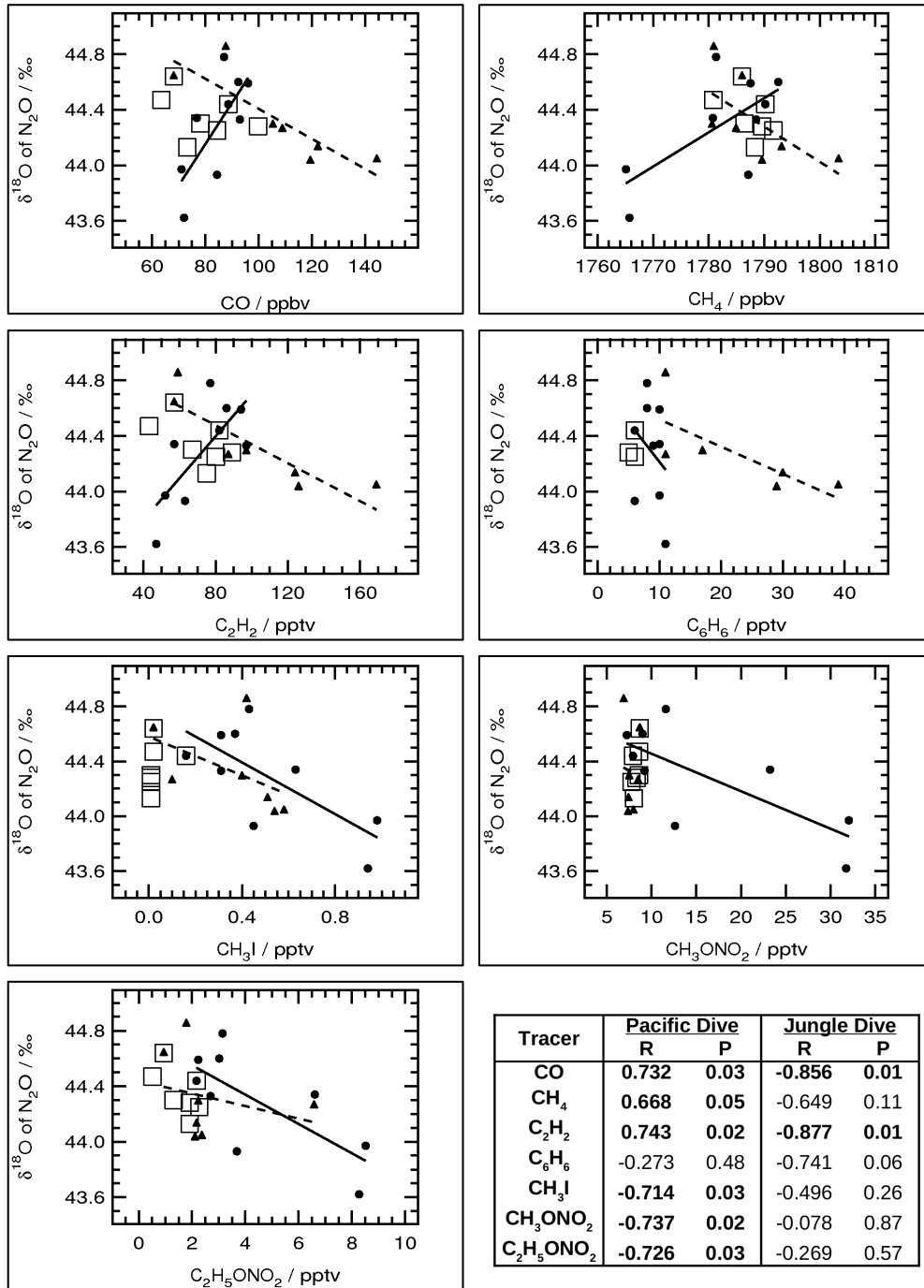


Figure 4.S3. The same as for Figure 4.S1 but for $\delta^{18}\text{O}$ of N_2O .

Supplementary tables

Table 4.S1. N₂O mixing ratio and isotopic composition for the CRAVE WB-57 samples

Flight Date	Time (GMT)	[N ₂ O] (ppb)	$\delta^{15}\text{N}^{\text{bulk}}$ (‰)	$\delta^{18}\text{O}$ (‰)	$\delta^{15}\text{N}^{\alpha}$ (‰)	$\delta^{15}\text{N}^{\beta}$ (‰)	Altitude (km)	Latitude (°N)	Longitude (°W)
20060119	19:18	317.7	6.34	44.13	16.55	-3.68	17.0	-1.1	82.1
20060119	19:22	319.3	6.60	44.25	15.50	-2.10	17.0	-0.8	82.0
20060119	19:23	318.2	6.31	44.68	15.84	-3.02	17.0	-0.7	82.0
20060119	19:27	318.1	6.16	44.81	16.83	-4.34	17.5	-0.3	82.1
20060119	19:30	317.2	6.45	44.53	14.47	-1.33	17.9	0.1	82.1
20060119	19:34	315.8	6.39	44.64	15.76	-2.79	18.2	0.5	82.2
20060119	19:42	315.6	6.46	44.63	15.69	-2.57	18.5	1.3	82.4
20060119	19:49	311.5	6.51	44.10	17.79	-4.61	18.8	2.2	82.5
20060121	17:18	319.1	6.54	44.48	17.48	-4.25	16.9	9.9	81.5
20060121	20:14	312.8	6.72	44.36	16.14	-2.50	19.3	9.9	82.2
20060127	18:01	319.9	5.98	44.09	14.97	-2.81	15.5	4.5	77.6
20060127	18:24	320.4	6.28	44.09	15.85	-3.09	14.7	6.0	79.2
20060127	20:24	319.9	6.11	44.79	15.96	-3.55	8.1	10.0	84.2
20060130	18:04	320.4	6.03	44.63	16.03	-3.79	13.4	8.3	78.3
20060130	19:41	320.0	6.26	44.00	16.43	-3.73	11.9	10.0	84.3
20060130	20:00	318.1	6.33	44.04	15.74	-2.88	2.1	9.9	84.5
20060202	19:54	317.3	6.14	43.99	16.31	-3.85	18.3	3.8	86.0
20060207	17:38	317.0	5.98	43.99	17.08	-4.97	17.8	1.3	81.1
20060207	17:46	318.2	6.27	44.44	16.09	-3.36	17.7	0.4	80.9
20060207	17:53	317.9	6.16	44.24	16.01	-3.51	17.3	-0.3	80.7
20060207	17:56	317.9	6.43	44.14	16.83	-3.79	16.0	-0.6	80.6
20060207	17:59	319.1	6.16	44.39	15.32	-2.79	14.1	-0.8	80.7
20060207	18:02	319.6	6.08	44.39	14.66	-2.30	12.3	-0.6	80.8
20060207	18:05	319.4	5.84	44.45	15.65	-3.78	11.5	-0.3	80.8
20060207	18:08	319.0	6.09	44.31	15.84	-3.48	11.8	0.0	80.9
20060207	18:11	319.3	6.38	44.20	16.13	-3.17	13.4	0.2	80.9
20060207	18:14	319.7	6.47	43.92	14.26	-1.09	14.5	0.6	81.0
20060207	18:18	318.1	6.34	43.52	15.93	-3.05	16.2	1.0	81.0
20060207	18:21	318.3	6.05	43.96	16.26	-3.99	16.8	1.3	81.1
20060207	18:25	317.7	6.08	44.05	15.54	-3.19	17.3	1.7	81.2
20060207	18:28	318.3	6.02	44.11	16.29	-4.07	17.7	2.1	81.3
20060207	18:32	318.0	6.16	44.41	14.36	-1.82	18.1	2.5	81.3
20060207	18:39	317.1	6.31	44.60	16.92	-4.14	18.7	3.3	81.5
20060207	19:01	315.4	6.50	44.59	16.87	-3.70	18.9	5.7	82.2
20060207	20:03	315.5	6.25	44.05	16.10	-3.41	18.0	9.9	84.3
20060209	19:10	321.4	6.01	44.65	15.42	-3.21	13.0	1.9	80.1
20060211	19:53	316.9	6.33	44.78	16.58	-3.73	17.8	21.2	85.9
20060211	19:57	318.6	5.70	43.91	15.38	-3.78	16.5	21.7	86.1
20060211	20:00	319.3	6.29	44.35	15.62	-2.84	14.4	22.0	86.3
20060211	20:03	319.4	6.32	44.38	14.97	-2.10	12.9	22.2	86.4
20060211	20:06	319.4	6.43	44.42	14.83	-1.75	13.3	22.5	86.5
20060211	20:09	319.2	6.10	43.90	16.21	-3.83	14.6	22.7	86.7
20060211	20:19	319.3	6.29	43.71	15.94	-3.16	16.4	23.3	87.5
20060211	20:33	315.3	6.44	44.22	16.31	-3.25	17.8	24.1	88.7
20060211	20:52	304.4	6.15	45.14	15.80	-3.31	18.5	25.4	90.3
20060211	21:11	310.8	6.50	44.69	16.57	-3.40	18.5	26.6	92.0
20060211	21:20	304.1	6.29	44.52	19.52	-6.82	18.6	27.2	92.6
20060211	21:39	301.9	6.76	45.36	18.66	-4.99	18.7	28.7	94.2

Table 4.S2. N₂O mixing ratio and isotopic composition for the TC⁴ WB-57 samples

Flight Date	Time (GMT)	[N ₂ O] (ppb)	$\delta^{15}\text{N}^{\text{bulk}}$ (‰)	$\delta^{18}\text{O}$ (‰)	$\delta^{15}\text{N}^{\alpha}$ (‰)	$\delta^{15}\text{N}^{\beta}$ (‰)	Altitude (km)	Latitude (°N)	Longitude (°W)
20070803	15:51	309.4	6.93	43.97	17.07	-3.03	18.3	10.0	84.2
20070803	15:53	312.2	6.86	43.86	16.93	-3.04	17.7	9.9	84.1
20070803	15:55	319.0	6.06	44.69	15.57	-3.24	16.2	10.0	84.0
20070803	15:56	319.9	5.74	43.79	15.99	-4.33	15.2	10.1	84.2
20070803	16:01	321.3	5.88	43.60	15.40	-3.45	13.4	9.9	84.2
20070805	15:11	320.8	6.32	44.43	16.19	-3.36	13.6	6.2	80.7
20070805	15:20	320.6	6.22	43.90	16.27	-3.65	14.0	6.4	81.3
20070805	15:23	321.5	5.98	43.55	15.55	-3.40	14.0	6.4	81.1
20070805	15:28	321.4	6.02	43.82	12.98	-0.69	14.0	6.5	80.7
20070805	15:33	320.8	6.32	45.09	18.31	-5.54	14.0	6.5	80.2
20070805	15:47	321.0	6.50	43.96	15.82	-2.62	14.6	6.2	80.4
20070805	15:52	320.9	5.79	44.01	15.13	-3.36	14.7	6.2	81.0
20070805	15:54	320.5	5.87	44.20	17.23	-5.34	15.4	6.2	81.2
20070805	15:56	320.1	6.14	44.58	17.60	-5.18	15.9	6.4	81.4
20070805	15:58	320.2	6.22	43.69	17.56	-4.96	16.3	6.5	81.3
20070805	16:03	319.7	6.16	43.96	16.35	-3.86	16.9	6.3	81.4
20070805	16:09	318.6	6.28	44.41	16.43	-3.68	17.4	6.9	81.7
20070805	16:15	314.8	6.15	44.54	16.41	-3.94	17.8	7.4	82.1
20070805	16:20	311.4	6.17	44.64	15.82	-3.28	18.1	8.0	82.5
20070805	16:35	320.4	6.51	44.41	16.77	-3.58	16.2	9.3	83.5
20070805	16:37	320.7	6.38	44.32	17.84	-4.92	14.9	9.5	83.8
20070805	16:40	320.7	6.28	44.64	13.41	-0.60	13.9	9.6	84.0
20070805	16:43	320.2	5.98	44.36	14.54	-2.36	12.6	9.8	84.2
20070805	16:45	321.1	6.32	44.13	17.19	-4.40	10.2	10.0	84.3
20070806	14:22	315.7	6.86	44.35	15.79	-1.88	17.2	4.5	90.7
20070806	14:27	319.7	5.85	43.56	17.03	-5.18	16.2	4.1	91.1
20070806	14:30	319.9	6.33	44.46	16.16	-3.31	15.8	3.9	91.4
20070806	14:35	319.9	5.74	44.14	15.32	-3.65	16.8	3.5	91.8
20070806	14:40	317.3	6.12	43.97	16.72	-4.30	17.2	3.1	92.2
20070806	14:47	320.6	5.86	44.08	17.59	-5.72	15.8	2.6	91.9
20070806	14:52	320.6	6.45	44.23	17.30	-4.24	14.8	2.3	91.5
20070806	14:56	320.9	6.35	45.06	14.71	-1.79	13.9	2.0	91.1
20070806	14:57	320.9	6.35	44.19	15.54	-2.64	13.7	2.0	91.1
20070806	15:02	320.8	6.38	44.37	16.36	-3.43	14.8	2.1	90.7
20070808	13:37	320.4	5.94	44.56	15.76	-3.70	12.7	5.9	82.4
20070808	13:41	320.4	6.45	44.21	16.29	-3.21	12.1	6.2	82.7
20070808	14:24	320.9	6.03	44.63	16.46	-4.24	11.5	6.7	83.8
20070808	14:28	320.6	6.23	44.45	14.84	-2.15	11.5	6.7	84.2
20070808	14:32	320.9	5.98	44.23	16.12	-3.97	11.7	6.9	84.4
20070809	15:16	315.1	6.50	44.76	17.15	-4.00	16.5	22.0	90.3
20070809	15:23	320.1	5.84	43.68	16.03	-3.32	14.3	22.7	90.7
20070809	15:31	319.1	6.32	44.53	16.07	-3.24	15.8	23.5	91.2
20070809	15:36	314.2	6.11	44.64	16.13	-3.82	16.7	24.0	91.5
20070809	15:51	309.7	6.39	44.26	16.19	-3.46	17.5	25.5	92.4
20070809	16:02	302.4	6.72	45.15	18.35	-4.45	18.3	26.6	93.1
20070809	16:08	295.8	6.54	44.88	14.50	-1.25	18.7	27.2	93.5
20070809	16:13	296.3	7.46	45.16	17.64	-2.80	19.1	27.7	93.8
20070809	16:15	298.7	7.08	45.09	17.97	-3.95	18.6	27.9	93.9
20070809	16:42	317.7	6.50	44.04	18.30	-5.17	1.9	29.4	94.9

Table 4.S3. N₂O isotopic composition for the TC⁴ DC-8 samples

Flight Date	Time (GMT)	$\delta^{15}\text{N}^{\text{bulk}}$ (‰)	$\delta^{18}\text{O}$ (‰)	$\delta^{15}\text{N}^{\alpha}$ (‰)	$\delta^{15}\text{N}^{\beta}$ (‰)	Altitude (km)	Latitude (°N)	Longitude (°W)
20070805	16:26	6.58	43.76	16.38	-3.02	11.3	6.3	78.5
20070805	16:34	6.00	44.54	16.53	-4.36	9.2	5.7	78.1
20070805	16:39	6.38	44.58	17.74	-4.83	7.8	5.6	77.9
20070805	16:42	6.05	44.42	14.34	-2.02	6.2	5.7	78.1
20070805	16:47	6.21	44.16	16.21	-3.61	4.2	5.5	78.0
20070805	16:53	5.84	44.57	15.81	-3.96	1.5	5.7	78.1
20070805	16:57	6.27	43.64	14.63	-1.88	0.3	5.7	77.9
20070808	16:25	5.96	43.62	16.23	-4.14	0.5	5.2	83.1
20070808	16:31	6.54	43.97	17.72	-4.49	0.5	5.1	82.7
20070808	16:39	6.28	44.34	16.90	-4.17	1.4	5.0	82.1
20070808	16:44	5.96	43.93	15.96	-3.87	2.9	5.0	81.7
20070808	16:48	6.65	44.60	15.75	-2.25	4.7	5.0	81.3
20070808	16:51	6.31	44.59	18.12	-5.35	6.0	5.0	81.0
20070808	16:56	6.27	44.78	14.79	-2.03	7.8	4.6	80.6
20070808	16:59	6.37	44.33	15.14	-2.19	9.2	4.4	80.3
20070808	17:13	5.64	44.44	15.78	-4.32	11.6	4.3	79.1
20070808	17:33	6.09	44.25	17.12	-4.79	11.6	4.9	77.0
20070808	17:43	6.16	44.13	17.89	-5.42	11.6	4.8	75.8
20070808	17:53	5.72	44.28	15.65	-4.02	11.6	4.8	74.8
20070808	18:03	6.51	44.30	16.81	-3.61	11.6	4.2	73.8
20070808	18:13	6.32	44.47	17.45	-4.65	11.6	3.5	72.9
20070808	18:23	6.01	44.64	15.73	-3.53	11.6	3.0	71.9
20070808	18:29	6.44	44.26	15.15	-2.07	10.4	2.7	71.3
20070808	18:31	6.27	44.29	15.81	-3.07	9.3	2.5	71.1
20070808	18:36	6.44	44.85	16.26	-3.18	6.1	2.2	70.8
20070808	18:38	6.26	44.13	17.90	-5.23	4.4	2.0	70.7
20070808	18:40	6.62	44.03	16.52	-3.09	2.4	1.8	70.5
20070808	18:42	5.82	44.04	19.15	-7.41	1.5	1.6	70.5

Table 4.S4. TC⁴ DC-8 mixing ratio data

Flight Date	Time (GMT)	C ₂ H ₂ (pptv)	C ₆ H ₆ (pptv)	CH ₃ I (pptv)	CH ₃ ONO ₂ (pptv)	C ₂ H ₅ ONO ₂ (pptv)	CO* (ppbv)	CH ₄ * (ppbv)
20070805	16:26	144	28	0.26	8.06	5.74	109.3	1806.3
20070805	16:34	177	38	0.22	7.17	4.92	117.8	1805.6
20070805	16:39	71	12	0.26	6.14	2.05	89.2	1787.9
20070805	16:42	60	7	0.16	6.09	1.84	84.0	1773.6
20070805	16:47	106	20	0.46	6.9	2.08	111.5	1795.6
20070805	16:53	124	21	0.6	9.74	3.87	109.2	1801.7
20070805	16:57	120	22	0.66	12.77	4.41	105.0	1800.8
20070808	16:25	47	11	0.94	31.74	8.27	72.0	1765.7
20070808	16:31	52	10	0.98	32.03	8.52	71.0	1765.1
20070808	16:39	57	10	0.63	23.23	6.61	76.8	1780.7
20070808	16:44	63	6	0.45	12.63	3.68	84.4	1787.1
20070808	16:48	86	8	0.37	9.00	3.02	92.4	1792.5
20070808	16:51	94	10	0.31	7.24	2.23	96.0	1787.5
20070808	16:56	77	8	0.43	11.60	3.14	87.0	1781.3
20070808	16:59	97	9	0.31	9.21	2.69	92.9	1788.5
20070808	17:13	82	6	0.16	7.93	2.17	88.6	1790.2
20070808	17:33	80	6	0.01	7.77	2.27	84.4	1791.6
20070808	17:43	75	-	0.01	8.04	1.90	73.2	1788.3
20070808	17:53	89	5	0.01	8.33	1.90	99.8	1789.6
20070808	18:03	67	-	0.01	8.60	1.30	78.2	1786.4
20070808	18:13	43	-	0.02	8.62	0.51	63.4	1780.8
20070808	18:23	57	-	0.02	8.69	0.94	68.1	1786.0
20070808	18:29	87	11	0.10	8.49	6.58	108.9	1784.9
20070808	18:31	97	17	0.40	7.53	2.23	105.3	1780.6
20070808	18:36	59	11	0.42	6.90	1.78	87.7	1780.9
20070808	18:38	124	30	0.51	7.44	2.17	122.2	1793.1
20070808	18:40	126	29	0.54	7.39	2.11	119.4	1789.6
20070808	18:42	169	39	0.58	8.00	2.36	144.4	1803.4

* Mixing ratios are the average of the *in situ* measurements of CO and CH₄ over the DC-8 canister filling times.

The isotopic composition of nitrous oxide over the ocean on a cruise between South Africa and Chile

Abstract

Measurements of the isotopic composition of N₂O were made on air samples collected in the marine boundary layer on the French research ship, Marion Dufresne, during a cruise between South Africa and Chile conducted as part of the "Organics over the Ocean Modifying Particles in both Hemispheres" (OOMPH) campaign between January and March, 2007. The dataset includes 50 measurements of $\delta^{15}\text{N}^{\text{bulk}}$ and $\delta^{18}\text{O}$ and 8 measurements of $\delta^{15}\text{N}^{\alpha}$ and $\delta^{15}\text{N}^{\beta}$. In general, the samples show little variation in either N₂O mixing ratio or isotopic compositions, with an average N₂O mixing ratio of 319.5 ± 0.7 ppbv, $\delta^{15}\text{N}^{\text{bulk}}$ value of $6.0 \pm 0.2\text{‰}$, $\delta^{15}\text{N}^{\alpha}$ of $14.9 \pm 0.8\text{‰}$, $\delta^{15}\text{N}^{\beta}$ of $-2.5 \pm 0.9\text{‰}$, and $\delta^{18}\text{O}$ of $43.8 \pm 0.2\text{‰}$. These means are similar to their tropospheric averages and the standard deviations are similar to the measurement precision. However, four samples had anomalously high N₂O mixing ratios, ranging from 323 to 344 ppbv. The N₂O in these samples was isotopically light in ¹⁵N and ¹⁸O, ranging from 4.9 to 6.0‰ for $\delta^{15}\text{N}^{\text{bulk}}$ and 42.6 to 43.9‰ for $\delta^{18}\text{O}$, and negatively correlated with the N₂O mixing ratio. Furthermore, the measured site-specific isotopic compositions were low in $\delta^{15}\text{N}^{\alpha}$ and high in $\delta^{15}\text{N}^{\beta}$ for these samples relative to the average. These results suggest that N₂O emitted from the Southern Ocean may be depleted in ¹⁸O and in ¹⁵N at the α -nitrogen position and averaged over the two positions while slightly enriched in ¹⁵N at the β -nitrogen, relative to the tropospheric background. This pattern of enrichments and depletions is similar to that of N₂O produced, most likely, by nitrification and/or nitrifier denitrification in the shallow waters of the oligotrophic subtropical North Pacific gyre reported by Popp *et al.* [2002], suggesting that N₂O in the South Atlantic may be produced by the same mechanism(s). The results demonstrate that, even with enhancements in the tropospheric N₂O mixing ratio as small as 1 – 8% (relative to a ~320 ppb background), the isotopic composition of the source of N₂O causing the enhancement can be measurably perturbed, and may thus provide a means for estimating the isotopic composition of the N₂O source from the Southern Ocean – an important uncertainty in the global isotopic budget of N₂O.

5.1. Introduction

N₂O is produced and consumed in the ocean by the microbial processes of nitrification and denitrification [e.g. Craig and Gordon, 1963; Kim and Craig, 1990]. Previous work has demonstrated that the isotopic composition of nitrous oxide dissolved in ocean water is a useful tool for estimating the relative amounts of nitrification and denitrification, as well as consumption, during denitrification [e.g. Kim and Craig, 1990; Popp *et al.*, 2002; Toyoda *et al.*, 2002; Charpentier *et al.*, 2007; Yamagishi *et al.*, 2007]. In addition to constraining the production mechanisms of N₂O in the ocean, several studies of the isotopic composition of dissolved N₂O in the ocean have also sought to determine the isotopic composition of N₂O emitted from the ocean to the atmosphere [e.g., Popp *et al.*, 2002; Toyoda *et al.*, 2002]. The latter is an important factor needed to balance the isotope budget of N₂O and ultimately to enable measurements of N₂O isotopic variations in the atmosphere to be used to constrain the

locations, identities, and magnitudes of N₂O sources. Indeed, N₂O isotope measurements may be an important addition to inverse modeling efforts to verify compliance with international treaties on greenhouse gas emissions, such as the Kyoto Protocol, for example, since inverse models based solely on N₂O mixing ratio measurements remain underconstrained [Hirsch *et al.*, 2006; Huang *et al.*, 2008; D'Amelio *et al.*, 2009], in part because the spatial and temporal variations in N₂O mixing ratio in the troposphere are small compared to the background. Yet few measurements of the isotopic composition of N₂O emitted by the oceans that would be needed for such analyses are currently available.

In particular, the isotopic composition of N₂O emitted by the Southern Ocean, defined as all regions of the ocean south of 30°S, is largely unknown; only two studies have been published, one set of measurements on a cruise in the Sub-Antarctic Zone between 42 and 54°S at 142–143°E [Nevison *et al.*, 2005] and one study with sampling locations in the eastern South Pacific at 31.90°S, 91.41°W and at 34.58°S and 72.43°W, with the former on the eastern edge of the subtropical South Pacific gyre and the latter in a coastal upwelling zone about 33km from the shore [Charpentier *et al.*, 2007]. At the same time, the magnitude of the N₂O source emitted from the Southern Ocean is also highly uncertain, with recent estimates ranging from as little as one-tenth to as much as one-third of the total global ocean source based on measurements of the global distribution of atmospheric N₂O and the N₂O surface anomaly (i.e., the difference between the measured partial pressure of N₂O in surface water and the atmospheric equilibrium partial pressure) [Nevison *et al.*, 1995; Nevison *et al.*, 2003]. Measuring the isotopic composition of N₂O over regions of the Southern Ocean may thus provide a useful means to reduce uncertainties in the magnitude of the source of N₂O from the Southern Ocean, and hence in the current understanding of the global N₂O budget and its isotopologues.

To these ends, the isotopic composition of N₂O was measured in 50 samples collected over the open ocean on a cruise between southern Africa and southern South America as part of the "Organics over the Ocean Modifying Particles in both Hemispheres" (OOMPH) campaign between January and March 2007. The goal was to provide new constraints on the isotopic composition of N₂O emitted from the Southern Ocean, including whether measurements of surface air over large regions of phytoplankton blooms in the South Atlantic Ocean that occur during austral summer [e.g. Bathmann *et al.*, 1997] and which may be sources of N₂O [e.g. Law and Ling, 2001] might provide additional quantitative information on the Southern Ocean source. The sampling campaign and measurement procedure are described in section 5.2, the results are discussed in section 5.3, and the conclusions are summarized in section 5.4.

5.2. Methods

A research cruise aboard the French research ship Marion Dufresne was carried out between South Africa and Tierra del Fuego, Chile from January through March 2007 as part of the OOMPH campaign (see, e.g., www.atmosphere.mpg.de/enid/oomph, accessed 23 April 2010). The ship track is shown in Figure 5.1. During a portion of the cruise between January 31 and February 4, the vessel passed through a region of significant phytoplankton, as determined by a dip in the CO₂ mixing ratio measured *in situ*, which is caused by the enhanced uptake of CO₂ for photosynthesis by the phytoplankton. As shown in Figure 5.1, the cruise was divided into two legs; the first was from South Africa to Chile and occurred

between January 21 and February 5, and the second was from Chile to South Africa and occurred between March 1 and March 20.

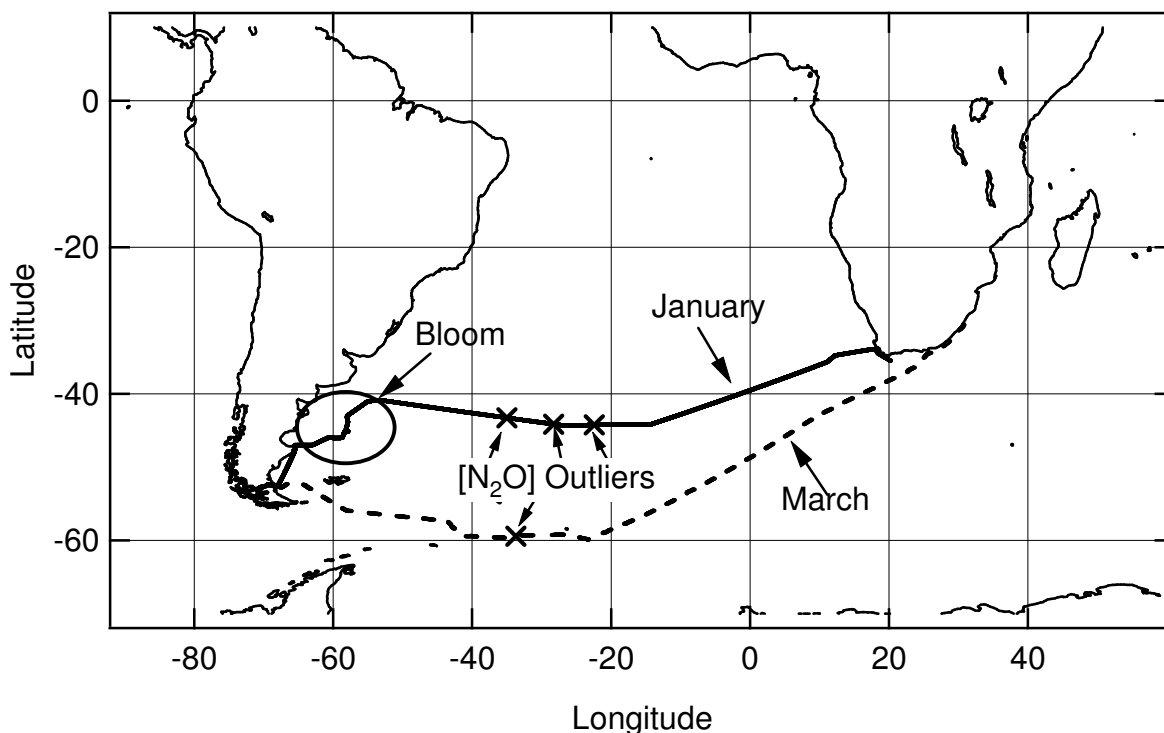


Figure 5.1. Ship track for the Marion Dufresne. The first leg of the cruise, from South Africa to Chile (solid line) was from January 20 to February 5, 2007. The second leg, from Chile to South Africa (dashed line) was from March 1 to March 20, 2007. Sampling locations for N_2O mixing ratio outliers are shown (exes). Also indicated is the approximate location where the ship encountered phytoplankton blooms between January 31 and February 3, 2007.

During each leg of the cruise, air samples were collected by pressurizing evacuated 2.3-L electropolished stainless steel canisters to ~3 bar using a metal bellows pump on the whole air sampler (WAS); air was sampled at an inlet at the top of the foremast (18 m above sea level) through 75 m of 1.27 cm outer diameter Teflon tubing [Williams *et al.*, 2010]. The mixing ratios of a number of trace gases, including hydrocarbons, alkyl nitrates, halogenated hydrocarbons, and N_2O , were measured in these samples by GC-FID, GC-ECD, and GC-MS at the University of Miami [Flocke *et al.*, 1999]. The accuracy of the N_2O mixing ratio measurements in this work is limited by the fact that the samples were not dried prior to measurement. A constant correction of 1.2% was applied to the wet measurements to make the average of “normal” samples match the AGAGE N_2O data from Cape Grim, Tasmania. For the analyses presented here, sensitivities to this correction were performed and are discussed as needed in the results section.

A number of criteria were used to select samples for which the N_2O isotopic composition was measured. First, most of the samples selected were collected during the first leg of the cruise since, based on tracer measurements and wind trajectory analyses, many of the samples collected during the second leg of the cruise were contaminated with emissions

from the ship [Williams *et al.*, 2010]. Second, samples with high mixing ratios of tracers of marine influence, such as CH₃I, CH₃ONO₂, and C₂H₅ONO₂ were selected, since samples with tracer mixing ratios such as these, collected over the tropical Pacific Ocean, had shown significant correlations with the measured N₂O isotopic composition (see Chapter 4). Third, samples were also selected to achieve good coverage of the entire first leg of the cruise. Fourth, four samples had high measured values of the N₂O mixing ratio (with the outlier samples determined by iterative implementation of Chauvenet’s criterion [Taylor, 1997]); these samples were selected for measurement with the goal of investigating the source of the mixing ratio enhancement.

The isotope measurements were made using the Continuous Flow Isotope Ratio Mass Spectrometry with on-line PreConcentration and Gas Chromatography (CF-PreCon-GC-IRMS) technique discussed in Chapter 2. Here, only the OOMPH sample handling procedures and a brief overview of the CF-PreCon-GC-IRMS technique are discussed. Samples were transferred directly from the WAS canisters to double-valved 100-mL measurement flasks. The flask pressure was determined using an absolute pressure transducer either by direct measurement or by expansion into a calibrated volume of the vacuum line after the sample had been isolated. The flasks were then placed directly on the PreCon for the isotope ratio measurements. Because the pressure in the measurement flasks was significantly above atmospheric pressure, the freeze time for the samples was increased to 2700 seconds to allow all of the N₂O in the sample to be trapped and all of the N₂ and O₂ to be vented. Other than this difference, the measurements were made as described in Chapter 2.

N₂O isotopic compositions are reported here as δ -values in “per mil” (‰), which is the part per thousand difference of the isotope ratio of the sample relative to a standard: $\delta = 1000 \cdot (R/R_{\text{standard}} - 1)$, where $R = {}^{15}\text{N}/{}^{14}\text{N}$ or ${}^{18}\text{O}/{}^{16}\text{O}$ and the subscript ‘standard’ refers to an international reference material, which is air-N₂ for $\delta^{15}\text{N}$ and Vienna Standard Mean Ocean Water (VSMOW) for $\delta^{18}\text{O}$. Two types of nitrogen isotopic compositions are reported: (1) $\delta^{15}\text{N}^{\text{bulk}}$, which is the ${}^{15}\text{N}$ isotopic composition averaged over the two nitrogen atom sites in N₂O, and (2) $\delta^{15}\text{N}^{\alpha}$ and $\delta^{15}\text{N}^{\beta}$, which represent the “site-specific” isotopic compositions – i.e., the ${}^{15}\text{N}$ isotopic composition at the central nitrogen atom (the “ α ” site) and the ${}^{15}\text{N}$ isotopic composition at the terminal nitrogen atom (the “ β ” site), respectively. In addition, the ‘Site Preference’ (SP) of the α -position relative to the β -position ($\text{SP} = {}^{15}\text{R}^{\alpha}/{}^{15}\text{R}^{\beta} - 1$) is reported, a form of the site-specific isotopic composition that is now frequently used, particularly in ecological studies in which it may be useful in discriminating between different production mechanisms [e.g. Bol *et al.*, 2003; Sutka *et al.*, 2006; Pérez *et al.*, 2006; Charpentier *et al.*, 2007].

Two aliquots are required to determine the site-specific isotopic composition of N₂O using the MAT-252 IRMS, one for $\delta^{15}\text{N}^{\text{bulk}}$ and $\delta^{18}\text{O}$, and a second for $\delta^{15}\text{N}^{\alpha}$ and $\delta^{15}\text{N}^{\beta}$. To determine $\delta^{15}\text{N}^{\text{bulk}}$ and $\delta^{18}\text{O}$ values, m/z 44, 45, and 46 (which correspond to isotopologues of N₂O⁺) are measured and compared with a standard for the first aliquot. To determine $\delta^{15}\text{N}^{\alpha}$, the NO⁺ fragment ion at m/z 30 and 31 is measured and compared with a standard for the second aliquot and the degree of ‘scrambling’ – i.e., the fraction of NO⁺ in the sample that included the β N-atom – is taken into account. The measured values for $\delta^{15}\text{N}^{\text{bulk}}$ and $\delta^{15}\text{N}^{\alpha}$ are then used to calculate $\delta^{15}\text{N}^{\beta}$, which in turn is combined with $\delta^{15}\text{N}^{\alpha}$ to calculate SP. Because the $\delta^{15}\text{N}^{\alpha}$ and $\delta^{15}\text{N}^{\beta}$ values of the working reference standard used in this work are not accurately calibrated to the air-N₂ scale [Griffith *et al.*, 2009], in order to report $\delta^{15}\text{N}^{\alpha}$ and

$\delta^{15}\text{N}^{\beta}$ relative to air- N_2 , tropospheric N_2O is used as a ‘transfer standard’ assuming for tropospheric N_2O a SP value of 18.7‰ [Yoshida and Toyoda, 2000] and a $\delta^{15}\text{N}^{\text{bulk}}$ value of 6.2‰, based on measurements of air collected on the UC Berkeley campus between September 2001 and November 2006.

The precision of the measurements based on their m/z 44 and 31 peak areas was ~0.13‰ for $\delta^{15}\text{N}^{\text{bulk}}$, ~0.20‰ for $\delta^{18}\text{O}$, and ~0.57‰ for $\delta^{15}\text{N}^{\alpha}$, as explained in Park [2005]. This precision was also confirmed by repeated measurement (N=4) of the one sample, yielding 0.13‰, 0.19‰, and 0.54‰, respectively. The precision enhancement relative to sample measurements discussed in Chapters 3 and 4 is due to the larger total amount of N_2O in these samples of ~3–3.6 nmol. Fifty total samples were measured for $\delta^{15}\text{N}^{\text{bulk}}$ and $\delta^{18}\text{O}$ — 42 of them once and 8 of them in quadruplicate, including the four samples designated as outliers with respect to their measured N_2O mixing ratio to achieve even higher precision. These four samples, as well four others (chosen essentially randomly), were also measured for the site-specific nitrogen isotopic composition, $\delta^{15}\text{N}^{\alpha}$ and $\delta^{15}\text{N}^{\beta}$, in quadruplicate.

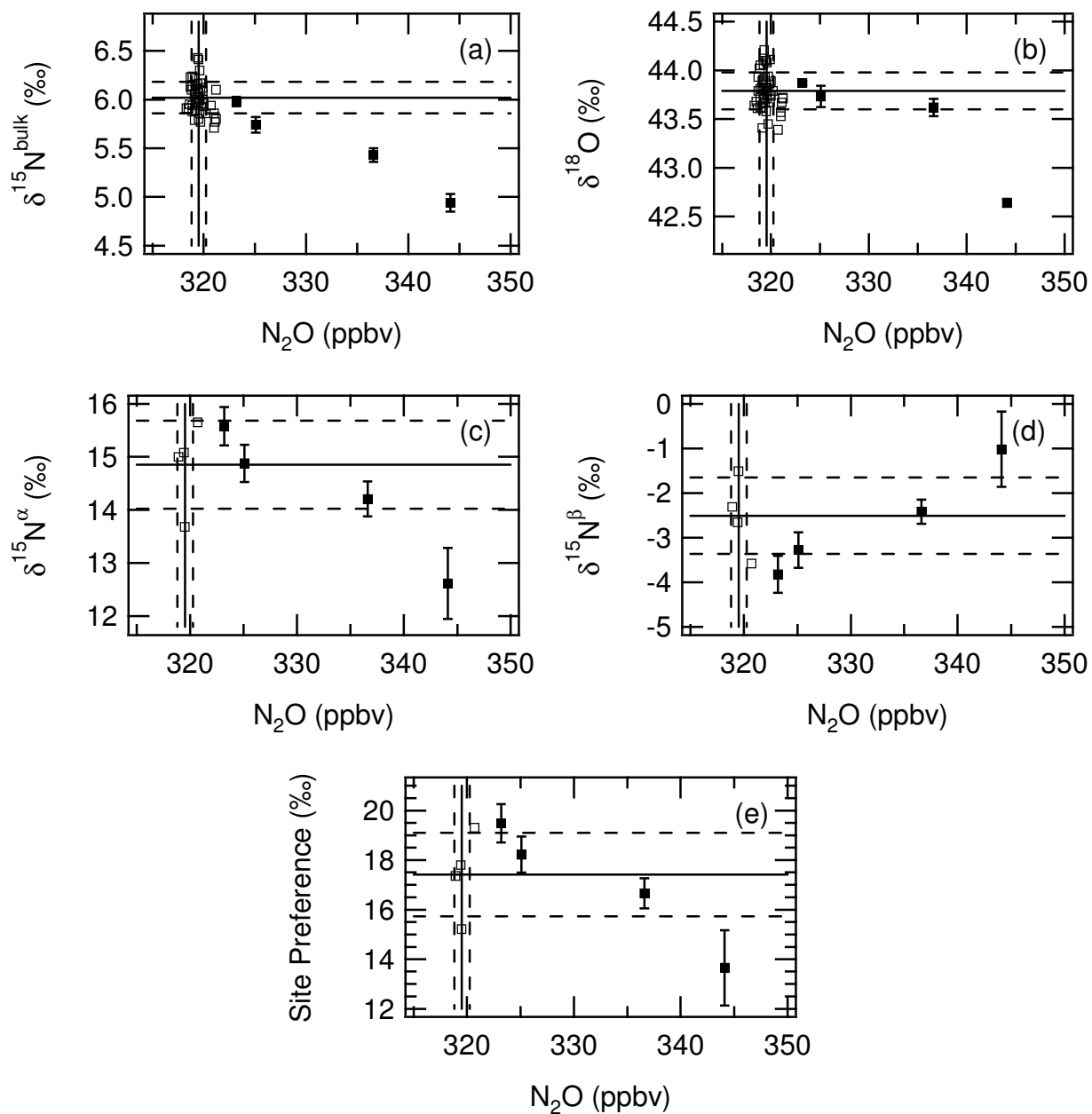


Figure 5.2. Nitrous oxide isotopic composition as a function of mixing ratio for (a) $\delta^{15}\text{N}^{\text{bulk}}$, (b) $\delta^{18}\text{O}$, (c) $\delta^{15}\text{N}^{\alpha}$, (d) $\delta^{15}\text{N}^{\beta}$, and (e) Site Preference. Solid lines represent the mean of all samples excluding the 4 with outlying N₂O mixing ratios outliers and the dashed lines are the corresponding standard deviations.

Table 5.1. N₂O mixing ratios and isotopic compositions for samples collected during the OOMPH campaign. N₂O mixing ratios were measured on wet samples and corrected by 1.2% to determine the dry mixing ratio shown here. The samples in bold are the N₂O mixing ratio outliers discussed in section 5.3.

Collection Date	Collection Time (GMT)	N ₂ O (ppb)	$\delta^{15}\text{N}^{\text{bulk}}$ (‰)	$\delta^{15}\text{N}^{\alpha}$ (‰)	$\delta^{15}\text{N}^{\beta}$ (‰)	$\delta^{18}\text{O}$ (‰)	Lat. (°)	Lon. (°)
20070121	14:10	319.1	6.22	-	-	43.89	-36.88	7.63
20070121	18:35	320.2	5.86	-	-	43.79	-37.26	6.56
20070121	22:28	319.6	5.99	-	-	43.82	-37.58	5.63
20070122	05:26	319.7	5.77	-	-	43.45	-38.14	4.02
20070122	11:18	319.1	5.79	-	-	43.82	-38.64	2.58
20070122	17:17	319.7	6.10	-	-	43.94	-39.13	1.11
20070122	23:39	319.2	5.97	-	-	43.91	-39.71	-0.58
20070123	05:26	320	5.96	-	-	43.74	-40.22	-2.11
20070123	17:30	319.3	5.96	-	-	43.71	-41.20	-5.05
20070123	23:14	318.7	6.23	-	-	43.79	-41.67	-6.49
20070124	06:26	319.2	6.11	-	-	44.06	-42.24	-8.24
20070124	11:57	319.4	6.02	-	-	43.67	-42.69	-9.62
20070124	19:13	319.4	6.11	15.08	-2.66	43.82	-43.30	-11.53
20070125	13:20	321.1	5.77	-	-	43.67	-44.15	-14.23
20070126	07:50	318.7	6.13	-	-	43.93	-44.20	-18.52
20070127	01:26	336.6	5.43	14.21	-2.42	43.62	-44.24	-22.40
20070127	13:13	321.0	5.86	-	-	43.57	-44.28	-24.86
20070128	01:00	325.1	5.74	14.88	-3.28	43.73	-44.14	-28.25
20070129	02:15	344.1	4.94	12.62	-1.02	42.64	-43.27	-34.99
20070130	02:50	318.9	6.24	15.00	-2.31	43.81	-42.37	-41.89
20070130	08:36	319.2	5.89	-	-	43.76	-42.15	-43.59
20070130	15:46	318.3	5.91	-	-	43.64	-41.87	-45.70
20070131	01:48	319.5	6.07	-	-	43.58	-41.48	-48.64
20070131	09:40	318.6	5.95	-	-	43.61	-41.19	-50.83
20070131	12:25	318.9	5.94	-	-	43.72	-41.08	-51.62

Table 5.1. continued

Collection Date	Collection Time (GMT)	N ₂ O (ppb)	$\delta^{15}\text{N}^{\text{bulk}}$ (‰)	$\delta^{15}\text{N}^{\alpha}$ (‰)	$\delta^{15}\text{N}^{\beta}$ (‰)	$\delta^{18}\text{O}$ (‰)	Lat. (°)	Lon. (°)
20070131	18:13	319.5	5.80	-	-	44.10	-40.95	-53.66
20070131	20:17	319.7	6.17	-	-	43.79	-40.98	-54.39
20070131	21:22	319.9	6.09	-	-	43.67	-40.99	-54.69
20070201*	00:25	319.9	6.12	-	-	43.74	-41.28	-55.42
20070201*	03:10	319.6	5.86	-	-	43.71	-41.70	-56.02
20070201*	09:24	319.2	6.07	-	-	43.66	-42.63	-57.43
20070201*	14:30	320.7	5.94	15.65	-3.58	43.39	-43.66	-57.96
20070201*	18:40	319.5	6.41	-	-	43.87	-44.75	-58.13
20070201*	21:20	318.9	6.14	-	-	44.05	-45.07	-57.91
20070202	00:20	319.1	6.05	-	-	43.61	-45.24	-58.35
20070202	03:05	319.1	6.06	-	-	43.41	-45.21	-58.32
20070202	09:26	319.9	6.00	-	-	44.11	-46.02	-58.99
20070202	12:07	321.2	6.10	-	-	43.72	-46.02	-59.69
20070202*	14:58	319.4	6.43	-	-	44.10	-46.00	-60.26
20070202*	18:12	319.6	6.30	-	-	44.08	-46.07	-60.91
20070202	21:20	319.5	5.97	13.68	-1.51	43.78	-46.31	-61.46
20070203	00:22	320	5.93	-	-	43.89	-46.52	-61.91
20070203*	09:12	318.9	5.88	-	-	43.62	-47.00	-63.51
20070203	21:19	319.4	6.16	-	-	43.93	-47.61	-65.49
20070204	05:40	321	5.71	-	-	43.53	-49.34	-66.26
20070302	15:00	319.3	6.00	-	-	44.21	-52.25	-66.21
20070307	20:39	321.2	5.80	-	-	43.71	-59.54	-33.92
20070307	23:43	323.2	5.98	15.58	-3.82	43.87	-59.44	-33.67
20070317	02:23	318.8	6.10	-	-	44.02	-37.88	20.61
20070318	02:43	318.5	5.91	-	-	43.68	-34.45	25.79

*Samples collected over phytoplankton blooms based on CO₂ decreases measured *in situ* (see Methods)

5.3. Results and Discussion

The measurements are shown in Table 5.1, where the samples with the measured N₂O mixing ratio outliers are in bold, and in Figure 5.2, where the isotopic compositions are shown as a function of N₂O mixing ratio for all samples measured. As shown in Table 5.2, the average isotopic compositions — excluding the four N₂O mixing ratio outliers — are 6.0±0.2‰ (N=46) for δ¹⁵N^{bulk}, 43.8±0.2‰ (N=46) for δ¹⁸O, 14.9±0.8‰ (N=4) for δ¹⁵N^α, and -2.5±0.9‰ (N=4) for δ¹⁵N^β, where the uncertainties given are 1σ and are similar to the measurement precisions. The average N₂O mixing ratio is 319.5±0.7 ppbv. For the subset of samples collected over phytoplankton blooms (as indicated by asterisks in Table 5.1), values for N₂O, δ¹⁵N^{bulk}, δ¹⁸O and δ¹⁵N^α are identical to these means at the 1σ level, and the single measured δ¹⁵N^β value for a bloom sample is well within 2σ of the mean.

Table 5.2. Summary of averages. Tropospheric averages are based on measurements of Boundary Layer air on the UC Berkeley campus between 2001 and 2006.

	Tropospheric Average	Average w/o [N ₂ O] Outliers	Outlier Average	Keeling Plot Result	Phytoplankton Bloom Sample Average
δ ¹⁵ N ^{bulk}	6.2±0.3 ^a	6.0±0.2 ^c	5.5±0.5 ^d	-9.4±1.4	6.1±0.2 ^e
δ ¹⁸ O	44.3±0.4 ^a	43.8±0.2 ^c	43.5±0.6 ^d	24.6±0.7	43.8±0.2 ^e
δ ¹⁵ N ^α	15.8±1.2 ^b	14.9±0.8 ^d	14.3±1.3 ^d	-21±9	15.65 ^f
δ ¹⁵ N ^β	-3.3±1.2 ^b	-2.5±0.9 ^d	-2.6±1.2 ^d	31±9	-3.58 ^f
Site Preference	19.2±2.4 ^b	17.4±1.7 ^d	17.0±2.5 ^d	-52±18	19.30 ^f
[N ₂ O]	-	319.5±0.7	332±10	-	319.5±0.6

^a N = 288

^b N = 239

^c N = 46

^d N = 4

^e N = 9

^f N = 1

In general, the variability of the isotopic composition and mixing ratios is small, as indicated by the small standard deviations for the averages given above relative to the measurement precision and the close cluster of data points in Figure 5.2, excluding the four N₂O outlier samples. Indeed, excluding these four N₂O outliers, the data mostly scatter about the measurement precision, with only a very weak anti-correlation for δ¹⁵N^{bulk} (R=-0.3) and δ¹⁸O (R=-0.2) with N₂O mixing ratio that is entirely due to a few points with N₂O mixing ratios of ~321 ppbv, which is slightly higher than the average. However, for the four samples with enhanced N₂O mixing ratios, the isotopic compositions are also significantly perturbed, as can be clearly seen in Figure 5.2. For δ¹⁵N^{bulk}, the values for all four of these samples are lower than the mean value, though the δ¹⁵N^{bulk} value corresponding to the lowest N₂O mixing ratio outlier is within its uncertainty of the mean of the other samples. For δ¹⁸O, the values are somewhat less distinct; only two of the four N₂O outliers are different from the mean at 1σ and one sample is greater than the mean. For δ¹⁵N^α and δ¹⁵N^β, recall that, in addition to the

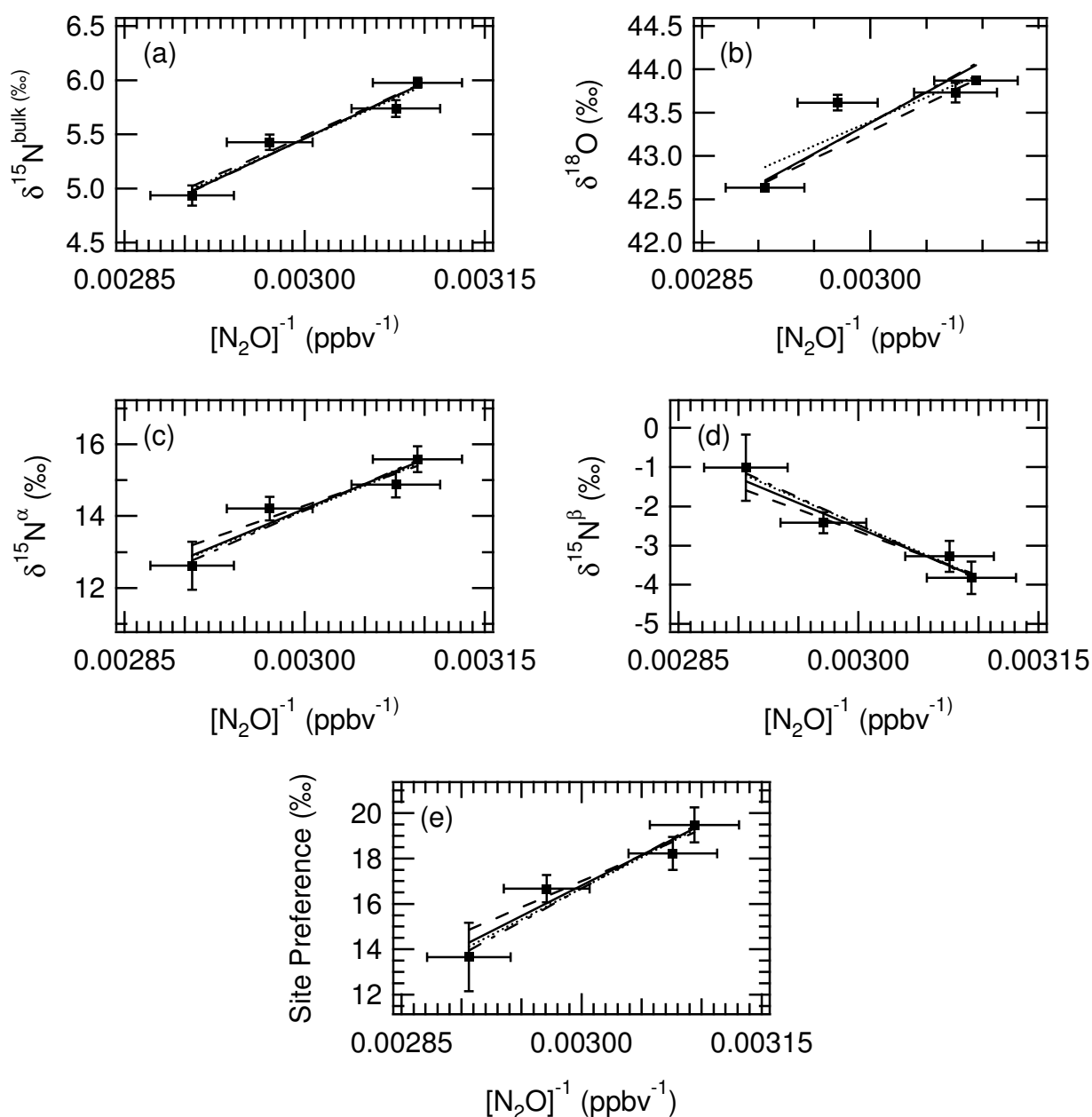


Figure 5.3. Keeling plots for (a) $\delta^{15}\text{N}^{\text{bulk}}$, (b) $\delta^{18}\text{O}$, (c) $\delta^{15}\text{N}^{\alpha}$, (d) $\delta^{15}\text{N}^{\beta}$, and (e) Site Preference for samples with outlier N_2O mixing ratios. $[\text{N}_2\text{O}]^{-1}$ error bars shown are based on an uncertainty of 1.2% in $[\text{N}_2\text{O}]$ and isotopic composition error bars are standard deviations of the means. Since the actual mixing ratio uncertainty is unknown, several types of regression lines are shown for comparison: unweighted (dotted), weighted only by uncertainty in y-data (dashed), weighted by uncertainty in both x- and y-data [Cantrell, 2008] assuming 1.2% uncertainty (solid), and weighted by uncertainty in both x- and y- data [Cantrell, 2008] assuming 5% uncertainty. The y-intercept values, which represent the source isotopic composition under the assumptions of the Keeling plot analysis, are given in Table 5.3.

four samples with enhanced N₂O mixing ratios, only four other samples were measured, so the mean values are not as well defined as they are for $\delta^{15}\text{N}^{\text{bulk}}$ and $\delta^{18}\text{O}$; however, in both cases, the sample with the highest N₂O mixing ratio is different from the mean at the 1 σ level.

Assuming that the enhanced N₂O mixing ratios in these four samples are each caused by an isotopically-similar ocean source mixing into an isotopically-similar tropospheric background, we can attempt to estimate the isotopic composition of the source responsible through a Keeling plot analysis [Keeling, 1958]. Keeling plots for $\delta^{15}\text{N}^{\text{bulk}}$, $\delta^{18}\text{O}$, $\delta^{15}\text{N}^{\alpha}$, $\delta^{15}\text{N}^{\beta}$, and Site Preference are shown in Figure 5.3; the y-intercepts on these plots represent the isotopic composition of the N₂O source, if such an analysis is valid. From the scatter plots alone, it is clear that the correlations of N₂O mixing ratio and isotopic compositions are strong and all negative except for $\delta^{15}\text{N}^{\beta}$: the greater the N₂O mixing ratio, the lower the isotopic values, except for $\delta^{15}\text{N}^{\beta}$ for which the higher N₂O mixing ratios correspond to higher isotopic values. Deriving the y-intercepts and their uncertainties, however, is more complicated; the actual dry N₂O mixing ratios and their uncertainty are unknown due to the somewhat arbitrary correction applied to the N₂O measurements to convert the measured mixing ratios to dry mixing ratios (see Methods section). Thus, the linear regression used to derive the intercept values was performed in several different ways, as summarized in Table 5.3. First, an unweighted least squares analysis was performed. Second, a standard weighted least square analysis was performed in which only uncertainty in the y-data is considered. Third, a linear regression weighted by uncertainties in both the x- and y-data [Cantrell, 2008] was performed, assuming a 1.2% uncertainty in the N₂O mixing ratio (i.e., the amount of the correction). The fourth regression was the same as the third, except that an uncertainty of 5% in the N₂O mixing ratio was assumed. In all of the weighted regressions, the isotopic composition measurements were weighted by their standard deviations. In general, regardless of which regression technique was applied, the calculated source isotopic compositions agreed within their uncertainties, suggesting that the results derived from the 4 samples here, at least, are robust.

Table 5.3. Summary of the Keeling plot results for the inferred source isotopic compositions (the y-intercepts in Figure 5.3 and their 1 σ uncertainties) using different linear regression techniques.

	Source Isotopic Composition			
	unweighted ^a	y-weighting only ^b	$\sigma([\text{N}_2\text{O}])=1.2\%$ ^c	$\sigma([\text{N}_2\text{O}])=5\%$ ^d
$\delta^{15}\text{N}^{\text{bulk}}$ (‰)	-9.3±2.3	-9.4±1.4	-10.0±2.4	-10.1±2.4
$\delta^{18}\text{O}$ (‰)	26.7±6.4	24.6±0.7	22.1±7.5	21.6±8.2
$\delta^{15}\text{N}^{\alpha}$ (‰)	-26±9	-21±9	-27±10	-30±9
$\delta^{15}\text{N}^{\beta}$ (‰)	38±6	31±9	36±8	40±7
SP (‰)	-66±15	-52±18	-63±18	-71±16

^a Unweighted least-squares regression.

^b Typical weighted least-squares where the only weighting is by uncertainty in y-data

^c Least-squares weighted by uncertainty in both x- and y-data [Cantrell, 2008], assuming 1.2% uncertainty in [N₂O].

^d Least-squares weighted by uncertainty in both x- and y-data [Cantrell, 2008], assuming 5% uncertainty in [N₂O].

We note, however, that there may be some additional uncertainty in the calculated source isotopic compositions from the Keeling plot analyses. First, the samples may not follow the main assumption of Keeling plot analyses that each sample is some mixture of the same two sources, each with a constant isotopic composition, since these four samples were collected at different times and places (see Table 5.1). Second, the range of N₂O mixing ratios is relatively small. For example, Pataki *et al.* [2003] showed that in Keeling plot analyses of CO₂, in general a range of ~75 ppm (relative to a ~380 ppm background) was required to obtain an intercept with an uncertainty of ~1‰, and below that the uncertainty increases rapidly, although other factors such as sample size and measurement precision can also play a role. A rough estimate based on the Pataki *et al.* study for CO₂ suggests that, for the observed 24 ppb range in N₂O relative to a 320 ppb background in this study, the expected uncertainty in the intercept is ~2-10‰. Interestingly, this estimate of uncertainty is similar to the uncertainties in the doubly-weighted regressions of the N₂O Keeling plot analysis. If this represents an ocean source of N₂O, even this degree of accuracy provides a step forward in efforts to characterize the isotopic composition of a Southern Ocean N₂O source, lacking much other data.

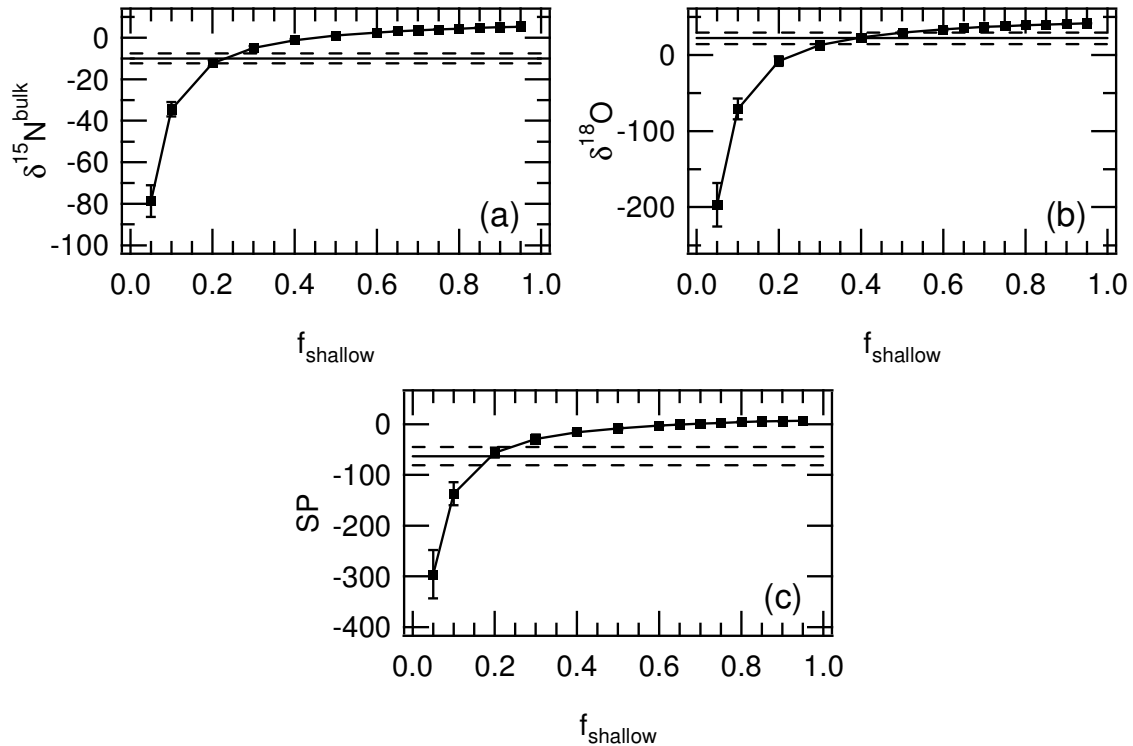


Figure 5.4. Comparison between (a) $\delta^{15}\text{N}^{\text{bulk}}$, (b) $\delta^{18}\text{O}$, and (c) Site Preference of N₂O for the shallow source in the oligotrophic subtropical North Pacific gyre as a function of its fractional contribution to N₂O at the isotopic minimum (see text) from measurement-based isotopic mass balance calculations by Popp *et al.* [2002] (given by the squares and their connecting lines) and the source isotopic compositions determined by Keeling plot analyses for the N₂O-outlier samples from the doubly-weighted regression assuming 1.2% uncertainty in [N₂O] (solid horizontal line) and the 1σ uncertainty in those values (dashed lines); see also Table 5.3.

Regardless of how accurately the Keeling plot analysis yields an isotopic composition for the source of N₂O in these high-N₂O samples, however, the pattern of enrichments and depletions should certainly be correct; the source has lower values of $\delta^{15}\text{N}^{\text{bulk}}$, $\delta^{18}\text{O}$, $\delta^{15}\text{N}^{\alpha}$, and SP than does tropospheric N₂O and the value of $\delta^{15}\text{N}^{\beta}$ is higher. This pattern is consistent with that observed in the shallow waters of the oligotrophic subtropical North Pacific gyre at depths from ~50-300m [Popp *et al.*, 2002]. In that region, analysis of depth profiles of the isotopic composition of N₂O led to the conclusion that there are two N₂O sources in the ocean, one located in shallow water and one located in deeper water. The isotopic compositions of the shallow source, δ_{shallow} , were determined as a function of the fraction of each (f_{shallow} and f_{deep}) that contributes to the measured N₂O at the depth of the minimum measured values of $\delta^{15}\text{N}^{\text{bulk}}$, $\delta^{18}\text{O}$ and SP based on two end-member isotopic mass balance calculations [Popp *et al.*, 2002]. A comparison between the results of those calculations and the calculated source isotopic composition in this work is shown in Figure 5.4. The source isotopic compositions from the Keeling plot analysis are shown as horizontal solid lines in the figure; they intersect the Popp *et al.* calculations at values for f_{shallow} of 17–24% for SP, 20–26% for $\delta^{15}\text{N}^{\text{bulk}}$, and 32–50% for $\delta^{18}\text{O}$. Thus, at least for $\delta^{15}\text{N}^{\text{bulk}}$ and SP, the source isotopic composition from the Keeling plot analysis here is consistent with that of the shallow source in the subtropical North Pacific gyre if f_{shallow} is ~17–26%. The range of f_{shallow} for $\delta^{18}\text{O}$ is larger and may seem inconsistent, but Kool *et al.* [2009] recently suggested that $\delta^{18}\text{O}$ of N₂O is often determined by oxygen exchange with water and may therefore be less reliable as an indicator of the production processes of N₂O than $\delta^{15}\text{N}^{\text{bulk}}$ and SP.

The proposed production mechanisms for N₂O in the shallow region of the subtropical North Pacific gyre are nitrification (i.e., oxidation of ammonia to nitrite via hydroxylamine, which produces N₂O as a side product) and/or nitrifier-denitrification (i.e., nitrification followed by reduction of nitrite to N₂O) [Dore *et al.*, 1998; Popp *et al.*, 2002]. In the South Pacific Ocean, measurements of the N₂O isotopic composition were used to suggest that nitrifier denitrification may play an important role in N₂O production there [Charpentier *et al.*, 2007]. Based on considerations related to both equilibrium and kinetic isotope effects, Popp *et al.* [2002] hypothesized that the SP of N₂O produced by either of these mechanisms ought to be $\geq 0\text{‰}$, and they used that to constrain f_{shallow} to be $>65\%$ and to estimate values for $\delta^{15}\text{N}^{\text{bulk}}$ of 3.5–5.5‰ and $\delta^{18}\text{O}$ of 35.5–41.5‰ for the shallow source for the North Pacific, which are distinctly different from the Keeling plot estimates here for the Southern Ocean of ~ -7 to -12‰ for $\delta^{15}\text{N}^{\text{bulk}}$ and ~ 14 to 33‰ for $\delta^{18}\text{O}$. Yet, Sutka *et al.* [2003; 2006] have shown that the SP of N₂O produced by both nitrification and nitrifier-denitrification can in some cases be $<0\text{‰}$, suggesting that a smaller value of f_{shallow} would have been calculated by Popp *et al.* [2002] and, hence, might have yielded isotopic compositions in their North Pacific study similar to those calculated here. Thus, it is possible that the isotopic composition of the source determined by the Keeling plot analysis of the four N₂O-enriched samples here is indeed similar to that of N₂O produced by nitrification and/or nitrifier denitrification in the ocean.

Besides an ocean source, however, it is useful to consider other possible sources. One possibility is that the samples enriched in N₂O were contaminated by ship exhaust. The Marion Dufresne uses diesel fuel and no data on the isotopic composition of N₂O emitted through diesel fuel combustion are available. However, two studies have been published on the isotopic composition of N₂O emitted by other types of fossil fuel combustion, one for gasoline combustion in automobiles [Toyoda *et al.*, 2008] and the other for coal combustion

in a furnace [Ogawa and Yoshida, 2005]. Both of these studies found values of $\delta^{18}\text{O}$ for the sources that were similar to the tropospheric average and SP values that were positive, neither of which are consistent with the results of the Keeling plot analysis here. For $\delta^{15}\text{N}^{\text{bulk}}$ the Keeling plot result of $-10.0 \pm 2.4\text{‰}$ is consistent with the gasoline combustion study result of $-4.9 \pm 8.2\text{‰}$, but not with the coal combustion study result of $9.2 \pm 5.3\text{‰}$. Thus, while the evidence is not conclusive, it seems unlikely that the isotopic composition of the enhanced N_2O in the four samples is due to contamination by ship exhaust.

Another possibility is a soil source. Although this seems unlikely given that the samples were collected in the marine boundary layer far from any significant land mass (see Figure 5.1), the calculated values of $\delta^{15}\text{N}^{\text{bulk}}$ and $\delta^{18}\text{O}$ from the Keeling plot analysis are not inconsistent with the wide range measured in natural and agricultural soils [e.g., Park *et al.*, 2010]. However, soil sources that have low values of $\delta^{15}\text{N}^{\alpha}$ typically also have low values of $\delta^{15}\text{N}^{\beta}$ [e.g., Park *et al.*, 2010], which is not consistent with the Keeling plot results, and may thus provide further evidence that the N_2O enhancements are not due to the influence of a soil source.

Finally, we note that correlations between the N_2O mixing ratios and the mixing ratios of other trace gas species with known sources were also investigated to determine if they might provide additional evidence for the likely source of the N_2O enhancements. Several tracers measured in the samples showed significant correlations ($R > 0.81$, $P < 0.1$) including dimethylsulfoxide (DMS), dichloromethane (CH_2Cl_2), propane (C_3H_8), and *n*-butane (C_4H_{10}), all of which have significant ocean sources [Charlson *et al.*, 1987; Keene *et al.*, 1999; Broadgate *et al.*, 1997]. While these correlations may indicate that the N_2O enhancement is coming from the ocean, none of the species shows an enhanced mixing ratio relative to those measured in other samples, and C_3H_8 and C_4H_{10} are also present in ship plumes [e.g., Chen *et al.*, 2005]. Thus, while the preponderance of evidence suggests that the enhanced N_2O mixing ratios in four samples is from an ocean source and that the Keeling plot analysis likely yields information on the isotopic composition of N_2O from the Southern Ocean, additional measurements are needed to verify this conclusion.

5.4. Conclusions

The isotopic composition of nitrous oxide was measured in samples collected over the South Atlantic Ocean on a cruise between southern Africa and southern South America. Most of the samples showed little variation in either N_2O mixing ratio or isotopic composition. Of the 50 samples measured for N_2O isotopic composition, four samples had enhanced N_2O mixing ratios ranging from ~ 323 to ~ 344 ppb relative to a background of ~ 319 ppb. The measured isotopic composition of N_2O in these samples was also perturbed relative to the average of the other samples by as much as -1.1‰ for $\delta^{15}\text{N}^{\text{bulk}}$, -1.2‰ for $\delta^{18}\text{O}$, -2.2‰ for $\delta^{15}\text{N}^{\alpha}$, and $+1.5\text{‰}$ for $\delta^{15}\text{N}^{\beta}$. An isotopic composition which may represent the isotopic composition of the N_2O source causing the mixing ratio enhancement was calculated from a Keeling plot analysis of these 4 outliers and yielded the values $-9.4 \pm 1.4\text{‰}$ for $\delta^{15}\text{N}^{\text{bulk}}$, $24.6 \pm 0.7\text{‰}$ for $\delta^{18}\text{O}$, $-21 \pm 9\text{‰}$ for $\delta^{15}\text{N}^{\alpha}$, $31 \pm 9\text{‰}$ for $\delta^{15}\text{N}^{\beta}$, and $-52 \pm 18\text{‰}$ for SP. These values appear to be consistent with calculations of the isotopic composition of N_2O produced in the shallow waters of the subtropical North Pacific gyre by nitrification and/or nitrifier denitrification, suggesting that N_2O produced by the same mechanism may be causing the observed N_2O mixing ratio enhancement reported here. They are not consistent with the

closest available proxies for the isotopic composition of N₂O emitted by ship exhaust, the other likely origin of the N₂O enhancement besides the ocean. Correlations between species emitted by the ocean and the N₂O mixing ratios in these samples provide further evidence that the ocean is the likely cause of the N₂O mixing ratio enhancement. Overall, these measurements over the open ocean demonstrate that, while the isotopic composition of nitrous oxide in the marine boundary layer is generally well mixed where there is no local source, where a local source exists that is intense enough to perturb the mixing ratio of N₂O, its isotopic composition can also be quantifiably perturbed and reflects the influence of that source. While more work is needed to assign the isotopic composition of N₂O from the South Atlantic Ocean with more certainty and to determine the extent to which it might vary between regions and seasons, results such as these can improve constraints on the isotopic compositions of N₂O sources. Such improvements will eventually allow inverse modeling of the small but significant spatial and temporal variations in the mixing ratio and isotopic composition of N₂O — such as those presented and discussed in Chapters 3 and 4 — to determine the magnitudes and geographic distributions of N₂O sources so that more effective mitigation strategies and treaty verifications can ultimately be achieved.

References

- Bathmann, U. V., R. Schreck, C. Klass, C. D. Dubischar, and V. Smetacek (1997), Spring development of phytoplankton biomass and composition in major water masses of the Atlantic sector of the Southern Ocean, *Deep Sea Res. II*, 44, 51-67.
- Bol, R., S. Toyoda, S. Yamulki, J. M. B. Hawkins, L. M. Cardenas, and N. Yoshida (2003), Dual isotope and isotopomer ratios of N₂O emitted from a temperate grassland soil after fertilizer application, *Rapid Commun. Mass Spectrom.*, 17, 2550-2556.
- Broadgate, W. J., P. S. Liss, and S. A. Penkett (1997), Seasonal emissions of isoprene and other reactive hydrocarbon gases from the ocean, *Geophys. Res. Lett.*, 24(21), 2675-2678.
- Cantrell, C. A. (2008), Technical Note: Review of methods for linear least-squares fitting of data and application to atmospheric chemistry problems, *Atmos. Chem. Phys.*, 8, 5477-5487.
- Charlson, R. J., J. E. Lovelock, M. O. Andreae, and S. G. Warren (1987), Oceanic phytoplankton, atmospheric sulfur, cloud albedo and climate, *Nature*, 326(16), 655-661.
- Charpentier, J., L. Farais, N. Yoshida, N. Boontanon, and P. Raimbault (2007), Nitrous oxide distribution and its origin in the central and eastern South Pacific Subtropical Gyre, *Biogeosci.*, 4, 729-741.
- Craig, H. and L. I. Gordon (1963), Nitrous oxide in the ocean and the marine atmosphere, *Geochim. Cosmochim. Acta*, 27, 949-955.
- D'Amelio, M. T. S., L. V. Gatti, J. B. Miller, and P. Tans (2009), Regional N₂O fluxes in Amazonia derived from aircraft vertical profiles, *Atmos. Chem. Phys.*, 9, 8785-8797.
- Dore, J. E., B. N. Popp, D. M. Karl, and F. J. Sansone (1998), A large source of atmospheric nitrous oxide from subtropical North Pacific surface waters, *Nature*, 396, 63-66.
- Flocke, F., *et al.* (1999), An examination of chemistry and transport processes in the tropical lower stratosphere using observations of long-lived and short-lived compounds obtained during STRAT and POLARIS, *J. Geophys. Res.*, 104(D21), 26,625-26,642.
- Griffith, D. W. T., S. D. Parkes, V. Haverd, C. Paton-Walsh, and S. R. Wilson (2009), Absolute calibration of the intramolecular site preference of ¹⁵N fractionation in tropospheric N₂O by FT-IR spectroscopy, *Anal. Chem.*, 81(6), 2227-2234.
- Hirsch, A. I., A. M. Michalak, L. M. Bruhwiler, W. Peters, E. J. Dlugokencky, and P. P. Tans (2006), Inverse modeling estimates of the global nitrous oxide surface flux from 1998-2001, *Global Biogeochem. Cycles*, 20, GB1008.
- Huang, J., *et al.* (2008), Estimation of regional emissions of nitrous oxide from 1997 to 2005 using multinetwork measurements, a chemical transport model, and an inverse method, *J. Geophys. Res.*, 113, D17313, doi:10.1029/2007JD009381.
- Keeling, C. D. (1958), The concentration and isotopic abundances of atmospheric carbon dioxide in rural areas, *Geochim. Cosmochim. Acta*, 13, 322-334.
- Keene, W. C., Khalil, M. A. K., Erickson, D. J., McCulloch, A., Graedel, T. E., Lobert, J. M., Aucott, M. L., Gong, S. L., Harper, D. B., Kleiman, G., Midgley, P., Moore, R. M., Seuzaret, C., Sturges, W. T., Benkovitz, C.M., Koropalov, V., Barrie, L. A., and Li, Y. F. (1999), Composite global emissions of reactive chlorine from anthropogenic and natural sources, reactive chlorine emissions inventory, *J. Geophys. Res.* 104, 8429-8440.

- Kim, K.-R. and H. Craig (1990) Two isotope characterization of N₂O in the Pacific Ocean and constraints on its origin in deep water, *Nature*, 347, 58-61.
- Kool, D. M., N. Wrage, O. Oenema, D. Harris, and J. W. Van Groenigen (2009), The ¹⁸O signature of biogenic nitrous oxide is determined by O exchange with water, *Rapid Commun. Mass Spectrom.*, 23, 104-108.
- Law, C. S. and R. D. Ling (2001), Nitrous oxide flux and response to increased iron availability in the Antarctic Circumpolar Current, *Deep Sea Res. II*, 48, 2509-2527.
- Nevison, C. D., R. F. Weiss, and D. J. Erickson III (1995), Global oceanic emissions of nitrous oxide, *J. Geophys. Res.*, 100(C8), 15,809-15,820.
- Nevison, C. D., J. H. Butler, and J. W. Elkins (2003), Global distribution of N₂O and the ΔN₂O-AOU yield in the subsurface ocean, *Global Biogeochem. Cycles*, 17, 1119, doi:10.1029/2003GB002068.
- Nevison, C. D., R. F. Keeling, R. F. Weiss, B. N. Popp, X. Jin, P. J. Fraser, L. W. Porter, and P. G. Hess (2005), Southern ocean ventilation inferred from seasonal cycles of atmospheric N₂O and O₂/N₂ at Cape Grim, Tasmania, *Tellus*, 57B, 218-229.
- Pataki, D. E., J. R. Ehleringer, L. B. Flannagan, D. Yakir, D. R. Bowling, C. J. Still, N. Buchmann, J. O. Kaplan, and J. A. Berry (2003), The application and interpretation of Keeling plots in terrestrial carbon cycle research, *Global Biogeochem. Cycles*, 17(1), 1022, doi:10.1029/2001GB001850.
- Park, S., T. Pérez, K. A. Boering, S. E. Trumbore, J. Gill, S. Marquina, and S. C. Tyler (2010), Can N₂O stable isotopes and isotopomers be useful tools to characterize sources and microbial pathways of N₂O production and consumption in tropical soils?, *Global Biogeochem. Cycles*, in press.
- Pérez, T., D. Garcia-Montiel, S. Trumbore, S. Tyler, P. de Camargo, M. Moriera, M. Piccolo, and C. Cerri (2006), Nitrous oxide nitrification and denitrification ¹⁵N enrichment factors from Amazon forest soils, *Ecol. Appl.*, 16(6), 2153-2167.
- Popp, B. N., M. B. Westley, S. Toyoda, T. Miwa, J. E. Dore, N. Yoshida, T. M. Rust, F. J. Sansone, M. E. Russ, N. E. Ostrom, and P. H. Ostrom (2002), Nitrogen and oxygen isotopomeric constraints on the origins and sea-to-air flux of N₂O in the oligotrophic subtropical North Pacific gyre, *Global Biogeochem. Cycles*, 16 (4), 1064-1073.
- Sutka, R. L., N. E. Ostrom, P. H. Ostrom, H. Gandhi, and J. A. Breznak (2003), Nitrogen isotopomer site preference of N₂O produced by *Nitrosomonas europaea* and *Methylococcus capsulatus* Bath, *Rapid Commun. Mass Spectrom.*, 17(7), 738-745.
- Sutka, R. L., N. E. Ostrom, P. H. Ostrom, J. A. Breznak, H. Gandhi, A. J. Pitt, and F. Li (2006), Distinguishing nitrous oxide production from nitrification and denitrification on the basis of isotopomer abundances, *Appl. Environ. Microbio.*, 72(1), 638-644.
- Taylor, J. R. (1997), *An introduction to error analysis*, University Science Books, Sausalito, Calif.
- Toyoda, S., N. Yoshida, T. Miwa, Y. Matsui, H. Yamagishi, U. Tsunogai, Y. Niojiri, and N. Tsurushima (2002), Production mechanism and global budget of N₂O inferred from its isotopomers in the western North Pacific, *Geophys. Res. Lett.*, 29(3), doi: 10.1029/2001GL014311.
- Williams, J. *et al.* (2010), Assessing the effect of marine isoprene and ship emissions on ozone, using modeling and measurements from the South Atlantic Ocean, *Environ. Chem*, 7, 171-182, doi:10.1071/EN09154.

- Yamagishi, H., M. B. Westley, B. N. Popp, S. Toyoda, N. Yoshida, S. Watanabe, K. Koba, and Y. Yamanaka (2007), Role of nitrification and denitrification on the nitrous oxide cycle in the eastern tropical North Pacific and Gulf of California, *J. Geophys. Res.*, 112, G02015, doi:10.1029/2006JG000227.
- Yoshida, N. and S. Toyoda (2000), Constraining the atmospheric N₂O budget from intramolecular site preference in N₂O isotopomers, *Nature*, 405, 330-334.

Experimental determination of isotope effects in the non-dissociative photoionization of molecular nitrogen

Abstract

Isotope effects in the non-dissociative photoionization of molecular nitrogen, $N_2 + h\nu \rightarrow N_2^+ + e^-$, have not been previously measured, and yet they are likely to play a role in determining the relative abundances of isotopic species containing nitrogen in interstellar clouds and planetary atmospheres. Since such isotopic compositions are often used to interpret atmospheric histories and/or chemical pathways, it is important that all possible isotope effects affecting these species are known. Here, we present measurements of the photoionization efficiency spectra of $^{14}N_2$, $^{15}N^{14}N$, and $^{15}N_2$ between 15.5 and 18.9 eV from experiments at the Advanced Light Source, Lawrence Berkeley National Laboratory's synchrotron facility. The spectra show significant shifts in peak energies and intensities due to isotopic substitution, and the ratio of photoionization cross-sections as a function of wavelength are as high as 4 for $\sigma(^{14}N_2)/\sigma(^{15}N_2)$ and as low as 0.4 at the experimental energy resolution of 6.5 meV. Integrating the photoionization cross-sections for each of the isotopologues over all wavelengths measured (and thus assuming "white light" and optically thin conditions) to obtain the photoionization rate coefficients, J , we find that the ratios of the J -values are $J(^{15}N^{14}N)/J(^{14}N_2) = 1.01 \pm 0.02$ and $J(^{15}N_2)/J(^{14}N_2) = 1.00 \pm 0.02$, suggesting that isotopic fractionation between N_2 and N_2^+ should be small under such conditions. However, in a model of Titan's dense, N_2 -rich atmosphere, isotopic self-shielding of the common isotopologue $^{14}N_2$ leads to regions of the atmosphere in which the photoionization ratio $J(^{15}N^{14}N)/J(^{14}N_2)$ is as large as 1.17, ranging from ~ 1.05 at 1400 km to ~ 1.17 at 900 km altitude. Since N_2^+ can react with various hydrocarbons to form HCN, such a mechanism may contribute to a quantitative explanation of the observation that HCN in Titan's atmosphere has a $^{15}N/^{14}N$ ratio that is larger than that of the parent N_2 by a factor of 2 to 4. In addition, the measurements also show that the peak at 15.68 eV, whose assignment has been the subject of recent debate, is most likely due to a Rydberg state converging to the $v'=2$ level of the $A^2\Pi_u$ molecular ion state based on the measured isotopic shifts in energy.

6.1. Introduction

Isotopic substitution can significantly affect the chemical and physical properties of atoms and molecules, such as absorption spectra, reaction rates, and atmospheric escape velocities. Such isotope effects can lead to measurable changes in the relative abundances of the isotopologues of molecules in planetary atmospheres and interstellar molecular clouds, and, hence, measurements of isotopic compositions can be used to interpret chemical and physical histories and/or chemical reaction pathways in these environments provided all relevant isotope effects are known.

Isotope effects in the non-dissociative photoionization of molecular nitrogen (R6.1)



had not been measured previously, however, despite their potential importance in a variety of environments, including interstellar molecular clouds [e.g., *Trevia and Herbst*, 2000] and planetary atmospheres on Earth [e.g., *Aikin*, 2001; *Kaye*, 1987], Mars [e.g., *Fox and Hać*, 1997], and Saturn's moon, Titan [*Wilson and Atreya*, 2004; *Waite et al.*, 2007; *Imanaka and Smith*, 2007]. For Titan, quantification of possible isotope effects in (1) may lead to a better understanding of the chemical processes currently occurring in Titan's atmosphere that produce pre-biotic organic compounds such as benzene and aerosols [*Wilson and Atreya*, 2004; *Waite et al.*, 2007; *Imanaka and Smith*, 2007] and of the origin and long-term evolution of its unusual and puzzling dense N₂ atmosphere [e.g., *Liang et al.*, 2007]. For Earth, reaction (1) may lead to enrichments or depletions in the isotope ratios of atmospheric trace species, such as NO, which may be useful as a tracer of stratospheric and thermospheric air masses in the mesosphere, and, hence, on atmospheric circulation in these regions [e.g., *Aikin*, 2001]. For Mars, the evolution of the martian atmosphere on a billion-year time scale may be better constrained by quantifying potential isotope effects in (1) that may lead to differences in the escape velocities of ¹⁵N vs. ¹⁴N due to dissociative recombination of N₂⁺ in Mars' upper atmosphere [e.g., *Fox and Hać*, 1997], similar to issues on Titan. In addition, the isotope effects themselves are interesting from a chemical physics perspective, including whether standard theories can account for them or whether they may be governed by more complex isotope-dependent quantum interference effects or quantum symmetry effects [*Vieitez et al.*, 2007]. Furthermore, isotope effects may help clarify the identity of particular absorption bands whose assignments are in question based on recent analyses [e.g. *Sommavilla et al.*, 2002, *Lefebvre-Brion*, 2005, *Somavilla and Merkt*, 2006].

In this chapter, measurements of the photoionization efficiency spectra of ¹⁴N₂, ¹⁵N¹⁴N, and ¹⁵N₂ using synchrotron radiation from the Advanced Light Source (ALS) of the Lawrence Berkeley National Laboratory from 15.5 eV to 18.9 eV are presented. The experimental results are used to clarify peak assignments and as input to a photochemical model of Titan's atmosphere to determine the ratios of photoionization rates and rate coefficients for ¹⁴N₂ and ¹⁵N¹⁴N relative to those for other processes, such as N₂ photodissociation, which are known to affect on the isotopic compositions of N₂ and HCN.

6.2. Methods

The experiment described here was carried out using a molecular beam apparatus coupled to the Chemical Dynamics Beamline (CDB) at the ALS. The apparatus has been described in detail elsewhere [*Nicolas et al.*, 2006; *Kostko et al.*, 2008], so only a brief overview and details specific to this experiment are discussed here. In order to determine the relative photoionization cross-sections as a function of wavelength for the three isotopologues of N₂, a molecular beam was formed from a 1:1:1 mixture of ¹⁴N₂: ¹⁵N¹⁴N: ¹⁵N₂ gases and then crossed at 90° with vacuum ultraviolet light from the ALS to form N₂⁺ ions which were detected using a time-of-flight mass spectrometer (TOF-MS).

The mixture was prepared by flowing each of the three isotopologues of N₂ through three different calibrated mass-flow controllers (MFCs; MKS 1179/20 sccm full range, Andover, MA) each controlled at the same rate of 2.5 sccm. ¹⁵N¹⁴N and ¹⁵N₂ were obtained from Icon Services (Summit, NJ) with stated purities of 99% and 98%, respectively, and were used without further purification. For ¹⁴N₂, a cylinder of research grade N₂ (Airgas, 99.999% purity) was used. If based solely on the general specifications for the accuracy of the MFCs

($\pm 1\%$ of full scale), the mole fraction for each isotopic species would be 0.33 ± 0.05 for each isotopic species. However, since there should be no significant isotope effects in photoionization to a continuum, the measurements themselves were used to reduce the uncertainty in the actual mixture composition. Using the average and standard deviation for the ratios of the signals for the different isotopologues in the featureless regions of the spectrum, the mole fractions are 0.339 ± 0.002 , 0.321 ± 0.002 , and 0.340 ± 0.002 for $^{14}\text{N}_2$, $^{15}\text{N}^{14}\text{N}$, and $^{15}\text{N}_2$, respectively.

The gas mixture was then expanded through a 100 μm diameter orifice into a vacuum chamber, forming a molecular beam. This beam was skimmed to 2 mm and then intersected perpendicularly with monochromated VUV light from the synchrotron with a bandwidth of ~ 6.5 meV FWHM, thus ionizing some of the N_2 to N_2^+ . The ions were then accelerated with Wiley-McLaren ion optics and separated by mass-to-charge ratio (m/z) in a commercial reflectron TOF mass spectrometer (R. M. Jordan Co., Inc., Grass Valley, CA) where they were detected by collecting the time-dependent signal from a microchannel plate detector with a multichannel-scaler card which was then integrated with a PC. The peaks corresponding to $^{14}\text{N}_2^+$, $^{15}\text{N}^{14}\text{N}^+$, and $^{15}\text{N}_2^+$ were each integrated for each 3meV energy step and then normalized by the photon flux, which was measured during the experiment using a NIST-calibrated Si-photodiode, thus yielding the photoionization efficiency (PIE) spectrum for each of the isotopologues. The resulting PIE spectrum for each isotopologue was then scaled by the inverse of its mole fraction derived from the experiment (as noted above) so the overall results would represent those for a 1:1:1 mixture.

Since the accuracy of the energy scale recorded at the CDB is limited by the mechanical precision of the monochromator and because we were most interested in the relative cross-sections rather than the absolute energies, the energy scale for the data reported here is calibrated by linear regression using the energies of well-known peaks in the $^{14}\text{N}_2$ spectrum [Lofthus and Krupenie, 1977]. In multiple runs in the same region of the spectrum over the course of two days, an average linear offset of 20 meV was observed, with a maximum of 40 meV. However, the relative peak energies (*i.e.*, the differences in energies between peaks) generally agreed to well within the 6.5 meV bandwidth of the experiment. After the energy scale calibration, the peak energies were in good agreement between different runs and with the energies used for the calibration from Lofthus and Krupenie [1977] to within the 6.5 meV bandwidth, which is similar to the average of the energy differences between other studies [Ogawa and Tanaka, 1962; Ogawa, 1964; Cook and Metzger, 1964; Cook and Ogawa, 1965; McCormack *et al.*, 1990; Somnavilla *et al.*, 2002]. Finally, the PIE spectra, which are relative cross-sections, were converted to absolute values using the absolute photoionization cross-sections from previous measurements for $^{14}\text{N}_2$ [Samson *et al.*, 1977; Itikawa *et al.*, 1986].

To test whether isotope effects in reaction R6.1 may play an important role in Titan's atmosphere, the isotope-specific photoionization cross-sections from the experiment were input into a photochemical model of Titan's atmosphere [Yung *et al.*, 1984; Liang *et al.*, 2007], . The diurnally-averaged one-dimensional model calculates the profiles of H, H_2 , C_1 - C_2 , N, N_2 , CN, HCN, NH, and isotopic compounds of nitrogen by solving the mass continuity equation:

$$\frac{\partial n_i}{\partial t} + \frac{\partial \varphi_i}{\partial z} = P_i - L_i,$$

where n_i is the number density for species i , φ_i the vertical flux, P_i the chemical production rate, and L_i the chemical loss rate, all evaluated at time t and altitude z . P_i and L_i are calculated based on the chemical schemes from previous work [Liang *et al.*, 2007]. The vertical flux is given by

$$\varphi_i = -\frac{\partial n_i}{\partial z} (D_i + K_{zz}) - n_i \left(\frac{D_i}{H_i} + \frac{K_{zz}}{H_{atm}} \right) - n_i \frac{\partial T}{\partial z} \left[\frac{(1 + \alpha_i) D_i + K_{zz}}{T} \right] + n_i w,$$

where D_i is the species' molecular diffusion, H_i the species' scale height, H_{atm} the atmospheric scale height, α_i the thermal diffusion parameter, T the temperature, K_{zz} the eddy mixing coefficient, and w the vertical wind. The vertical transport (K_{zz} and w) used in this work is set to be the same as that used by Liang *et al.* [2007].

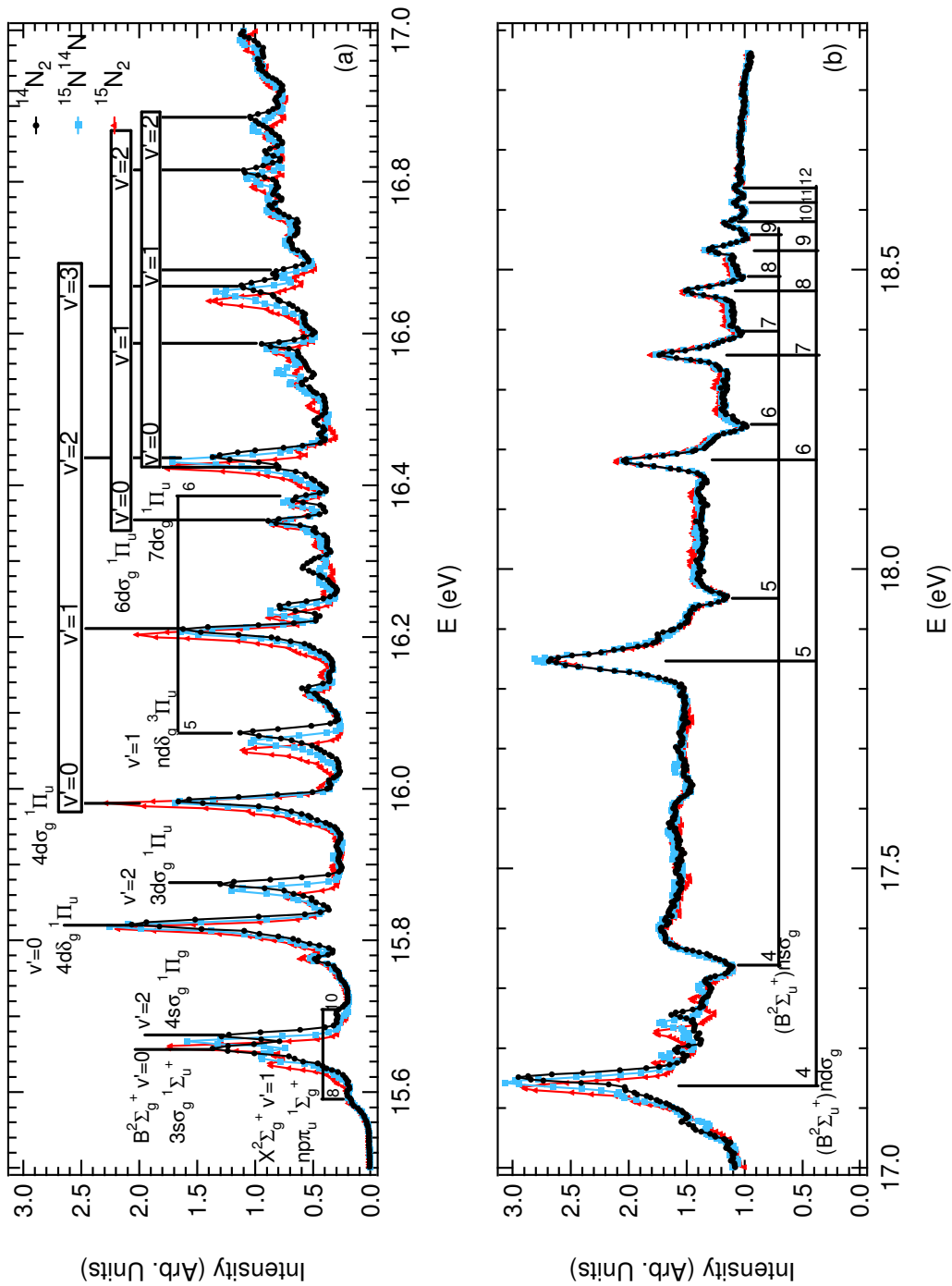


Figure 6.1. Normalized photoionization efficiency spectra for $^{14}\text{N}_2$, $^{15}\text{N}^{14}\text{N}$, and $^{15}\text{N}_2$ for (a) 15.5 – 17.0 eV and (b) 17.0 – 18.9 eV. The raw data have been scaled by the inverses of their respective calculated mole fractions (see text) to represent a 1:1:1 mixture.

6.3. Results and Discussion

Figure 6.1 shows the PIE spectrum for each isotopologue from 15.5 to 18.9 eV along with peak assignments. The major features in the photoionization spectrum are autoionizing

Rydberg states converging to vibrational levels of the second ($A^2\Pi_u$) and third ($B^2\Sigma_u^+$) ionized states of N_2 . The measurements show that the energy and/or intensity of many of the peaks are altered by isotopic substitution. The general trend for the energy shifts observed is that the peaks occur in the order $^{15}N_2$, $^{15}N^{14}N$, $^{14}N_2$ from lowest to highest energy. This is the trend predicted by simple theory [Herzberg, 1950] for autoionizing Rydberg states of N_2 that converge to vibrational levels above $v=0$ within the excited electronic states of N_2^+ . The relative peak intensities require a more detailed theoretical treatment to predict [e.g., Halmann and Laulicht, 1965], however, and no generalizable trends are predicted or observed.

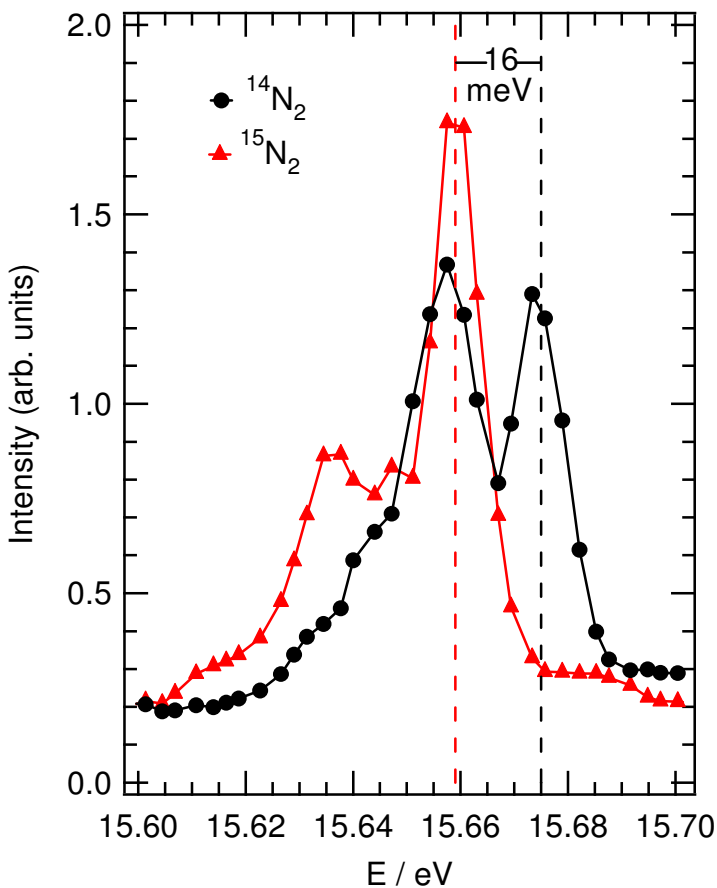


Figure 6.2. PIE spectra for $^{14}N_2$ (circles) and $^{15}N_2$ (triangles) from 15.6 to 15.7 eV. Dashed lines indicate peak-centers based on Voigt-profile fits. Based on the measured 16 meV isotope shift between $^{14}N_2$ and $^{15}N_2$, the peak at 15.68 eV for $^{14}N_2$ most likely corresponds to the autoionizing Rydberg state, $(A^2\Pi_u v'=2)4s\sigma_g^1\Pi_u$.

The PIE spectra shown in Figure 6.1 and particularly their isotopic energy shifts can be used to clarify the several peak assignments for which uncertainty still exists. For example, the peak at 15.68 eV has recently been the subject of debate in which three different groups have assigned this one peak to three different states: (1) the $v=44$ level of the $b^1\Sigma_u^+$ valence state [Somavilla and Merkt, 2006; Somavilla et al., 2002], (2) the Rydberg state

Table 6.1. Summary of proposed state assignments for the feature at 15.68 eV and the associated isotope shifts between $^{14}\text{N}_2$ and $^{15}\text{N}_2$. The measured isotope shift matches most closely that predicted for the $(\text{A}^2\Pi_u v'=2)4s\sigma_g^1\Pi_u$ state.

Proposed State Assignment	Reference	$E(^{14}\text{N}_2) - E(^{15}\text{N}_2)$
$v'=44$ $b^1\Sigma_u^+$	Sommavilla and Merkt, 2006	0.037 ^a
$(\text{A}^2\Pi_u v'=1)3d\sigma_g^1\Pi_u$	Lefebvre-Brion, 2006	0.008 ^b
$(\text{A}^2\Pi_u v'=2)4s\sigma_g^1\Pi_u$	Jungen et al., 2003	0.015 ^b
Measured	This work	0.016 ^c

^a Predicted in Lefebvre-Brion [2005] by solving the coupled equations for the relevant states, the b^1 valence state and two Rydberg states $c'(X^2\Sigma_g^+ v'=0)3p\sigma$ and $e'(X^2\Sigma_g^+ v'=0)4p\sigma$.

^b Calculated as a vibrational isotope shift since the only term in the energy of a Rydberg state is the energy of the state to which the Rydberg series converges (i.e., a vibrational level of the $\text{A}^2\Pi_u$ electronic state): $\Delta E = (1 - \rho)\{\omega_e - \omega_e\chi_e(1 + \rho)\}v - \omega_e\chi_e(1 + \rho)v^2$ [Herzberg, 1950], where $\rho = (\mu/\mu_i)^{1/2}$, and μ and μ_i are the reduced masses of the “normal” and isotopically substituted molecules, yielding 7.0015 and 7.5001 for $^{14}\text{N}_2$ and $^{15}\text{N}_2$, respectively. For the $\text{A}^2\Pi_u$ state $\omega_e = 0.23601$ eV and $\omega_e\chi_e = 0.001861$ eV [Lofthus and Krupenie, 1977].

^c Derived from measurements by fitting the two peaks at 15.66 and 15.68 eV to Voigt profiles. The result is the same for all three runs (i.e., to within < 0.0005 eV) under any of the following conditions (1) if Gaussian or Lorentzian profiles are used instead of Voigt, (2) if additional features are included in the fits, or (3) if the uncalibrated energy scale is used instead of the calibrated scale. using Gaussian or Lorentzian profiles, or when fitting additional features in the region, and for all 3 runs, and whether using a calibrated or uncalibrated energy axis.

Table 6.2. Energies and isotope shifts for the P(1) progression. The results here suggest that the peaks in this series correspond to autoionizing Rydberg states converging to the $v = 0 - 3$ levels of the $\text{A}^2\Pi_u$ electronic state.

$E(^{14}\text{N}_2)$	$E(^{14}\text{N}_2) - E(^{15}\text{N}_2)$	
	Measured ^a	Calculated ^b
15.98	0.004	0
16.21	0.007	0.008
16.44	0.014	0.015
16.66	0.019	0.022

^a See Table 6.1 footnote c for fitting details.

^b Calculated isotope shifts assuming the peaks are autoionizing Rydberg states converging to the $v = 0 - 3$ levels of the $\text{A}^2\Pi_u$ electronic state. See Table 6.2 footnote b for a description of the calculation. $(\text{A}^2\Pi_u v'=1)3d\sigma_g^1\Pi_u$ [Lefebvre-Brion, 2005], and (3) the Rydberg state $(\text{A}^2\Pi_u v'=2)4s\sigma_g^1\Pi_u$ [Jungen et al., 2003].

In addition to Figure 6.1, this feature is also shown in Figure 6.2 for $^{14}\text{N}_2$ and $^{15}\text{N}_2$ on an expanded energy scale. Because each of the proposed states should exhibit distinct energy shifts between $^{14}\text{N}_2$ and $^{15}\text{N}_2$, the measurements presented here can clarify the origin of this peak. As shown in Table 6.1, the experimental results clearly rule out the $v'=44$ $b^1\Sigma_u^+$ valence state. And, although the relatively wide experimental bandwidth of 6.5 meV means that the $(A^2\Pi_u, v'=1)3d\sigma_g^1\Pi_u$ state cannot be completely ruled out, the measured isotope shift best matches that predicted for the $(A^2\Pi_u, v'=2)4s\sigma_g^1\Pi_u$. Because the energies of the Rydberg states upon isotopic substitution are expected to be well-predicted by simple theory, the experimental results thus strongly favor assignment to the $(A^2\Pi_u, v'=2)4s\sigma_g^1\Pi_u$ state.

The measured isotope shifts also clarify and correct the states involved in the peaks occurring at 15.98, 16.21, 16.44, and 16.66 eV for $^{14}\text{N}_2$. These peaks were first identified as a vibrational progression of Rydberg states converging to the $A^2\Pi_u$ state of N_2^+ in the VUV absorption spectrum of N_2 [Ogawa, 1964] and later were tentatively interpreted as corresponding to the states $(A^2\Pi_u, v'=0)4d\sigma_g^1\Pi_u$, $(A^2\Pi_u, v'=1)4d\sigma_g^1\Pi_u$, $(A^2\Pi_u, v'=1)5d\sigma_g^1\Pi_u$, and $(A^2\Pi_u, v'=3)4d\sigma_g^1\Pi_u$, in order of increasing energy [Lefebvre-Brion, 1993]. However, as shown in Table 6.2, the successive increase in isotope shifts observed for these peaks instead follows closely the calculated isotope shifts for the first four vibrational levels of the $A^2\Pi_u$ state, suggesting that the third member of the series is the $(A^2\Pi_u, v'=2)4d\sigma_g^1\Pi_u$ state rather than the $(A^2\Pi_u, v'=1)5d\sigma_g^1\Pi_u$ state.

In addition to the magnitudes of the energy shifts, the isotope effects as a function of wavelength are quite distinct, as shown in Figure 6.3 in which the ratio of the photoionization cross-sections are shown for $^{15}\text{N}^{14}\text{N}/^{14}\text{N}_2$ and its inverse $^{14}\text{N}_2/^{15}\text{N}^{14}\text{N}$ in (a) and $^{15}\text{N}_2/^{14}\text{N}_2$ and its inverse $^{14}\text{N}_2/^{15}\text{N}_2$ in (b) [Note that the ratios are given for both light/heavy and heavy/light in order to satisfy both chemists and isotope geochemists who prefer different conventions]. The light/heavy cross-section ratios can exceed a factor of 4 for the 6.5 meV bandwidth of the experiment. The extent to which isotopic fractionation of N_2 — as well as of species that may react with the resulting N_2^+ — occurs over a range of wavelengths (as in a planetary atmosphere, for example), however, depends on the ratios of the photoionization rate coefficients, J , for the different isotopologues for which the energy-dependent photoionization cross-sections are convolved with the energy-dependent radiation intensity by integrating over the energy region of interest

$$J = \int_{E_i}^{E_f} \sigma(E)I(E)dE, \quad (\text{E6.1})$$

where the integral is over the energies E_i to E_f ; $\sigma(E)$ is the photoionization cross-section; and $I(E)$ is the intensity of the radiation. Under 'white light' irradiation and optically thin conditions, the ratios of the J -values over the entire experimental energy range are $J(^{15}\text{N}^{14}\text{N})/J(^{14}\text{N}_2) = 1.01 \pm 0.02$ and $J(^{15}\text{N}_2)/J(^{14}\text{N}_2) = 1.00 \pm 0.02$. To see if structure in the solar spectrum changes the ratio of these simple J -values, the data can also be convolved using solar flux measurements from the NASA SEE instrument on the TIMED satellite [Woods *et al.*, 2005], shown in Figure 6.3 (c), for $I(E)$ in Equation 6.1, yielding 1.00 ± 0.02 for $J(^{15}\text{N}^{14}\text{N})/J(^{14}\text{N}_2)$ and 0.98 ± 0.02 $J(^{15}\text{N}_2)/J(^{14}\text{N}_2)$. Thus, to zeroth order in an optically thin planetary atmosphere under solar irradiation, isotopic fractionation via reaction R6.1 may not be significant at these energies.

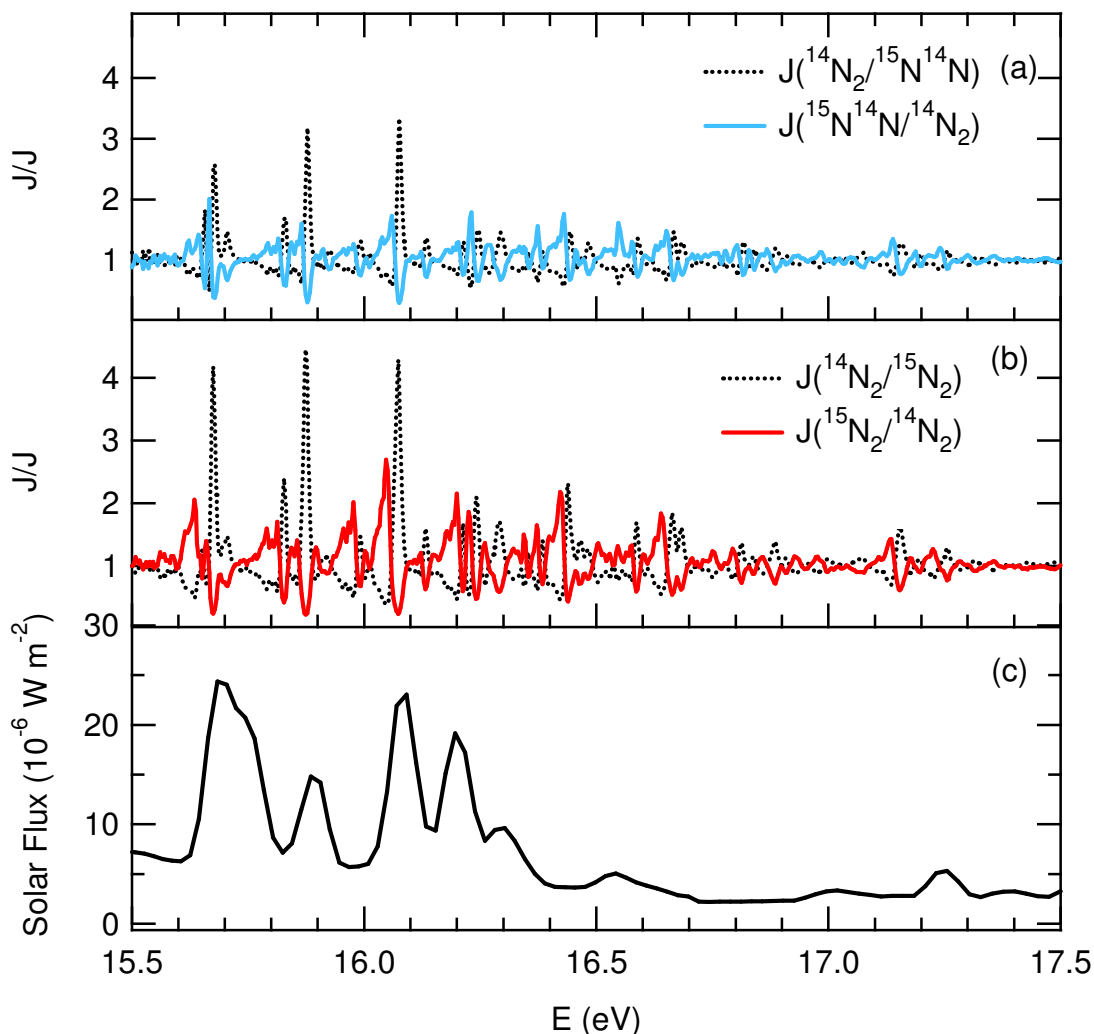


Figure 6.3. Ratios of photoionization cross-sections for (a) $^{14}\text{N}_2/^{15}\text{N}^{14}\text{N}$ and its inverse $^{15}\text{N}^{14}\text{N}/^{14}\text{N}_2$ and (b) $^{14}\text{N}_2/^{15}\text{N}_2$ and its inverse $^{15}\text{N}_2/^{14}\text{N}_2$ over the range 15.5 – 17.5 eV (Note that because the isotope shifts are negligible between 17.5 and 18.9, this region is not included here). The solar spectrum at 625 km in Earth’s atmosphere recorded by the TIMED/SEE instrument is shown in (c) over the same energy range.

The analysis described above applies to optically thin conditions in a simplified atmosphere in which no other species alter the actinic flux at altitudes where N_2 photodissociation is important. However, in the dense, N_2 -rich atmosphere of Titan, isotopic self-shielding may occur in which the radiation propagating from the top of the atmosphere to lower altitudes is attenuated much more rapidly by the common isotopologue $^{14}\text{N}_2$ than by the rare isotopologue $^{15}\text{N}^{14}\text{N}$. Hence, at some altitude, the atmosphere becomes optically thick in the wavelengths absorbed by $^{14}\text{N}_2$ but allows the wavelengths absorbed by $^{15}\text{N}^{14}\text{N}$ to continue to propagate. In principle, this process could lead to an increasingly larger photoionization rate coefficient for $^{15}\text{N}^{14}\text{N}$ relative to $^{14}\text{N}_2$ with decreasing altitude.

To test the extent to which isotopic self-shielding due to N_2 photoionization could significantly affect the relative photoionization rates of $^{14}\text{N}_2$ vs. $^{15}\text{N}^{14}\text{N}$, and hence may play a

role in determining the isotopic composition of N_2 and HCN in Titan's atmosphere, the measured cross-sections were included in a 1D photochemical model of Titan's atmosphere [Yung *et al.*, 1984; Liang, *et al.*, 2007]. The model results are given in Figure 6.4 and show that — due to isotopic self-shielding — the J-value for $^{15}\text{N}^{14}\text{N}$ photoionization is larger than that for $^{14}\text{N}_2$ in Titan's atmosphere and significantly larger than the ratio predicted simply using Equation 6.1. For example, at 1100 km, where the rate of N_2 photoionization is at its maximum (see left panel of Fig 6.4), the ratio of photoionization J-values, $J(^{15}\text{N}^{14}\text{N})/J(^{14}\text{N}_2)$, is 1.08 (see right panel of Fig 6.4; note that in the right panel, the ratios of J values are plotted as $[J(^{15}\text{N}^{14}\text{N})/J(^{14}\text{N}_2) - 1] \times 100$], which is the fractionation constant in percent]. At 900 km, where the photoionization rates are $\sim 30\%$ of their maximum, the ratio $J(^{15}\text{N}^{14}\text{N})/J(^{14}\text{N}_2)$ reaches a value as high as 1.17. [Note that the higher value of the ratio of ~ 1.20 at 600 km corresponds to where the photoionization rate is near zero.]

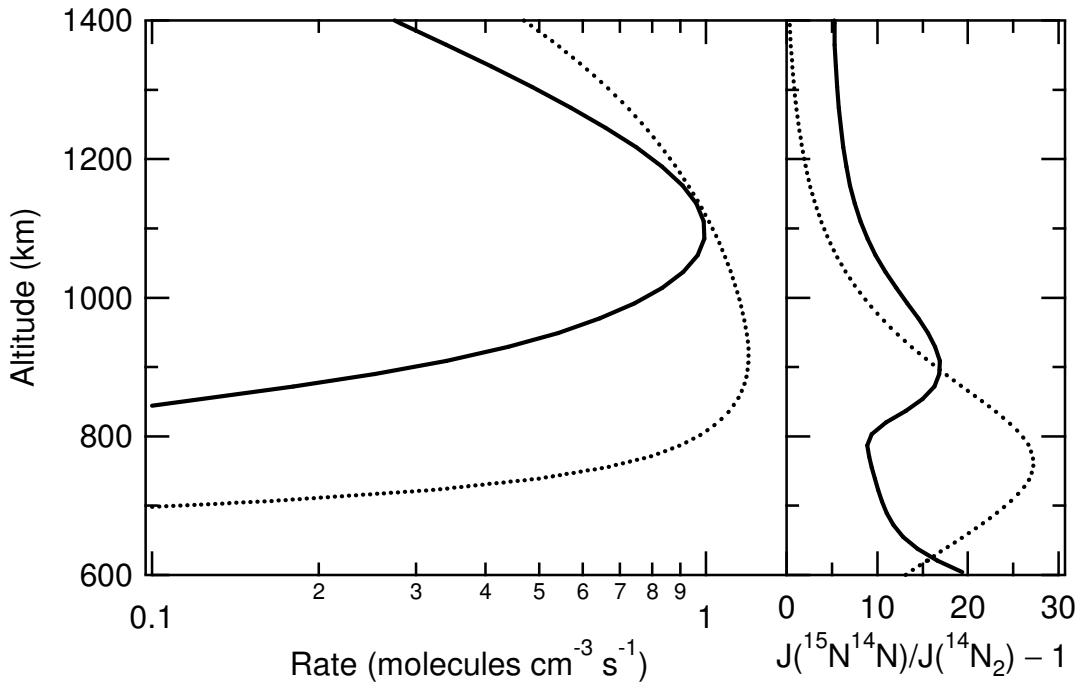


Figure 6.4. Left panel: Model-calculated rates for N_2 photoionization (solid line) and N_2 photodissociation (dotted line) for $^{14}\text{N}^{14}\text{N}$ in Titan's atmosphere, using the same N_2 profile as in Liang *et al.* [2007]. Right panel: Fractionation constants ($J(^{15}\text{N}^{14}\text{N})/J(^{14}\text{N}_2) - 1$) for the model-calculated isotope-specific rate coefficients, J , for photoionization (solid line) and photodissociation (dotted line) showing the effects of isotopic self-shielding by $^{14}\text{N}^{14}\text{N}$. The values for photoionization have been multiplied by factor of 100 to give the fractionation constant in percent.

Recently, Liang *et al.* [2007] calculated N₂ photodissociation rates for R6.2



in the same model of Titan's atmosphere and the corresponding ratio of J-values for R6.2 for ¹⁴N₂ and ¹⁵N¹⁴N, including isotopic self-shielding, using photodissociation cross-sections calculated using the diabatic coupled-channel Schrödinger equation model [Liu *et al.*, 2007]. The contribution of photodissociation to the destruction rate of N₂ is ~ 1.7 times larger than that for photoionization (see left panel of Fig 6.4), while their calculated photodissociation cross-sections and model results for the ratio of photodissociation rate coefficients, J(¹⁵N¹⁴N)/J(¹⁴N₂), are as high as 28 (see right panel of 6.4), which is almost 24 times larger than the maximum ratio for photoionization. Since N atoms formed by the photodissociation of N₂ can react with various hydrocarbons to form HCN, Liang *et al.* [2007] used this model to show that such very large isotope effects calculated for N₂ photodissociation could explain the previously puzzling observations that HCN has a ¹⁵N/¹⁴N ratio that is larger by a factor of 2 to 4 than that of the parent N₂ in Titan's atmosphere, including those from the CIRS and INMS instruments on the Cassini orbiter [Vinatier, *et al.*, 2007; Waite *et al.*, 2005] and the Huygens Probe GCMS instrument [Niemann *et al.*, 2005], and consistent with all the other ground-based observations of ¹⁵N/¹⁴N in HCN [Gurwell *et al.*, 2004; Marten *et al.*, 2002]. However, the modeled HCN isotopic composition was significantly too enriched in ¹⁵N relative to the observations [Liang *et al.*, 2007]. It is possible that adding in the 60% contribution to the photodestruction of N₂ from photoionization, with its much smaller isotope effects, followed by reaction of the product N₂⁺ with various hydrocarbons to form HCN [Anicich and McEwan, 1997; McEwan and Anicich, 2007], could account for the model-observation difference of Liang *et al.* [2007] and thus serve to quantitatively resolve the puzzle surrounding the difference in isotopic composition of HCN versus N₂ in Titan's atmosphere.

In addition, the very large differences in isotopic fractionation arising from photoionization versus photodissociation of N₂ suggested by the isotope-specific J-values modeled here for Titan's atmosphere may also provide a new means of determining the relative importance of chemical pathways for the production of organic compounds and aerosol (or "tholins") on Titan. Cassini measurements reveal two distinct mechanisms for organic synthesis (see recent reviews by Waite *et al.* [2009] and Cravens *et al.* [2009]). A new synthesis process that is largely driven by ion chemistry occurs in the ionosphere of Titan, above 1000 km, in addition to the neutral chemistry that occurs lower in the atmosphere [Yung *et al.*, 1984]. Fig. 6.4 shows that the isotopic fractionations by photoionization and photodissociation of N₂ — the starting points of these two synthetic processes — are distinct. Hence, measurements of the nitrogen isotopic composition of organic compounds and tholins could offer a powerful means to discriminate between their origins. While isotopic fractionation of nitrogen in the atmosphere of Titan due to neutral chemistry has been modeled by Liang *et al.* [2007], a similar study of isotopic fractionation of nitrogen due to ion chemistry has not been done. The experimental and modeling results presented here provide a strong motivation to pursue such a study.

6.4. Conclusions

The photoionization efficiency spectra measured for the isotope-specific non-dissociative photoionization of molecular nitrogen reveal experimentally for the first time the shifts in peak energies and changes in peak intensities for the autoionizing Rydberg states between 15.5 and 17.3 eV. The measured isotope shifts in the feature at 15.68 eV for $^{14}\text{N}_2$ have helped to clarify the peak assignment; the measurements do not agree with the calculated isotope shifts for the $v=44$ level of the $b^1\Sigma_u^+$ valence state, but rather they agree most closely with the predicted isotope shift for an autoionizing Rydberg state converging to the $v'=2$ level of the $A^2\Pi_u$ (although the $v'=1$ level cannot be completely ruled out due to the experimental energy resolution). The ratios of the PIE cross-sections reveal individual energies at which the photoionization of the common isotopologue, $^{14}\text{N}_2$, is favored by as much as a factor of 4. However, integrated over all energies, the results show that, under 'white light' and optically thin conditions, isotopic fractionation between N_2 and N_2^+ is small, with $J(^{15}\text{N}^{14}\text{N})/J(^{14}\text{N}_2) = 1.01 \pm 0.02$ and $J(^{15}\text{N}_2)/J(^{14}\text{N}_2) = 1.00 \pm 0.02$; when convolved with measurements of the solar spectrum at the top of atmosphere, the effects are not detectable, yielding $J(^{15}\text{N}^{14}\text{N})/J(^{14}\text{N}_2) = 1.00 \pm 0.02$ and $J(^{15}\text{N}_2)/J(^{14}\text{N}_2) = 0.98 \pm 0.02$. Incorporation of the measured photoionization cross-sections as a function of energy into a 1-D model of Titan's atmosphere shows that isotopic self-shielding can lead to ratios of J-values for $^{15}\text{N}^{14}\text{N}/^{14}\text{N}_2$ as high as 1.17, although this is almost 24 times smaller than that predicted to result from N_2 photodissociation using photodissociation cross-sections calculated theoretically [Liang *et al.*, 2007]. The large differences that the results presented here suggest for the isotopic fractionation of nitrogen in Titan's atmosphere by the photoionization versus photodissociation of N_2 may help to resolve current discrepancies between observations and models of the isotopic composition of HCN, which is a factor of 2 to 4 enriched in ^{15}N relative to the N_2 from which it is formed. In addition, the results also suggest that measurements of the isotopic composition of organic gases and aerosols could be used to establish the relative importance of ion versus neutral chemistry in the photochemical formation of these species in different regions of Titan's atmosphere. In general, these first measurements of isotope effects in the non-dissociative photoionization of N_2 demonstrate that this reaction is likely to play a previously ignored and potentially important role in isotopic fractionation in planetary atmospheres.

References

- Aikin, A. C. (2001), Isotope identification in NO as chemical tracer in the middle atmosphere, *Phys. Chem. Earth (C)*, 26(7), 527-532.
- Anicich, V. G. and M. J. McEwan (1997), Ion-molecule chemistry in Titan's ionosphere, *Planet. Space Sci.*, 45(8), 897-921.
- Cravens, T. E., R. V. Yelle, J. E. Wahlund, D. E. Shemansky and A. F. Nagy (2009) "Composition and structure of the ionosphere and thermosphere." In *Titan from Cassini-Huygens*, Editors, R. H. Brown, J. P. Lebreton and J. H. Waite, Springer, p.259-295.
- Cook, G. R. and P. H. Metzger (1964), Photoionization and absorption cross-sections of O₂ and N₂ in the 600- to 1000- Å region, *J. Chem. Phys.*, 41(2), 321-336.
- Cook, G. R. and M. Ogawa (1965), Photo-ionization of N₂ in the 735-804Å region, *Can. J. Phys.*, 43, 256-267.
- Dehmer, P. M., P. J. Miller, and W. A. Chupka (1984), Photoionization of N₂ X¹Σ_g⁺, v'' = 0 and 1 near threshold. Preionization of the Worley-Jenkins Rydberg series, *J. Chem. Phys.*, 80(3), 1030-1038.
- Fox, J. L. and A. Hać (1997), The ¹⁵N/¹⁴N isotope fractionation in dissociative recombination of N₂⁺, *J. Geophys. Res.*, 102(E4), 9191-9204.
- Gurwell, M. A. (2004), Submillimeter Observations of Titan: Global Measures of Stratospheric Temperature, CO, HCN, HC3N, and the Isotopic Ratios ¹²C/¹³C and ¹⁴N/¹⁵N, *Astrophys. J.*, 616, L7-L10.
- Halmann, M. and I. Laulicht (1965), Isotope Effects on Vibrational Transition Probabilities III: Ionization of Isotopic H₂, N₂, O₂, NO, CO, and HCl Molecules, *J. Chem. Phys.*, 43(5), 1503-1509.
- Herzberg, G. (1950), *Molecular Spectra and Molecular Structure. I. Spectra of Diatomic Molecules*, Van Nostrand-Reinhold, Princeton, New Jersey.
- Imanaka, H., and M. A. Smith (2007), Role of photoionization in the formation of complex organic molecules in Titan's upper atmosphere, *Geophys. Res. Lett.*, 34, L02204, doi:10.1029/2006GL028317
- Itikawa, Y., M. Hayashi, A. Ichimura, K. Onda, K. Sakimoto, K. Takayanagi, M. Nakamura, H. Nishimura, and T. Takayanagi (1986), Cross sections for collisions of electrons and photons with nitrogen molecules, *J. Phys. Chem. Ref. Data*, 15(3), 985-1010.
- Jungen, Ch., K. P. Huber, M. Jungen, and G. Stark (2003), The near-threshold absorption spectrum of N₂, *J. Chem. Phys.*, 118(10), 4517-4538.
- Kaye, J. A. (1987), Mechanisms and observations for isotope fractionation of molecular species in planetary atmospheres, *Rev. Geophys.*, 25(8), 1609-1658.
- Kostko, O., L. Belau, K. R. Wilson, M. Ahmed (2008), Vacuum-ultraviolet (VUV) photoionization of small methanol and methanol-water clusters, *J. Phys. Chem. A*, 112(39), 9555-9562.
- Lefebvre-Brion, H. (2005), Assignment in the near-threshold absorption spectrum of N₂, *J. Chem. Phys.*, 122, 144315.
- Lefebvre-Brion, H. and K. Yoshino (1993), Tentative interpretation of the Rydberg series converging to the A²Π_u state of N₂⁺, *J. Mol. Spectrosc.*, 158, 140-146.

- Liang, M. C., A. N. Heays, B. R. Lewis, S. T. Gibson and Y. L. Yung (2007), Source of nitrogen isotope anomaly in HCN in the atmosphere of Titan, *Astrophys. J. Lett.*, *664*, L115-118.
- Liu, X., D. E. Shemansky, C. P. Malone, P. V. Johnson, J. M. Ajello, I. Kanik, A. N. Heays, B. R. Lewis, S. T. Gibson, and G. Stark (2008), Experimental and coupled-channels investigation of the radiative properties of the $N^2 \text{ c}^4 \text{ } ^1\Sigma_u^+ - X^1\Sigma_g^+$ band system, *J. Geophys. Res.*, *113*, A02304, doi:10.1029/2007JA012787.
- Lofthus, A. and P. H. Krupenie (1977), The spectrum of molecular nitrogen, *J. Chem. Phys. Ref. Data*, *6*(R5.1), 113-307.
- Marten, A., T. Hidayat, Y. Biraud, and R. Moreno (2002), New millimeter heterodyne observations of Titan: Vertical distributions of nitriles HCN, HC₃N, CH₃CN, and the isotopic ratio ¹⁵N/¹⁴N in its atmosphere, *Icarus*, *158*(2), 532-544.
- McEwan, M. J. and V. G. Anicich (2007), Titan's ion chemistry: A laboratory perspective, *Mass Spectrom. Rev.*, *26*, 281-319.
- McCormack, E. F., S. T. Pratt, J. L. Dehmer, and P. M. Dehmer (1990), Double-resonance spectroscopy of autoionizing states of N₂ near the ionization threshold, *Phys. Rev. A*, *42*(9), 5445-5451.
- Nicolas, C., J. N. Shu, D. S. Peterka, M. Hochlaf, L. Poisson, S. R. Leone, and M. Ahmed (2006), Vacuum ultraviolet photoionization of C₃, *J. Am. Chem. Soc.*, *128*(1), 220-226.
- Niemann, H. B., *et al.* (2005), The abundances of constituents of Titan's atmosphere from the GCMS instrument on the Huygens probe, *Nature*, *438*, 779-784.
- Ogawa, M. and Y. Tanaka (1962), Rydberg absorption series of N₂, *Can. J. Phys.*, *40*, 1593-1607.
- Ogawa, M. (1964) Vibrational isotope shifts of absorption bands of N₂ in the spectral region 720 – 830 Å, *Can. J. Phys.*, *42*, 1964, 1087-1096.
- Samson, J. A. R., G. N. Haddad, and J. L. Gardner (1977), Total and partial photoionization cross-sections of N₂ from threshold to 100 Å, *J. Phys. B: Atom. Molec. Phys.*, *10*(9), 1749-1759.
- Sommavilla, M. and F. Merkt (2006), On the rotational structure of a prominent band in the vacuum-ultraviolet spectrum of molecular nitrogen, *J Electron Spectrosc. Rel. Phenom.*, *151*, 31-33.
- Sommavilla, M., U. Hollenstein, G. M. Greentham, and F. Merkt (2002), High-resolution laser absorption spectroscopy in the extreme ultraviolet, *J. Phys. B: At. Mol. Opt. Phys.*, *35*, 3901-3921.
- Trevis, R. and E. Herbst (2000), The possibility of nitrogen isotopic fractionation in interstellar clouds, *Mon. Not. R. Astron. Soc.*, *317*, 563-568.
- Wilson, E. H. and S. K. Atreya (2004), Current state of modeling photochemistry of Titan's mutually dependent atmosphere and ionosphere, *J. Geophys. Res.*, *109*, E06002.
- Vieitez, M. O., T. I. Ivanov, J. P. Sprengers, C. A. de Lange, W. Ubachs, B. R. Lewis, G. Stark (2007), Quantum-interference effects in the o¹Π_u(v=1)~b¹Π_u(v=9) Rydberg-valence complex of molecular nitrogen, *Molec. Phys.*, *105*(11), 1543-1557.
- Vinatier, S. B. Bézard, C. A. Nixon (2007), The Titan ¹⁴N/¹⁵N and ¹²C/¹³C isotopic ratios in HCN from Cassini/CIRS, *Icarus*, *191*, 712-721.
- Waite, J. H., *et al.* (2005), Ion Neutral Mass Spectrometer results from the first flyby of Titan, *Science*, *308*, 982-986.

- Waite, J. H., D. T. Young, T. E. Cravens, A. J. Coates, F. J. Crary, B. Magee, and J. Westlake (2007), The process of tholin formation in Titan's upper atmosphere, *Science*, *316*, 870-875.
- Waite, J. H., D. T. Young, J. H. Westlake, J. I. Lunine, C. P. McKay and W. S. Lewis (2009) "High-altitude production of Titan's aerosols." In *Titan from Cassini-Huygens*, Editors, R. H. Brown, J. P. Lebreton and J. H. Waite, Springer, p.201-214.
- Woods, T. N., F. G. Eparvier, S. M. Bailey, P. C. Chamberlin, J. Lean, G. J. Rottman, S. C. Solomon, W. K. Tobiska, and D. L. Woodraska (2005), Solar EUV Experiment (SEE): Mission overview and first results, *J. Geophys. Res.*, *110*, A01312, doi:10.1029/2004JA010765.
- Yung, Y. L., M. Allen, and J. P. Pinto (1984), Photochemistry of the atmosphere of Titan: Comparison between model and observations, *Astrophys J. Suppl. Ser.*, *55*(3), 465-506.